Development of a Liver Targeted Macromolecular Iron Chelator for the Treatment of Iron Overload

by

Usama Abbasi

BMLSc, The University of British Columbia, 2014

A THESIS SUBMITTED IN PARTIAL FULFILLMENT OF THE REQUIREMENTS FOR THE DEGREE OF

DOCTOR OF PHILOSOPHY

in

THE FACULTY OF GRADUATE AND POSTDOCTORAL STUDIES

(Pathology and Laboratory Medicine)

THE UNIVERSITY OF BRITISH COLUMBIA

(Vancouver)

November 2020

The following individuals certify that they have read, and recommend to the Faculty of Graduate and Postdoctoral Studies for acceptance, a dissertation entitled:

Development of a liver-targeted macromolecular iron chelator for the treatment of iron overload

submitted by   Usama Abbasi   in partial fulfillment of the requirements for

the degree of   Doctor of Philosophy

in   Pathology and Laboratory Medicine

Examining Committee:

Jayachandran N. Kizhakkedathu, Professor, Pathology & Laboratory Medicine, UBC
Supervisor

Mark Scott, Professor, Pathology & Laboratory Medicine, UBC
Supervisory Committee Member

Heather Leitch, Clinical Professor, Medicine, UBC
University Examiner

Shyh-Dar Li, Professor, Pharmaceutical Sciences, UBC
University Examiner

Additional Supervisory Committee Members:

Donald E. Brooks, Professor, Pathology & Laboratory Medicine, UBC
Supervisory Committee Member

Edward Pryzdial, Clinical Professor, Pathology & Laboratory Medicine, UBC
Supervisory Committee Member

Abstract

Patients with thalassemia, myelodysplastic syndromes, sickle cell disease and other acquired anemia require life sustaining and often repeated red blood cell transfusions. Since humans lack an iron excretion pathway, excess iron results in systemic iron overload either due to an underlying genetic component or acquired through disease pathogenesis or repeated transfusions. Toxicity arises from the generation of reactive oxygen species and elicits considerable damage. The resulting iron toxicity accounts for a majority of premature deaths, primarily from liver and heart dysfunction and failures. The current standard of care for the treatment of transfusion-dependent iron overload is iron chelation therapy, which effectively reduces the toxicity associated with labile iron by lowering the iron burden. However, the toxicity, shorter circulation time and non-specificity of the current iron FDA approved iron chelators proved challenging and patient compliance are poor for this life-long therapy.

Recently, Dr. Kizhakkedathu's team developed a macromolecular iron chelating system with decreased toxicity, increased half-life and iron excretion profiles compared to the current standard iron chelator, deferoxamine in mice. Further, since the discovery of the asialoglycoprotein receptor and its specificity for N-acetyl galactosamine, there has been significant research pertaining to liver targeting and delivery of various drugs. Thus, we hypothesize that a macromolecular iron chelating system conjugated with liver targeting groups would enhance the iron removal from liver thereby preventing complications due to iron overload.

In this thesis, a novel class of liver targeted macromolecular iron chelators were developed for the treatment of iron overload. The macromolecular scaffold was optimized for hepatocyte uptake *in vitro* and HPG-GalNAc$_{50}$ and HPG-TAG$_2$ were selected for iron chelation. The tolerability, biodistribution, and excretion of liver targeted iron chelating systems, HPG-DFO-GalNAc and HPG-DFO-TAG, were investigated *in vivo*. Remarkably, HPG-DFO-GalNAc and HPG-DFO-TAG exhibited significant hepatocyte accumulation with immediate lysosomal localization and subsequent rapid excretion with over 70% eliminated within 24 h. Liver targeted iron chelating systems with higher DFO units translated into superior systemic iron removal in a mice iron overload model. This thesis demonstrates the utility of liver targeted iron chelator for the removal of excess iron.

Lay Summary

Blood disorders, such as thalassemia, are a major global health concern and patients require regular blood transfusions. Over time, these patients develop iron-overload. This complication arises because blood transfusions introduce excess iron and humans lack ways to excrete iron. Excess iron is dangerous and can result in organ failure, particularly liver and heart failures, and death. Currently, iron overload is treated with drugs, referred to as chelators, that selectively bind iron. Since these chelators are readily excreted, iron is removed with them. However, these chelators are limited by their ability to remove iron and are toxic because they interact with other organs non-specifically. As such, iron overload remains a major concern affecting major organs, including the liver.

Currently, no liver targeted chelator exists. In this thesis, liver targeted chelators were developed by attaching chelators and liver specific sugars to a polymer. Liver targeted chelators removed iron better than current chelators.

Preface

Ethics approval was obtained from UBC for experiments conducted at the Center for Blood Research. All ethics approvals for mouse experiments were obtained from UBC and complied with the Canadian Council of Animal Care guidelines and animal care protocol (A18-0276). This dissertation was carried out with the supervision of Dr. Jayachandran N. Kizhakkedathu at the Center for Blood Research, UBC, Vancouver.

In **Chapter 1**, I was responsible for the literature review. Dr. Srinivas Abbina and Arshdeep Gill assisted in the section 1.3.2. **Figure 2** and **Figure 3** were made with the assistance of Ayşegulnur Kabaca. **Figure 4**, **Figure 5** and **Figure 9** were made by Dr. Srinivas Abbina and used in this thesis with his permission.

In **Chapter 2**, the synthesis of HPG was performed by Irina Chafeeva and Dr. Srinivas Abbina. The synthetic scheme for liver targeting systems (with and without chelators) and their controls were designed by Dr. Srinivas Abbina. The synthesis of these macromolecules were performed jointly, under his supervision. and the synthesis was conducted. I was responsible for the designing, conducting and analyzing all experiments. Under my supervision, Semipe Oni (summer intern and undergraduate academic assistant) conducted confocal microscopy experiments.

In **Chapter 3**, tritiated macromolecules were synthesized by Dr. Srinivas Abbina and I assisted as needed. All animal studies were performed at the BC Cancer Research Centre Investigational Drug Program under Dr. Nancy Dos Santos. Nicole Wretham managed all animal studies and worked with Maryam Oosooly. Together, Nicole and Maryam administered intravenous treatment injections, termination of mice, collected blood, and harvested and processed organs. For pharmacokinetic, biodistribution and excretion experiments, Nicole and Maryam conducted radioactivity measurements, and I analyzed all the results in consultation with Dr. Srinivas Abbina. For *in vivo* liver cellular distribution studies, Lily E. Takeuchi and I designed and analyzed the experiments, Nicole Wretham and her team handled the mice, and Lily E. Takeuchi, Iren Constantinescu and I performed data collection. For all *in vitro* studies, I designed, conducted and analyzed the experiments. For intracellular kinetic investigations, Dr. Libin Abraham was consulted for developing a fixation and staining protocol.

In **Chapter 4**, all animal studies were performed at the BC Cancer Research Centre Investigational Drug Program under the supervision Dr. Nancy Dos Santos and Nicole Wretham. Nicole and her team conducted injection administration, mice termination, harvested organs and collected blood. I processed and

analyzed all the collected mouse samples. The processing of liver and kidneys for histological examination was carried out by Wax-it Histology Services Inc.

In **Chapter 5**, I designed, conducted and analyzed all experiments. Under my supervision, Kendrew Wong (summer intern) and Vriti Bhagat (summer intern) conducted preliminary experiments for the unified-ferene assay.

Table of Contents

List of Tables

List of Figures

List of Symbols

Å	Angstrom
β	Beta
K_i	Binding affinity
°C	Degrees in Celsius
DPM	Disintegrations per minute
g	gram
G	Gravitational force or centrifugal force for centrifuges
kDa	Kilo Dalton
Kg	Kilogram
L	Liter
μg	microgram
μL	microliter
μm	micrometer or micron
μM	micromolar
mg	milligram
mL	milliliter
mM	millimolar
M	Molar

Mol%	Mole percentage
nm	nanometer
nM	nanomolar
ppb	Parts per billion
%	Percentage

List of Abbreviations

^{1}H-NMR or NMR	Proton nuclear magnetic resonance or nuclear magnetic resonance
7-AAD	7 – Aminoactinomycin D
AAS	Atomic absorption spectrometry
AF	Asialofetuin
ANOVA	Analysis of variance
APC	Allophycocyanin
ASGPR	Asialoglycoprotein receptor
BCA	Bradford Coomassie Assay
BSA	Bovine serum albumin
C57Bl/6	Mouse strain: C57 black 6
Cal-AM	Calcein acetoxymethyl ester
CD68	Cluster of differentiation 68, marker for Kupffer cells
CO_2	Carbon dioxide
DCF	2',7' –dichlorofluorescein
DCFDA / H2DCFDA	2',7' –dichlorofluorescein diacetate
DFO	Deferoxamine
DFO-Fe	Deferoxamine – iron chelated complex
DFP	Deferiprone

DFX	Deferasirox
DMEM	Dulbecco's minimum essential media
DMF	Dimethyl formamide
DMSO	Dimethyl sulfoxide
Dr	Dram
EDTA	Ethylenediamine tetraacetic acid
EEA1	Early endosomal antigen 1
EMEM	Eagle's minimum essential media
FAC	Ferric ammonium citrate
FDA	Food and drug administration (U.S. government body)
Fe	Iron
Fe^{2+} and Fe^{3+}	Ferrous and ferric iron, respectively
Fe-Dex	Iron-dextran
FITC	Fluorescein isothicyanate
GalNAc	N-acteylgalactosamine
GAPDH	Glyceraldehyde 3-phosphate dehydrogenase
Gluc	Glucose
h	Hour
H_2O_2	Hydrogen peroxide

H-Alk   HPG-Alkyne$_{115}$

HBSS   Hank's balanced salt solution

HCl   Hydrochloric acid

HD   HPG-DFO$_{15}$

HD$_{40}$-GalNAc   HPG-DFO$_{40}$-GalNAc$_{50}$

HD-GalNAc   HPG-DFO$_{15}$-GalNAc$_{50}$

HD-TAG   HPG-DFO$_{15}$-TAG$_2$

HeLa   Henrietta Lacks cervical cancer cell line

Hep3B   Hepatocellular carcinoma cell line

HepG2   Hepatocellular carcinoma cell line

H-GalNAc$_{20}$ HPG-GalNAc$_{20}$

H-GalNAc$_{50}$ HPG-GalNAc$_{50}$

H-GalNAc$_{70}$ HPG-GalNAc$_{70}$

H-Gluc$_{10}$ HPG-Glucose$_{10}$

H-Gluc$_{20}$ HPG-Glucose$_{20}$

H-Gluc$_{40}$ HPG-Glucose$_{40}$

H-Gluc$_{60}$ HPG-Glucose$_{60}$

HNO$_3$ Nitric acid

HPG   Hyperbranched polyglycerols

H-TAG$_2$	HPG-TAG$_2$
IC$_{50}$	Half-maximum inhibitory concentration or value
ICP-MS	Inductively coupled plasma mass spectrometry
ID	Injected dose
IgG	Immunoglobulin G
JC10	A dye used to assess mitochondrial membrane potential
LAMP1	Lysosomal associated membrane protein 1
LIP	Labile iron pool
MCC	Mander's co-localization coefficient
MTT	3-(4,5-dimethylthiazolyl-2)-2,5-diphenyltetrazolium bromide
MWCO	Molecular weight cut off
NTBI	Non-transferrin bound iron
OD 595 nm	Optical density at 595 nm
PBS	Dulbecco's phosphate buffered saline
PEG	Polyethylene glycol
pFe^{2+} or pFe^{3+}	Potential of ferrous or ferric iron
Rab7	Ras-like GTPase protein 7
RBC	Red blood cells
RNA	Ribonucleic acid

ROS	Reactive oxygen species
TAG	Tri-antennary N-acetylgalactosamine
TBI	Transferrin bound iron
TfR1	Transferrin receptor 1
u-ferene	The unified-ferene assay
UV-VIS	Ultraviolet-visibile

Acknowledgements

First and foremost, all praise is to the One and Only. All things come from Him. This has been a journey and through each and every struggle, I look back and I am glad and grateful for where I stand. This has not been the path I had planned to embark on but this was surely the path I was meant to take. May this work and may my journey be of righteous benefit for humankind, ameen.

This dissertation was conducted under the supervision of Dr. Jayachandran N. Kizhakkedathu. I am thankful for his guidance and for being approachable. I am grateful to my colleague and my mentor, Dr. Srinivas Abbina. He has been instrumental in my graduate journey over the past 6 years – from hashing out ideas, troubleshooting experiments, brainstorming next ideas and strategies, to his valued guidance on both academic and non-academic life ventures. He has been a real support system. Frankly, if it was not him for him, I would not have embarked on this Ph.D. journey. In addition, I would like to give a special shout out to Arshdeep Gill. We have shared many late nights in the lab and he has been a partner that made this journey all the more worthwhile.

In addition, I would like to extend my warm gratitude to former and present Kizhakkedathu team members including Dr. Manu Thomas Kalathottukaren, Dr. Prashant Kumar, Benjamin Lai, Iren Constantinescu, Irina Chafeeva, Dr. Narges Hadjesfandiari, Dr. Anil Parambath, Dr. Erika Siren, Lily E. Takeuchi, Sreeparna Vappala, Emaan Abbasi, Daniel Luo, Haisle Moon, Hossein Yazdani Ahmadabadi, Youping Li, Dr. Kai Yu, Chanel La, Dr. Yan Mei and the summer interns under my supervision, Semipe Oni, Kendrew Wong and Vriti Bhagat. I am also thankful for Dr. Libin Abraham who gave his time, guidance and personal insights.

I am grateful for my committee members; Dr. Edward L. G. Pryzdial (Chair), Dr. Mark Scott and Dr. Donald E. Brooks. Thank you for providing me with constructive criticism and sharing valued insights.

I would also like to thank the Investigation Drug Program at the BC Cancer Research Center for their assistance with the animal studies, especially Nicole Wretham and Dr. Nancy Dos Santos. I am also grateful to the funding agencies that have supported my research including the CIHR and CBR.

Finally, I am most grateful for the love and support from my family and friends – especially Samia El Joueidi and Rehmatullah Sheikh. Your endless and relentless love and support was integral to my success.

Dedication

This thesis is dedicated to my family: Mom and Dad wanted a doctor and they got one. Not that kind, but still a doctor. The emotions in this journey have been wild. And I am grateful for your love, your support and your encouragement. I am blessed and I have you to thank for. I love you. Emaan, you have been a silent passenger in this journey and your support has been incredible. Thank you family.

This thesis is dedicated to my friend and mentor: Dr. Srinivas Abbina. You are an inspiration. Never have I witnessed the human-form of passion and love for science. It has been contagious. While it is no secret that I embarked this journey after taking on your advice, I got a lot more out of it than we both know. You have been there every step of the way and I couldn't have asked for any one else to be a part of this research journey. Thank you.

This thesis is dedicated to my brother and partner in crime; Arshdeep Gill. Silent Thunder beats Velvet thunder or whatever. You have been there for me whenever need be – and I am genuinely grateful. Lots of love guy.

This thesis is also dedicated to Samia El Joueidi who entered my life through the thick of this research. This Ph.D. has been a journey for the both of us – we went from seeing each other to being engaged! And my goodness, I am so happy to have this journey turn into something bigger! I am thankful for your love, support and your faith in me. To all those late nights in the lab! I appreciate you – thank you for being an emotional, spiritual and mental pillar. To our next Ph.D. I love you.

Chapter 1: Introduction

1.1. Iron in the body

1.1.1. Role of Iron

Iron is an essential mineral for all eukaryotes; it serves as a prosthetic group for a variety of proteins involved in central cellular processes. These include DNA synthesis (e.g., ribonucleotide reductases, DNA polymerases)[1], respiration (e.g., cytochromes in the electron transport chain)[2] and oxygen transport (e.g., hemoglobin and myoglobin)[3]. Iron's unique ability to serve both as an electron donor and acceptor endows its versatility as a biological catalyst. However, this facile property that permits cyclic redox reactions has enormous damaging potential through the Haber-Weiss reaction[4–6] **(Figure 1)**; free redox active iron catalyzes the production of hydroxide anions and hydroxide radicals increasing cellular reactive oxygen species (ROS) resulting in non-specific oxidative damage.[5–7] These radical species disrupt metabolic functions resulting in cell cycle arrest[8] and apoptosis[9] through peroxidation of cellular organelles and biological molecules, including proteins, lipids and DNA.[10,11]

$$(1) \quad Fe^{2+} + H_2O_2 \rightarrow Fe^{3+} + OH^- + OH^{\cdot} \qquad \text{Fenton reaction}$$

$$(2) \quad Fe^{3+} + O_2^{\cdot} \rightarrow Fe^{2+} + O_2$$

$$(3) \quad O_2^{\cdot} + H_2O_2 \xrightarrow{Fe^{3+}} OH^- + OH^{\cdot} + O_2 \qquad \text{Haber-Weiss reaction}$$
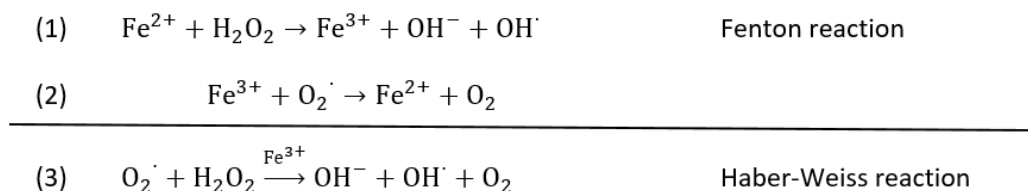
Figure 1. The Haber-Weiss reaction for the generation of hydroxyl radicals. The Fenton reaction (1) explains the decomposition of hydrogen peroxide by Fe(II). The sum of iron-mediated radical generation (3) is known as the Haber-Weiss reaction.

1.1.2. Iron homeostasis in the human body

Vertebrates have evolved highly specialized mechanisms to maintain cellular iron homeostasis via the coordinated regulation of iron uptake, storage, export, and recycling **(Figure 2A)**. The adult human body maintains a total of $3 - 5$ g of iron throughout their lifespan. Systemic iron homeostasis involves intestinal iron uptake, iron utilization in hemoglobin, iron recycling in the reticuloendothelial system and iron storage predominantly in the liver.

1
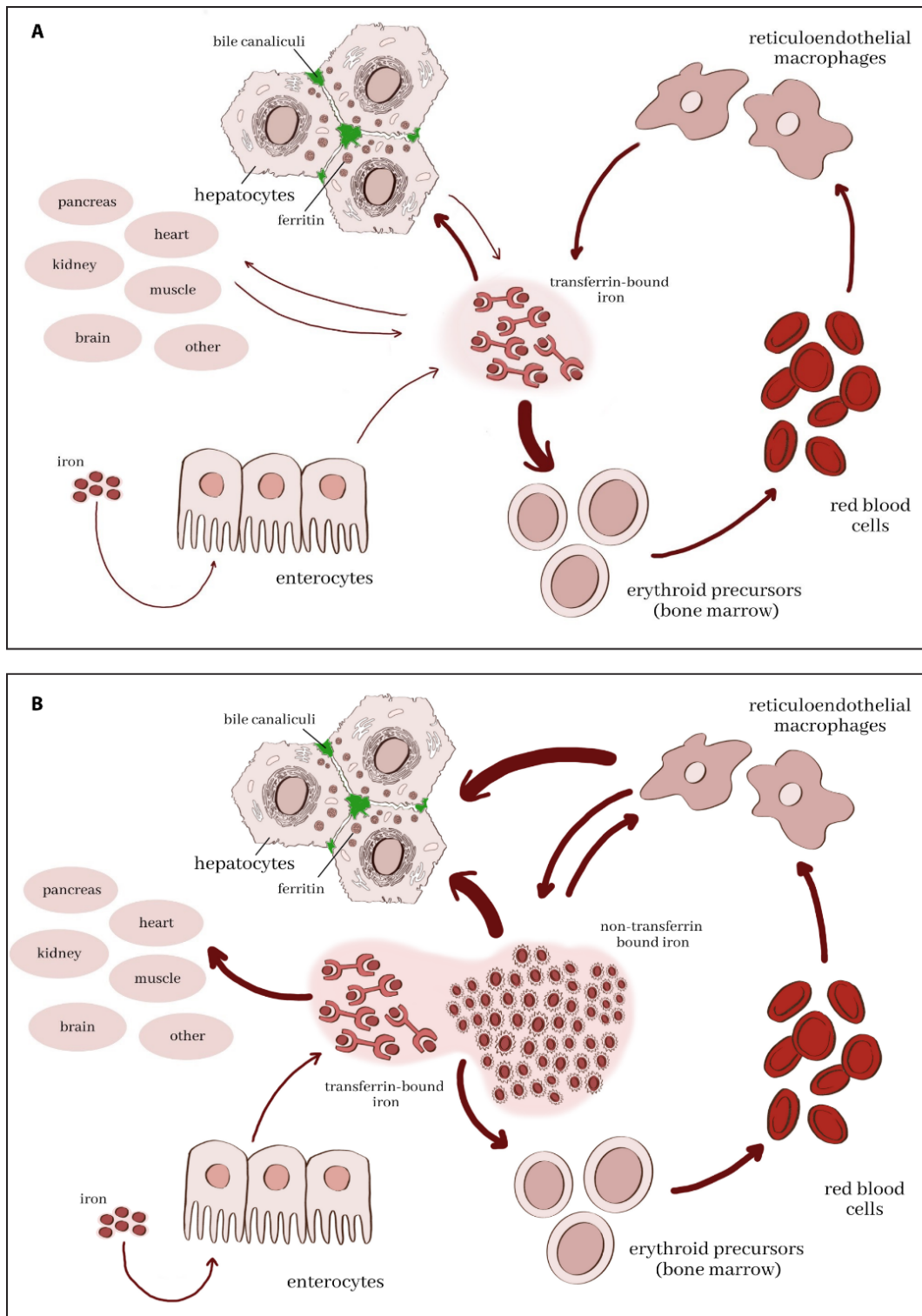
Figure 2. Iron acquisition, distribution and storage under (A) healthy and (B) iron overload conditions.

1.1.2.1. Iron acquisition

Normally, iron is only acquired through dietary iron, classified as either non-heme or heme iron, and accounts for minor obligate losses including desquamation and sloughed mucosal cells.[12–14] Since intestinal iron uptake is small, usually between 1 to 2 mg of iron per day, the regulation of iron uptake is critical because there is no known physiological pathway for iron excretion.

Dietary non-heme iron is absorbed at the brush border of duodenal enterocytes through the concerted action of the membrane-associated ferrireductase duodenal cytochrome B, which reduces ferric (Fe^{3+}) iron into ferrous (Fe^{2+}) iron, and the divalent metal transporter 1 (DMT1), which then transfers Fe^{2+} into the enterocytes.[15–17] Heme iron is taken up by a process that is not yet well characterized[18]; literature suggests that intestinal heme is possibly internalized via receptor mediated endocytosis[19,20] or by a high-affinity heme transporter, heme-responsive-gene-1[21,22].

1.1.2.2. Iron transport and utilization

Iron is then transported out of the enterocytes, through the only known iron exporter – ferroportin, and shuttled by transferrin (Tf) via the portal blood for downstream metabolism systemically. Ferroportin, encoded by the *SLC40A1* gene, is responsible for cellular iron export in other cells including macrophages and hepatocytes.[23–25] In enterocytes, the basolaterally located ferroportin works in conjunction with the membrane-bound hephaestin or soluble ceruloplasmin, ferroxidases that oxidize Fe^{2+} to Fe^{3+}, to load extracellular iron into Tf.[14,24,26,27] Transferrin (Tf), an abundant plasma transport protein that tightly binds ferric iron (Fe^{3+}), is responsible for almost all of the distribution of iron within circulation.[28] Holo-Tf maintains two Fe^{3+} ions in a redox-inert state whilst facilitating regulated iron transport and uptake.

Almost all dietary iron is incorporated into heme. The majority of heme synthesis takes place in developing erythroid cells in the bone marrow, whereas the remaining occurs in the liver.[29] The heme pathway is a series of sequential reactions that takes place in both the mitochondria and the cytosol.[29–31] Heme is an essential co-factor involved in multiple biological processes including oxygen transport and storage, electron transport and as a catalyst for redox reactions.[31]

Analogous to heme, iron-sulfur clusters serves as prosthetic groups required for a wide variety of proteins involved in electron transport, forming substrate binding sites and promoting enzymatic process, and acting as metabolic sensors.[3,32] This is another major metabolic pathway that consumes iron within the mitochondria

1.1.2.3. Iron recycling and storage

Macrophages in the reticuloendothelial systems, particularly the liver and the spleen, phagocytose and clear senescent or damaged red blood cells (RBCs) from circulation in order to recycle the iron.[33] Engulfed RBCs are digested by hydrolytic enzymes in phagolysosomes releasing heme from hemoglobin, which is then degraded by heme oxygenase 1 to release iron, biliverdin and carbon monoxide.[22] In doing so, the recycled iron is either reincorporated in the bone marrow by erythrocyte precursors as heme or stored in hepatocytes.[33]

Iron is safely stored with ferritin. Ferritin serves as an iron depot and its biological significance is two fold; first, the combination of heavy and light chains that fold in a helical bundle result in a large cavity that can accommodate up to 4500 iron atoms, and secondly, ferritin sequesters redox-active ferrous iron into a stable inert ferric iron coordinated with the ferrihydrite core of ferritin.[3,34–36]

Under normal conditions, liver is the primary organ for iron storage since hepatocytes are the major site for ferritin synthesis. As a result, the liver plays a critical role between iron storage and systemic iron homeostasis.

1.1.2.4. Systemic iron regulation

Systemic iron homeostasis is primarily regulated by hepcidin. Hepcidin is an iron regulatory peptide hormone predominantly produced by hepatocytes.[37–42] While, hepcidin is also synthesized by macrophages and cells in other non-hepatic tissues, only hepatocyte-derived hepcidin regulates systemic iron homeostasis.[27,42–45] To date, hepcidin is only known to be transcriptionally regulated; stimulatory pathways include iron loading and inflammation, while inhibitory pathways include iron deficiency, hypoxia and erythropoiesis.[44,46] Hepcidin expression is regulated by both plasma iron and tissue iron stores, which may allow both iron status indices to regulate systemic iron.[44]

The hepcidin/ferroportin axis is the primary regulator for systemic iron homeostasis because hepcidin modulates the expression of ferroportin. At a molecular level, hepcidin binds to ferroportin and induces ubiquitination of lysine residues in the cytosolic loop of ferroportin within minutes.[47] This induces endocytosis of ferroportin for subsequent proteolysis in the lysosomes.[47–49] It is unclear whether internalization is mediated by clathrin or other alternate endocytic machinery.[50] Therefore, under iron replete conditions, hepcidin expression is up regulated to decrease intestinal absorption of iron and the efflux of iron into circulation by decreasing ferroportin expression.[33] While, under iron deplete conditions, dietary iron absorption is increased by down regulating hepcidin expression in order to increase ferroportin expression on enterocytes thereby increasing the efflux of iron in circulation.[33]

1.1.3. Cellular iron

1.1.3.1. Metabolically active iron

In circulation, greater than 95% of iron is bound to transferrin.[33] At a cellular level, transferrin-bound iron (TBI) is acquired via receptor-mediated endocytosis following the interaction between holo-Tf and its receptor, the ubiquitously expressed transferrin receptor 1 (TfR1).[26,51] Acidification of the endosome induces a conformational change in the Tf:TfR1 complex, releasing Fe^{3+}. The liberated iron is reduced by a ferrireductase, STEAP3, and transported across the endosomal membrane into the cytosol by DMT1.[51,52] The apo-Tf:TfR1 complex is shuttled back to the cell surface, where the apo-Tf is recycled back into the blood stream.

Alternatively, under pathophysiological conditions of iron overload, excess iron circulates bound to a mixture of low-molecular weight molecules, collectively referred to as non-transferrin-bound iron (NTBI).[53,54] NTBI is rapidly taken up by hepatocytes along the sinusoidal membrane; a reductase converts Fe^{3+} of NTBI to Fe^{2+}, possibly by prion protein[55,56], which then translocates *via* the ZIP14 transmembrane metal-ion transporter.[57–59]

Newly acquired cellular iron enters a poorly-characterized, transient pool of redox-active iron complexes – the labile iron pool (LIP).[60–62] The evidence for the existence of such a pool comes from studies that mobilize intracellular iron with chelators, which suggest that the LIP exists as a mixture of low molecular weight complexes.[30,63] Recent investigations suggest the presence of iron chaperone proteins that maintain and distribute iron in a redox-stable state; monothiol glutaredoxins are involved in cytosolic iron

distribution and iron-sulfur cluster assembly, and mammalian poly(C)-binding proteins have been identified as chaperones involved in ferritin mineralization and by binding to DMT1 to regulate the influx of iron from Tf-TfR1 receptor mediated endocytosis.[64–69]

The LIP plays a key role in cellular iron homeostasis as it serves as a cross-roads of metabolic pathways.[62] As such, the LIP was exclusively thought to exist in the cytosol, however emerging evidence indicates the presence of LIP in other subcellular compartments including the nucleus, mitochondria – the main site for iron metabolism involving heme and iron-sulfur cluster synthesis – and endosomes/lysosomes – involved in the degradation of iron-containing molecules and organelles.[70–72] **Figure 3** is a diagrammatic representation for the fate of cellular iron.
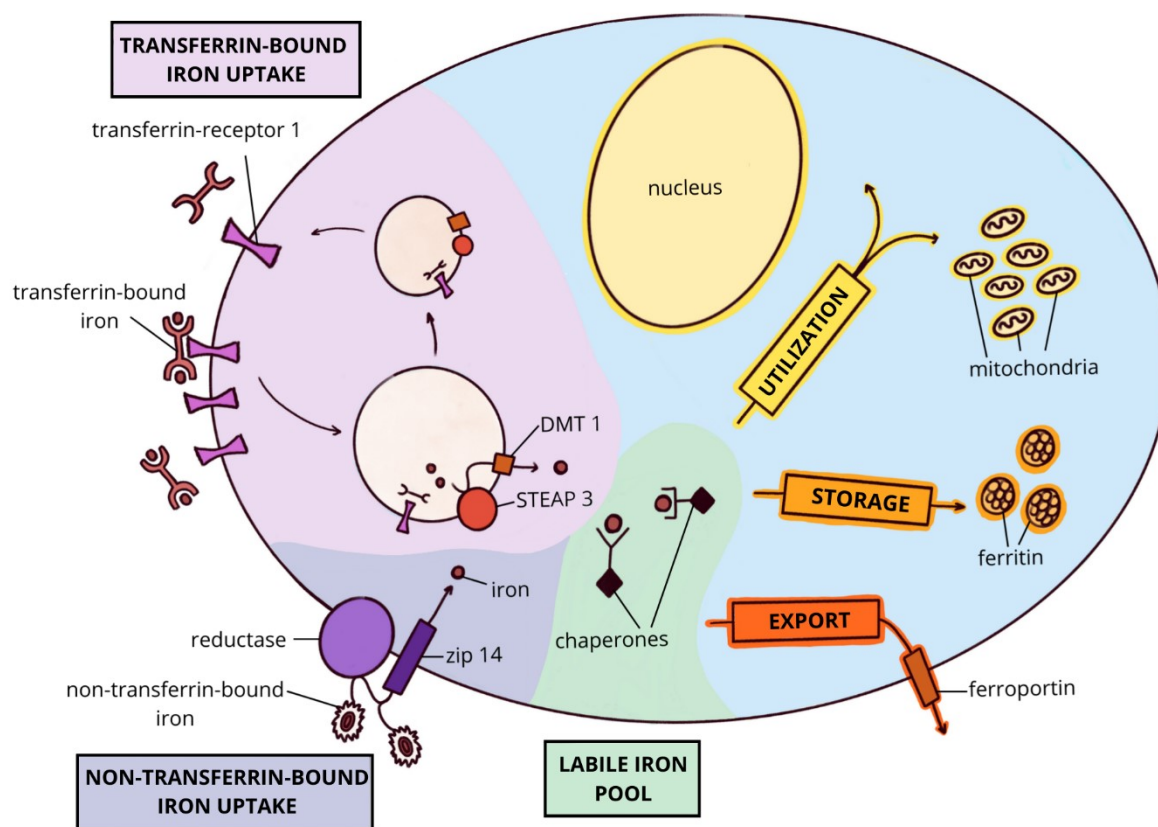
Figure 3. Diagrammatic representation of the fate of cellular iron. Cells acquire iron either as transferrin-bound iron (under normal conditions) or non-transferrin-bound iron (under pathological conditions of excess iron). Once internalized, this iron enters a labile iron pool. Depending on the cellular demands, this iron is either utilized, stored or exported back into circulation.

1.1.3.2. Cellular iron regulation

Cellular iron homeostasis is distinct from systemic iron regulation in order to meet its individual iron requirement. Cellular iron uptake, storage and export is regulated post-transcriptionally by the mRNA binding proteins iron regulatory protein (IRP) and iron response elements (IRE) system.[73,74] IRPs bind to the IREs in the untranslated regions (UTRs) of mRNA transcripts of key proteins in iron metabolism; IRP binding to IREs in the 5' UTRs result in suppressing the translation of the mRNAs including ferritin and ferroportin, whereas IRP binding to IREs in the 3' UTRs result in enhancing stability of mRNAs including transferrin receptor 1 (TfR1) and divalent metal transporter 1 (DMT1).[26,73]

This IRP-IRE system enables rapid changes in key iron metabolism proteins in response to intracellular iron concentration.[73,74] Under iron-replete state, IRPs have decreased IRE binding activity which results in increase translation of iron storage and export proteins, ferritin and ferroportin, and decreased translation of iron uptake proteins, TfR1 and DMT1.[23,52] The opposite occurs under iron-deplete state; IRPs readily bind to IREs which result in decrease translation of ferritin and ferroportin, and increased translation of TfR1 and DMT1.

1.2. Iron overload

Humans lack a proper physiological pathway for the removal of iron. Consequently, iron homeostasis relies on a complex feedback mechanism between iron acquisition, utilization and storage. Iron overload disorders can develop and iron can accumulate in the liver due to a disturbance in iron homeostasis **(Figure 2B)**, which results in a wide array of conditions and diseases; 1. Primary iron overload – a genetic predisposition that impacts key elements of iron homeostasis results in various types of hereditary hemochromatosis, 2. Secondary iron overload – hemosiderosis develops secondary to systemic diseases, typically due to ineffective erythropoiesis, and the subsequent regular transfusions needed to ameliorate it, and 3. Cirrhosis-related hemosiderosis due to chronic liver diseases and dietary iron overload.[75–79]

1.2.1. Primary iron overload

Iron overload in hereditary hemochromatosis (HH), also referred to primary iron overload, is due to a genetic predisposition that mis-regulates key elements involved in iron homeostasis – including the HFE protein, hepcidin production, transferrin receptor 2 and ferroportin, which result in an abnormal increase

in iron absorption.[80] HH presents with increased iron biomarkers, such as serum iron and ferritin concentrations, total iron-bind capacity, serum transferrin saturation, and hepatic iron concentrations.[81] Moreover, iron deposits in parenchymal organs, notably the liver amongst others, and may result in cirrhosis, cardiomyopathy and diabetes.[80] The risk of liver cancer also increases by 200 fold.[80]

Most cases of HH are associated with a mutation in the HFE gene, clinically classified as Type 1 HH. The HFE protein complexes with transferrin receptor 2 control hepcidin regulation.[82] Consequently, abnormal HFE protein results in excessive iron accumulation by decreasing hepcidin production and secretion from the liver, as well as over stimulating iron absorption in duodenal enterocytes.[83,84] The average prevalence for type 1 HH was 0.4% for homozygous mutations and 9.2% for heterozygous mutations.[83,85] Despite the high prevalence, the penetrance was low due to the autosomal recessive inheritance as well as other genetic and environmental factors affecting the phenotypic presentation.[83]

Non-HFE hemochromatosis are rarer forms of HH, with allele frequencies below 0.001%.[83] In juvenile hemochromatosis, also classified as Type 2 HH, hepcidin production is decreased due to a mutation in the transcription regulator, hemojuvelin (Type 2A HH), or in the hepcidin peptide itself (Type 2B HH). This form of hemochromatosis presents before the age of 30 years.[80] Further, mutations in the transferrin receptor 2 (TfR2) are classified as Type 3 HH. Although the function of TfR2 is presently unknown, current works propose a regulatory role for TfR2 involved in the activation of hepcidin.[86] Lastly, mutations in ferroportin, classified as Type 4 HH, also result in iron overload though the phenotypic presentation can vary. Mutations in ferroportin can result in either a loss of sensitivity to hepcidin, which results in an iron overload similar to hepcidin deficiency, or in a loss of iron export function, which results in iron accumulating predominantly in macrophages.[83,87]

1.2.2. Secondary iron overload

In secondary iron overload, hemosiderosis occurs secondary to hematologic disorders associated with ineffective erythropoiesis. Main erythroid disorders that can lead to iron overload include the thalassemia syndromes, sideroblastic anemias, congenital dyserythropoietic anemias and acquired myelodysplastic syndromes.[88] Inherited hemoglobin disorders are considered as the most pervasive monogenic diseases worldwide.[89] Thalassemia syndromes arise from a genetic mutation from either defective α-globin and β-globin synthesis. While mutations in α-globin are typically asymptomatic, impaired β-globin production results in the expansion of erythroblasts and leads to chronic anemia.[28,90] It is estimated that 1% to 5% of

the global population are carriers for thalassemic mutations and this disease is highly prevalent the regions surrounding sub-Saharan Africa, the Mediterranean and the Middle East, and the Indian subcontinent.[89] Alongside this, myelodysplastic syndromes (MDS), a heterogenous group of myeloid neoplasms, are associated with ineffective and irregular hematopoiesis that affects 4 individuals out of every 100,000 individuals in the United States with the incidences substantially rising with age.[91]

Patients suffering from ineffective erythropoiesis undergo rapid iron turnover, over 10 times greater than individuals with normal erythropoiesis[77], and experience increased intestinal resorption of iron.[92] In addition to this, patients also require frequent and chronic red blood cell transfusions to address the ensuing anemia.[75,76] A patient is deemed to be transfusion-dependent when they receive an average of 2 RBC units per month.[93] Despite strict monitoring of serum ferritin levels and liver iron concentrations, iron overload and hemosiderosis can still develop.[93]

Each transfusion introduces approximately 250 mg of iron; transfused heme-bound iron gets turned over as they near the end of their life span and recycled for further use.[94] Initially, this excess iron is safely bound to transferrin or stored in ferritin within reticuloendothelial macrophages.[76] As the iron burden increases beyond the capacities of macrophages, excess iron is stored within hepatocytes.[95] Under normal physiological conditions, liver iron content is usually less than 1 mg iron per gram of liver.[96] However, in patients suffering from iron overload, the liver iron content can exceed 15 to 20 mg iron per gram of liver.[97] Gradually, the accumulation of iron saturates transferrin and gives rise to non-transferrin-bound-iron (NTBI) in the serum, which is rapidly taken up by various organs, including the liver, heart, brain, and pancreas, contributing to the redox-active intracellular labile iron pool.[53,54,60,61] Hemosiderin deposits also accumulate within various tissues.[98–100] The increase in bioactive iron induces oxidative stress and damage, resulting in the clinical manifestation of liver fibrosis, cirrhosis and hepatocellular carcinoma.[94] Liver dysfunction and failure, along with heart failure, account for over 75% of premature deaths in patients despite extensive treatment.[101,102]

1.2.3. Cirrhosis-related iron accumulation

Chronic liver disease (CLD) results in the progressive destruction of regenerative parenchyma leading to fibrosis and cirrhosis. Cirrhosis disrupts liver architecture, with fibrotic bands and vascular distortion, and leads to portal hypertension and liver failure. There are various etiologies for CLD that are either metabolic – non-alcoholic fatty liver disease, viral – hepatitis infections, toxin-induced – most commonly seen in alcoholic liver disease, or autoimmune diseases.[103–106] CLD incidences have been reported to increase

annually, ranging from 1% to 2%.[103,107] In 2017, 1.5 billion persons had CLD resulting from non-alcoholic fatty liver disease (60%), hepatitis infections (38%) and alcoholic liver disease (2%).[108,109] CLD also accounted for 3.5% of deaths worldwide.[110]

Non-alcoholic fatty liver disease (NAFLD) includes a spectrum of liver dysfunctions including hepatic steatosis, non-alcoholic steatohepatitis and cirrhosis.[103,108] Characteristic findings pertaining to iron biomarkers in patients for NAFLD include hyperferritinemia, normal to mildly elevated transferrin saturation, and mild liver hemosiderosis.[103] Although the mechanism for excess iron observed in NAFLD is still sought after, it is believed to be due to the combination of iron leakage, from necrosis and cell death, and leptin-induced hepcidin production which results in iron accumulation in Kupffer cells.[103]

Hepatitis infections are often asymptomatic but can lead to liver damage. Hepatic iron accumulation and iron overload are mainly found in patients infected with hepatitis C virus – 30% to 40% of patients have elevated iron biomarkers including serum iron, ferritin and transferrin saturation.[103] Recent findings suggest a hepatitis C virus-mediated suppression of hepcidin transcription which leads to iron accumulation.[103]

Alcoholic liver disease (ALD), which includes hepatitis, steatosis, fibrosis and cirrhosis, is a major liver disease in developed countries and characterized by hepatic iron overload in half of its patients.[103] ALD is associated with elevated serum ferritin concentration, transferrin saturation, liver iron content, and a decrease in hepcidin levels.[103] Ethanol has been proposed to down-regulate hepcidin, which increase intestinal iron absorption and the efflux of iron into circulation.[103] Excess hepatic iron and ethanol cause oxidative stress which exacerbates liver injury.

While the underlying mechanisms leading to cirrhosis-related hemosiderosis is still under investigation, iron accumulation is often associated with disease progression and further complications leading to hepatocellular carcinoma.[103,108]

1,2-HOPO **3-hydroxypyranone** **Catechol** **Hydroxamate** **PBT2** **Coumarin**

N,N'-di(2-hydroxybenzyl)ethylenediamine-N,N'-diacetic acid (HBED) **CN128** **M30** **Deferasirox**

Dopamine receptor agonist hybrids (D607) **Curcumin** **Desferrioxamine** **FBS0701**

Deferiprone **Semicarbazone derivatives (pyridoxal isonicothinoyl hydrazone)(PIH)** **Desferrithiocin derivatives**

Figure 4. The structures of reported iron chelators - both FDA approved and potential candidates.

1.3. Iron chelation in the treatment of iron overload

The current standard of care for the treatment of transfusion-dependent iron overload is iron chelation therapy utilizing small organic molecules (**Figure 4**); iron chelators bind specifically to iron (III) and these chelates are readily eliminated *via* the urine and/or feces, hence lowering the iron burden.[76,77,94,111] As such, iron chelation treatment lowers the redox active iron concentrations and, subsequently, reduce oxidative damage and iron-induced toxicities.[5,7,60,112–114] The design of these chelators require optimized circulation half-life, high specificity and affinity for iron, cell membranes permeability, toxicity, tolerability, and mode of administration to have maximal efficacy.

Iron chelation is used to manage the iron burden in patients, who suffer from hemoglobinopathies or myelodysplastic syndromes, receiving upwards of 10 transfusions.[94] In addition to transfusion dependent iron overload pathogenesis, iron chelators have been extensively investigated as a potential therapy in different diseases including cancer, neurodegenerative diseases, diabetes, and infections.[115–127] Currently, there are only 3 FDA approved iron chelators (**Figure 4)**; deferoxamine (DFO, Desferal, desferrioxamine mesylate), deferiprone (DFP, L1, Ferriprox), and deferasirox (DFX, Exjade, Jadenu).

1.3.1. FDA approved chelators

1.3.1.1. Deferoxamine

Desferal is the first iron chelator to be FDA approved in 1968. This hexadentate fungal siderophore stably binds iron, at a 1:1 molar ratio with an iron binding affinity of 26.6 (p[Fe^{3+}]), such that it is no longer redox active.[4,128] The iron chelated is from DFO interacting with either NTBI present in plasma which is then renally cleared or hepatocellular iron, after being actively acquired, which undergoes biliary excretion.[94,128–130] DFO chelation therapy has been shown to effectively reduce serum ferritin, hepatic and myocardial iron burden.[131–133] The effectiveness of DFO is demonstrated by improved survival, with a significant drop in mortality by age 20, and decreased morbidity, with a reduction in the incidence of iron-induced heart disease, diabetes and hypogonadism.[128,134]

However, the main limitation is poor adherence due to the mode of administration as well as the adverse effects. DFO chelation requires either intravenous or subcutaneous administration over 8 to 24 hours a day, 5 to 7 days a week at a dose of 20-40 mg/kg/day. This is because it is not orally available, due to its

large hydrophilic structure, and has a very short half-life of 20 to 30 minutes.[4] In addition, patients can also experience severe neurotoxicity, hypersensitivities and ophthalmological impairment at these doses.[101,130,135–137] In the event of an infection, patients no longer receive DFO since it DFO is a siderophore and iron bound to DFO can be used by bacteria, viruses and fungi.

1.3.1.2. Deferiprone

Deferiprone underwent clinical trials in the 1980s and was licensed in several countries in the 1990s before being approved by the FDA in 2011. This small molecular weight synthetic bidentate chelator that binds iron with an iron binding affinity of 19.9 (p[Fe^{3+}]) at 3:1 molar ratio of chelator to iron.[128,138] This small lipophilic chelator is administered orally, in 3 divided doses, and has a half-life between 3-4 hours.[4,138]

In patients suffering from transfusional iron overload secondary to thalassemia, DFP chelation therapy significantly lowers serum ferritin, similar to DFO after 12 months.[139] The effect was greater in patients with higher serum ferritin baselines, upwards of 2,500 µg/L.[140,141] Furthermore, DFP can also mobilize intracellular iron from the liver and the heart, although its efficacy is conflicted. An average decrease in liver iron concentrations was reported at 30 months of chelation, however, several other trials showed an initial decrease at 6 months followed by an increase at the 33rd month of chelation.[111,142,143] Similarly, a reduction in myocardial iron burden was observed at higher DFP dose (92 mg/kg) with improved heart functions, but not at a lower dose of 75 mg/kg.[139,142]

Oral administration of DFP offers an advantage with regards to patient compliance and there are several clinical trials underway investigating different oral formulations for improved pharmacokinetic and pharmacodynamic properties.[144,145] However, efficacy with DFP therapy is greatly limited because it is readily metabolised by the liver, which diminishes the iron coordination.[138,146] Due to the 3:1 stoichiometry required to stably bind iron, incomplete iron chelation can still render them to be redox active and elicit subsequent oxidative damage.[138,147,148] Moreover, patients can also experience severe side effects including gastrointestinal discomfort, agranulocytosis and neutropenia.[138]

1.3.1.3. Deferasirox

Deferasirox is the most recent iron chelator to be approved by the FDA, in 2005, for the treatment of transfusion associated iron overload.[128,149] This synthetic tridentate iron chelator binds to iron at a stoichiometric ratio of 2 chelator per iron, with an iron binding affinity of 22.6 (p[Fe^{3+}]).[128] DFX is also orally bioavailable, like DFP, and, due to its half-life of 12-16 hours, it allows for a once-daily administration.[128,149] This chelator has the longest circulation time of all the FDA approved iron chelators and is present in plasma for more than 24 hours with 90% in the free drug from.[150]

Iron chelation therapy with DFX has shown a significant reduction in serum ferritin, liver and heart iron burden.[131,133,151,152] A dose-dependent reduction in serum ferritin and liver iron content was observed over a 1 year period in thalassemia major patients; treatment with 20 mg/kg DFX daily stabilized serum ferritin and maintained liver iron content, whereas treatment with 30 mg/kg DFX daily significantly reduced both serum ferritin and liver iron content.[131] When comparing DFX to DFO, DFX significantly reduced serum ferritin whilst having similar safety evaluations as DFO.[131,153] In addition, similar to DFO, DFX significantly reduced cardiac iron.[132]

DFX offers significant improvement in patient compliance, due to its daily oral dosing and long half-life, as well as being the first to be formally assessed in children as young as 2 years old.[154] Despite this, several studies report severe side effects including renal toxicity, thrombocytopenia, gastrointestinal discomfort and hepatic dysfunction.[128,155]

1.3.2. Advancements for iron chelators

So far, only three chelators are approved by FDA for iron chelation therapy and numerous chelators have been in different stages of clinical trials. As such, there is value in designing and developing new Fe(III) specific chelators with ideal properties; chelators must have a high therapeutic index with minimal toxicity to allow for the mobilization and elimination of labile iron, from the plasma as well as intracellularly, such that it offers hepatic and cardiac protection from iron-induced toxicity. In addition, the mode of administration and dosage will impact patient compliance and the subsequent economic burden.

1.3.2.1. Small molecule iron chelators

There is a huge demand in designing and developing new Fe (III) specific chelators with ideal properties including high iron binding, efficacy, and excretion with minimal toxicities. A number of chelators, including family of hydroxypyridinones, polyphenols, semicarbazones (PIH) desferrithiocin derivatives, clioquinols (PBT2), curcumin hybrids, and dopamine receptor agonist hybrids (D607) have been intensively investigated in different preclinical as well as clinical studies.[115,116,156–166] For example, in order to improve selectivity toward iron (III), N,N'-bis(2-hydroxybenzyl)- ethylenediamine-N,N'-diacetic acid (HBED) was developed, which binds with ferric iron very strongly (log $K1$ = 40).[164] In addition, hydroxypyridinone and hydroxypyranone hexadentante ligands were synthesized with varying iron binding constants ranging from pFe^{3+} 27.6 to 23.5.[165]

Moreover, a desferrithiocin derivative FBS0701, is currently studied in different clinical trials, particularly, for treating thalassemia and sickle cell anemia with transfusional siderosis.[162,163] In a multicentre phase 2 study, the safety and tolerability of FBS0701 at therapeutic doses compared favourable with other oral chelators. Further, this novel oral once-daily chelator also demonstrated iron chelation efficacy by decreasing liver iron content in at least 44% of the patients over a 24-week period.[162,163] FBS0701 has also been investigated as an antimalarial agent and blocks transmission.[166]

1.3.2.2. Macromolecular iron chelators

Low molecular weight iron chelators are often associated with toxicities, due to non-specific distribution and off-site interactions, as well as relatively short circulation half-lives. Macromolecular approaches circumvent these shortcomings, principally by increasing their molecular mass, and have been well documented in enhancing iron chelator's biological activity.[167–171] Macromolecular approaches can be categorized intro three broad classes **(Figure 5)**; polymeric iron chelators, polymer conjugates of small molecular chelators, and polymeric nanoparticle formulations.
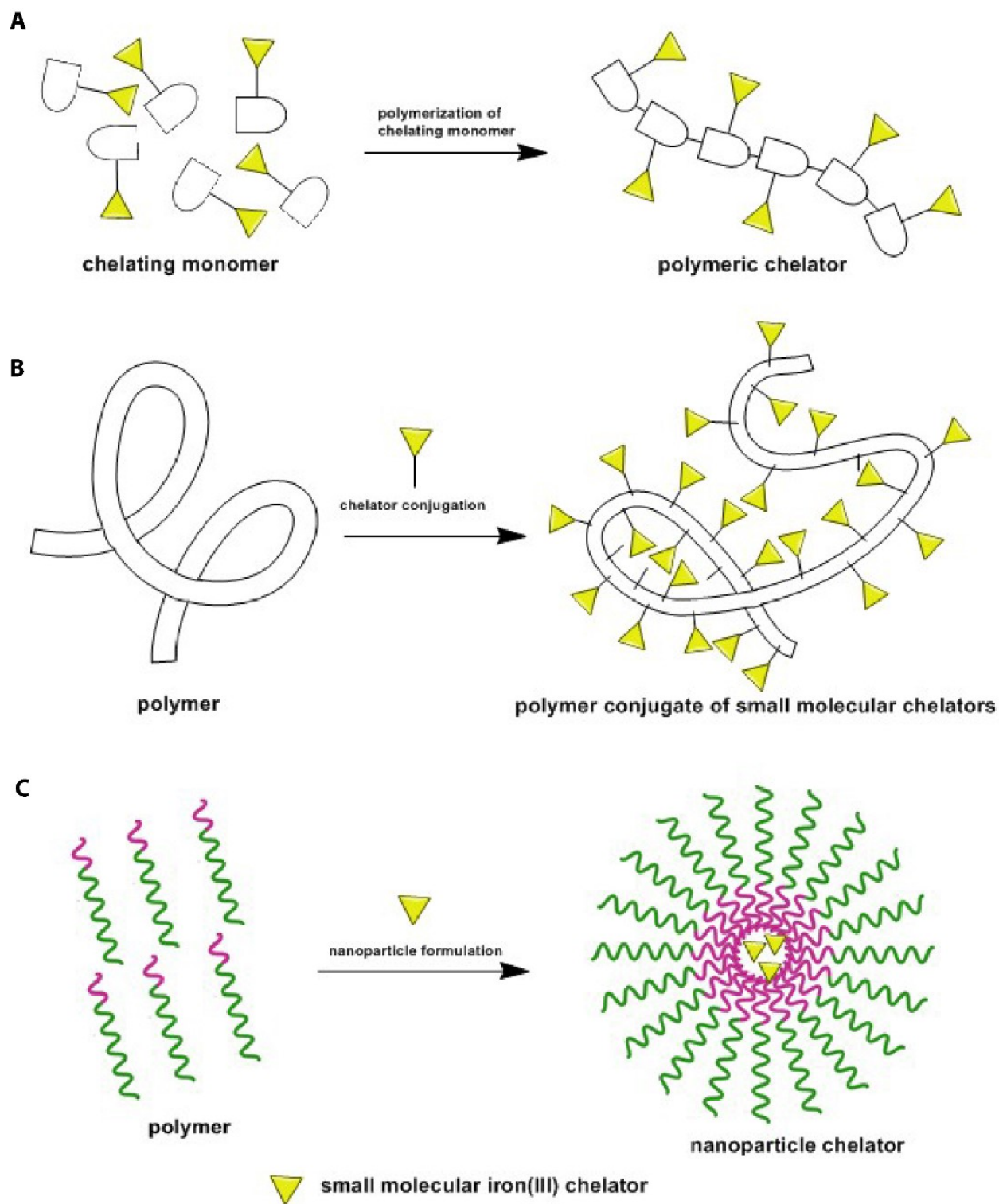
Figure 5. A visual representation of macromolecular chelators - **(A)** polymeric chelators, **(B)** polymer conjugates of small molecular chelators, and **(C)** polymeric nanoparticle formulations.

Polymeric iron chelators

Polymeric chelators are polymers that have inherent chelating moieties present as part of their backbone. Most often the monomer itself acts as an iron chelator and is incorporated into the polymer backbone to generate a macro-chelator **(Figure 5A)**.[172] This approach allows for higher binding affinities for iron because the flexibility in the backbone can enable better coordination bonds and sequester iron in the interior of the polymer.[172–174] Further, surface modifications of polymeric iron chelators can also improve its cell targeting ability. Various polymeric chelators of the hexadentate monomeric chelator, hydroxypyridin-4-one, are well known for their enhanced solubility and high iron binding coefficients.

For instance, polymeric chelator was developed via copolymerization of 3-hydroxypyridin-4-one and 2-hydroxyethyl acrylate and showed a binding constant of 10^{33} for Fe(III), which is relatively high in comparison to other small molecule Fe (III) chelators such as DFO.[172] Similarly, a multiple hydroxamic acid containing PEG-type tri block polymeric chelators exhibited a polymeric architecture-dependent iron binding constants ranging from log K_1 of 11 to 28.3.[175] Further, a novel co-polymer chelator, DIBI (poly[(N-vinylpyrrolidone)-co-(3-hydroxy-1-[N-(methacrylamido)ethyl]-2-methylpyridin-4(1H)-one), exhibited *in vivo* anti-infective activity in 2 distinct methicillin-resistant Staphylococcus aureus mouse models, as well as anti-inflammatory and anti-bacterial effects in an experimental sepsis model.[174,176–178]

These systems have demonstrated potential clinical utility in iron overload as well with enhanced elimination of iron after intraperitoneal administration, as well as significantly reduced intestinal iron absorption.[179–181]

Polymer conjugates of small molecular chelators

Macromolecular chelators are also generated by the conjugation of small molecular Fe(III) specific chelators to polymeric scaffolds **(Figure 5B).**[182–184] In general, polymer selection depends on various physical and chemical characteristics including water solubility, simplicity of synthesis and functionalization, and biocompatibility.[185] Several families of polymers, including polyglycerol[182–184,186], poly-L-lysine[187], dextran[188], hyaluronic acid[189], hydroxyethyl starch[188,190], alginate[191], polyallylamines[173,181], polyrotaxanes[192], and nanogels[193,194] have been conjugated with chelators. Chelators often used for this approach are well characterized with defined iron binding parameters. Efforts have focused around the

modification of DFO because its hexadentate ligand coordination bypasses the geometric arrangement of chelators to stably bind iron.

Earlier reports used natural polymers, such as dextran, cellulose, starch, and hydroxyethyl starch.[190,195,196] DFO conjugated to dextran or hydroxyethyl starch showed improved circulation times and toxicity profiles whilst maintaining iron chelation.[190] Similar observations were found for the modification of cellulose with DFO with a significantly reduction in serum ferritin.[195] Impressively, the first human trails was conducted with DFO conjugated to starch and showed clinically significant iron excretion after a single dose.[196] In addition, a wide variety of synthetic polymers have also been investigated to this end. For example, the use of polyethylene glycol (PEG), a FDA approved polymer, was reported to enhance biocompatibility and improve its toxicity while pro-longing its circulation times.[186] More recently, our group developed and extensively investigated a novel semi-dendritic hyperbranched polyglycerol (HPG) polymer which offers many advantages, including biocompatibility, easy one-pot synthesis, an abundance of easily modifiable hydroxyl groups, low toxicity, and high water solubility.[185,197] Conjugation of DFO to HPG demonstrated a substantial increase in the circulation time which also translated to significantly improve iron excretion profiles.[183,184,198] Most of these systems showed enhanced therapeutic efficiency when compared to their native unconjugated small molecular chelator counterparts due to their extended circulation half-life and reduced toxicity. **Figure 6** shows the structure of HPG.
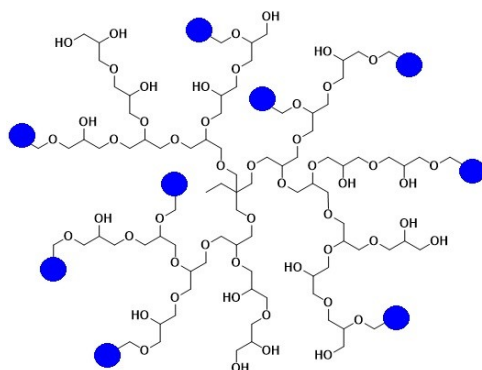
Figure 6. The chemical structure of an HPG-based macromolecular chelator. The blue circles represents DFO being decorated on HPG.

Polymeric nanoparticle formulations

Formation of polymeric micelle nanoparticles is another prominent approach to improving efficacy, solubility, and controlled release of small molecular drugs **(Figure 5C)**.[118,199–203] A formulation of DFO using an amphiphilic copolymer, monomethoxypoly(ethylene glycol)(mPEG)-poly(lactic-co-glycolic acid) (PLGA), improved the delivery of DFO.[200] Further, this strategy also improves organ targetability – a brain targeted DFO delivery system was developed using a rabies virus glycoprotein on a mPEG-PLGA DFO formulation.[199] In addition, polymeric micelle formed by self-assembly of deferiprone conjugated PEG-polypeptide copolymers improved its chelation efficiency.[204]

1.3.2.3. Limitations with current iron chelation strategies

Strategies to safely increase circulation times for DFO has shown to improve its chelation efficacy *in vivo*. However, a major limitation for long circulating therapeutics is the non-specific organ accumulation, especially to treat chronic illnesses.[181,183,184,205,206] The challenge lies in maintaining its pharmacokinetic properties whilst preventing bioaccumulation. Researchers have focused on renal excretion by using polymer scaffolds that are sufficiently small in size to meet the kidney clearance limit, or designed renal clearable nanoparticles using charged polymers.[187,207] Alternatively, biodegradable approaches have been designed that are either enzymatically cleavable, reactive oxygen species triggered or pH sensitive.[182,205,206,208,209] Both enzymatically cleavable and ROS triggered polymers have been observed to degrade into smaller fragments followed by increased elimination when compared to DFO alone.[205,206] Further, *in vivo* efficacy also suggests a reduction in both serum ferritin and iron-mediated toxicity. [205,206] However, a detailed biodistribution analysis of these systems is yet to be performed. On the other hand, pH-sensitive biodegradable polymers, synthesized as copolymers of HPG using ketal containing monomers, have been better characterized.[208,209] This design yielded increased circulation times with less than 10% accumulation in organs, and enhanced iron excretion when compared to DFO alone.[182] In addition to the non-specific distribution for long circulating therapeutics, increasing the circulation times for DFO may pose another challenge in patients that develop infections – especially since iron bound to DFO can be used by other organisms, particularly *Yersinia*.[128]

These works are at the forefront of designing novel systems that improve the efficacy of DFO whilst minimizing its toxicity with the end goal to treat iron overload disorders. Currently, there are no liver targeting strategies for the delivery of DFO. The design and development of liver targeted iron chelating

systems will offer two unique advantages; first, a critical organ involved in iron homeostasis can be protected from iron mediated toxicity, and second, these systems can be eliminated through the hepatic-biliary route minimizing non-specific accumulation.

1.4. Rationale for targeting the liver

1.4.1. The liver

The liver is a vital organ critical for numerous physiological processes including iron homeostasis, metabolism, detoxification and immunity amongst others. The functional units are hexagonal-shaped lobules with a central hepatic venule and portal triads, including the portal vein, the hepatic artery and the bile duct, at each corner.[210] The liver is unique in that it receives approximately 1.5 L of blood per minute *via* the portal triads – of which 75% is from the portal vein and 25% is from the hepatic artery – and flows through the hepatic sinusoids into the hepatic venule.[211–213]

Hepatic lobules are composed primarily of parenchymal cells or hepatocytes, and non-parenchymal cells. Hepatocytes account up to 80% of liver cells and carry out key metabolic and detoxification functions.[211,214] These cells have physiologically distinct luminal membranes; the basolateral membrane interacts with the blood from the sinusoids whereas the apical membrane forms the bile canaliculi and excrete metabolic by-products into the bile duct.[211,212] Non-parenchymal cells play a supportive and regulatory role within the liver and include the following; stellate cells store fat and vitamin A as well as playing a role in hepatic regeneration, Kupffer cells are resident macrophages, accounting for 80% to 90% of the body's macrophage population, and are involved in innate immunity, and sinusoid endothelial cells are fenestrated with pores ranging from 50 to 180 nm which help regulate intrahepatic blood flow.[211,212,215]

1.4.2. Liver targeting

1.4.2.1. The asialoglycoprotein receptor

The asialoglycoprotein receptor (ASGPR) plays a major role in the homeostasis of serum glycoproteins by clearing desialylated glycoproteins, including pro-thrombotic components, serum immunoglobin-A and cellular fibronectin.[216–219] The ASGPR is expressed almost exclusively by hepatocytes, at densities of 0.5 to 2 million ASGPR per hepatocyte, which far exceeds the extra-hepatic expression in testes, intestinal and

renal epithelial cells, macrophages and thyroid glands.[220–225] Taken together, the vast accessibility to the vascular compartment with minimal expression elsewhere renders ASGPR as a valuable candidate for liver targeting.

The ASGPR (**Figure 7** and **Figure 8**) is composed of two distinct polypeptides, H1 and H2 subunits with a molecular mass of 50 and 46 kDa respectively.[223] H1 and H2 subunits form a non-covalent heteromeric complex *via* coiled-coiled interaction, at a ratio of 2-5:1 respectively, and is basolaterally confined.[226–229] Both subunits are a single-spanning C-type transmembrane protein with a calcium dependent carbohydrate recognition domain; the H1 subunits mediates carbohydrate recognition and H2 subunit accounts for the expression and functional activity of the ASGPR.[226,229–231]

The crystal structure of the carbohydrate recognition domain identifies key functional groups interacting with its carbohydrate ligands; the sugars' 3- and 4- hydroxyl groups coordinate with the calcium ion[226,232], requiring equatorial and axial orientation[233], and circular arrangement of the hexose forms a hydrophobic patch which interacts with tryptophan's indole side change[226,234]. Any modification of the 3- and 4-hydroxyl group or the introducing steric hindrance results in decreased binding.[235] The anomeric and 6-hydroxyl interact with the solvent rather than the carbohydrate recognition domain.[226]
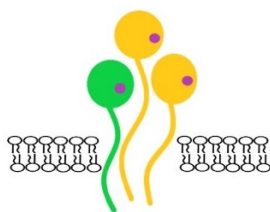
Figure 7. A representation of the asialoglycoprotein receptor (ASGPR). H1 and H2 subunits are represented by orange and green colors, respectively. The carbohydrate recognition domain is demarcated by the dark spot on each subunit.
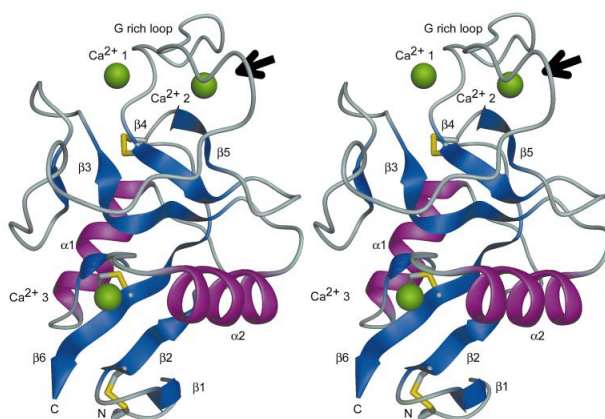
Figure 8. A ribbon diagram of the carbohydrate recognition domain on the H1 subunit of ASGPR. The two a-helices are shown in magenta, the b-strands in blue, the calcium ions in green and the three disulphide bridges in yellow. Both the N and the C terminus are on the bottom of the image. The division of the structure into two subdomains can be seen. Note the sharp bend in b-strand 3. The sugar binds to calcium ion 2 in front of the glycine-rich loop in the upper part of the picture (marked by a blackarrow). This structure has been described by Meier et al[236] and has been reused with the appropriate permission. (License number: 4932120386970, Content publisher: Elsevier)

Galactose Azide
(Gal)

N-acetylgalactosamine Azide
(GalNAc)

Triantennary N-acetylgalactosamine
(TAG)
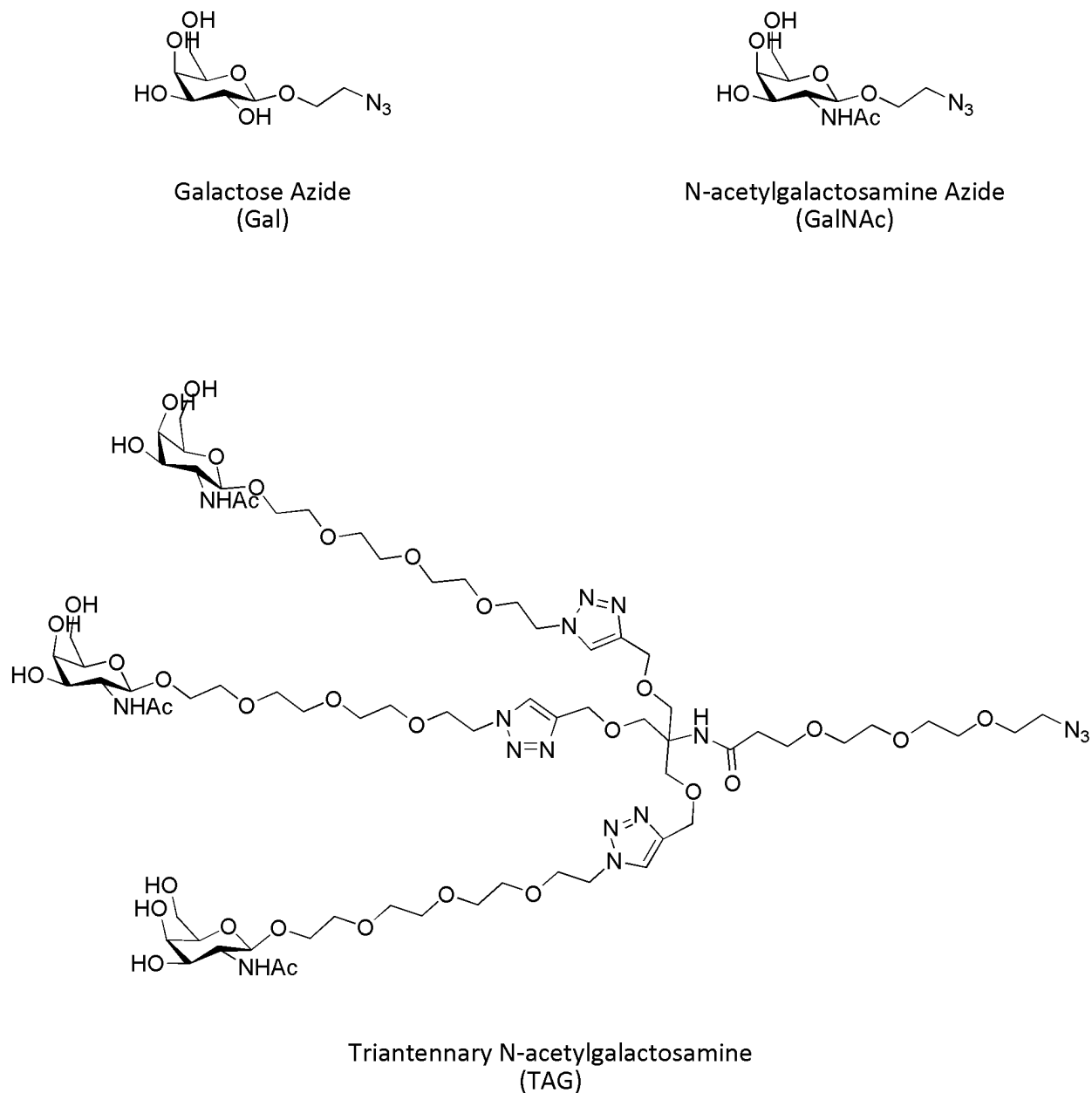
Figure 9. The structures of ASGPR-specific sugars. The ASGPR exhibits high affinities for Galactose (Gal), N-acetylgalactosamine (GalNAc) and triantennary N-acetylgalactosamine (TAG). These sugars were modified with an azide group to allow for convenient click-chemistry. The structure of TAG is novel with deliberate geometric constraints. The PEG linker was added to have optimal spacer length between terminal GalNAc units and orthogonal conjugation chemistry. TAG was designed by Dr. Srinivas Abbina and developed in our laboratory.

1.4.2.2. The ASGPR and ligand interaction

The ASGPR exhibits high affinities for non-reducing terminal galactose (Gal) and N-acetyl galactosamine (GalNAc), 10 to 50 fold higher than Gal.[237–239] Beyond the specificity these sugars, binding affinities also depends on its valency; Gal as a monosaccharide exhibits a dissociation constant (K_d) of 10^{-4} M whereas bi-, tri- and tetra-antennary terminal exhibit dissociation constants of 10^{-6}, 5×10^{-9} and 10^{-9} M.[236,240] **Figure 9** shows the structures of these sugars.

The spatial arrangements in branched terminal Gal of GalNAc sugars significantly enhance ASGPR binding affinity due to the cluster effect - the simultaneous interactions with the carbohydrate recognition domains of different ASGPRs.[223,240–243] The desirable spatial geometry for at least 3 Gal or GalNAc sugar spacing are 25-30 Å apart.[242,243] In *in vitro* competition assays with radiolabelled asialo-oromucosoid, galactosides with a sugar spacing of 20 Å revealed an inhibitory constant of 0.2 μM whereas galactosides with a sugar spacing of 4 Å had an inhibitory constant of 390 μM.[242,243] Interestingly, sugars exceeding 30 Å precluded the cluster effect.[237]

Further, the interaction between the ASGPR and its ligand is influenced by the glycosidic linkages.[223] In monosaccharides, the anomeric configuration showed minimal effect on binding. However, in multi-antennary sugars and glycoproteins, α-linkages (α1-3 linkages) resulted in approximately a 200-fold decrease in ASGPR affinity when compared to β-linkages (β1-4 linkages), which resemble endogenous ligands.[237,244,245] This is likely due to the altered spatial arrangement surrounding the C3-OH which prevents the cluster effect on ASGPR binding.[246]

Once ASGPR binds to its ligand, this complex migrates along the plasma membrane to clathrin-coated pits.[223,247] These pits are formed by the polymerization of clathrin-1, with adapter and assembly proteins, and facilitate budding.[248–250] Dynamin facilitates the separation of ASGPR-ligand vesicles from the plasma membrane.[217,223] These endosomes then connect with the actin cytoskeleton and the endocytic machinery to migrate towards the acidic endocytic recycling compartment.[251–253] At pH of below 6, the binding affinity for calcium ions in the carbohydrate recognition domain decreases and subsequently, the ASGPR-bound ligand dissociates.[217,254] The ligand is sorted to late endosomes which mature into lysosomes for degradation.[223,254] The sorting of internalized ligand is influenced by association and dissociation rate constants, valency of ligand and its density.[225,255] The ASGPR returns back to the plasma membrane *via*

the recycling endosomes for further clearance of desialylated glycoproteins.[254] The ASGPR has a degradation half-life of 15 – 20 hours and an internalization turn-over time of up to 20 minutes.[225,256–258]

1.4.2.3. Applications of ASGPR-mediated liver targeting

The principal advantage of using ASGPR as a means to target the liver enables high drug concentration within the cells whilst minimizing generalized systemic distribution and toxicities. This is due to the high specificity for its ligands, the predominant hepatic expression of ASGPR and its efficient internalization kinetics. In addition to ligand identity and densities, the design of ASGPR mediated systems require particular attention with regards to particle size[241,259–261], charge[262,263], and hydrophobicity[264–266].

ASGPR-mediated systems show contradictory biodistribution findings for the effect of particle size on liver targeting. For instance, a tri-antennary GalNAc terminated glycosides incorporated into liposomes ranging from 30 to 90 nm, showed liver specific uptake with 85% uptake within 30 minutes of injection for 30 nm sized particles whereas particles larger than 70 nm did not result in ASGPR processing.[241] In support of this, PEGylated nano-particles with similar anion charge and surface Gal densities showed hepatocyte-specific accumulation for particles sized 50 nm and Kupffer cell-specific accumulation for particles sized 140 nm.[259] In addition, high density lipoproteins and low density lipoproteins, sized 11.2 nm and 22.2nm, derivatized with tri-antennary Gal moieties showed 96% and 93% uptake by the hepatic parenchymal cells after 10 minutes of dose.[260,261] While there seems to be an upper size limit for ASGPR ligand processing *in vitro* and *in vivo*, gold sols coated with ASGPR glycoproteins, either asialofetuin or lactosylated bovine serum albumin, revealed hepatocyte uptake for particles sized only up to 7.8 nm whereas particles of all sizes (2.2 to 11.7 nm) were found in Kupffer cells and sinusoidal endothelial cells.[267] On the other hand, DNA polyplexes with galactosylated poly-L-lysine, with particle sizes as large as 180 nm, were successfully targeted to hepatocytes.[268] Similarly, the genetic delivery of luciferase using asialofetuin-protamine lipoplexes, particle size ranging from 180 to 300 nm, were found to be 12 fold higher.[269] In addition, liposomes with soybean-derived sterylglucoside also exhibited high liver accumulation, despite being 200 to 227.4 nm in size.[270,271]

In addition to particle size, hydrophobicity and charges of these systems also influence ASGPR-mediated liver targeting of these systems. Hydrophilic nanocarriers, such as PEG or HPG, exhibit long circulation times and can readily bypass clearance by reticuloendothelial systems. A 2% to 5% PEGylation of lipoplexes improved pDNA expression by 63% and 77% respectively in HepG2 cells when compared to non-PEGylated lipoplexes.[265] Moreover, positively charged systems interact electrostatically with the

anionic functional groups in the ASGPR.[223] Lipoplexes with a higher cationic ratio revealed higher hepatocyte uptake via ASGPR.[272] Galactosylated poly-L-lysine showed higher liver accumulation when compared to unmodified poly-L-lysine, with 98% hepatocyte uptake.[263] Interestingly, comparing poly-L-lysine and poly-gutamic acid systems, the effect of galactosylation was more evident in poly-glutamic acid systems. Taken together, the design of ASGPR-targeted systems for liver specificity is heavily influenced by the selection of macromolecular carrier.

ASGPR mediated strategies have been extensively investigated for its liver targeting capabilities for drug and gene delivery.[223,232,273] Many approaches have taken advantage of endogenous desialylated glycoproteins as natural ligands to the ASGPR in achieving liver-targeted delivery of various drugs. Amongst the plethora of glycoproteins, asialofetuin (AF) and asialo-oromucosoid (ASOR) have been utilized in drug and gene delivery. AF-labelled liposomes demonstrated rapid clearance from systemic circulation with 90% accumulating in the liver after 60 min of injection, unlike fetuin-labelled liposomes *in vivo*.[274,275] Hepatocyte specificity was confirmed with competitively inhibition by co-treatment with unlabeled and unbound asialofetuin.[274–276] Further, enhanced liver targeting improved the protective effect of vitamin E in mice modelled for acute liver injury.[277] In addition, successful *in vivo* gene transfer was observed for asialofetuin-appended cationic liposomes for antitumor activity into liver tumours.[278,279]

Similarly, ASOR conjugated to poly-L-lysine (PLL) was observed to rapidly accumulate in the parenchymal cells of liver; 63% of the radioactive injected dose found after 10 mins of the injection and immunohistochemical analysis confirmed hepatocyte-predominant uptake.[280] This system was used for gene delivery with markedly higher transfection rates observed *in vitro*.[280] *In vivo*, this system was used to deliver apoptin specifically to hepatocarcinoma cells, which showed significant signs of regression.[281]

Lactoferrin, a glycoprotein belonging to the transferrin family, can also bind with the ASGPR amongst other receptors.[282,283] This protein is unique in its binding kinetics is independent of galactose inhibition, suggestive of binding to a different site on the ASGPR.[282,283] Lactoferrin conjugated to PLL conferred hepatocyte-specific gene transfer.[284] More recently, lactoferrin-PEGylated liposomes containing doxorubicin demonstrated significantly improved antitumor efficacy against hepatocellular carcinoma when compared to non-targeted controls *in vivo*.[285,286]

In addition to employing desialylated glycoproteins, hepatic targeting of drugs or genetic materials has been mediated through the direct galactosylation of various macromolecular carriers; dextran[287–289], polyethylene glycol (PEG)[170,264,285,286,290–295], poly-L-lysine (PLL)[268,296–301], poly-glutamic acid[302–305],

polyethylenimine (PEI)[306–312], chitosan[313–320], dendrimers[321–328], and their derivatives[303,304,329–345] have been galactosylated and investigated as macromolecular carriers.

Doxorubicin was targeted to hepatocytes *via* galactose sugars as a cancer therapeutic and resulted in *in vitro* HepG2 toxicity[318] as well as superior anticancer activity in phase 1 clinical trials[330,337,338]. Doxorubicin has also been targeted to hepatocarcinoma cells using polymeric drug carriers conjugated with lactobionic acid with improved liver cancer cell targetability and enhanced drug potency.[316,343,346–348] Primaquine, for the treatment of malaria, has been delivered to the liver through either GalNAc or pullulan systems with increased hepatocyte uptake.[288,305] Vitamin K has also been delivered to the liver using Gal system which resulted in continuous anti-hemorrhagic activity in a hemorrhagic mouse model.[304,340] On the other hand, the delivery of small interfering RNA conjugated to GalNAc greatly limited off-target hepatocyte toxicity.[349] DNA was delivered at a higher transfection rates, almost 6 times higher, using galactose.[294,350]

Advances in ASGPR-mediated based targeting offers major advantages to address hepatocellular carcinoma, hepatitis and malaria, amongst others. In fact, the recent FDA approvals, Onpattro and Givlaari, of ASGPR-mediated systems to target silencing RNA to the liver further validates the success of this approach. Onpattro is a lipid nanoparticle formulation that delivers small interfering RNA molecules to inhibit the synthesis of transthyretin protein specifically in the liver, using GalNAc as the ASGPR-mediated ligand.[351,352] This nucleic acid-based strategy is currently used for the treatment of hereditary transthyretin amyloidosis, after showing improved in clinical outcomes.[353] Similarly, Givlaari is another small interfering RNA molecule, conjugated to GalNAc to enable hepatic delivery, that degrades the aminolevulinate synthase-1 enzyme for the treatment of acute hepatic porphyria.[354] Currently undergoing phase 3 clinical trial (NCT03338816), Givlaari has demonstrated a 92% decrease in aminolevulinic acid when compared to placebo control group.[355]

There is also emerging evidence for ASGPR-mediated strategies in the chelation of intracellular metals. A cyclodecapeptide conjugated to GalNAc was used to deliver a copper chelator to hepatocytes and reduced intracellular copper concentrations.[344] This is of particular interest as it showcases the tremendous potential of ASGPR mediated strategies in the treatment of iron overload disorders by potentially mitigating the current limitation surround iron chelation therapy and offering the advantage of lowering the iron burden from the liver.

1.5. Thesis rationale, hypothesis and specific aims

1.5.1. Thesis rationale

Iron overload in patients with thalassemia, myelodysplastic syndromes, sickle cell disease and other acquired anemia is a serious complication that arises from the necessary and repeated red blood cell transfusions. Since humans lack a proper iron excretion pathway, excess iron results in systemic iron overload either due to an underlying genetic component or acquired as through disease pathogenesis or through repeated transfusions. The resulting iron toxicity accounts for a majority of premature deaths, primarily from liver and heart dysfunction and failure.[101,102]

Iron chelation therapy is the only treatment, with only 3 FDA approved iron chelators, for patients suffering from systemic iron overload.[94,101] Deferoxamine, DFO, is amongst the gold standard for iron chelation in patients with iron overload and reduces the iron burden from patients, which, subsequently, reduces the insulting redox-active iron. A combination of iron chelators are also used in more challenging clinical scenarios.[128,356] However, the success of these chelators to protect patients from iron-mediated damage is subpar because they are beset by limitations including systemic toxicity, suboptimal iron excretion poor circulation and high costs.[94,137]

Although there has been significant research in iron chelation over the past 40 years, there is still a need to find safe approaches whilst increasing iron chelation efficacy either through either the development of novel low molecular weight chelators or employing macromolecular strategies.[357–359] Our expertise lies in developing biocompatible polymers for clinical uses and DFO conjugation to these polymers have yielded improved systemic iron removal and increased tolerability.[182,183,198] However, there still remains an unmet need to effectively and specifically protect key organs, primarily the liver and the heart, affected by iron-induced toxicity.

Currently, no organ targeted chelation strategies are available. Since the liver is the primary storage organ and a key regulator in iron homeostasis, the selective removal of excess liver iron could be invaluable to protect the liver and to restore iron homeostasis. In addition, the removal of liver iron may elicit systemic iron redistribution to reduce the iron burden in other organs as well. Moreover, since the discovery of the asialoglycoprotein receptor (ASGPR) and its specificity for galactose and N-acetyl galactosamine, there has been a lot of research pertaining to liver targeting and delivery of various drugs.[181,230,318–320]

Taken together, our goal was to develop a novel class of liver targeted macromolecular iron chelator for the removal of hepatic iron. We approached this using our expertise in developing biocompatible and multi-functional polymers in combination with previous reports of both DFO and ASGPR ligands modification strategies.

1.5.2. Global aim:

The aim of this thesis is to develop a novel class of liver targeted, high molecular weight macromolecular iron chelators and to assess their liver specificity, tolerability and efficacy when compared to similar non-liver targeted macromolecular iron chelator and to the small molecular weight iron chelator, DFO.

1.5.3. Global thesis hypothesis:

A high molecular weight, biocompatible macromolecule (hyperbranched polyglycerol – HPG) conjugated with iron chelators, DFO, and liver targeting groups would enhance the excretion of hepatic iron thereby preventing complications of the liver due to iron overload. **Figure 10** shows a schematic representation of the liver targeting macromolecular iron chelating system.
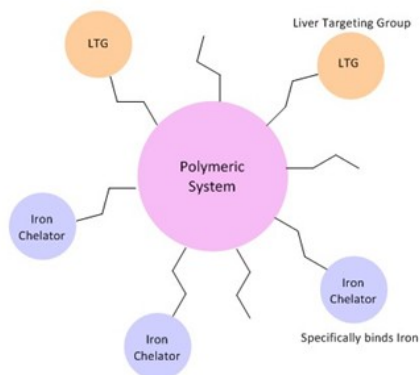
Figure 10. A schematic representation of the liver targeting macromolecular iron chelating system. HPG will be decorated with a liver targeting group (LTG) and an iron chelator, DFO.

1.5.4. Specific aims:

1.5.4.1. Specific aim 1:

The first aim of this thesis was to design and develop a library of liver targeting macromolecular iron chelators to maximize hepatocyte uptake using HPG polymer as the scaffold. The experimental hypothesis was that a macromolecular iron chelating system conjugated with sufficient liver targeting groups will demonstrate hepatocyte-specific uptake.

HPG polymers represent a unique class of polymers conveniently and consistently synthesized in a one-step reaction, yielding a highly biocompatible and multi-functional polymer with relatively narrow polydispersity. The selection of HPG stemmed from previous reports using HPG-DFO to generate non-toxic macromolecular iron chelators with significantly improved tolerability and efficacy.[183,184,198] Furthermore, DFO was used as the iron chelator because it is clinically use and it binds to iron at a 1:1 stoichiometric ratio, enabling stable coordination bonds once attached to the polymer.

To achieve sufficient hepatocyte uptake, the density liver targeting ligands, which include either N-acetyl galactosamine (GalNAc) or triantennary-N-acetyl galactosamine (TAG), were first optimized using flow cytometry and confocal laser scanning microscopy. Then, DFO units were conjugated to these system to re-assess any changes in their liver targeting functionality . The results are described in **Chapter 2**.

1.5.4.2. Specific aim 2:

The second aim of this thesis was to investigate the trafficking, intracellular distribution and clearance of liver targeting macromolecular iron chelators. The experimental hypothesis was that the optimized liver targeting macromolecular iron chelating systems will undergo ASGPR dependent receptor-mediated endocytosis and traffic through the endocytic pathway to enter the lysosome followed by excretion through the biliary/fecal route.

Earlier reports have demonstrated increased circulation times for DFO conjugated to HPG systems.[183,184,198] To better understand liver targeted macromolecular iron chelating systems, the circulation, biodistribution and excretion profiles were investigated in healthy mice. In addition, the *in vivo* hepatic distribution were investigated to better understand the distribution of these systems between hepatocytes and Kupffer cells. To expand the current understanding of how these system traffic

within hepatocytes after internalization, the kinetics for intracellular distribution were performed *in vitro* using confocal laser scanning microscopy. The results are described in **Chapter 3**.

1.5.4.3. Specific aim 3:

The third aim of this thesis was to investigate the molecular and functional properties of liver targeted iron chelators which affect iron mobilization, excretion and tolerance in mouse models. The experimental hypothesis was that the optimized liver targeting macromolecular iron chelating systems will reduce the iron burden from mice, particularly from the liver when compared to either non-targeted macromolecular DFO or DFO alone.

Intracellular hepatic delivery of DFO is novel and therefore directly affects its toxicity within living organisms. In order to best understand the utility of liver targeted macromolecular iron chelating systems, first the tolerability of these systems was assessed in normal mice. Following this, the performance of these systems was investigated through changes in iron excretion and iron burden in an *in vivo* iron overload model using iron-dextran. The results are described in **Chapter 4**.

1.5.4.4. Specific aim 4:

The fourth aim of this thesis was to investigate the chelation and mobilization of labile cellular iron and the subsequent cellular responses to liver-specific macromolecular iron chelators. The experimental hypothesis was that liver-targeting macromolecular iron chelating systems will mitigate the cellular responses to excess redox-active iron by chelating the labile cellular iron.

Mechanistic insights into the mode of action for hepatic targeted delivery of DFO would be invaluable to better understand how these systems work and what factors may influence its chelation efficiency. To achieve this, an *in vitro* iron overload cell model was first developed. Then, the performance of these systems was investigated with regards to mitigating redox activity and subsequent changes to both total and labile iron. The results are described in **Chapter 5**.

1.5.5. Significance and novel contributions:

Nanomedicine has received significant attention in the recent years with a particular focus to yield improved clinical outcomes. Herein, we propose a novel strategy towards developing safe and effective

liver targeting macromolecular iron chelating systems for the treatment of iron overload and the protection of the liver from iron toxicity. This has tremendous potential to shift the treatment of iron overload as well as offering a blueprint to treat other liver diseases.

There are three main significant contributions to the wider scientific community. First, the design and development of liver targeting systems using HPG, a biocompatible polymer, to deliver DFO to the liver is novel in itself. This application has been investigated under both *in vitro* and *in vivo* conditions, and the intracellular processing and distribution of these systems provide novel insights that can be correlated to excretion modalities of these molecules.

Second, an *in vitro* iron overload cell model has been developed after an in-depth literature review. Within literature, establishing such models vary tremendously with regards to cell lines, iron source, iron treatment conditions and duration. Subsequently, this diversity results in significant differences in the measured outcomes, either cellular function or response to iron treatment. Therefore, the process to develop an adequate *in vitro* iron overload cell model – one with elevated reactive oxygen species, labile and total iron whilst maintaining normal cellular functions – has been documented in detail with the purpose of demonstrating the importance of key parameters and their impact on reproducibility.

Third, a novel unified ferene (*u*-ferene) assay was developed to quantify both labile and total iron from the same preparation of biological samples – a 2-in-1 assay. This addresses a key limitation; current iron determination techniques, either total or labile iron, have minimal overlap in their quantification methodologies despite requiring extensive expertise and specialized instrumentation. This assay is in agreement with other techniques employed within the literature for the measurement of labile iron and offers the same sensitivity as the current gold standard, inductively coupled plasma mass spectrometry for total iron measurements. This assay offers an economic and accessible alternative for the wider scientific community.

Chapter 2: Design and development of liver specific macromolecular iron chelators.

2.1. Overview

To date, there are no strategies available for the targeted removal of iron from specific organs, particularly from the liver. Hepatic iron overload is a major cause of mortality and morbidity in a wide array of pathogenesis. Therefore, the design and development of a novel class of liver specific macromolecular iron chelators is an important next step within the field of chelation therapy.

In this chapter, a library of liver targeting systems were first developed to optimize for hepatocyte binding and uptake with regards to the identity and density of asialoglycoprotein receptor (ASGPR) specific ligands – N-acetylgalactosamine (GalNAc) and tri-antennary N-acetylgalactosamine (TAG) units. Ideal candidates were carried forward for further modification with deferoxamine (DFO), due to its 1:1 stoichiometry, and the hepatocyte responses were re-assessed. The binding and uptake of all liver targeting systems, with or without DFO, were measured in HepG2 cells, as a model for hepatocytes, using flow cytometry for high-throughput analysis. The internalization of these systems was further confirmed by confocal scanning laser microscopy. The cytotoxicity of liver targeting chelating systems was also analyzed and compared with both non-liver targeted macromolecular chelator and small molecule weight chelators.

Hepatocyte binding and uptake was greatly influenced by both the identity and density of ASGPR specific ligands. First, HPG decorated with 50 GalNAc units (H-GalNAc$_{50}$) outperformed all other liver targeting systems including 70 GalNAc units. Second, HPG decorated with 2 TAG units (H-TAG$_2$) outperformed 20 GalNAc units, likely due to a higher ASGPR affinity observed by multi-antennary ligands, which offers a synthetic advantage for additional chelator incorporation to the scaffold. Both H-GalNac$_{50}$ and H-TAG$_2$ were carried forward for DFO conjugation to generate liver targeted iron chelating systems (HD-GalNAc and HD-TAG, respectively). These liver targeting chelating systems demonstrated hepatocyte binding and uptake, though lower than their non-DFO parent systems. Confocal laser scanning microscopy confirmed the intracellular distribution of these systems, often qualitatively co-localizing with the endocytic pathway. In addition, liver targeting chelating systems were well tolerated *in vitro*. Based on the data in this chapter, some of these systems have been selected as the focus of further investigations in the next chapters.

2.2. Background

Humans have highly specialized mechanisms that regulate iron homeostasis and the liver plays a central role in coordinating iron homeostasis; all acquired iron enters the liver, 80% of which is comprised of hepatocytes, where it is either stored or utilized intracellularly, or mobilized for systemic demands.[211,214] A perturbance in iron homeostasis can result in hepatic iron overload, either through genetic or acquired disorders, and iron deposits in other the primary organs including heart, spleen, and kidney. An increased iron burden results in pathology mediated by the generation of reactive oxygen species (ROS) catalyzed by the Haber-Weiss reaction.[5,6]

Under normal physiological conditions, liver iron content is usually less than 1 mg iron per gram (dry weight) of liver.[96] However, in patients suffering from iron overload, the liver iron content can exceed 15 to 20 mg iron per gram of liver.[97] Hepatic iron overload and the consequent damage is one of the major causes of mortality and morbidity in different pathologies, including hereditary hemochromatosis, transfusion-related iron overload, hepatitis C infection, alcoholic fatty liver disease, chronic hepatopathies, hepatic fibrosis and inflammation, and cirrhosis.[75–78] In addition, the increased bioactive iron stores can also trigger metabolic pathogenesis such as insulin resistance, metabolic syndrome, and non-alcoholic fatty liver disease.[79]

Liver dysfunction and failure, along with heart failure, account for over 75% of premature deaths in iron overload patients despite intensive treatment. Iron chelation therapy uses small molecular chelators to mitigate redox activity associated with elevated labile iron and to reduce the iron burden in iron overloaded tissues. Small molecular chelators such as deferoxamine (DFO), deferiprone (DFP), and deferasirox (DFX), have shown some promise in reducing hepatic and myocardial iron burden in some patients, however, these are beset by limitations including unfavorable pharmacokinetics and pharmacodynamics, systemic toxicity, nonspecific tissue distribution and suboptimal iron excretion.[94,137]

Since the liver is the primary storage organ and a key regulator in iron homeostasis, the selective removal of excess liver iron could be invaluable to protect the liver and to restore iron homeostasis. Currently, there are no active liver targeting strategies for the directed excretion of iron from liver. In this chapter, we investigate key parameters required to design liver specific iron chelating systems. We hypothesize that a macromolecular iron chelating system conjugated with sufficient liver targeting groups will demonstrate hepatocyte-specific uptake. We anticipate that this novel class of liver targeted

macromolecular chelators will offer two potential advantages over existing chelating therapies; (1) a vital organ involved in iron homeostasis can be protected from iron mediated toxicity, and (2) the removal of excess hepatic iron could decrease the iron burden from other organs more readily.

In order to achieve liver targetability, the ASGPR was the focal point in the design of these new chelators because it has proven to be a valuable strategy for both drug and gene delivery.[223,232,273] The ASGPR is basolaterally expressed almost exclusively by hepatocytes at densities of 0.5 to 2 million ASGPR per hepatocyte and it readily interacts with the vascular compartments.[220–225] In addition, this receptor exhibits high affinity for non-reducing terminal sugars; in order of increasing affinity – galactose (Gal), N-acetylgalactosamine (GalNAc), and tri-antennary N-acetylgalactosamine (TAG).

Further, the design of these carriers is significantly influenced by particle size[241,259–261], charge[262,263], and hydrophobicity/hydrophilicity[264–266]. Typically, smaller particles with higher affinity sugars (GalNAc or TAG) are observed to accumulate in hepatocytes whereas larger particles with Gal are observed to accumulate in Kupffer cells because these non-parenchymal cells also have a galactose-binding receptor similar to the ASGPR.[363–366] In addition, hydrophilic nanocarriers, such polyethylene glycol or hyperbranched polyglycerols (HPG), exhibit improved circulation times as they readily bypass the reticuloendothelial system.[223,367] Previous work in our laboratory has extensively investigated HPGs and reported significantly improved circulation times, enhanced biocompatibility and convenient functional capacity for these systems.[185]

Taken together, the design of liver targeting macromolecular chelators requires particular attention to the identity and density of ASGPR specific ligands decorated on a HPG polymeric scaffold. Therefore, a library of liver targeting systems was developed with either GalNAc or TAG sugars, and screened for hepatocyte binding and uptake. Ideal candidates were selected for chelator conjugation and their liver targetability were re-assessed. DFO was selected as the iron (III) chelator because it has been thoroughly investigated, FDA approved and stably binds iron at a 1:1 stoichiometric ratio.

2.3. Methods

2.3.1. Materials

Eagle's Minimum Essential Media (EMEM), Dulbecco's Minimum Essential Media (DMEM), and Dulbecco's Phosphate Buffered Saline (PBS), N-acetyl galactosamine (GalNAc), 16% paraformaldehyde, and 8 well chamber slides were purchased from Thermo Fisher Scientific. Deferoxamine mesylate, fetal bovine serum, tissue culture treated 48-well cell culture plates, ethylenediaminetetraacetic acid (EDTA), copper sulfate pentahydrate, anhydrous dimethylformamide (DMF), propargyl bromide, methanol, acetone, dialysis bags (MWCO-5 and 8 kDa), dimethyl sulfoxide (DMSO), sodium chloride, and sodium L-ascorbate were obtained from Sigma-Aldrich. 7-AAD solution was acquired from BioLegends. Hoescht solution was acquired from Invitrogen. For cellular assay kits, the MTT assay kit was purchased from ATCC (20-1010K).

2.3.2. Synthesis of liver targeting macromolecular iron chelators

All macromolecules were designed by Dr. Srinivas Abbina and synthesized in the Kizhakkedathu laboratory. A general protocol has been outlined here. **Figure 11** shows the synthetic scheme.

2.3.2.1. Synthesis of alkyne functionalized HPG

Hyperbranched polyglycerol (HPG) (93 to 110 kDa, polydispersity index of 1.2) was dried at 70 °C under vacuum for 12 h and dissolved in anhydrous DMF. To this solution, sodium hydride (2.5 equivalents with respect to the targeted 120 hydroxyl groups) was added in small portions under argon and stirred for 1.5 h. To this cloudy solution, propargyl bromide (1.8 equivalents with respect to the targeted OH groups) was added and stirred for an additional 24 h. The reaction mixture was concentrated and dissolved in a minimal amount of methanol. The polymer was precipitated from acetone (3 times), dissolved in water (30 mL), and further purified by dialysis for 48 h (water replacements for every 5 h, MWCO-5 kDa). The polymer solution was lyophilized, and the number of alkyne groups on HPG was confirmed by NMR spectroscopy (^{1}H-NMR). This is the first reaction in **Figure 11**.
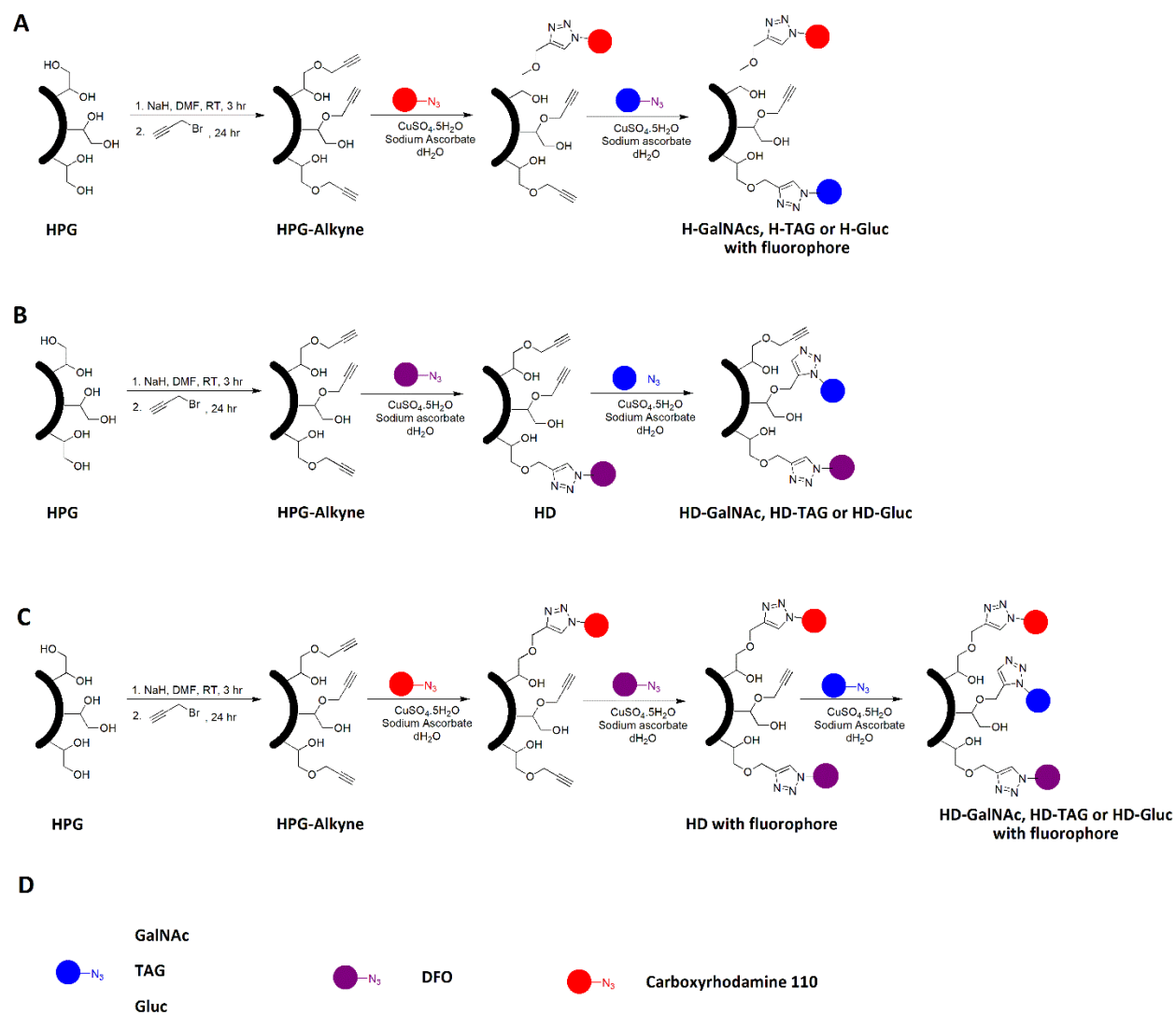
Figure 11. A schematic representation of synthesis for the of generation of liver targeted macromolecular systems. This summarizes the synthetic scheme for (A) HPG decorated with fluorophores and sugars, (B) HPG decorated with chelators and sugars, and (C) HPG decorated with fluorophore, chelators and sugars. The structures of HPG (**Figure 6**) and the different sugars (**Figure 9** and **Figure 12**) have been shown previously. All polymers were synthesized using a copper catalyzed click chemistry. A schematic representation illustrating the final molecules have been shown in **Figure 13**.

2.3.2.2. Synthesis of HPG decorated with sugars

The obtained HPG-alkyne$_{115}$ was dissolved in deoxygenated water (100 mL). To this solution, either N-acetylgalactosamine (GalNAc) azide, tri-annetenary N-acetylgalactosamine (TAG) azide or glucose (Gluc) azide (previously prepared by our laboratory, 1.2 equivalents with respect to the targeted alkyne groups) (**Figure 12**), copper sulfate pentahydrate (30 mol%), and sodium ascorbate (30 mol%) were added and stirred for 3 days at room temperature. Different numbers of alkyne groups were targeted for different sugar systems; HPG-GalNAc systems – 20, 40 and 60 alkyne groups were targeted, HPG-TAG system – 2 alkyne groups were targeted, and for HPG-Gluc systems – 10, 20, 40 and 60 alkyne groups were targeted.
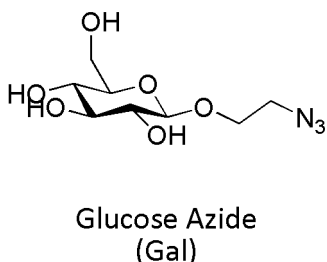
Glucose Azide
(Gal)

Figure 12. The structure of glucose azide

The solution was worked up, as described in section 2.3.2.5. The number of GalNAc, TAG and Gluc groups were determined by NMR spectroscopy. **Figure 11A** illustrates the synthesis of HPG decorated with sugars. A summary of all HPGs decorated with sugars have been summarized in **Table 1**. The acronyms listed under the "ID" column in **Table 1** will be followed through the thesis.

2.3.2.3. Synthesis of HPG decorated with DFO and sugars

The obtained HPG-alkyne$_{115}$ was dissolved in deoxygenated water (100 mL). To this solution, deferoxamine (DFO) azide (1.5 equivalents with respect to the targeted 15 alkyne groups, 20 mM solution in DMSO), copper sulfate pentahydrate and sodium ascorbate (2 equivalents with respect to the targeted alkyne groups) were added under argon and stirred at 70 °C for five days. This resultant solution (referred

to HPG-DFO solution for clarity) was then split in 4 equal parts in order to synthesize HPG-DFO (HD), HPG-DFO-GalNAc (HD-GalNAc), HPG-DFO-TAG (HD-TAG) and HPG-DFO-Gluc (HD-Gluc).

1. HD: The HPG-DFO solution was worked up, as described below.

2. HD-GalNAc: To the HPG-DFO solution, GalNAc (1.5 equivalents with respect to the targeted 60 alkyne groups), copper sulfate pentahydrate and sodium ascorbate (30 mol%) were added and stirred for an additional 3 days at RT.

3. HD-TAG: To the HPG-DFO solution, TAG (1.5 equivalents with respect to the targeted 5 alkyne groups), copper sulfate pentahydrate and sodium ascorbate (30 mol%) were added and stirred for an additional 3 days at RT.

4. HD-Gluc: To the HPG-DFO solution, Gluc (1.5 equivalents with respect to the targeted 60 alkyne groups), copper sulfate pentahydrate and sodium ascorbate (30 mol%) were added and stirred for an additional 3 days at RT.

The resultant solutions of HPG-DFO, HPG-DFO-GalNAc, HPG-DFO-TAG and HPG-DFO-Gluc were worked up, as described in section 2.3.2.5. The number of DFO units on the polymer was determined by UV-Vis spectroscopy.[224] The number of sugar units on the polymer were determined by NMR spectroscopy. **Figure 11B** and **Figure 11C** illustrates the synthesis of HPG decorated with DFO and sugars. A summary of all HPGs decorated with DFO and sugars have been summarized in **Table 2**. The acronyms listed under the "ID" column in **Table 2** will be followed through the thesis.

2.3.2.4. Fluorescent labelling of liver targeting systems with and without DFO

In order to ensure similar fluorescent spectrum of all molecules (**Appendix Figure 1**)**,** carboxyrhodamine-110 azide (Broadpharm) were conjugated to the obtained HPG-alkyne$_{115}$ prior to further modifications with sugars (as described in section 2.3.2.2.) (**Figure 11A**) or with DFO and sugars (as described in section 2.3.2.3.) (**Figure 11C**). Carboxyrhodamine 110 azide has an extinction coefficient of 74,000 M^{-1}cm^{-1}, an excitation maximum at 501 nm and an emission maximum at 523 nm as per the manufacturer. **Appendix Figure 2** shows the chemical structure for this dye.

The obtained HPG-alkyne$_{115}$ was dissolved in deoxygenated water and deoxygenated DMSO. To this solution, carboxyrhodamine-110 azide (1.5 equivalents with respect to HPG-alkyne$_{115}$) solution in DMSO (1 mg/mL), copper sulfate pentahydrate and sodium ascorbate (15 mol%) were added under argon and

stirred at 70°C for five days. This resultant solution was carried forward (without any work up) for all further modification; conjugations of sugars (described in section 2.3.2.2.) or conjugation of DFO and sugars (described in 2.3.2.3.).

2.3.2.5. Purification of HPG-based liver targeting systems and liver targeting chelating systems.

The reaction solution was quenched with EDTA (10 equivalents to copper sulfate) and dialyzed against water and 0.1% NaCl solution. Dialysates were replaced for every 8 h for 2 days (MWCO-8 kDa). The polymer solution was again washed with EDTA solution (1 M) and NaCl solution (1 M) through Amicon® Ultra Centrifugal filters (10 kDa, Thermofischer) and concentrated as needed.

2.3.3. Cell culture

A hepatocellular carcinoma cell line, HepG2 cell line (ATCC HB-8065), was used as a model for hepatocytes. HepG2 cells were cultured and maintained in accordance with manufacturer's protocol. Cells were maintained in EMEM with media being replaced every 2 to 3 days. For all experiments, HepG2 cells with passage numbers between 3 – 9 were used.

A cervix carcinoma cell line, HeLa cell line (ATCC CCL-2), has been reported as an ASGPR negative cell line and was used as negative control.[368] HeLa cells were cultured and maintained in accordance with manufacturer's protocol. Cells were maintained in DMEM with media being replaced every 1 to 2 days. Passage numbers for these cells were undetermined.

2.3.4. *In vitro* binding and uptake of liver targeting systems

The binding and uptake of liver targeting systems were investigated using flow cytometry. HepG2 cells were seeded in 48 well plates at a seeding density of 50,000 cells per well and allowed to adhere for 2 days before replacing the media. Cells were then maintained for 4 days with media being replaced every 2 days. The binding and uptake of fluorescently labelled liver targeting systems by HepG2 cells were investigated by first screening for an ideal liver targeting system over a range of concentrations and time, and then monitoring changes in these liver targeting systems when modified with DFO.

2.3.4.1. Investigation of binding and uptake of liver targeting systems

A range of concentrations from 5 x 10^{-12} M to 1 x 10^{-5} M were prepared for liver targeting systems (H-TAG$_2$, H-GalNAc$_{20}$, H-GalNAc$_{50}$ and H-GalNAc$_{70}$) and its non-liver targeting controls (H-Gluc$_{10}$, H-Gluc$_{20}$, H-Gluc$_{40}$ and H-Gluc$_{60}$) in EMEM. Cells were then incubated with liver targeting systems and their controls (0.2 mL for each concentration) at 37°C for 2 h. As a negative control, cells were treated with media only. The binding and uptake of these systems were analyzed by flow cytometry.

2.3.4.2. Time dependent binding and uptake of liver targeting systems

Liver targeting systems (H-GalNAc$_{20}$, H-GalNAc$_{50}$ and H-GalNAc$_{70}$) were incubated over 24 h (0.5, 1, 2, 3, 4, 6, 11 and 24 h) at 37°C. H-GalNAc$_{20}$ at 4.0 µM, H-GalNAc$_{50}$ at 0.4 µM, and H-GalNAc$_{70}$ at 0.3 µM were prepared in EMEM. These concentrations were determined by their half maximal activity over the concentration range of 5 x 10^{-12} M to 1 x 10^{-5} M, as described above. The binding and uptake of these systems (0.2 mL for each concentration) were analyzed by flow cytometry.

2.3.4.3. Investigation of binding and uptake of selected liver targeting chelating systems

Similar to the previous concentration profiles, liver targeting chelating systems (HD-GalNAc and HD-TAG), liver targeting systems (H-GalNAc$_{50}$ and H-TAG$_2$) and non-liver targeting controls (H-Alk, HD, HD-Gluc) were incubated at a range of concentrations (0.2 mL for each concentration) from 5 x 10^{-12} M to 1 x 10^{-5} M prepared in EMEM for 2 h at 37°C. As a negative control, cells were treated with media only. The binding and uptake of these systems were analyzed by flow cytometry.

2.3.4.4. Determination of half inhibitory (IC$_{50}$) concentrations of selected liver targeting chelating systems

To compare the binding and uptake activity of liver targeting systems (H-GalNAc$_{50}$ and H-TAG$_2$) and their respective chelating systems (HD-GalNAc and HD-TAG), competitive inhibition assays were performed using free unlabelled GalNAc. Fluorescently labelled macromolecules (400 nM) were prepared with increasing concentrations of GalNAc (ranging from 1 x 10^{-9} M to 1 x 10^{-1} M) in EMEM. Cells were treated (0.5 mL) for 2 h at 37°C. The binding and uptake were analyzed by flow cytometry. Data was reported in percentages of maximum activity – i.e. median fluorescence intensities for all cells were normalized to cell treated with liver targeting systems in the absence of GalNAc. The half inhibitory (IC$_{50}$) concentrations were determined using a four parameter model in Graphpad Prism.

2.3.5. Investigation of non-ASPGR mediated binding and uptake of liver targeting systems

The binding and uptake of optimized liver targeting systems were also investigated for non-ASGPR mediated processes using flow cytometry. In 48 well plates, HepG2 cells were seeded at a density of 50,000 cells per well and HeLa cells were seeded at a seeding density of 30,000 cells per well. Cells were allowed to adhere for 2 days before replacing the media. Cells were then maintained for 4 days with media being replaced every 2 days. The binding and uptake of fluorescently labelled liver targeting systems were investigated in two different experimental conditions, outlined below.

2.3.5.1. Influence of concentration of liver targeting chelating systems on binding and uptake in HeLa cells

A range of concentrations, from 5×10^{-12} M to 1×10^{-5} M, for liver targeting chelating systems (HD-GalNAc and HD-TAG), liver targeting systems (H-GalNAc$_{50}$ and H-TAG$_2$) and non-liver targeting controls (H-Alk, HD, HD-Gluc) were prepared in DMEM. HeLa cells were incubated (0.2 mL) for 2 h at 37°C. Cells were also treated with media only, as a negative control. The binding and uptake of these systems were analyzed by flow cytometry.

2.3.5.2. Influence of concentration of liver targeting chelating systems on binding and uptake in HepG2 cells at 4°C

Similarly, a range of concentrations, from 5×10^{-12} M to 1×10^{-5} M, for liver targeting chelating systems (HD-GalNAc and HD-TAG), liver targeting systems (H-GalNAc$_{50}$ and H-TAG$_2$) and non-liver targeting controls (H-Alky, HD, HD-Gluc) were prepared in EMEM and stored at 4°C. Cells were also treated with media only, as a negative control. HepG2 cells were incubated (0.2 mL) for 2 h on ice to prevent active endocytic event.[369] Ice was replaced every h. The binding and uptake of these systems were analyzed by flow cytometry.

2.3.6. Flow cytometry

All cells were washed three times with PBS (0.5 mL), trypsinized and pelleted at 500 G for 5 mins. Cells were resuspended in PBS (1 mL) with 7-AAD (5 μL) for 15 mins at room temperature. Then, at least 10,000 cells were analyzed by flow cytometry. Apoptotic cells were gated using the APC emission filter (660/10 nm) and the binding or uptake of fluorescently tagged systems were gated using the FITC emission filter (530/20 nm). Median fluorescence intensities were reported in live cells only – i.e. 7-AAD negative cells.

2.3.7. Confirmation of intracellular presence of liver targeting systems

HepG2 cells were seeded in 8 well chamber slides (Falcon) at a density of 25,000 cells per well. Cells were allowed 2 days to adhere before replacing media. In order to identify intracellular compartments, transferrin-647 (Thermofischer, transferrin conjugated to Alexa 647) was used to label the recycling endocytic compartments and Lysotracker (Invitrogen) was used to stain the lysosomes. Either transferrin-647 (10 μg/mL) or Lysotracker (100 nM) were co-incubated with liver targeting systems. Cells were treated (0.25 mL) with either H-TAG$_2$ (3.5 μM), H-GalNAc$_{20}$ (6.5 μM), H-GalNAc$_{50}$ (400 nM), H-GalNAc$_{70}$ (300 nM) or H-Gluc$_{60}$ (6.5 μM) prepared in EMEM for 2 h at 37°C.

After 2 h, cells were washed with PBS twice (0.5 mL) and fixed in 4% paraformaldehyde (0.3 mL) for 20 mins at room temperature. Cells were washed again twice with PBS (0.5 mL) and the nuclei were stained with 4 μM Hoescht in PBS (0.3 mL) for 10 mins at 37°C. At least 100 nuclei were imaged immediately using a Leica SP5 inverted laser scanning confocal microscope at a 63X oil-immersion objective. The acquisition settings for laser lines, power and respective emission filers have been outlined in the **Appendix Table 1**.

2.3.8. *In vitro* cytotoxicity for liver targeting chelating systems

Changes in metabolic activity were monitored to assess changes in cellular function when HepG2 cells were treated with either macromolecular chelators (HD, HD-GalNAc and HD-TAG) or small molecular weight chelators (DFO, DFX and DFP) over a range of concentrations. The MTT (3-(4,5-dimethylthiazolyl-2)-2,5-diphenyltetrazolium bromide) assay (ATCC 20-1010K) was used, according to the manufacturer's protocol.

HepG2 cells were seeded at a density of 20,000 cells per well in a 96 well plate. Media (200 μL) was replaced on the 3rd day, allowing cells to adhere for 2 days. Cells were treated with either macromolecular chelating systems (200 μL) or small molecular weight chelators (200 μL) at varying concentrations ranging from 50 μM to 1 nM for 24 h at 37°C. MTT gets reduced into insoluble formazan salts by metabolically active cells. In brief, cells were treated with a 10% MTT solution prepared in EMEM (100 μL) for 2 h at 37°C. Then, cells were lysed to solubilize the formazan precipitates using a detergent-induced reagent (ready made with the kit) (200 μL) overnight at room temperature. Absorbance was measured at 570 nm on SpectraMax 190 Microplate Reader from Molecular Devices. Metabolic activity was reported as follows; (mean570 nm treated cells / mean570 nm untreated cells) x 100%

In order to determine the most appropriate protocol, preliminary studies were performed to assess the effect of seeding density and HepG2 cell replication on the changes of metabolic activity. HepG2 cells doubled every 48 h, consistent with manufacturer's characterization. Additionally, confluency was also compared to seeding density and subsequent changes in metabolic activity. Interestingly, confluency did not change as a function of seeding density or time of growth, however total cell count and metabolic activity increased linearly.

2.3.9. Statistical analyses

All experiments were performed in at least independent triplicates and presented with error bars that correspond to standard deviations. Technical replicates were also performed, but only independent triplicates were used for statistical analysis. All statistical analyses were performed using GraphPad Prism 7 (Grahpad Software, San Diego, USA). The statistical tests and appropriate multiple comparison tests were outlined in the figure legends.

2.4. Results

2.4.1. Physical properties of the library of liver targeting systems and the selected liver targeting chelating systems.

Hyperbranched polyglycerol (HPG, 100 KDa) was chosen as the polymeric scaffold since it has been extensively investigated by our laboratory. This polymer offered superior *in vitro* cytocompatibility and blood compatibility as well as *in vivo* tolerance when compared to PEG at similar molecular weights.[185,370] In addition, the pharmacokinetic properties for 100 kDa HPG were favourable in mice with long circulation half-life of ~ 40 h and minimal non-specific accumulation.[185,370–372] Lastly, HPG offers convenient multi-functionalization compared to other relevant polymeric systems.

The ASGPR is expressed almost exclusively by hepatocytes, at densities of 0.5 to 2 million ASGPR per hepatocyte , which far exceeds the extra-hepatic expression in testes, intestinal and renal epithelial cells, macrophages and the thyroid gland.[220–225] The ASGPR has been the focus of many liver targeting drug and gene delivery approaches.[223,232,273] Based on this, we chose an ASGPR-based targeting approach to design liver targeted macromolecular iron chelating systems. The design of the macromolecular iron (III) specific chelators involves click-chemistry mediated conjugation of ASGPR specific ligands either a monoantennary carbohydrate, GalNAc, or a triantennary carbohydrate, TAG, and Fe(III) specific small molecular chelator, DFO (**Figure 13**). The synthetic scheme is illustrated in **Figure 11**. The chemical structural analysis of these systems was performed using NMR spectroscopy to characterize the number of chelators or sugars attached to the polymer (**Appendix Figure 3** to **Appendix Figure 6**). To confirm the number of conjugated DFO units, UV-Vis spectroscopy was also performed (**Appendix Figure 7**). The molecular weight and hydrodynamic size were measured using gel permeation chromatography coupled multi-angle light scattering detector and quasi-elastic light scattering detector respectively.

Henceforth, all macromolecular systems will be referred to by their abbreviations as summarized by table 1 and table 2, under the ID column. This nomenclature begins with the polymer (H for HPG) followed by the chelator (D for DFO) and then either ASGPR specific sugars (GalNAc or TAG) or control sugars (Gluc). For macromolecular systems without chelators, the numerical subscript that follows the sugar represents the number of sugars present. For macromolecular systems with chelators, numerical subscript only follows the chelator when there are 40 DFO units attached.
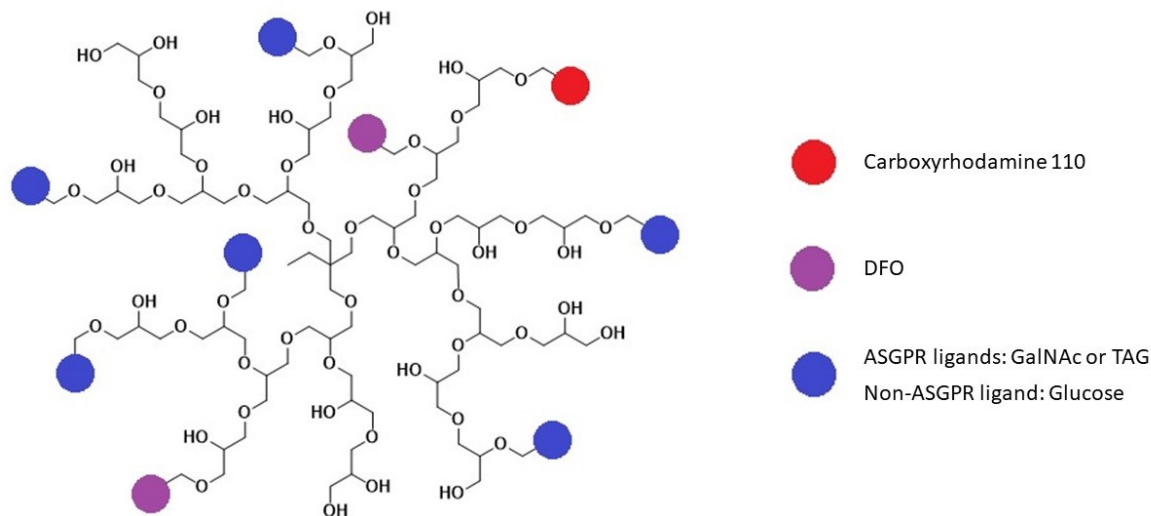
Figure 13. A schematic representation of HPG-based macromolecular liver targeting system with a Fe (III) specific chelator.

First, a library of liver targeting systems (without DFO) was developed to screen for optimal hepatocyte binding and uptake. Different densities of GalNAc and TAG groups were conjugated on to the polymer scaffold; GalNAc densities varied from 20 to 70 (H-GalNAc$_{20}$, H-GalNAc$_{50}$, and H-GalNAc$_{70}$), while only 2 TAG units (H-TAG$_2$) were used since multi-antennary terminal carbohydrates exhibit higher binding affinity towards ASGPR. A set of negative controls were also prepared, following a similar synthetic protocol, using glucose because it resembles the structure of GalNAc whilst exhibiting lower affinity for the ASGPR. A set of glucose conjugated HPGs were prepared with varying number of glucose units (H-Gluc$_{10}$, H-Gluc$_{20}$, H-Gluc$_{40}$, and H-Gluc$_{60}$) to resemble their ASGPR-specific counterparts. The characteristics of liver targeting systems and their controls have been summarized in **Table 1**.

After screening ASGPR-specific ligand densities for the most efficient hepatocyte binding and uptake under *in vitro* conditions (described in section 2.4.2.), the best candidates were carried forward for chelator modification. While HPG has been modified with varying units of DFO (ranging from 10 to 120)[183,184,198], best liver targeting systems were modified with 15 DFO units as a proof of concept for liver targeted iron chelation. The conjugation of either ASGPR specific ligand or DFO was achieved using a click-chemistry approach. The characteristics of liver targeting chelating systems have been summarized in **Table 2**. While most of the thesis investigated 15 DFO systems, a 40 DFO system was also prepared for functional comparison in **Chapter 4**. This step-wise approach will better guide future investigations in the development of these novel liver targeted macromolecular iron chelators.

Table 1. The characteristics of liver targeting systems (without chelator) and their controls.

Name	ID	MW (kDa)	PDI	Hydrodynamic size (nm)	ASGPR-specific ligand		Number of Glucose	Number of DFO
					Number of GalNAc	Number of TAG		
Liver targeting systems								
HPG-GalNAc$_{20}$	H-GalNAc$_{20}$	123	1.2	9.4 ± 0.3	20	-	-	-
HPG-GalNAc$_{50}$	H-GalNAc$_{50}$	150	1.3	7.5 ± 0.4	50	-	-	-
HPG-GalNAc$_{70}$	H-GalNAc$_{70}$	167	1.3	11.9 ± 0.4	70	-	-	-
HPG-TAG$_2$	H-TAG$_2$	123	1.2	10.7 ± 0.3	-	2	-	-
Non-liver targeting systems								
HPG-Glucose$_{20}$	H-Gluc$_{20}$	121	1.2	9.4 ± 0.4	-	-	20	-
HPG-Glucose$_{40}$	H-Gluc$_{40}$	132	1.2	9.8 ± 0.4	-	-	40	-
HPG-Glucose$_{60}$	H-Gluc$_{60}$	150	1.2	10.1 ± 0.3	-	-	60	-
HPG-Glucose$_{10}$	H-Gluc$_{10}$	118	1.2	9.3 ± 0.3	-	-	10	-

Table 2. The characteristics for liver targeting chelating systems and their controls.

Name	ID	MW (kDa)	PDI	Hydrodynamic size (nm)	ASGPR-specific ligand		Number of Glucose	Number of DFO
					Number of GalNAc	Number of TAG		
Liver targeting systems								
HPG-DFO$_{15}$-GalNAc$_{50}$	HD-GalNAc	202	1.5	17.6 ± 0.5	50	-	-	15
HPG-DFO$_{15}$-TAG$_2$	HD-TAG	155	1.3	11.9 ± 0.4	-	2	-	15
HPG-DFO$_{40}$-GalNAc$_{50}$*	HD$_{40}$-GalNAc	205	1.6	21.0 ± 0.1	50	-	-	40
Non-liver targeting systems								
HPG-DFO$_{15}$-Glucose$_{50}$	HD-Gluc	253	3.5	43.6 ± 0.8	-	-	50	15
HPG-DFO$_{15}$	HD	132	1.4	13.6 ± 0.4	-	-	-	15
HPG-Alkyne$_{115}$	H-Alk	131	1.9	18.4 ± 0.5	-	-	-	-

*HD$_{40}$-GalNAc was investigated for its *in vivo* chelation efficacy <u>only</u>. This provided a functional comparison for DFO density, comparing liver targeting chelating systems with either 15 or 40 DFO units, as a proof concept - this would be invaluable to demonstrate the importance of DFO density and pursue this as part future investigation mentioned in **Chapter 6**.

2.4.2. The selection of an optimal liver targeting system from the library.

The library of liver targeting systems (**Table 1**) was screened for hepatocyte binding and uptake with respect to ASGPR specific ligand identity and density. HepG2 cells, a hepatocellular carcinoma cell line, was used as a model for hepatocytes. Glucose systems served as negative controls for ASGPR mediated binding and uptake.

First, the binding and uptake of liver targeting systems were investigated over a wide range of concentrations (with respect to polymers) incubated at 2 h (**Figure 14A and Figure 15)**. H-GalNAc$_{50}$ and H-GalNAc$_{70}$ show significantly more binding and uptake at 50 nM followed by H-TAG$_2$ at 500 nM and then H-GalNAc$_{20}$ at 5 µM when compared to H-Gluc$_{60}$ (p < 0.0001, p < 0.001, p = 0.0405 and p = 0.0010, respectively). This comparison was made to H-Gluc$_{60}$ because it has been conjugated with the most glucose sugars. Moreover, at concentrations of 1 µM and above, H-GalNAc$_{50}$ had significantly more binding and uptake when compared to H-GalNAc$_{70}$ ($^{\#}$p = 0.0156 (1 µM), $^{\#\#\#}$p = 0.0010 (5 µM), and $^{\#\#\#}$p = 0.0030 (10 µM)). H-GalNAc$_{20}$ and H-TAG$_2$ were not significantly different in their binding and uptake in HepG2 cells. When comparing liver targeting systems to their non-liver targeting glucose controls (**Figure 15** and **Appendix Figure 8**), H-GalNAc$_{50}$, H-GalNAc$_{70}$ and H-TAG$_2$ showed significantly more binding and uptake at concentrations of 50 nM (p < 0.0001 for these three comparisons) and above. In contrast, H-GalNAc$_{20}$ show significantly more binding and uptake at concentrations of 1 µM and above (p < 0.0001). The density and type of ASGPR targeted ligands significantly influence binding and uptake of these systems; enhanced hepatocyte binding and uptake was shown with increasing GalNAc densities, and TAG units outperformed GalNAc units (H-TAG$_2$ vs H-GalNAc$_{20}$) (**Figure 14**).

Given the observed differences in cellular binding and uptake with GalNAc densities over a wide range of concentrations at 2 h, cellular responses to these systems were investigated over a period of 24 h (**Figure 14B**). HepG2 cells were treated with half-maximum binding and uptake concentrations determined from their concentration profiles to ensure signal detection – 4.0 µM of H-GalNAc$_{20}$, 0.4 µM of H-GalNAc$_{50}$, and 0.3 µM H-GalNAc$_{70}$. H-GalNAc$_{50}$ had significantly higher uptake after 1 h (p = 0.0305) and H-GalNAc$_{70}$ had significantly higher uptake after 2 h of treatment (p = 0.0030) when compared to H-GalNAc$_{20}$. After 6 h of treatment, H-GalNAc$_{50}$ had significantly higher median fluorescence intensity when compared to H-GalNAc$_{70}$ (p = 0.0041).

Cellular uptake analysis by flow cytometry does not discern between cell-surface bound and internalized liver targeted system. Therefore, to confirm the hepatocyte uptake of these liver targeting polymers, internalization studies were performed using confocal scanning laser microscopy (**Figure 16** and **Figure 17**). HepG2 cells were incubated with all liver targeting systems and H-Gluc$_{60}$ (control) for 2 h. Intracellular compartments were traced by co-incubating cells with either transferrin-647 (**Figure 16**) to trace early and recycling endosomes, or Lysotracker (**Figure 17**) to trace late endosomes and lysosomes. All liver targeting systems had a punctate-like intracellular distribution, often qualitatively co-localizing with either transferrin-647 or Lysotracker, whereas H-Gluc$_{60}$ showed minimal signal. This provides confirmatory evidence for the intracellular presence of these liver targeting systems.

Taken together, H-GalNAc$_{50}$ and H-TAG$_2$ were selected as optimal candidates to be carried forward for chelator modification. This is because H-GalNAc$_{50}$ outperformed all other liver targeting systems from the library with regards to their concentration and time profiles. Similarly, H-TAG$_2$ was superior than H-GalNAc$_{20}$'s concentration profile and offered the advantage for additional polymer modification; 2 TAG unit compared to 20 GalNAc conjugated to HPG.
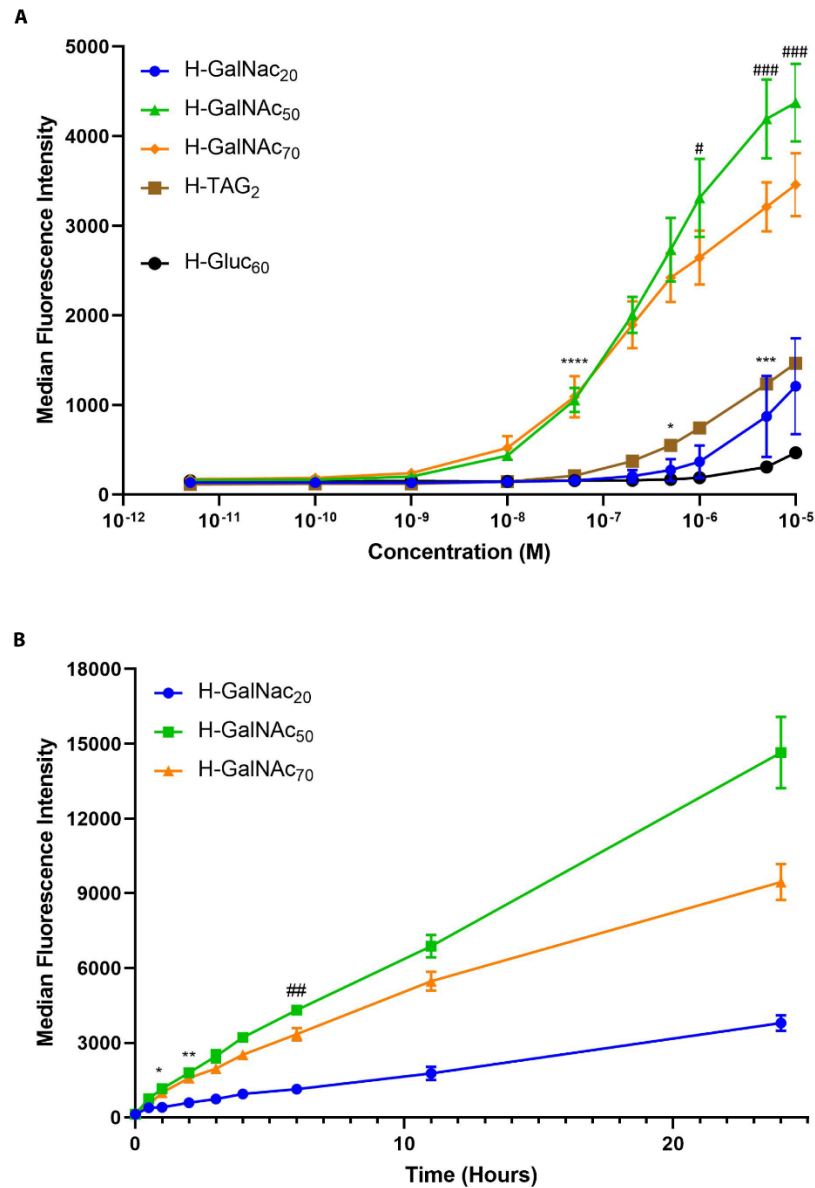
Figure 14. The binding and uptake of liver targeting systems. The binding and uptake of sugar HPG systems were analyzed in at 10,000 cells (A) over a range of concentrations incubated at 2 h and (B) over a period of 24 h at fixed concentrations. To compare the increase in median fluorescence intensities over a range of concentrations, a 2-way ANOVA with either Dunnett's or Sidak's multiple comparisons test were performed. Similarly, to compare the increase in median fluorescence intensities over a period of 24 h, 2-way ANOVA with Tukey's multiple comparisons test was performed. Error bars show standard deviations for a sample size of 3 independent replicates. All statistical analysis were performed on Graphpad Prism where **** or #### represents $p < 0.0001$, *** or ### represents $p < 0.0010$, ** or ## represents $p < 0.0100$ and * or # represents $p < 0.0500$.
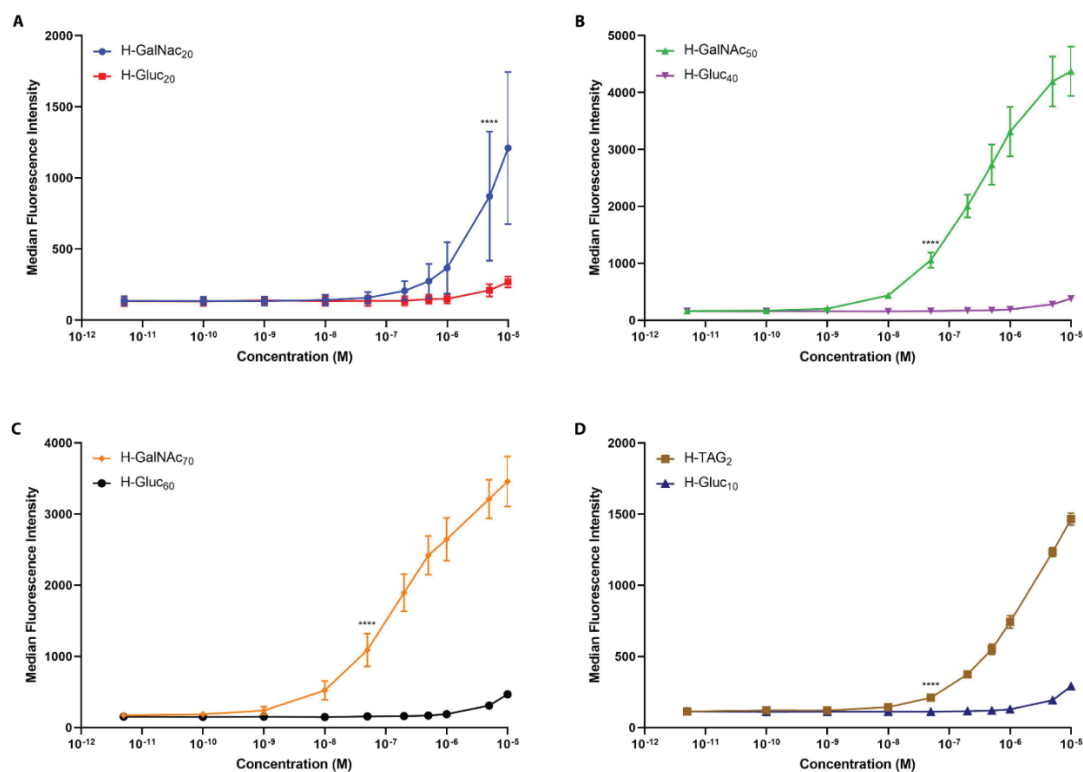
Figure 15. The binding and uptake of liver targeting systems and their non-targeting controls in HepG2 cells. Cells were treated with carboxyrhodamine-tagged polymers at a range of concentrations for 2 h at 37°C. At least 10,000 cells were analyzed using the 488 nm laser and the FITC emission filter (530/20 nm). (A) H-GalNAc$_{20}$ and H-Gluc$_{20}$. (B) H-GalNAc$_{50}$ and H-Gluc$_{40}$. (C) H-GalNAc$_{70}$ and H-Gluc$_{60}$. (D) H-TAG$_2$ and H-Gluc$_{10}$. Error bars show standard deviations for a sample size of 3 independent replicates. A 2-way ANOVA with Sidak's multiple comparisons test was performed to compare liver targeting polymers with their respective controls. All statistical analyses were performed in Graphpad Prism where **** represents $p < 0.0001$.
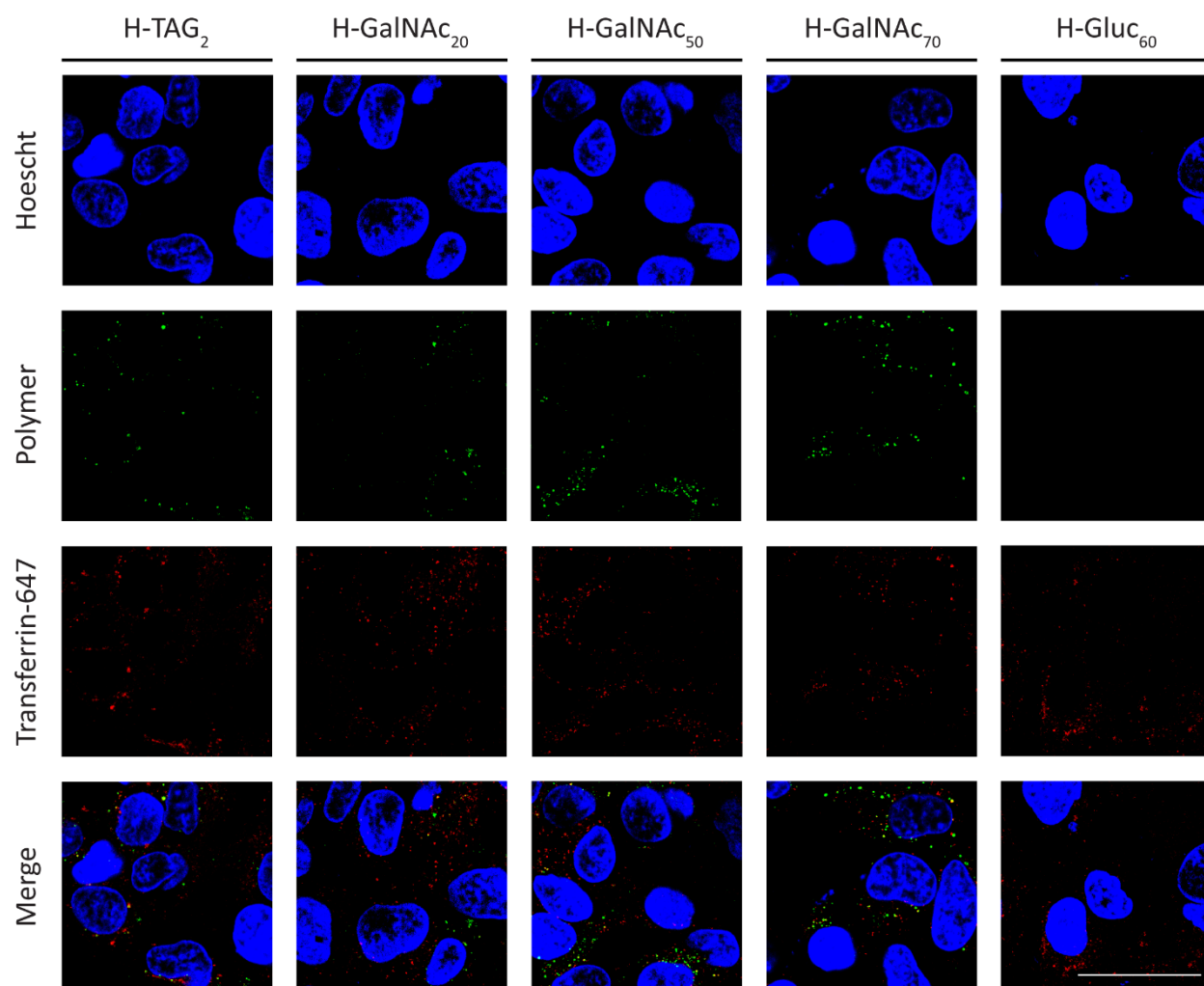
Figure 16. Tracing liver targeting systems with early and recycling endosomes in HepG2 cells. Fluorescently labelled H-TAG$_2$ (3.5 µM), H-GalNAc$_{20}$ (6.5 µM), H-GalNAc$_{50}$ (0.4 µM), H-GalNAc$_{70}$ (0.3 µM) and H-Gluc$_{60}$ (6.5 µM) were incubated for 2 h. Cells were washed in PBS and fixed in 4% PFA for 20 min at RT. Nuclei were stained using Hoechst. The recycling endosomes have been traced using transferrin-647 (10 µg/mL). All cells were imaged at 4.0 zoom using a 63X objective. At least 100 cells were imaged using Leica SP5 inverted confocal scanning laser microscope. Representative images are shown. Scale bar represents 1 µm.
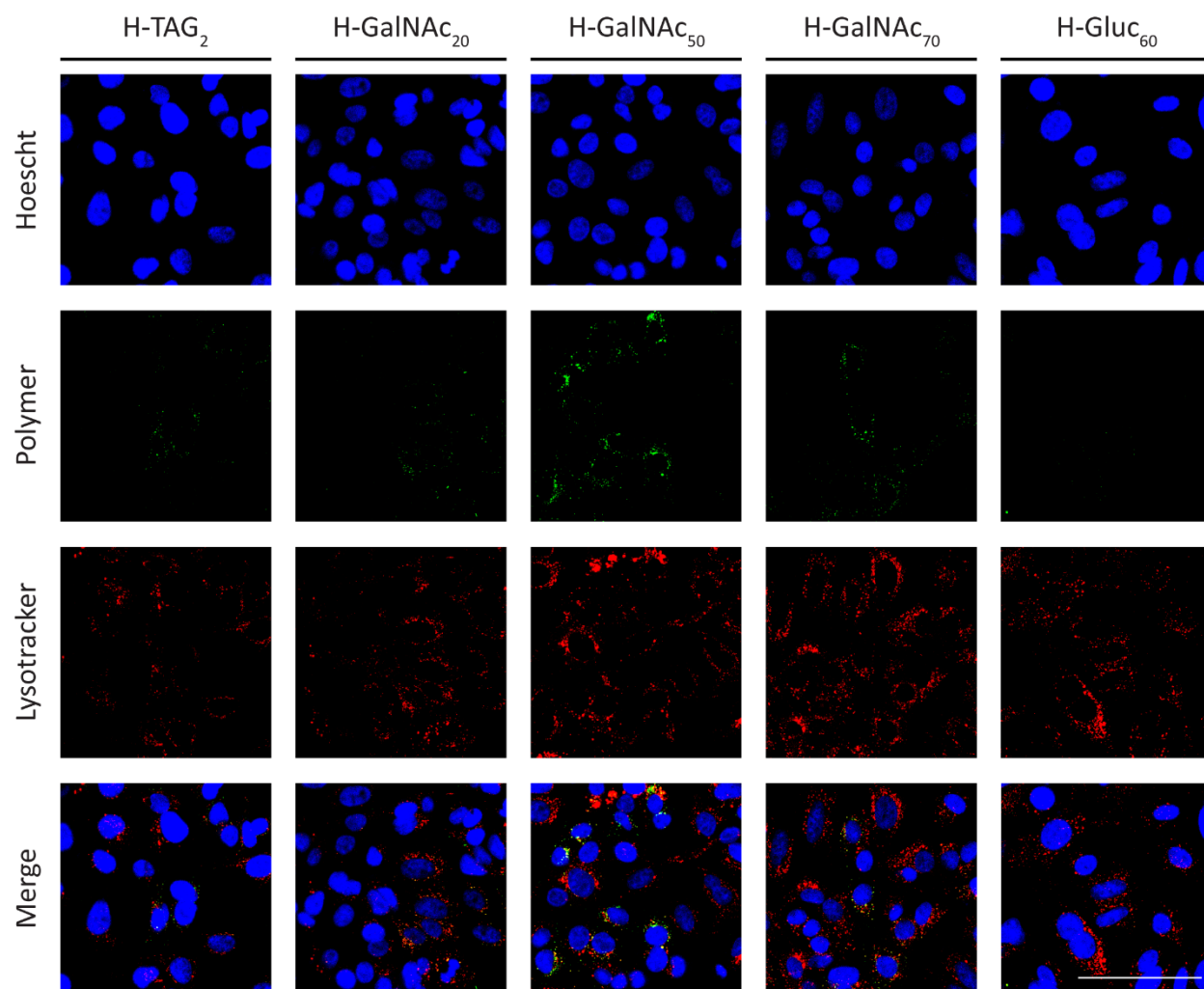
Figure 17. Tracing liver targeting systems with lysosomes in HepG2 cells. Fluorescently labelled H-TAG$_2$ (3.5 μM), H-GalNAc$_{20}$ (6.5 μM), H-GalNAc$_{50}$ (0.4 μM), H-GalNAc$_{70}$ (0.3 μM) and H-Gluc$_{60}$ (6.5 μM) were incubated for 2 h. Cells were washed in PBS and fixed in 4% PFA for 20 min at RT. Nuclei were stained using Hoechst. The lysosomes were identified using Lysotracker (100 nM). All cells were imaged at 4.0 zoom using a 63X objective. At least 100 cells were imaged using Leica SP5 inverted confocal scanning laser microscope. Representative images are shown. Scale bar represents 1 μm.

2.4.3. *In vitro* binding and uptake for liver targeting chelating systems

H-GalNAc$_{50}$ and H-TAG$_2$ were selected from the library of liver targeting systems based on binding and uptake. These systems were conjugated with iron (III) specific chelator, DFO, to generate liver targeting chelating systems to sequester and excrete excess iron. Due to the synthetic challenge, HPG scaffolds were first conjugated to 15 DFO followed by 50 GalNAc (HPG-DFO$_{15}$-GalNAc$_{50}$ and referred to as HD-GalNAc) or 2 TAGs (HPG-DFO$_{15}$-TAG$_2$ or referred to as HD-TAG) using click chemistry. To account for any ASGPR-independent binding and uptake due to the inherent property of polymeric systems, several controls were used; (1) HPG modified with sufficient number of alkynes groups (HPG-Alkyne$_{115}$ or referred to as H-Alk), (2) HPG conjugated to 15 DFO units (HPG-DFO$_{15}$ or referred to as HD), and (3) HPG conjugated to 15 DFO units and 50 glucose units (HPG-DFO$_{15}$-Glucose$_{50}$ or referred to as HD-Gluc). The characteristics of all liver targeting chelating systems and their controls is summarized in **Table 2**.

The binding and uptake of liver targeting chelating systems and their controls were investigated in HepG2 cells over a range of concentrations for 2 h and assessed by flow cytometry (**Figure 18A**). The binding and uptake of both liver targeting chelating systems (HD-GalNAc and HD-TAG) showed enhanced HepG2 cellular response when compared to the non-liver targeting controls (HD-Gluc, HD, H-Alk). Particularly, HD-GalNAc exhibited a significantly higher binding and uptake response when compared to HD-Gluc starting at 10 nM (p = 0.0025). Similarly, HD-TAG exhibited a significantly higher binding and uptake response when compared to HD-Gluc starting at 5 μM (p < 0.0001). Further, HD-GalNAc had superior binding and uptake when compared to HD-TAG starting at 10 nM (p = 0.0254) and above. Despite the enhanced uptake of liver targeting chelating systems relative to their controls, it is important to note that the cellular response to HD-GalNAc and HD-TAG were significantly lower than their non-chelator counterparts, H-GalNAc$_{50}$ and H-TAG$_2$, at concentrations of 1 μM ([##]p = 0.0013 and [##]p = 0.0096) and above.
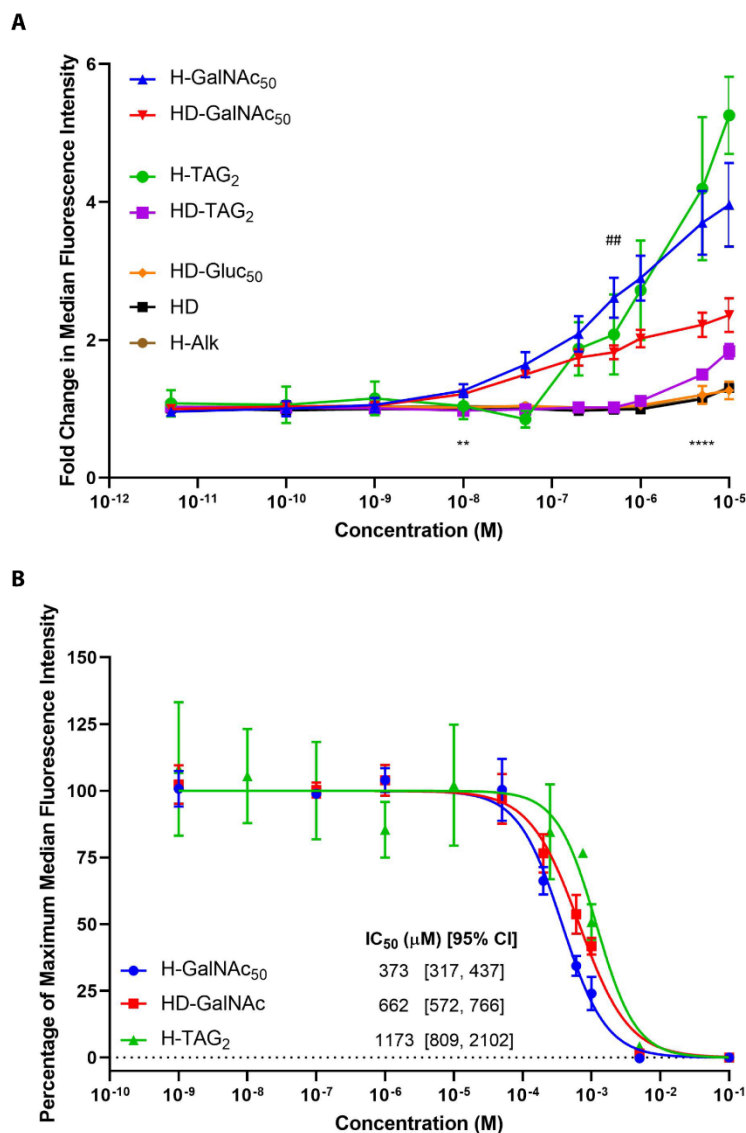
Figure 18. The binding and uptake of liver targeting chelating systems. (A) The concentration profiles for liver targeting chelating systems and their controls were measured in at least 10,000 cells. A 2-way ANOVA with Dunnett's multiple comparisons test were performed to compare cellular responses with HD-Gluc. Additionally, a 2-way ANOVA with Sidak's multiple comparisons test were performed to compare cellular responses amongst liver targeting systems (with and without DFO). (B) The IC_{50} values were determined by increasing the concentration of unlabelled GalNAc as a competitive inhibitor for ASGP-R. The median fluorescence intensities were normalized to the median fluorescence intensity in cells treated without GalNAc and presented as a percentage. Error bars show standard deviations for a sample size of 3 independent replicates. Graphpad Prism was used for the determination of IC_{50} concentrations and all statistical analyses. **** represents $p < 0.0001$ and ** or ## represents $p < 0.0100$.

Since decreased cellular binding and uptake was observed for liver targeting systems conjugated with DFO compared to those without DFO, all ASGPR specific polymeric systems were quantitatively compared with respect to the half-maximal inhibitory concentrations (IC_{50} values or concentrations) (**Figure 18B**). HepG2 cells were co-treated with fluorescently labelled polymers (H-GalNAc$_{50}$, HD-GalNAc, H-TAG$_2$, and HD-TAG) at 400 nM and with unlabelled GalNAc at varying concentrations ranging from 1 nM to 0.1 M. GalNAc is a natural ligand for ASGPR and therefore serves as a competitor. The IC_{50} value for H-GalNAc$_{50}$ was 373 µM with 95% confidence intervals [317, 437], which is significantly lower than the IC_{50} value of HD-GalNAc, 662 µM with 95% confidence intervals [572, 766]. In other words, HD-GalNAc has a higher IC_{50} concentration which suggests a stronger ASGPR interaction and/or quicker internalization and ASGPR recycling kinetics compared to H-GalNAc$_{50}$.[225] In addition, the IC_{50} concentration of H-TAG$_2$ was 1173 µM with 95% confidence intervals [809, 2102]. Since a decrease in signal was not observed for HD-TAG, the IC_{50} concentration was not determined.

In order to assess the influence of the polymeric backbone on non-specific or ASGPR-independent uptake, concentration dependent experiments were repeated in two different conditions (**Figure 19**); first, HeLa cells were treated with polymers for 2 h at 37°C because these cells have been reported as a ASGPR-negative cell line[368], and second, HepG2 cells treated with polymers for 2 h on ice because a reduction in temperature (below 10°C) has been reported to prevent endocytosis[369]. No appreciable binding or uptake was observed in HeLa cells, with the exception of H-TAG$_2$ and HD-TAG (**Figure 19A**); H-TAG$_2$ showed significantly higher cellular response at concentrations of 1 µM ($p < 0.0001$) and above, and HD-TAG exhibited significantly higher cellular response at concentrations of 5 µM ($p < 0.0001$) and above. Moreover, no appreciable binding or uptake was observed in HepG2 cells maintained at 4°C across all polymeric systems (**Figure 19B**). These observations suggest that there is minimal non-specific uptake occurring due to the polymeric backbone. Interestingly, only TAG decorated systems show binding and uptake in HeLa cells.
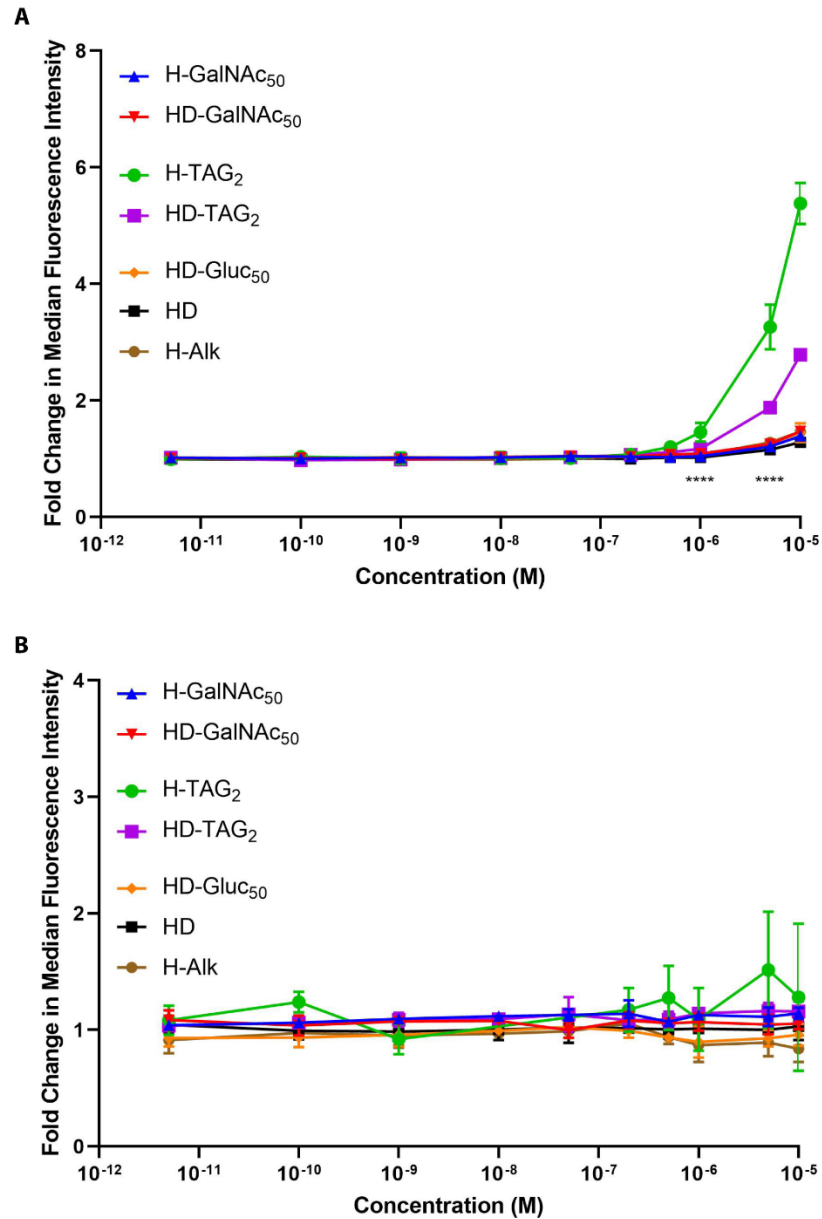
Figure 19. The non-specific or ASGPR-independent binding and uptake of all liver targeting chelating systems and their controls. The response of all carboxyrhodamine-tagged polymers was measured over a range of concentrations. At least 10,000 cells were analyzed using the 488 nm laser and the FITC emission filter (530/20 nm). (A) HeLa cells have been used as an ASGPR negative cell line. (B) HepG2 cells incubated with polymers at 4°C minimizes receptor mediated endocytosis. Error bars show standard deviations for a sample size of 3 independent replicates. A 2-way ANOVA with Dunnett's multiple comparison tests were performed to compare the uptake of all systems against HD-Gluc using Graphpad Prism.

Lastly, the internalization of liver targeting chelating systems was confirmed by using confocal scanning laser microscopy (**Figure 20**). HepG2 cells were co-incubated with either H-GalNAc$_{50}$, HD-GalNAc, and HD-Gluc for 2 h and transferrin-647 to trace early and recycling endosomes. A punctate-like intracellular distribution was observed, consistent with the observations made previously in **Figure 16** and **Figure 17**. Similarly, some qualitative co-localization with transferrin-647 was observed. This provides additional evidence for the intracellular uptake of liver targeting systems conjugated with 15 DFO units.
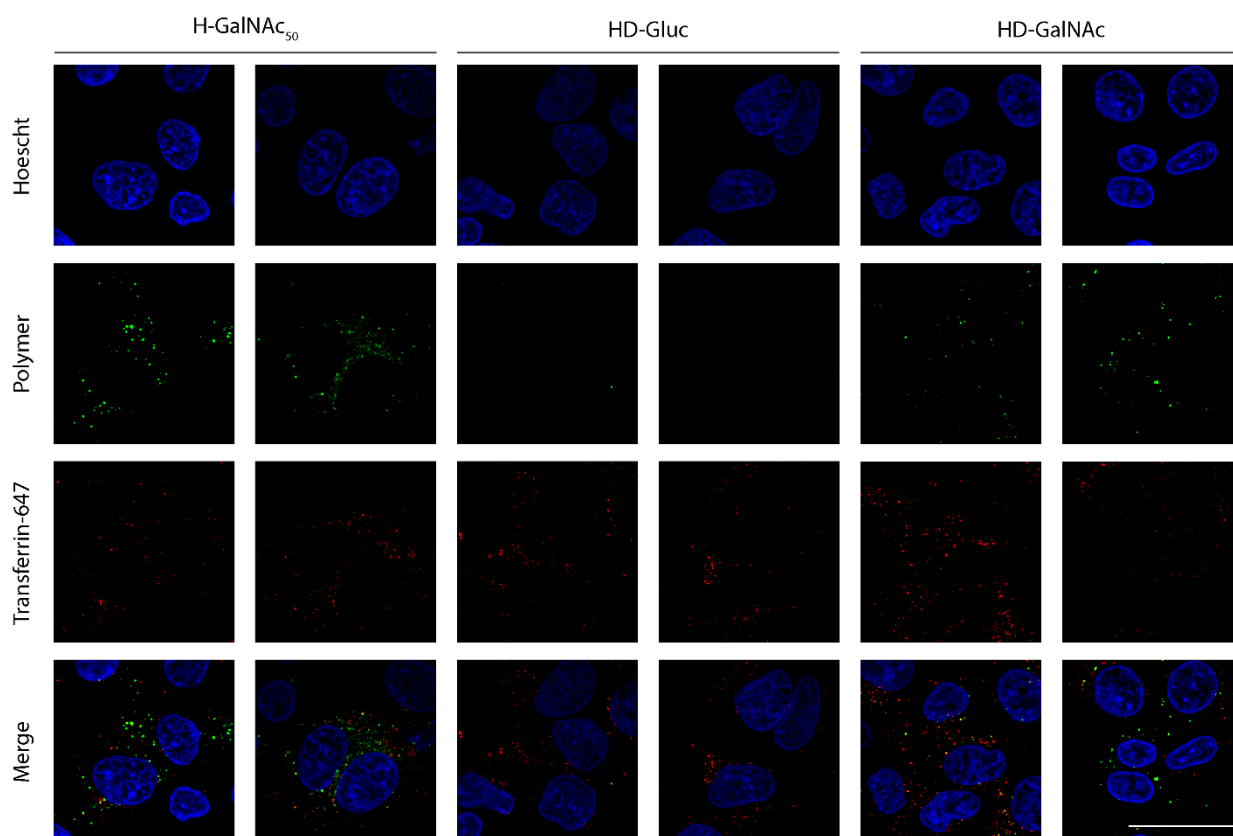
Figure 20. The confirmation of intracellular presence of liver targeting macromolecules in HepG2 cells. Fluorescently labelled H-GalNAc$_{50}$, HD-Gluc and HD-GalNAc were incubated for 2 h at a polymer concentration of 1 μM. Cells were washed in PBS and fixed in 4% PFA for 20 min at RT. Nuclei were stained using Hoechst. Early and recycling endosomes were traced using transferrin-647 (10 μg/mL). All cells were imaged at 4.0 zoom using a 63X objective. At least 100 cells were imaged using Leica SP5 inverted confocal scanning laser microscope. Representative images are shown. Scale bar represents 1 μm.

2.4.4. Cytotoxicity of liver targeting chelating systems

Cytocompatibility of liver targeting iron chelating systems (HD-GalNAc and HD-TAG) were investigated in HepG2 cells over a range of chelator-equivalent concentrations. The effect of conjugation chemistry, the liver targetability and subsequent binding and uptake of these systems were observed by measuring changes in cellular metabolic activity. These were compared with a non-liver targeting chelating system (HD) and with FDA approved small molecular weight chelators (DFO, DFP and DFX). All chelating systems, either liver targeting chelators, non-liver targeting chelator and small molecular chelators, were well tolerated (metabolic activity of 75% and above when normalized to untreated cells) over a range of concentrations, from 1 nM to 50 µM.
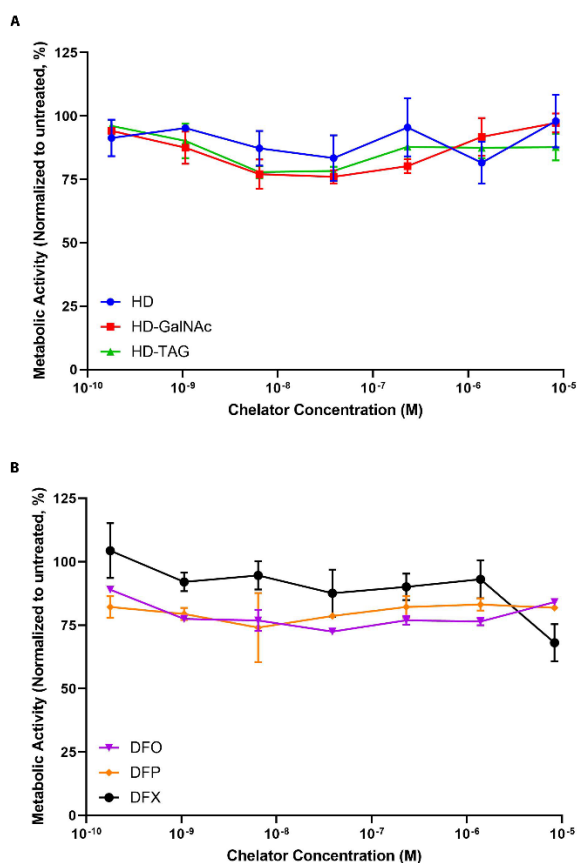
Figure 21. The cytotoxicity of liver targeting chelating systems and their controls in HepG2 cells. The metabolic activity was measured by the MTT assay in response to chelator treatments (A) macromolecular iron chelators – HD, HD-GalNAc and HD-TAG, and (B) small molecular weight iron chelators – DFO, DFP and DFX. A wide range of chelator-equivalent concentrations (from 1 nM to 50 µM) were assessed. Error bars show standard deviations for a sample size of 3 independent replicates.

2.5. Discussion

Hepatic iron burden, along with cardiac iron overload, is a major clinical concern for patients suffering from primary and secondary iron overload as well as other iron induced pathogenesis. The resulting iron toxicity accounts for a majority of premature deaths in these conditions.[101,102] Although iron chelation therapy using Fe(III) specific small molecular chelators showed reduction in hepatic iron accumulation in patients over long-term and intense treatment, these chelators are beset by limitations including toxicities, short circulation times and poor patient compliance principally due its non-specific distribution and off-site interactions. Macromolecular approaches circumvent these shortcomings by using polymers to increase solubility and circulation times, thereby enhancing iron chelators' biological availability and reducing its toxicity. These systems have been reported to remove hepatic iron attributed to the clearance by reticuloendothelial systems, although with fairly low efficiencies.[192] To date, liver targeted delivery of iron chelators remain at large. The liver is a primary iron storage organ and key regulator in iron homeostasis. We anticipate that the selective and rapid removal of excess bioactive liver iron could be of great significance to protect liver from oxidative damage and reduce iron burden.

Liver targeted therapeutic approaches take advantage of the C-type lectin receptor on hepatocytes, the ASGPR; it is almost exclusively present within hepatocyte, it is basolaterally expressed where it readily interacts with the vascular compartment, it has well known high affinity ligands including galactose, N-acetylgalactosamine and tri-antennary N-acetylgalactosamine, and it has efficient internalization and recycling kinetics.[217,223,254] These strategies have been extensively investigated for the delivery of drug and genetic material.[223,232,273] This pursuit has been recently validated with FDA approvals for Onpattro and Gilvaari, from Alnylam Pharmaceuticals, which deliver silencing RNA directly to the hepatocytes.[352,354,373]

An important caveat that needs to be addressed in the design of liver targeted therapeutic approaches lies in bypassing the reticuloendothelial system, in particular the Kupffer cells. Kupffer cells are resident macrophages part of the reticuloendothelial system and are heavily involved in the clearance of foreign substance through phagocytosis.[211,212,215] These cells clear negatively charged molecules *via* scavenger receptors.[374–376] Further, they also possess a C-type lectin receptor, with a high preference to mannose and fucose sugars, as well as galactose sugars.[220,226,232,366,377]

As such, it is imperative that particular attention is given to both the ASGPR-specific ligand and the physical properties of carrier systems because these can influence its accumulation either into hepatocytes or non-

parenchymal Kupffer cells. For instance, PEGylated nano-particles decorated with galactose showed hepatocyte-specific accumulation for particles sized 50 nm and Kupffer cell-specific accumulation for particles sized 140 nm.[259] Similarly, lactosylceramide decorated liposomes resulted in a 48% accumulation in hepatocytes and 27% in non-parenchymal cells.[378]

Therefore, in the design of liver targeting chelating systems, GalNAc and TAG units were selected because they exhibit significantly higher ASGPR affinity when compared to Gal sugars.[237–239] The sugar densities were optimized on the polymer scaffold. HPG was selected as the polymeric scaffold for three reasons; first, hydrophilic polymers bypass the reticuloendothelial systems and hence Kupffer cells as it evades opsonization[226,367], second, HPG systems are highly biocompatibility with long circulating times and offers multi-functional modification[185,370–372], and third, HPG systems have been reported to increase chelation efficiency whilst minimizing toxicities associated with DFO in mice models[183,184,198].

A library of liver targeting systems was developed to screen for the most efficient hepatocyte binding and uptake (**Table 1**) because density of galactosylation has been reported to influence cellular response.[379–382] For instance, the uptake of galactosylated liposomes with a 5.0% Gal yielded the highest uptake ratio between parenchymal and non-parenchymal cells when compared to liposomes with 3.5% and 7.5% liposomes.[379] Similarly, a correlation was observed between the parenchymal uptake of galactosylated poly-L-glutamic acid and number of galactose residues.[380] The binding and uptake of HPG-based fluorescently labelled liver targeting systems were investigated in HepG2 cells using flow cytometry. HepG2 cells were used as *in vitro* model for hepatocytes, despite having lower levels of ASGPR – 80,000 ASGPR per HepG2 cell compared to 0.5 to 2 million ASGPR per hepatocyte.[220–225,383] In order to ensure similar fluorescent intensities for all systems, the HPG scaffold was first modified with a fluorescent tracer molecule, carboxyrhodamine 110 before being attached with chelator or sugar molecules (**Appendix Figure 1**).

H-GalNAc$_{50}$ had superior binding and uptake in both 2 h and 24 h incubation studies when compared to H-GalNAc$_{20}$ and H-GalNAc$_{70}$. These observations suggest that the density of GalNAc on the HPG scaffold influence its binding and uptake response likely due to the balance between available ASGPR and those occupied, either undergoing internalization or recycling, rendering it inaccessible.[225] Since the multivalency of galactose has been directly correlated with increased uptake[381,382], this was observed when comparing H-GalNAc$_{20}$ and H-GalNAc$_{50}$. When compared to H-GalNAc$_{70}$, it is possible that H-

GalNAc$_{50}$ exhibits faster internalization and recycling of ASGPR, allowing for more ASGPR-mediated events to occur.

Further, H-TAG$_2$ was selected because it offers the advantage for further polymer modification since HPG decorated with 2 TAG units outperformed HPG with 20 GalNAc units in its binding and uptake over a 2 h period. Tri-antennary GalNAc ligands exhibit ASGPR affinities in the nanomolar range whereas monoantennary GalNAc ligands exhibit affinities in the micromolar range.[236–240] Ligands with higher binding affinities take longer to dissociate from the internalized receptor, and therefore can influence the recycling kinetics.[257,258] Consistent with this, HPG scaffold decorated with 2 TAG undergo more ASGPR-mediated endocytic events than HPG scaffold decorated with 20 GalNAcs.

Thus, H-GalNAc$_{50}$ and H-TAG$_2$ systems were carried forward for the development of liver targeting chelating systems. DFO was selected as the iron (III) chelator of choice primarily due to its hexadentate coordination of iron. This FDA approved chelator also exhibits high iron binding constant (log β = 31) and has been extensively investigated.[384] In addition, previous work from our laboratory highlights the success of using HPG to increase its chelation efficiency by conjugating 10 to 129 units of DFO per polymer.[183,184,198] For this reason, 15 DFO units were deemed sufficient to impart chelating functionality. However, as illustrated in **Chapter 4**, the chelation efficiency of these liver targeting systems can be increased by increasing the number of DFO units. Additional work will be required to optimize liver targeting systems with respect to the number of DFO unit and the subsequent pharmacokinetic properties (as part of future directions).

Despite showing significantly improved cellular responses when compared to non-liver targeting control systems, HD-GalNAc and HD-TAG exhibited lower binding and uptake when compared to their non-chelator counterparts, H-GalNAc$_{50}$ and H-TAG$_2$. It is essential to highlight that HPG systems were first modified with DFO followed by the ASGPR specific ligands in order to ensure sufficient GalNAc or TAG attachment. This synthetic hurdle likely influences the surface distribution of ASGPR specific ligands, which has important implications in the binding and uptake of liver targeting chelating systems. It is also possible for DFO to perturb ASGPR-mediated endocytosis through the chelation of calcium. The carbohydrate recognition domain in the subunits of ASGPR is calcium dependent as it coordinates with the ligands hydroxyl groups.[226,232] Often, removing calcium serves to significantly decrease ASGPR-mediated endocytosis.[385] This should be investigated in future investigations.

To quantitatively compare the differences between liver targeting chelating systems and their non-chelator counterparts, IC_{50} values were determined using unlabelled GalNAc as the antagonist. The same polymer concentration was used in this assay to allow for a direct quantitative comparison. The IC_{50} value for H-TAG_2 was statistically the highest whereas the IC_{50} value for HD-TAG was not determined. This may be due to insufficient binding or uptake, despite using higher polymer concentrations (up to 5 μM) and higher fluorescent labelling. Alternatively, it is also possible that HD-TAG may require higher GalNAc concentrations to inhibit its cellular response since no reduction in median fluorescence intensity was observed, unlike all other systems (**Appendix Figure 9**). Notably, HD-GalNAc had a significantly higher IC_{50} value compared to H-$GalNAc_{50}$. In other words, a higher concentration of antagonist was required to reduce the binding and uptake of HD-GalNAc by 50% which suggests a stronger ASGPR interaction and internalization. This is likely due to the surface distribution of GalNAc sugars being more favourable in HD-GalNAc compared to H-$GalNAc_{50}$. This also suggests that DFO is unlikely to chelate calcium to negatively influence the interaction with the carbohydrate recognition domain on the ASGPR. Additional work should be performed to quantify ASGPR binding affinities for these systems using surface plasmon resonance or isothermal titration calorimetry.

Next, non-specific binding and uptake were assessed in a ASGPR negative cell line – HeLa cells[368], as well as in HepG2 cells maintained on ice to prevent endocytic processes[369]. With the exception of TAG decorated systems, there were no significant differences observed in the cellular responses in HeLa cells when comparing liver targeting chelating systems and their controls. It is possible that TAG decorated systems show non-specific binding and uptake mediated by the flexible PEG linker, however simply TAG units (before modification for HPG conjugation) did not show HeLa binding and uptake (**Appendix Figure 10**). While it is also possible that HeLa cells possess a receptor for galactose moieties according older reports[386,387], this is unlikely because several reports also use HeLa cells as a ASGPR negative cell line when investigating ASGPR-mediated delivery[382,388,389]. Alternatively, additional cell lines should be explored, particular Kupffer cells, to assess non-specific binding and uptake.

Lastly, *in vitro* cytotoxicity was assessed by measuring changes in metabolic activity of HepG2 cells treated with a wide range of chelator-equivalent concentrations. Both macromolecular chelators and small molecule chelators were well tolerated.

Taken together, these investigations support the conclusion that HD-GalNAc and HD-TAG maintained a significantly higher binding and uptake in *in vitro* conditions when compared to their non-liver targeted controls. GalNAc decorated systems displayed minimal non-specific uptake and HD-GalNAc exhibited a stronger ASGPR interaction and subsequent internalization as compared to H-GalNAc$_{50}$. In contrast, non-specific cellular response was observed for TAG decorated systems and H-TAG$_2$ exhibited significant higher IC$_{50}$ values whereas the IC$_{50}$ value for HD-TAG was undetermined. Nonetheless, both liver targeting systems were characterized for the pharmacokinetic properties in mice (**Chapter 3**). These will provide valuable insights into the design of liver targeting chelating systems achieving hepatocyte-specific vs non-parenchymal-specific uptake.

2.6. Conclusions

Herein, the design and development of liver specific macromolecular chelators have been documented. HPG was used as a macromolecular carrier to target the ASGPR by using high affinity ligands, either GalNAc or TAG. Both the identity and density of these sugars greatly influence their cellular binding and uptake. After screening the library of liver targeting systems, the optimized targeting systems – H-GalNAc$_{50}$ and H-TAG$_2$, were further modified with DFO.

HD-GalNAc and HD-TAG systems exhibited significantly higher binding and uptake compared to their controls, however these were lower than their parent systems, H-GalNAc$_{50}$ and H-TAG$_2$. Interestingly, HD-GalNAc had a higher observed IC$_{50}$ value than H-GalNAc$_{50}$ which suggests a stronger ASGPR interaction and subsequent internalization. Further, confocal investigations confirmed the intracellular presence of liver targeting systems, exhibiting a punctate-like distribution that often qualitatively co-localizes with the endocytic pathway. The data from this chapter justify the selection of HD-GalNAc and HD-TAG for further investigations in subsequent chapters to better characterize this novel class of liver specific iron macromolecular chelators.

Chapter 3: Investigation of pharmacokinetic properties, excretion and trafficking of liver targeted macromolecular iron chelators.

3.1. Overview

The previous chapter described the design of liver targeted macromolecular iron (III) chelators (HD-GalNAc and HD-TAG) by optimizing for ASGPR ligands and densities *in vitro*. In this chapter, the pharmacokinetic properties and biodistribution were investigated with a particular focus on liver targetability and excretion modalities. Within the liver, the cellular accumulation was also examined to delineate between ASGPR-mediated uptake by parenchymal hepatocytes and non-ASGPR-mediated clearance by non-parenchymal Kupffer cells. Additional intracellular processing and trafficking were investigated to shed mechanistic insights on excretion performance of these systems.

The ASGPR-specific ligands incorporated on HPG resulted in significant liver specificity when compared to the non-targeted control, HD. The liver targeted systems showed minimal non-specific accumulation in other vital organs. Remarkably, the selection of the ligands influenced the pharmacokinetic profiles of the liver targeting chelating systems with respect to vascular residency, non-specific distribution and route of excretion. HD-GalNAc demonstrated significantly higher liver uptake and minimal vascular residency when compared to HD-TAG. Further, both HD-GalNAc and HD-TAG were rapidly excreted within 24 h. However, HD-GalNAc was eliminated equally between the hepatobiliary and renal routes whereas HD-TAG was excreted predominantly through the hepatobiliary route. The intracellular fate for liver targeting polymers revealed rapid lysosomal accumulation, which may explain the rapid excretion observed. Additionally, differences in intracellular trafficking were attributed to the ASGPR-specific ligand as well as DFO conjugation. Taken together, the selection of the ASGPR-specific ligands demonstrated significant total excretion whilst achieving liver targeting. These studies provide sufficient evidence to investigate HD-GalNAc and HD-TAG for their iron chelation efficacy.

3.2. Background

A diverse repertoire of nanomaterials has been developed for a wide range of clinical and biomedical application, however, very few have made it past clinical trials. The limited success has been attributed to the insufficiencies in overcoming biological barriers, including the opsonization and phagocytosis by the reticuloendothelial system and the subsequent endosomal compartmentalization[390], resulting in the non-specific accumulation of nanomaterials. The subsequent toxicities have been reported to be one of the main caveats in clinical translation.[373,391]

A vast amount of research has investigated strategies that navigate these barriers by carefully designing materials with respect to particle size, charge, shape, deformability and degradability. For example, nanoparticles with diameters less than 5 nm rapidly undergo renal clearance[392,393] whereas particles up to 200 nm accumulated within the liver[394] and splenic filtration accounts for the retention of materials up to 500 nm[395]. The prolonged accumulation of materials by the reticuloendothelial organs, especially the liver, can influence its physiology.[396] Passive hepatobiliary excretion is mediated by both parenchymal and non-parenchymal cells, including Kupffer cells, stellate cells and sinusoidal endothelial cells, and has been reported to take between days to month to completely eliminate.[396–401] Additionally, rigid particles have been demonstrated to be readily cleared[402] whereas 'softer' particles maintained longer circulation times, attributed to its flexibility through fenestrated capillaries[403].

Of particular interest, active targeting moieties have been employed to enhance cell specific uptake which avoid non-specific distribution and subsequent toxicities. The delivery of therapeutic cargo to the liver has been the subject of many investigations since the discovery of ASGPR and its high affinity ligands – Gal, GalNAc and their multi-antennary forms.[219,223,273] For instance, the recently FDA approved patisiran (Onpattro) and givosiran (Givlaari) demonstrated desired liver targetability and enhanced therapeutic outcomes for hereditary transthyretin-mediated amyloidosis and acute intermittent porphyria, respectively.[352,354]

Despite the years of investigations, there is great variability in efficient ASGPR-mediated liver targeting. This is due to a combination of both the physical properties of carriers as well as the ASGPR-specific ligands and their densities, which influences the uptake and accumulation of cargo by either parenchymal cells or non-parenchymal resident macrophages, Kupffer cells.[223] Kupffer cells also possess a similar receptor that recognizes Gal and GalNAc, however with lower affinities.[260,267,330,366] In addition to this, there is very

limited information on the intracellular processing and excretion of liver targeted synthetic materials that are greater than kidney clearance limit (between 5 and 15 nm).[393,404]

Chapter 2 reported the screening and selection of HPGs decorated with either GalNAc or TAG, and the subsequent changes in cellular response after DFO conjugation. Here, we investigate the pharmacokinetic, biodistribution and excretion properties for HD-GalNAc and HD-TAG and the underlying intracellular fate. We hypothesized that the liver targeted macromolecular chelating system will undergo ASGPR-mediated endocytosis by hepatocytes, trafficked to the lysosomes for processing and excreted in the feces *via* the hepatobiliary route.

In order to challenge this hypothesis, HD-GalNAc and its control were first assessed in a pilot investigation to explore experimental parameters required in a detailed pharmacokinetic analysis. This accounted for the influence of radiolabelling chemistry, the selection of an appropriate control and the time points of interest. Then, detailed pharmacokinetic and biodistribution analyses were performed to understand how HD-GalNAc and HD-TAG behave with respect to vascular retention, liver targetability, non-specific distribution and excretion in C57Bl/6 mice. Liver targetability was further examined to discern whether these systems accumulate within parenchymal cells or non-parenchymal cells through fluorescently labeled molecules *in vivo*. The different excretion modalities uncovered prompted the additional investigations into the kinetics of intracellular trafficking in order to correlate physiological responses on a cellular level.

Taken together, earlier *in vitro* analyses optimized for the identity and densities of ASGPR-specific ligand. Herein, the translation of these liver targeting chelating systems were further investigated *in vivo* to provide an understanding into the role of ASGPR-specific ligands on the physiological responses and processing organ-targeted synthetic materials. The aim of this work is to add valuable insights into the design of polymeric drug carriers to the wider scientific community.

3.3. Methods

3.3.1. Materials

Eagle's Minimum Essential Media (EMEM), Dulbecco's Phosphate Buffered Saline (PBS), 0.25% trypsin-EDTA, Trypan blue, Hoechst, goat anti-rabbit Alexa-568 and goat anti-mouse Alexa-568 was purchased from Thermo Fisher Scientific. Fetal bovine serum, normal goat serum, saponin, hydrochloric acid, hydrogen peroxide, ethylenediaminetetraacetic acid (EDTA), sodium bicarbonate, ammonium chloride, acetic acid, collagen type 1, collagenase IV, dimethyl sulfoxide (DMSO), 16% paraformaldehyde, asialofetuin (AF), scintillation cocktail, Hanks' balanced salt solution, 25G and 28G needles, 4 Å molecular sieves, sodium hydride, MWCO 1kDa dialysis tube, and 0.2 μm syringe filter were obtained from Sigma-Aldrich. IBIDI μ-slides were purchased from IBIDI. Solvable was acquired from Perkin Elmer. Tritiated methyl iodide was acquired from American Radiolabeled Chemicals. Mouse anti-human EEA1, mouse anti-human Rab7, mouse anti-human LAMP1 and rabbit anti-human TfR1 antibodies were purchased from Abcam. Alexa-647 anti-ASGPR antibodies were obtained from Santa Cruz Biotechnologies. FITC anti-mouse CD68 antibodies were obtained from Biolegends.

3.3.2. Synthesis of liver targeting macromolecular iron chelators

The synthesis protocols have been described in **Chapter 2** and all liver targeting macromolecular systems have been summarized in **Table 1** and **Table 2**. Here, additional details for radiolabelling and fluorescently labeling of these systems have been outlined.

3.3.2.1. Tritium labelling of macromolecular chelating systems

Tritium labelling of both liver targeting chelating systems (HD-GalNAc and HD-TAG) and their non-liver targeting controls (HD-Gluc and HD) were performed as per our previous protocol, targeting 1% of the hydroxyl groups.[182] All polymers were previously stored in water (4°C). These were dialyzed against anhydrous DMSO for 2 days and dialysates were replaced twice. The resultant solution underwent three repeated freeze-thaw cycles to remove dissolved oxygen. The concentration of the solution was confirmed by thermogravimetry and stored over pre-dried 4 Å molecular sieves.

The polymeric systems were transferred into a pre-dried Schlenk flask for tritium labelling. Sodium hydride (3 equivalents with respect to the targeted hydroxyl groups) was added slowly in small portions under

argon and the solution was stirred at room temperature (20°C to 24°C) for 2 h. Tritiated methyl iodide (1 equivalent with respect to the targeted hydroxyl groups) was added slowly and the solution was stirred for 20 h. The reaction mixture was quenched with dropwise addition of water to quench the unreacted sodium hydride. The reaction mixture was dialyzed against water (MWCO-1 kDa) until the radioactivity of the dialysate was less than 100 DPM for 48 h. Tritium labeled polymers were filtered through 0.2 μm syringe filter.

The activity of all tritium labelled polymers were measured by scintillation counting. The concentrations (mg/mL) of the macrochelators were adjusted by concentrating the solutions under vacuum. Osmolarity of the chelator solutions were adjusted by adding the appropriate amount of sodium chloride. These were prepared before animal experiments.

3.3.2.2. Fluorescent labelling of macromolecular chelating systems

Fluorescent labelling of all liver targeting molecules with carboxyrhodamine 110 azide was described in **Chapter 2**. Carboxyrhodamine labelled macromolecules were used for all *in vitro* investigations. For *in vivo* investigations, cyanine 5.5 azide (Lumiprobe) was used because of its near-infrared emission (excitation maximum at 684 nm and emission maximum at 710 nm). The synthetic protocol cyanine 5.5 azide is similar to that of carboxyrhodamine, and therefore it will not be outlined here.

3.3.3. Cell culture

A hepatocellular carcinoma cell line, HepG2 cell line (ATCC HB-8065), were cultured and maintained in accordance with manufacturer's protocol. Cells were maintained in EMEM with media being replaced every 2 to 3 days. For all experiments, HepG2 cells with passage numbers between 3 – 9 were used.

3.3.4. *In vitro* binding and uptake of tritiated liver targeting chelating systems

HepG2 cells were seeded at a density of 60,000 cells per well in a 48 well plates and allowed 48 h to attached and proliferate. On day 3, cells were treated with 1 μM of tritiated HD-GalNAc and HD-Gluc for 2 h at 37°C. Cells were rinsed thrice with PBS (0.5 mL), detached using 0.25% trypsin-EDTA (0.5 mL) for 10 min at 37°C and pelleted at 500 g for 5 min. The cell pellet was resuspended and transferred into scintillation cocktail (5 mL). Radioactivity was measured by performing scintillation counts.

3.3.5. Intracellular distribution and trafficking investigations

IBIDI chamber μ-slides were coated with rat collagen type 1 for 4 h following manufacturer's recommendation; 4 well chamber slides were coated with 30 μg/mL collagen (700 μL) in 2% acetic acid, and 8 well chamber slides were coated with 35 μg/mL collagen (300 μL) in 2% acetic acid. All slides were thoroughly rinsed with PBS just before seeding. Following collagen coating, HepG2 cells were seeded at 60,000 cells per well in 4 well chamber slides (1 mL) or 30,000 cells per well in 8 well chamber slides (0.5 mL). Cells were allowed to attach for 2 days. To ensure proper attachment, cells were maintained for 3 additional days before any treatment with media changes occurring every 1-2 days.

Three different treatments were performed to understand the intracellular distribution and kinetics for these macromolecules; 3.3.5.1. Intracellular distribution of macromolecules after continuous incubation for either 2 or 24 h, 3.3.5.2. Pulse-chase kinetic investigations of intracellular trafficking, and 3.3.5.3. Bafilomycin-induced inhibition of endosomal maturation. All imaging experiments were fixed and stained for various organelles, outlined in section 3.3.5.4. All quantitative analyses performed were in section 3.3.5.5.

3.3.5.1. Intracellular distribution of liver targeting systems after incubation for either 2 or 24 h

To screen for differences in cellular responses to liver targeting systems, HepG2 cells were grown in an 8-well chamber slides as described previously. Cell were incubated with 1 μM of H-GalNAc$_{50}$ and HD-GalNAc prepared in EMEM (200 μL) for the full duration of either 2 h or 24 h at 37°C. After incubation period, cells were washed twice with PBS (0.5 mL) and then fixed, as described in section 3.3.5.4. The endocytic pathway was traced using antibodies to identify early endosomes, early and recycling endosomes, late endosomes, and lysosomes.

3.3.5.2. Pulse-chase kinetic investigations of intracellular trafficking for liver targeting systems

Intracellular distribution and kinetics of liver targeting polymers (H-GalNAc$_{50}$, H-TAG$_2$, HD-GalNAc and HD-TAG) and an endogenous ASGPR-specific protein, asialofetuin, (AF) were investigated by a series of pulse-chase experiments conducted in 4-well chamber slides. First, cells were pulsed with either 4 μM of polymers or 1 g/mL of AF for 30 min (200 μL). Then, cells were treated with fresh media (500 μL) for either 0, 1, 2, 16, 24 h to chase the internalized macromolecules. After the chase periods, cells were washed

twice with PBS (0.5 mL) and then fixed, as outlined in section 3.3.5.4. After accounting for the differences in cellular responses to the continuous incubation of macromolecules, the endocytic pathway was traced using antibodies to label early endosomes, late endosomes, and lysosomes. The ASGPR was stained using ASGPR antibodies. The pulse chase kinetic investigations of liver targeted systems were compared to asialofetuin (AF) with respect to early endosomes and lysosomes.

3.3.5.3. Bafilomycin-induced inhibition of endosomal maturation

The uptake and intracellular distribution of polymer systems (H-GalNAc$_{50}$, H-TAG$_2$, HD-GalNAc and HD-TAG) were disturbed using bafilomycin-A1, a vacuolar ATPase inhibitor that prevents the acidification of endosomes.[405] All experiments were performed in 4-well chamber slides. First, HepG2 cells were pre-treated with 50 nM of bafilomycin (200 μL) for 1 h. Then, cells were pulsed with 4 μM of polymers (200 μL) for 30 minutes followed by a chase of 1 h with fresh media. Cells were washed with PBS (0.5 mL) twice and then fixed, as mentioned in section 3.3.5.4 Early endosomes and lysosomes were stained.

3.3.5.4. Fixation and compartment-specific immunostaining

After polymer treatments outlined in section 3.3.5.1, 3.3.5.2., and 3.3.5.3., cells were washed twice with PBS (0.5 mL). HepG2 cells were fixed in 4% paraformaldehyde (200 μL) prepared in EMEM without phenol red for 30 minutes, followed by a single wash with PBS (0.5 mL). Then, cellular compartments were stained following either a single antibody staining or a double antibody staining protocol, outlined below. After this, cells were washed twice and maintained in PBS (0.5 mL) until confocal laser scanning microscopy. A work-flow has been provided in the **Appendix** for further clarity (**Appendix Figure 11**).

Intracellular compartments were immunostained using either a single antibody staining to visualize ASGPR or a double antibody staining to visualize early endosomes, recycling endosomes, late endosomes, and lysosomes. The primary and secondary antibodies used have been summarized in **Appendix Table 2**. In all experiments, the nucleus was counterstained using Hoechst. The protocols for a single antibody and a double antibody approach vary – both are detailed below.

Single antibody staining:

ASGPRs were identified using an Alexa-640 conjugated anti-ASGPR antibody at dilution of 1:200. After fixation, cells were treated with staining buffer (0.005% saponin in PBS with anti-ASGPR antibody and

Hoechst at a dilution of 1:5000) (200 μL) for 45 minutes at room temperature. Cells were washed twice and maintained in PBS (0.5 mL) until confocal laser scanning microscopy.

Double antibody staining:

Early endosomes, recycling endosomes, late endosomes, and lysosomes were stained using unlabelled primary antibodies against EEA1, TfR1, Rab7, and LAMP1 respectively. After fixation, cells were pre-treated with blocking buffer (10% normal goat serum and 0.005% saponin in PBS) (200 μL) for 45 minutes at room temperature. Then, cells were treated with unlabelled primary antibodies, at a dilution of 1:200, in blocking buffer (200 μL) for an additional 60 minutes at room temperature. Cells were washed twice with PBS (0.5 mL) to remove any unbound antibodies.

Following this, cells were then treated with secondary staining buffer (0.005% saponin in PBS with Alexa-568 secondary antibodies against the unlabelled primary antibodies (anti rabbit or anti mouse) and Hoechst at a dilution of 1:5000) (200 μL) for 45 minutes at room temperature. Cells were washed twice and maintained in PBS (0.5 mL) until confocal laser scanning microscopy.

3.3.5.5. Confocal scanning laser microscopy

At least 100 cells were captured per treatment from multiple fields of view. All images were acquired on a Leica SP5 inverted laser scanning confocal microscope equipped with a 405, 488 and 633 laser, an HCX PL APO lambda blue 63.0x 1.40 oil objective and 3 photomultiplier tubes (PMT) detectors. Sequential scanning was performed starting with the longest laser wavelength to the shortest. Scanner settings have been summarized in **Appendix Table 3**. Images were exported in 16-bit as TIFF.

3.3.5.6. Image analyses

Fluorescence intensities from immunostaining were quantified using a custom MATLAB code for image thresholding, as described in detail elsewhere.[406,407] This script creates a binary mask for fluorescent spots of different sizes defined by sigma, a variable that represents the radius in pixels. In short, Laplacian of Gaussian filters were applied at varying widths to identify regions of fluorescent intensities in acquired images. Then, a binary mask was created with pixel intensities above a threshold set as 1 and anything below set as 0. This threshold is defined as a number of standard deviations above the mean background noise. Sigma and threshold values used visually agreed with fluorescent signals and no spurious

background detections were observed. These values have been summarized in **Appendix Table 4**. All MATLAB scripts are available upon request.

Subsequently, Mander's co-localization coefficients (MCC) were quantified on the resultant binary masks using the JACoP plugin (Just Another Co-localization Plugin) in ImageJ.[407–410] MCCs measures co-occurrence and provides fractions of overlap attributed to a particular probe – i.e. MCCs measures the overlap of the liver targeted systems' signal with the cellular compartment antibody signal, and vice versa. For the purpose of these investigations, data was presented as MCCs percentage of liver targeted polymers' signal overlapping in antibody signal, ranging from 0% to 100%. A sample step-wise processing of raw images acquired into binary masks for Mander's co-localization analyses has been showed in **Appendix Figure 12**.

3.3.6. *In vivo* pharmacokinetic and biodistribution investigation of liver targeting chelating systems

All the animal studies were carried out at the Experimental Therapeutics laboratory, B.C. Cancer Research Centre, Vancouver, BC, Canada. All the protocols were approved by the Institutional Animal Care Committee (IACC), UBC. For all studies, female C57Bl/6 mice between 6 to 9 weeks were used.

3.3.6.1. A pilot biodistribution assessment of a liver targeting chelating system and its control

Tail vein injections were administered at a dose of 10 mg/kg with injection volumes of 200 µL/20 g mice. At 2 and 24 h post-injection, mice were terminated by CO_2 inhalation. Each treatment group had a total of 3 mice. Blood and organs (liver, spleen, kidneys, heart and lungs) were collected, as described below in section 3.3.6.3 and 3.3.6.4. respectively. The radioactivity of tritiated HD-GalNAc and HD-Gluc were measured in plasma and digested organs, and reported as an average percentage of the injected dose (ID).

3.3.6.2. A detailed investigation of selected liver targeting chelating systems

The plasma circulation times, organ biodistribution and excretion profiles of tritiated HD-GalNAc and HD-TAG were investigated over the course of 144 h. Tritiated HD was also investigated, as a non-liver targeting control, for the first 24 h. HD-Gluc were not investigated, as concluded from the pilot study (section 3.3.5.1). Mice were individually weighed and injected at a dose of 10 mg/kg with injection volumes of 200

µL/20 g mice) intravenously through the tail vein. Body weights of the mice were monitored. Mice treated with either HD-GalNAc or HD-TAG were terminated after 1, 4, 8, 24, 72, and 144 h of injection, whereas those treated with HD were terminated after 8 and 24 h of injection. Each treatment group had a total of 3 mice. All mice were terminated by CO_2 inhalation at the desired time points. Blood, organs and excrement collection and processing were performed as outlined below (section 3.3.6.3., 3.3.6.4., and 3.3.6.5., respectively) Radioactivity measurements were reported as an average percentage of the ID.

3.3.6.3. Collection and processing of blood

Blood was collected at the desired time point *via* cardiac puncture with a 25G needle and placed into a corresponding microtainer tube. Then, plasma was separated by centrifuging samples at 2500 rpm for 15 min and transferred to a separate tube. Radioactivity was measured in an aliquot (50 µL) with scintillation cocktail (5 mL).

3.3.6.4. Collection and processing of organs

Upon termination of the mice, whole liver, spleen, lung, heart and kidneys were harvested, rinsed in PBS, weighed and processed for radioactivity measurements. All organs were homogenized prior to scintillation counts. Whole livers were prepared into a 30% homogenate in a known amount of water using a Polytron tissue homogeniser. and small aliquots of homogenate (200 µL) in triplicates were transferred to scintillation vials. All other organs were homogenized and digested using Solvable® (500 µL). Vials were incubated at 50°C overnight or until samples were completely dissolved, then cooled on ice prior to the addition of 200 mM EDTA (50 µL), 10 M HCl (25 µL) and 30% H_2O_2 (200 µL). This mixture was incubated at room temperature for several h before the addition of scintillation cocktail (5 mL). The radioactivity was measured through scintillation counts for all samples in triplicates. Triplicate aliquots (10 µL) of stock tritiated compound were analysed for specific activity determination.

3.3.6.5. Collection and processing of excrement

For urine and feces collection, mice were housed in metabolic cages during the entire course of the study (144 h group). All the urine and feces were collected from the metabolic cages and transferred into pre-weighed tubes. For feces collection, a homogenate solution of 10% (or 5% if there was limited feces collected) feces in water was made using the Polytron tissue homogeniser and processed similar to organs

as mentioned above. Urine (100 μL) and feces (200 μL) samples were read in triplicates by the liquid scintillation counter.

3.3.7. *In vivo* liver cellular distribution of liver targeted chelating systems

The *in vivo* hepatic distribution of cyanine 5.5 labelled HD, HD-GalNAc and HD-TAG were investigated as reported elsewhere.[411] A saline control group was also used. At least 3 mice were used for each polymer at each time point. Each mouse was injected with fluorescently-tagged liver targeted molecules *via* the tail vein at a dose of 10 mg/kg with injection volumes of 200 μL/20 g mouse using a 28G needle.

Mice were briefly restrained during tail vein injections and, if needed, a heat lamp was used to dilate the vein. After 0.5, 2 or 8 h of injection, mice were sacrificed with isoflurane and liver perfusions were performed immediately. Using an injection pump; pre-warmed 0.5 mM EDTA in HBSS (15 to 20 mL) was perfused *via* the portal vein until the liver blanched followed by the perfusion of warm digestion media consisting of DMEM with 100 U / mL collagenase IV (15 mL) for 5 to 7 minutes. The liver was excised and placed in additionally digestion medium for another 10 to 15 minutes. After this, liver cells were mechanically separated with tweezers and passed through a 120 μm sterile filter. All cells were washed with red blood cell lysis buffer (ammonium chloride 0.15 M, sodium bicarbonate 0.01 M, and EDTA 1.2 mM)[412] thrice followed by PBS wash once (10 mL). Kupffer cells were identified using anti-CD68 antibodies. Hepatocytes were identified as CD68 negative cells. The gating is shown in **Appendix Figure 13**. At least 10,000 cells were analyzed in the BD FACS Calibur equipped with 2 lasers, 488 and 635 nm. Percentage of cells positive for liver targeted polymers were determined by gating for cells using unlabelled controls.

3.3.8. Statistical analysis

All experiments were performed in at least independent triplicates and presented with error bars that correspond to standard deviations. Technical replicates were also performed, but only independent triplicates were used for statistical analysis. All statistical analyses were performed using GraphPad Prism 7 (Grahpad Software, San Diego, USA). The statistical tests and appropriate multiple comparison tests were outlined in the figure legends.

3.4. Results

3.4.1 A pilot biodistribution assessment of liver targeting macromolecules

Liver targeting chelating systems, HD-GalNAc and HD-TAG, selected in **Chapter 2** from earlier *in vitro* investigations were next evaluated for their *in vivo* pharmacokinetic behavior. First, the liver targeting chelating systems and their controls, HD and HD-Gluc, were tritiated by converting hydroxyl groups into $[^3H_1]$ methyl ethers. In order to ensure that these liver targeting chelating systems still retained their binding and uptake profiles observed earlier, an *in vitro* binding and uptake assay (**Figure 22**) was performed in HepG2 cells. The scintillation counts (DPM) for HD-GalNAc were significantly higher than HD-Gluc when treated at 1 µM (p = 0.0002) – there was 4 fold difference observed. This confirms that chemical modifications required to radiolabel liver targeting systems did not significantly impact their *in vitro* responses.
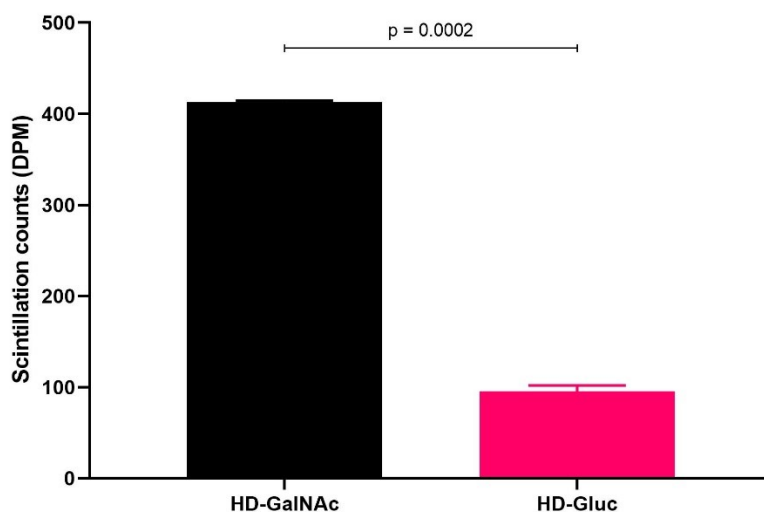
Figure 22. The binding and uptake of tritiated liver targeting chelating system and its non-liver targeting control. Scintillation counts were measured in HepG2 cells treated with 1 µM of either HD-GalNAc or HD-Gluc for 2 h at 37°C. Error bars show standard deviations for a sample size of 3 replicates. A t-test was performed to compare the uptake of HD-GalNAc with HD-Gluc using Graphpad Prism.

Next, a preliminary study was performed using HD-GalNAc and HD-Gluc to assess the hypothesized liver targetability in C57Bl/6 mice (**Figure 23**). Tritiated macromolecules were injected intravenously and the concentration (reported as an average percentage of ID) of tritiated HD-GalNAc and HD-Gluc were measured in the plasma, liver, kidneys, heart, spleen and lungs at 2 h and 24 h post injections. At 2 h post injection, HD-GalNAc was rapidly cleared from circulation when compared to HD-Gluc, with 1.2% vs 33.5% of the injected dose (ID) remaining in plasma ($p < 0.0001$), respectively. Similarly, preferential hepatic accumulation was observed for HD-GalNAc when compared to HD-Gluc, with 35.9% vs 11.2% of the ID present in the liver ($p<0.0001$), respectively.

Similarly, at 24 h, the hepatic accumulation of both HD-GalNAc and HD-Gluc were maintained at 31.3% and 15.4% of the ID, respectively ($p < 0.0001$). The pilot assessment of biodistribution *in vivo* confirmed the hypothesis that decorating HPG-based chelating systems with ASGPR-specific ligands, as seen with GalNAc, exhibited high liver specificity when compared to its control. Based on these observations, detailed pharmacokinetic, biodistribution and excretions investigations were performed on HD-GalNAc and HD-TAG.
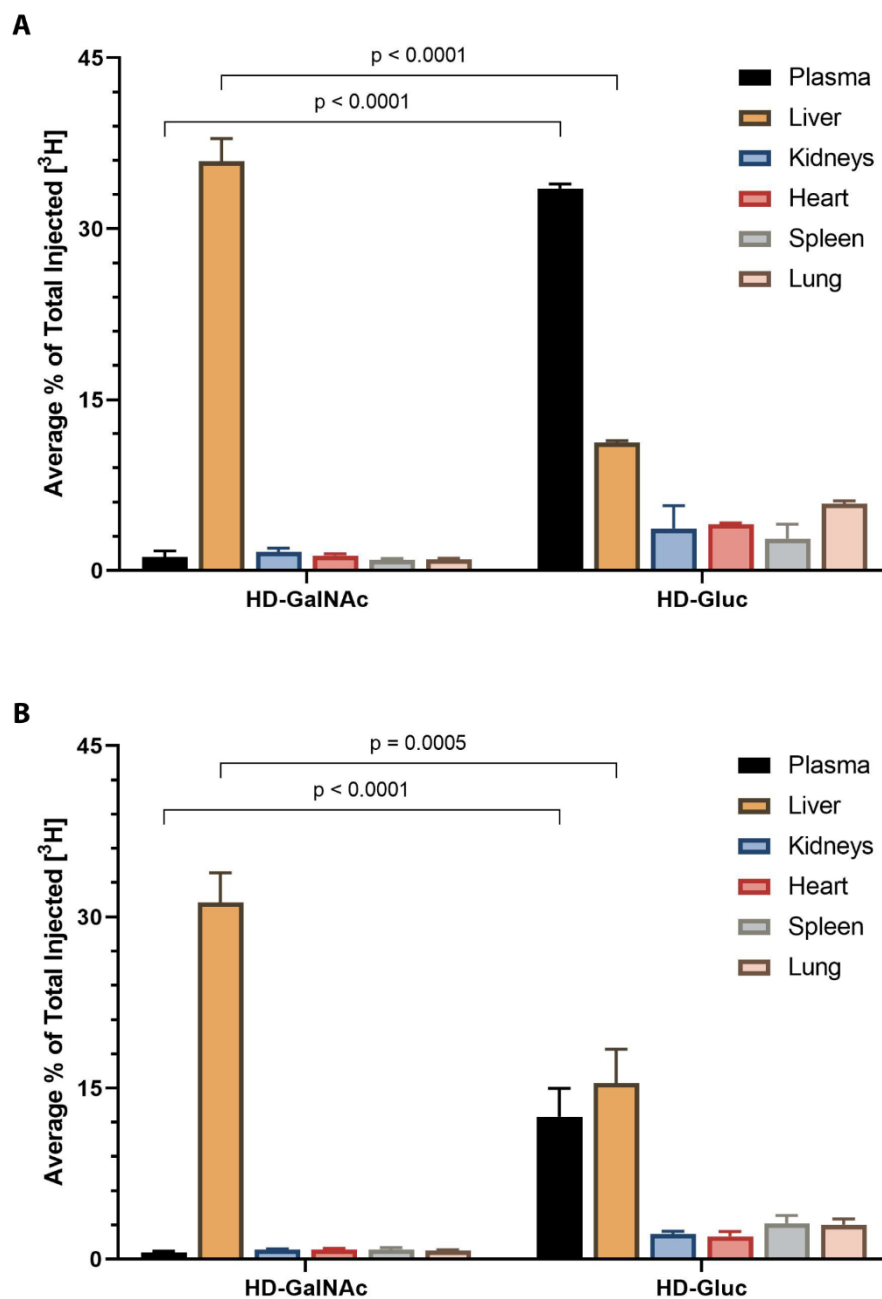
Figure 23. A pilot *in vivo* biodistribution investigation for tritium labelled liver targeting chelating system and its non-liver targeting counterpart. 10 mg/kg of [^{3}H] labelled polymers were intravenously injected in C57BL/6 mice and radioactivity was measured in plasma and various organs at either (A) 2 h or (B) 24 h post injection. Error bars show standard deviations for a sample size of 3 independent mice. A 2-way ANOVA with Sidak's multiple comparison test were performed using GraphPad Prism.

3.4.2. Evaluation of the biodistribution and pharmacokinetic profiles for liver targeting chelating systems

Detailed pharmacokinetic investigations of HD-GalNAc and HD-TAG were performed to assess circulation half-life, biodistribution and excretion profiles over 144 h after injecting C57Bl/6 mice with tritiated macromolecules (**Figure 24** to **Figure 27**). The biodistribution and excretion of these liver targeting chelating systems were compared to non-liver targeted HD at 8 and 24 h after injection. HD was used as a control because previous works from our laboratory focused on HD systems and their *in vivo* iron chelation efficacy.[183,198,371] Additionally, HD-Gluc was omitted in these studies because the pilot *in vivo* biodistribution investigation provided sufficient evidence for poor liver specificity of this control.

The circulation half-lives of the liver targeting chelating systems were calculated using a two compartment model.[187] The distribution half-life for HD-GalNAc and HD-TAG were 1.7 h and 2.0 h respectively. The elimination half-life for HD-GalNAc and HD-TAG were 98.0 h and 27.0 h. Remarkably, the non-linear regression analysis for HD-GalNAc and HD-TAG were significantly different ($p < 0.0001$) (**Figure 24A**).

Next, the biodistribution of liver targeting chelating systems were evaluated and compared to the non-liver targeting control, HD. Both HD-GalNAc and HD-TAG exhibited preferential accumulation in the liver almost immediately after injection (**Figure 24B**). HD-GalNAc demonstrated 31% ± 3% and 33% ± 1% of the ID accumulating in the liver after 1 and 4 h, respectively. Similarly, HD-TAG demonstrated 20% ± 2% and 17% ± 4% of the ID accumulating in the liver after 1 and 4 h, respectively. Over the duration of the study, both liver targeting chelating systems decreased with 20% ± 2% of the ID remaining for HD-GalNAc and 15% ± 1% of the ID remaining for HD-TAG by 144 h. When comparing between the liver targeting chelating systems, HD-GalNAc revealed significantly higher hepatic accumulation over the first 72 h when compared to HD-TAG ($p < 0.0001$ for all comparisons). In addition, there was minimal non-specific distribution observed in other organs including kidneys, heart, spleen and lungs. HD-GalNAc had a sub-3% accumulation in the other organs over the course of the 144 h (**Figure 24C**). On the other hand, HD-TAG had approximately a 5-8% accumulation in the other organs initially which then decreased below 5% for the kidneys, heart and lungs (Fig. 3D). Notably, the splenic accumulation of HD-TAG also decreased during the first 72 h but then exhibited an increase at the 144 h time point (**Figure 24D**). When compared to the non-targeted control – HD (**Figure 25**), the biodistribution profiles confirmed the high liver specificity for both HD-GalNAc and HD-TAG at 8 h ($p < 0.0001$ and $p = 0.0124$, respectively) and 24 h ($p < 0.0001$ and $p = 0.0015$, respectively). HD also exhibited minimal non-specific distribution.
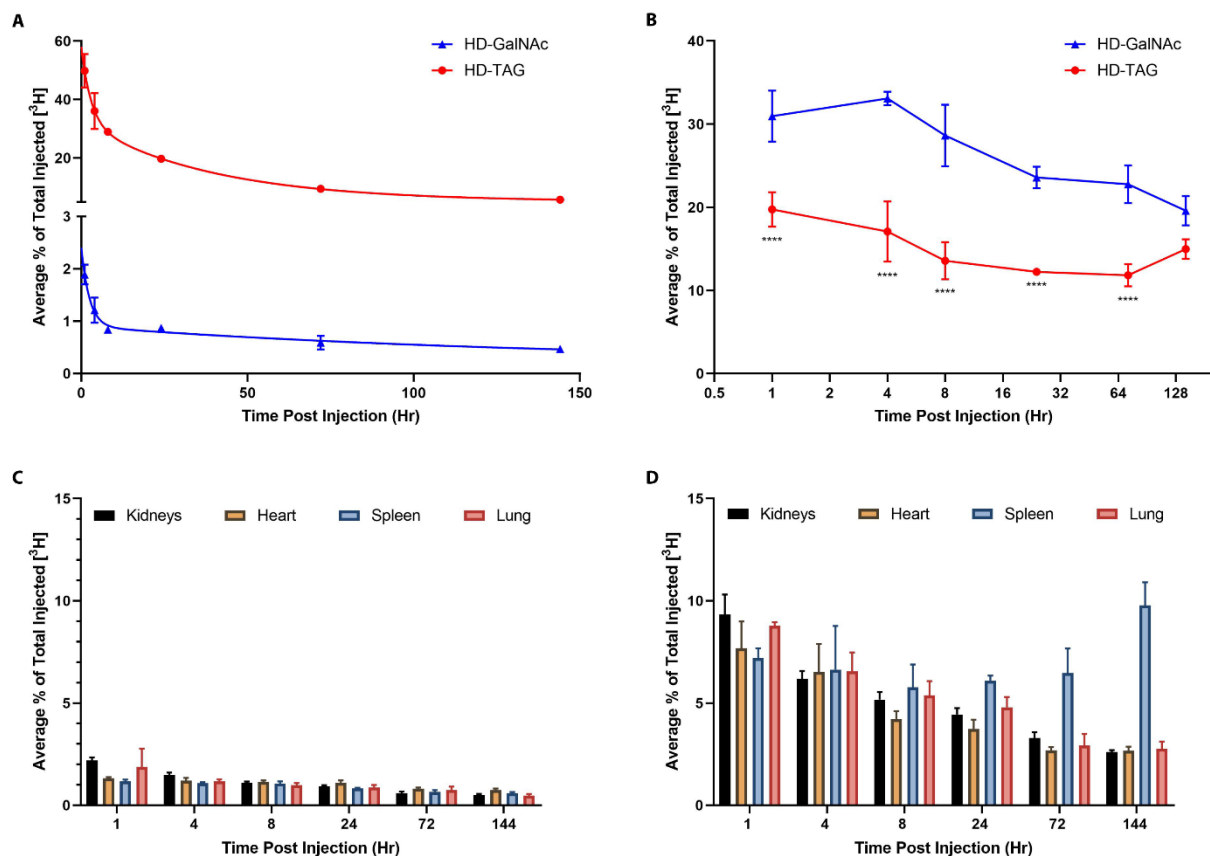
Figure 24. Pharmacokinetic and biodistribution of tritium labeled liver targeting macromolecular chelating systems in C57BL/6 mice. Tritium labelled systems were injected at 10 mg/kg dose intravenously into mice. Radioactivity was measured through scintillation counts in (A) plasma and (B) liver. Nonspecific biodistribution of (C) HD-GalNAc and (D) HD-TAG were also measured in other organs including kidneys, heart, spleen and lungs. Error bars show standard deviations for a sample size of 3 mice. Circulation times were determined using a two-phase decay non-linear regression analysis in Graphpad Prism. Extra-sums-of-squares F Test was performed to compare the two non-linear regression analyses for circulation half-lives. 2-way ANOVA with Sidak's multiple comparison test were performed to compare the accumulation of these liver targeting systems in the liver. **** represents a $p < 0.0001$.
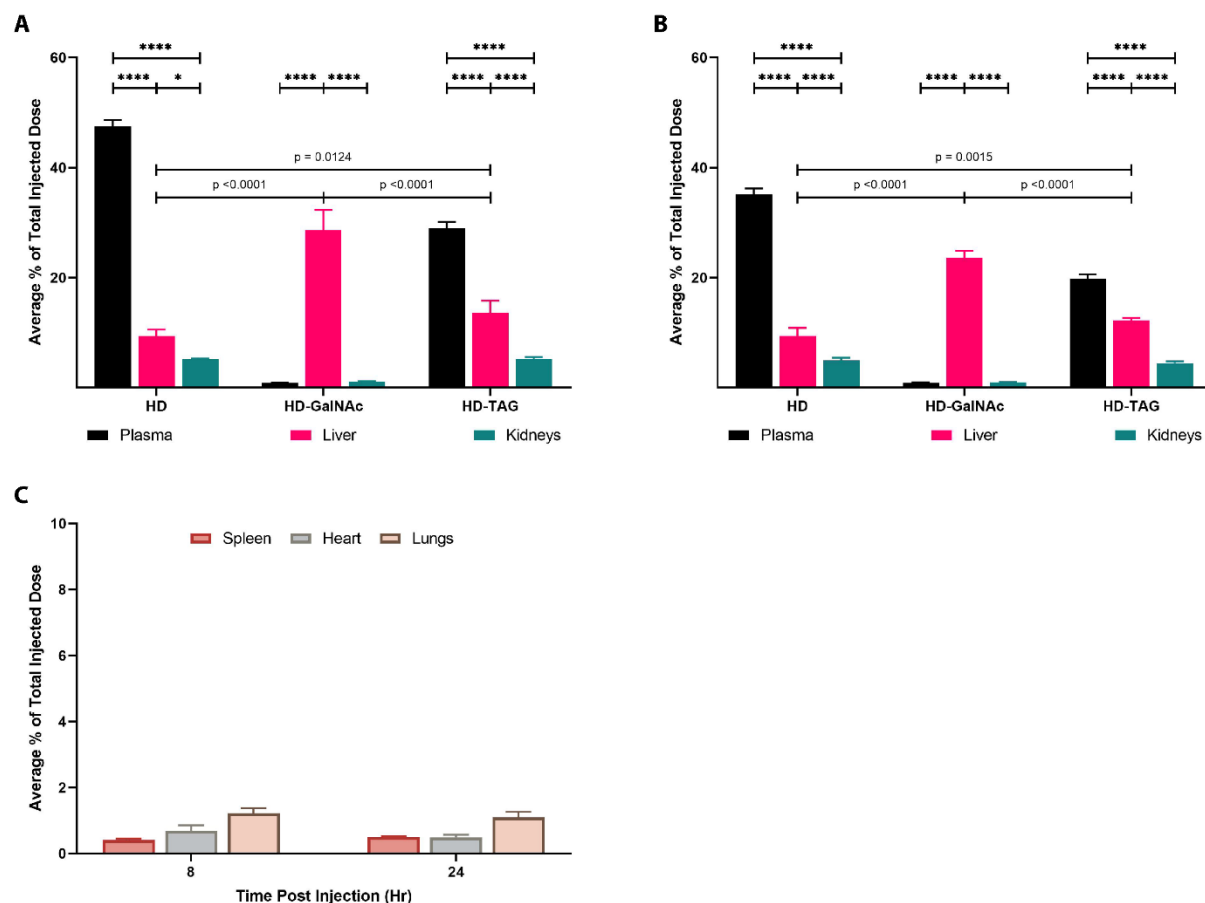
Figure 25. Biodistribution properties of tritium labeled non-liver targeting macromolecular chelating control in C57BL/6 mice. Tritium labelled HD were injected at 10 mg/kg dose into mice. Radioactivity was measured through scintillation counts in plasma and the excretory organs (liver and kidneys) at (A) 8 h and (B) 24 h after injection. (C) Non-specific biodistribution of HD were also measured in other organs including heart, spleen and lungs. Error bars show standard deviations for a sample size of 3 mice. 2-way ANOVA with Tukey's multiple comparison test were performed to compare the accumulation of these liver targeting systems in the plasma, liver and kidneys. Similarly, the differences in hepatic accumulation was also compared. **** represents a $p < 0.0001$, *** represents a $p < 0.0010$, ** represents a $p < 0.0100$, and * represents a $p < 0.0500$.

Lastly, the excretion of these macromolecular chelators were examined in two separate comparisons; first, the excretion of HD-GalNAc and HD-TAG were compared to HD in the first 24 h because liver targeted chelating systems exhibited rapid elimination (**Figure 26**), and second, the excretion of HD-GalNAc and HD-TAG were compared over the full duration of 144 h (**Figure 27**).

Notable differences were observed for the excretion at 8 h and 24 h post injection *via* feces, the hepatobiliary route, and *via* urine, the renal route (**Figure 26**). At 8 h post injection of tritiated polymers, 48% of the ID of HD-TAG ($p < 0.0001$, HD-TAG vs HD) and 26% of the ID of HD-GalNAc ($p < 0.0001$, HD-GalNAc vs HD) were excreted through the hepato-biliary pathway, whereas HD showed less than 5% of the ID excreted (**Figure 26A**). Significantly higher fecal excretion was observed for HD-TAG compared to HD-GalNAc ($p < 0.0001$). On the other hand, HD-GalNAc showed 32% of the ID in urine at 8 h, whereas HD-TAG and HD showed no excretion in the collected urine samples (**Figure 26B**).

At 24 h post injection of polymers, HD-GalNAc and HD-TAG did not show considerable increase in fecal excretion (**Figure 26C**); the excretion of HD-GalNAc and HD-TAG decreased dramatically after 8 h with only an additional 6% and 10% of the ID over 24 h respectively. In contrast, an additional 15% of the ID of HD was measured in the feces – 4 times more than that excreted at 8 h. Similarly, HD-GalNAc only exhibited an addition of 5% of the ID in the urine, whereas HD-TAG and HD showed 19% and 32% of the ID, respectively (**Figure 26D**).

Notably, when comparing the route of excretion (**Figure 26E** and **Figure 27**), HD-GalNAc was equally excreted through both the hepatobiliary and renal route of excretion, despite having less than 3% of the ID in the kidneys at all times. In contrast, HD-TAG exhibited a hepatobiliary dominate route of excretion with 75% of the polymer excreted in the feces ($p < 0.0001$ when comparing 24 h fecal excretion to urinal excretion) despite exhibiting significantly lower liver accumulation compared to HD-GalNAc.
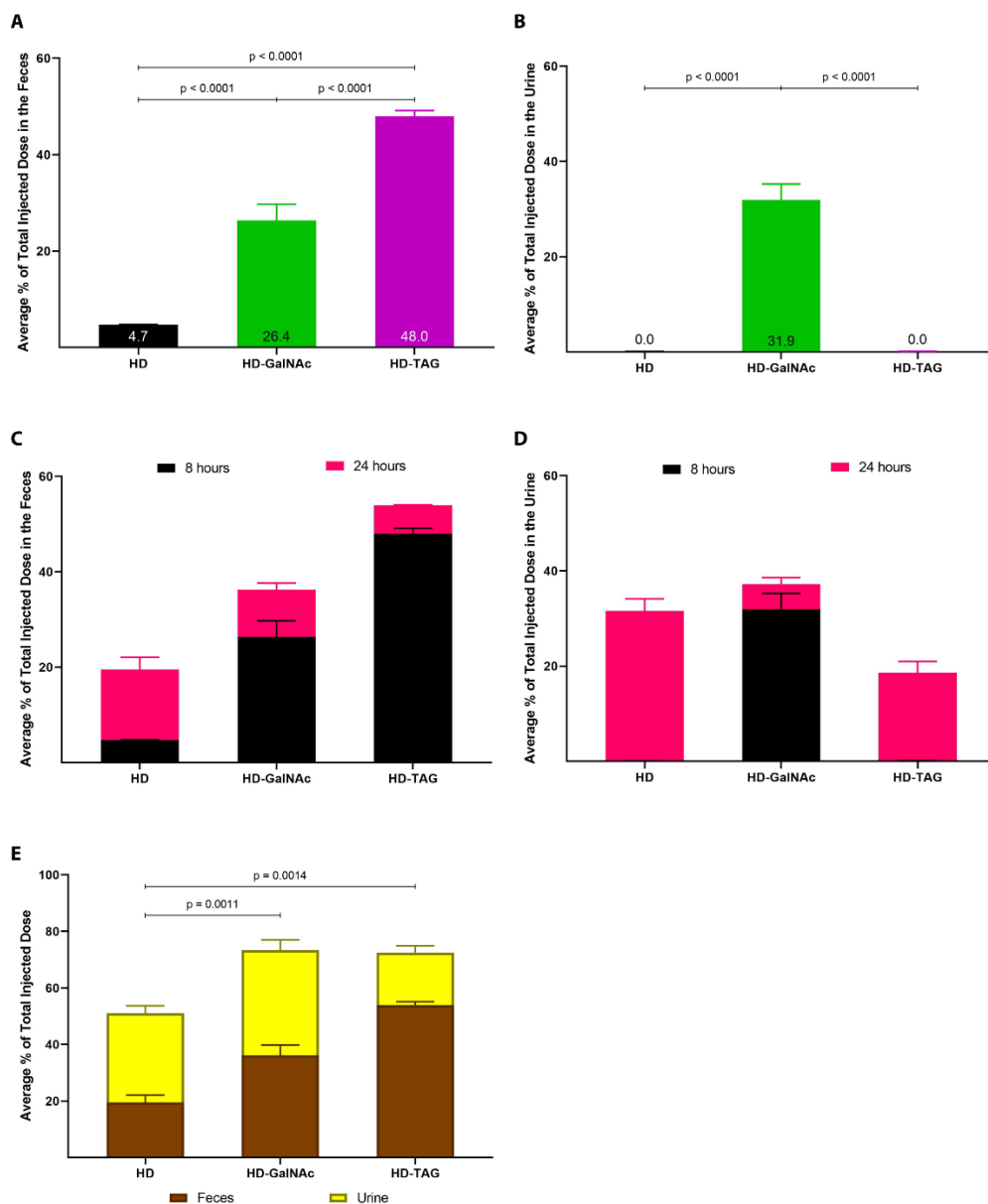
Figure 26. The excretion of liver targeting chelation systems over the first 24 h. (A) The hepatobiliary and (B) the renal elimination of these radiolabelled rapid excretion systems from mice were also investigated at 8 h post injection. 1-way ANOVA with Tukey's multiple comparison tests were performed. At 24 h post injection, the cumulative excretion *via* (C) the hepatobiliary and (D) the renal pathways were measured from the same study. (E) The proportion of excretion *via* the feces and the urine for all macromolecular chelators were determined after 24 h post injection. The average percentage of the total ID were calculated from 3 mice per treatment. Error bars show standard deviations. All statistical analyses were performed using GraphPad Prism where **** represents p < 0.0001 and * represents p < 0.05.

Remarkably, the total liver targeted chelating systems excreted after 24 h post injection was greater than 70% of the ID, with no appreciable differences observed between HD-GalNAc and HD-TAG despite the significantly different excretion route (**Figure 27**); HD-GalNAc exhibited 73% ± 5% and HD-TAG exhibited 73% ± 3% of the ID. The excretion of these systems was significantly higher compared to HD, which revealed a total excretion of 51% ± 4% of the ID ($p = 0.0011$, HD-GalNAc vs HD, and $p = 0.0014$, HD-TAG vs HD) (**Figure 26E**).

After 144 h, a significant increase in total excretion of HD-TAG was observed from 73% ± 3% of the ID after 24 h to 85% ± 3% of the ID after 144 h ($p = 0.0066$). Despite this, the total excretion of HD-GalNAc and HD-TAG were still not significantly different (**Figure 27**). Only a slight increase in the total excretion of HD-GalNAc was observed at 144 h post injection.

A

■ 49.3% Feces   ☐ 50.7% Urine

Average % of injected HD-GalNAc excreted = 73.4

B

■ 74.4% Feces   ☐ 25.6% Urine

Average % of injected HD-TAG excreted = 72.5

C

■ 50.4% Feces   ☐ 49.6% Urine

Average % of injected HD-GalNAc excreted = 78.4

D

■ 74.7% Feces   ☐ 25.3% Urine

Average % of injected HD-TAG excreted = 84.8
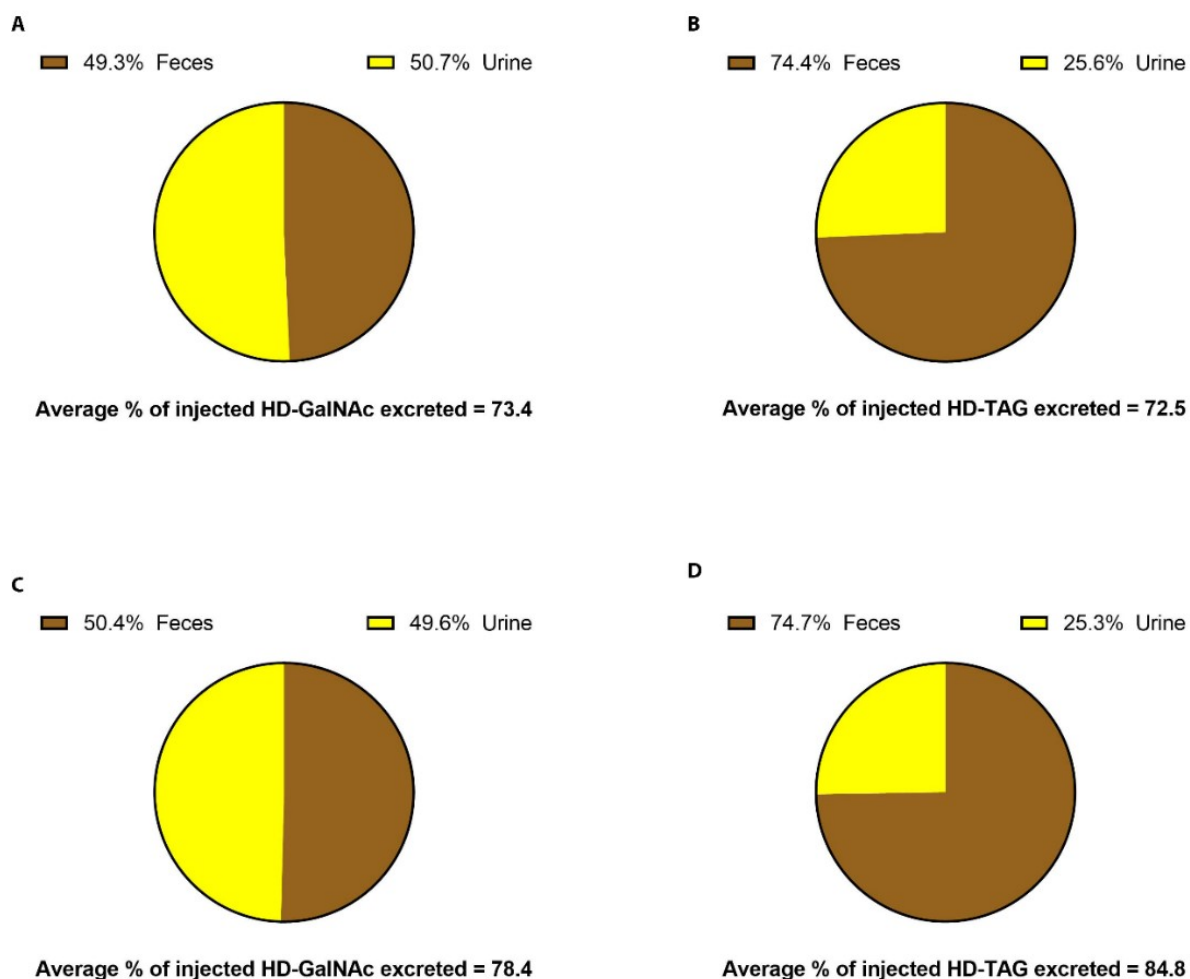
Figure 27. The excretion of liver targeting chelation systems over 144 h. The total excretion of HD-GalNAc at (A) 24 h and (C) 144 h and the total excretion of HD-TAG at (B) 24 h and (D) 144 h were measured using tritiated polymers at the end the 144 h period. The average percentage was determined from 3 mice per treatment. For each polymer at each time point, an unpaired t-test was performed to compare mode of excretion using Graphpad Prism.

3.4.3. *In vivo* hepatic distribution of liver targeting chelating systems

In order to shed light on the possible mechanism of rapid excretion shown by liver targeted chelating systems, the liver distribution of fluorescently labeled HD-GalNAc, HD-TAG and HD were examined in C57Bl/6 mice using flow cytometry. Liver cells were separated using collagenase perfusion and, using anti-CD68 antibodies, Kupffer cells were identified as CD 68 positive population whereas hepatocytes were identified as CD68 negative population. The percentage of cells positive for fluorescently labeled macromolecules were determined by gating for cells using unlabelled control. A representative gating dot plot has been shown in **Appendix Figure 13**.

Over the course of the 8 h time point (**Figure 28**), mice treated with HD-GalNAc exhibited 0.4% to 1.2% positively stained hepatocytes and mice treated with HD-TAG exhibited 0.2% to 5.7% positively stained hepatocytes. Only after 8 h of injection, signal was detected in Kupffer cells, with less than 0.05% of Kupffer cells positively stained. Both HD-GalNAc and HD-TAG accumulated almost exclusively in the hepatocytes despite the percentages of these cells being low.

On the other hand, non-targeted HD exhibited increasing accumulation in both hepatocytes and Kupffer cells over 8 h. At 0.5 h, 2.1% of the hepatocytes stained positive compared to 0.2% of the Kupffer cells that stained positive (****$p < 0.0001$, positively stained hepatocyte vs positively stained Kupffer cells). At 2 h, there were no appreciable differences between hepatocytes and Kupffer cells (6.7% and 5.6%, respectively). By 8 h, significantly more Kupffer cells stained positive for HD macromolecules when compared to hepatocytes (*$p = 0.0119$, 32.2% of Kupffer cells vs 21.6% hepatocytes).

These observations seem to be consistent with the rapid excretion observed by HD-GalNAc and HD-TAG from the detailed pharmacokinetic and biodistribution investigations described earlier. To further evaluate the intracellular processing of these macromolecules under *in vitro* conditions, their cellular distribution in HepG2 cells was assessed and analyzed by confocal microscopy (**Figure 29**). HepG2 cells were incubated with carboxyrhodamine labelled polymers for 30 mins and then media was replaced with fresh media for an additional 1 h. Cellular distribution of liver targeted macromolecules were traced with respect to lysosomes (LAMP1). Both HD-TAG and HD-GalNAc qualitatively co-localized with LAMP1, suggesting lysosomal accumulation consistent with observations made in **Chapter 2**. Minimal to no HD uptake was observed, which is also consistent with the 0.5 h *in vivo* liver distribution for this non-targeted control.
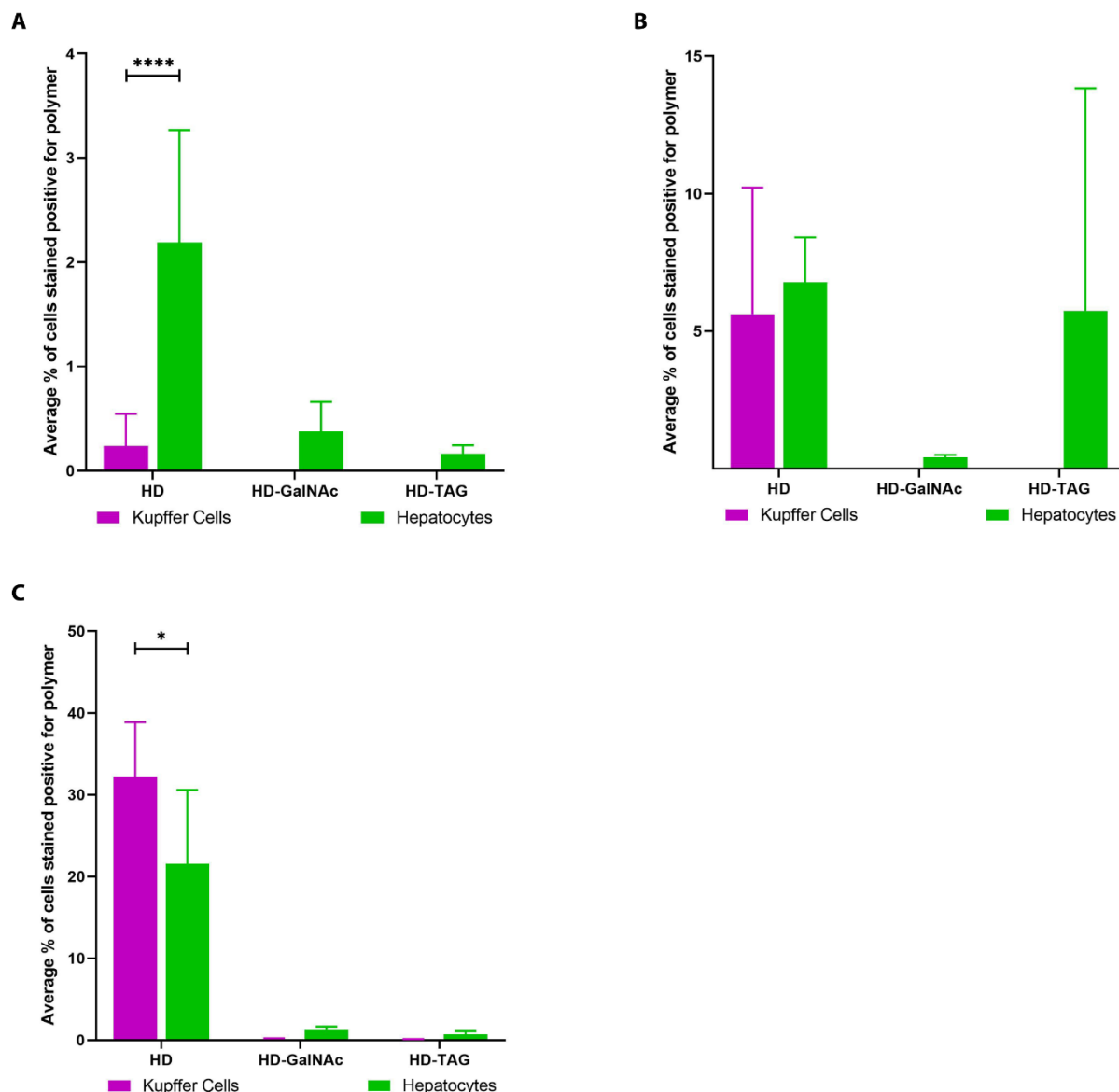
Figure 28. *In vivo* **hepatic distribution of fluorescently labelled liver targeting chelating systems and its control at (A) 0.5 h, (B) 2 h and (C) 8 h post injection.** The liver was harvested, processed and separated. Hepatocytes and Kupffer cells were labeled using anti-CD68 antibodies and the uptake of molecules were analyzed in at least 20,000 cells using flow cytometry. Data was presented as an average percentage of cells staining positive for fluorescently labelled HD, HD-GalNAc and HDTAG, from 3 mice per treatment per time point. A 2-way ANOVA with Sidak's multiple comparison test was performed to compare differences in cellular accumulation. All statistical analysis were performed using GraphPad Prism.
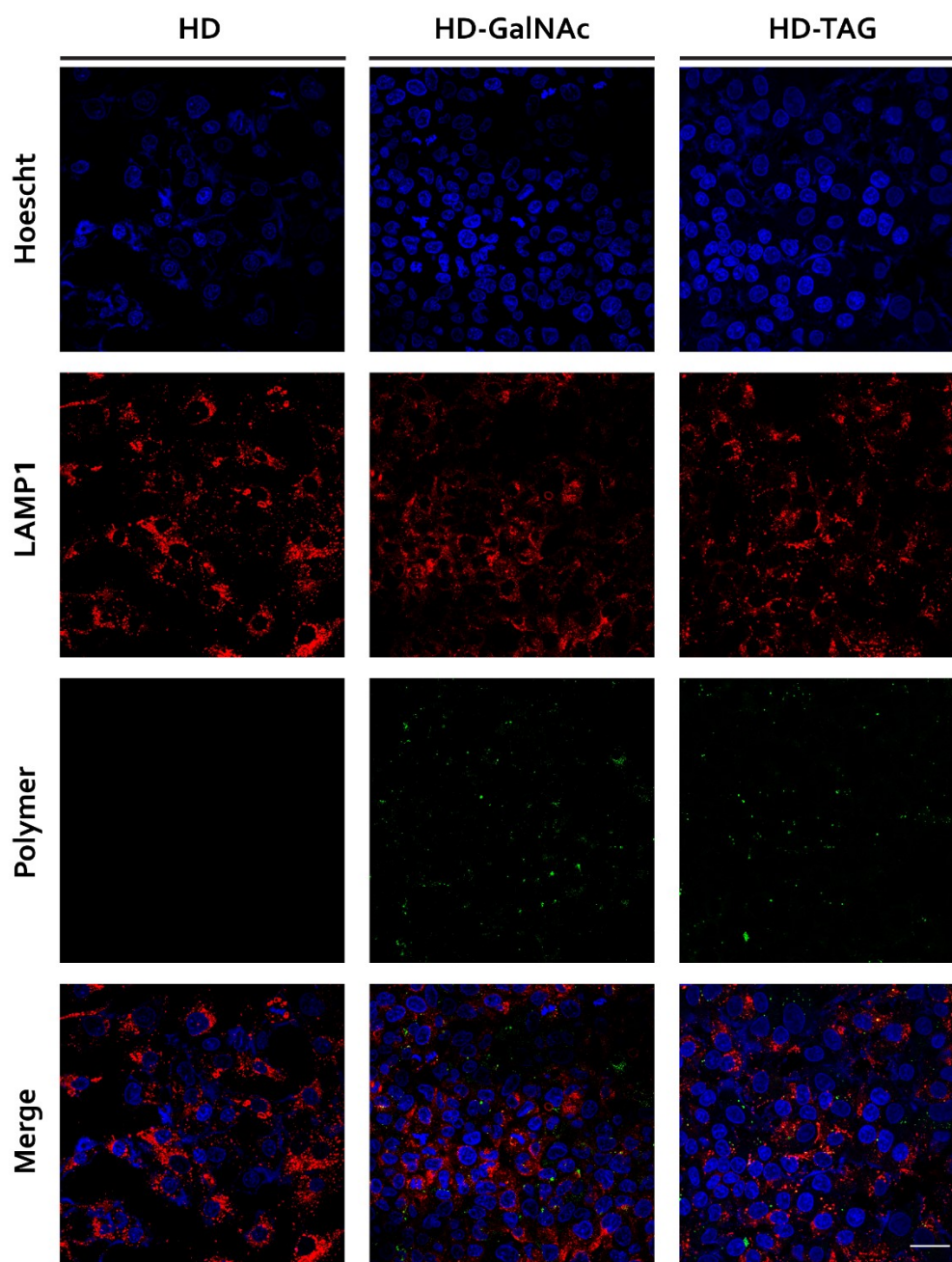
Figure 29. Intracellular distribution of fluorescently-labelled liver targeting systems and its control in HepG2 cells. Cells were pulsed with fluorescent macromolecules for 30 min and then chased with fresh media for 1 h. Images were acquired using confocal laser scanning microscopy with immunostaining to identify lysosomes (LAMP1). Nucleus was stained using Hoechst, represented as blue. Lysosomes were stained using mouse anti-human LAMP1 antibodies, represented as red. HD, HD-GalNAc and HD-TAG were fluorescently labelled with carboxyrhodamine, represented as green. At least 100 cells were imaged. Representative confocal micrographs are shown here.

3.4.4. Kinetic investigations into the intracellular trafficking of liver targeting chelating systems

HD-GalNAc and HD-TAG exhibited hepatocyte specific uptake within the liver which may shed light on the liver-mediated rapid excretion from previous *in vivo* investigations. To further assess the hypothesis that hepatocyte uptake mediated rapid excretion of HD-GalNAc and HD-TAG, the intracellular trafficking of these liver targeting chelating systems were investigated with respect to the rate of intracellular movement. This is because ASGPR-mediated cellular uptake is dependent on the ligand lectin interaction and the availability of receptors to readily interact with the ligand.[225] To evaluate the role of ASGPR kinetics on the observed excretion profiles, HepG2 cells were treated with fluorescently labelled HD-GalNAc and HD-TAG to compare differences in the endocytic pathway using confocal laser scanning microscopy. Mander's co-localization coefficients (MCCs) shows the percentage of HD-GalNAc and HD-TAG signal overlapping with the compartment-specific antibody signal. For the sake of clarity, MCCs and percentage of HD-GalNAc and HD-TAG signal overlapping with antibody signal were used interchangeably.

Initial studies compared the intracellular distribution in cells treated with H-GalNAc$_{50}$ and HD-GalNAc for either 2 h or 24 h (**Figure 30** and **Appendix Figure 14** to **Appendix Figure 17**) to observe for any differences between these liver targeting systems. The endocytic pathway was traced using endocytic markers to identify early endosomes (EEA1), recycling endosomes (TfR1), late endosomes (Rab7), and lysosomes (LAMP1). H-GalNAc$_{50}$ treated cells showed increasing trends in MCCs for EEA1, Rab7 and LAMP1 from 2 to 24 h. In fact, MCC for EEA1 was significantly higher when comparing 2 h to 24 h incubations – an increase from 12% to 31% of the H-GalNAc$_{50}$ signal overlapping with EEA1 signal was observed (p = 0.0313). A decreasing trend in the MCC was observed for TfR1 (**Figure 30A**). Similarly, on the other hand, HD-GalNAc treated cells also showed increasing trends in MCC for Rab7 and LAMP1 from 2 h to 24 h (**Figure 30B**). Unlike H-GalNAc$_{50}$ however, there was a significant decrease in the MCC when comparing 2 to 24 h incubations for both EEA1 and TfR1 (p = 0.0064 and p = 0.0028, respectively). At 2 h, 66% of the HD-GalNAc signal overlapped with EEA1 signal and 71% of the HD-GalNAc signal overlapped with TfR1 signal. Whereas at 24 h, 27% of the HD-GalNAc signal overlapped with EEA1 signal and 31% of the HD-GalNAc signal overlapped with TfR1 signal.

At 24 h, cells treated with either H-GalNAc$_{50}$ or HD-GalNAc exhibited greater than 50% of the polymer signal overlapping with LAMP1 signal, which suggests lysosomes as the final destination. While the conjugation of DFO doesn't change its intracellular distribution, the rate of progression through the endocytic pathway is affected (**Figure 30**).
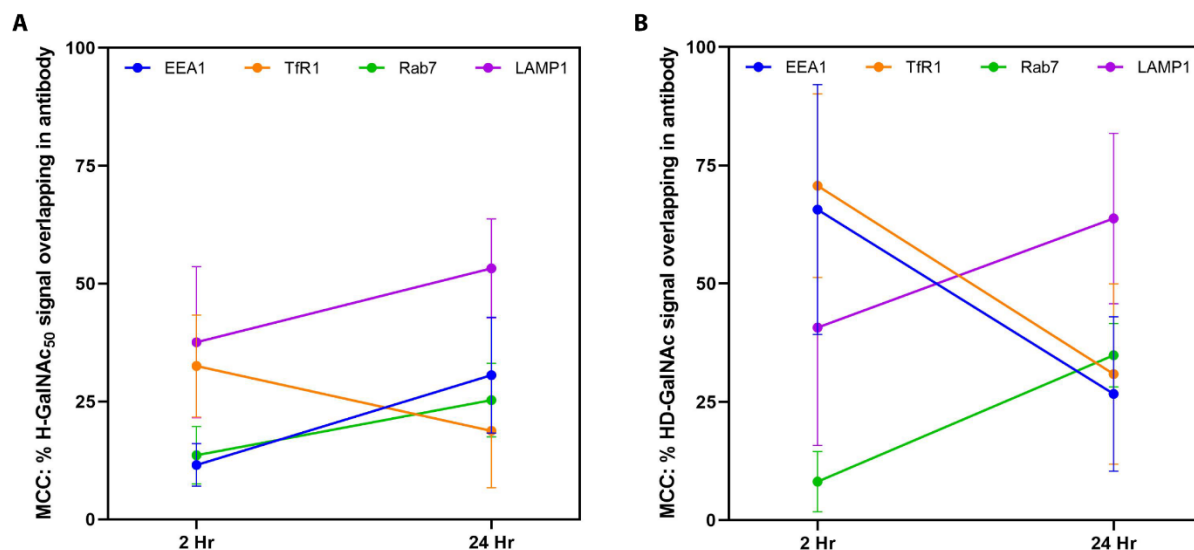
Figure 30. The intracellular distribution of (A) H-GalNAc$_{50}$ at 1 μM and (B) HD-GalNAc at 1 μM incubated for either 2 or 24 h in HepG2 cells. HepG2 cells were incubated with H-GalNAc$_{50}$ or HD-GalNAc for either the full duration of 2 or 24 h at 37°C. Polymers were present throughout the entire duration of the experiment. The endocytic pathway was traced using fluorescent immunostaining to identify early endosomes (EEA1), recycling endosomes (TfR1), late endosomes (Rab7) and lysosomes (LAMP1). At least a 100 cells were acquired and analyzed. Mander's Co-localization Coefficients (MCCs) were reported as a percentage of polymer signal overlapping with immunostaining signal for the different antibodies. MCCs were calculated from at least 5 different regions of interest and the error bars show standard deviations. 2-way ANOVA with Sidak's correction was performed to compare differences in MCCs at a particular endocytic compartment at either 2 or 24 h. All statistical analyses were performed using GraphPad Prism.

Based on these observations, the kinetic differences in the endocytosis of liver targeted polymers towards the lysosomes were then investigated in detail using pulse-chase investigations. HepG2 cells were 'pulsed' with fluorescent polymers for 30 min and then 'chased' by replacing the media with fresh media (i.e. no fluorescent polymer) for an additional 0, 1, 2, 16 and 24 h (**Figure 31** and **Appendix Figure 18** to **Appendix Figure 35**). Similar to the previous experiment, the endocytic pathway was traced using endocytic markers to identify early endosomes (EEA1), late endosomes (Rab7), and lysosomes (LAMP1). The ASGPR was also traced (ASGPR). Co-localization of liver targeted systems – H-GalNAc$_{50}$ (**Figure 31A**), HD-GalNAc (**Figure 31B**), H-TAG$_2$ (**Figure 31C**) and HD-TAG (**Figure 31D**) with different endocytic compartments were measured and quantitatively compared using MCCs.

Cells treated with all polymers exhibited rapid lysosomal co-localization, which increased further with chase time. Immediately after pulsing the cells with polymers (0 h chase), the MCCs for LAMP1 were significantly higher when compared to the MCCs for the endocytic markers; H-GalNAc$_{50}$ showed 52% overlap with LAMP1 compared to the 23% overlap with EEA1 and 0% overlap with both Rab7 and ASGPR ($p < 0.0001$ for all comparisons), HD-GalNAc showed 56% overlap with LAMP1 compared to the 23% overlap with EEA1 and 0% overlap with both Rab7 and ASGPR ($p < 0.0001$ for all comparisons), H-TAG$_2$ showed 37% overlap with LAMP1 compared to the 26% overlap with EEA1 ($p = 0.0009$), 20% overlap with Rab7 ($p < 0.0001$) and 0% overlap with ASGPR ($p < 0.0001$), and HD-TAG showed 57% overlap with LAMP1 compared to the 26% overlap with EEA1, 21% overlap with Rab7 and 1% overlap with ASGPR ($p < 0.0001$ for all comparisons). Further, the percentage of polymer signal overlapping with LAMP1 signal significantly increased when comparing the MCCs determined from a chase of 0 h to 24 h; H-GalNAc$_{50}$ increased from 52% to 62% ($p < 0.0001$), HD-GalNAc increased from 56% to 69% ($p < 0.0001$), H-TAG$_2$ increased from 37% to 75% ($p < 0.0001$) and HD-TAG increased from 57% to 74% ($p < 0.0001$). Notably, the MCCs for polymer signal overlapping with ASGPR were between 0% to 2% for all polymers at all chase times.
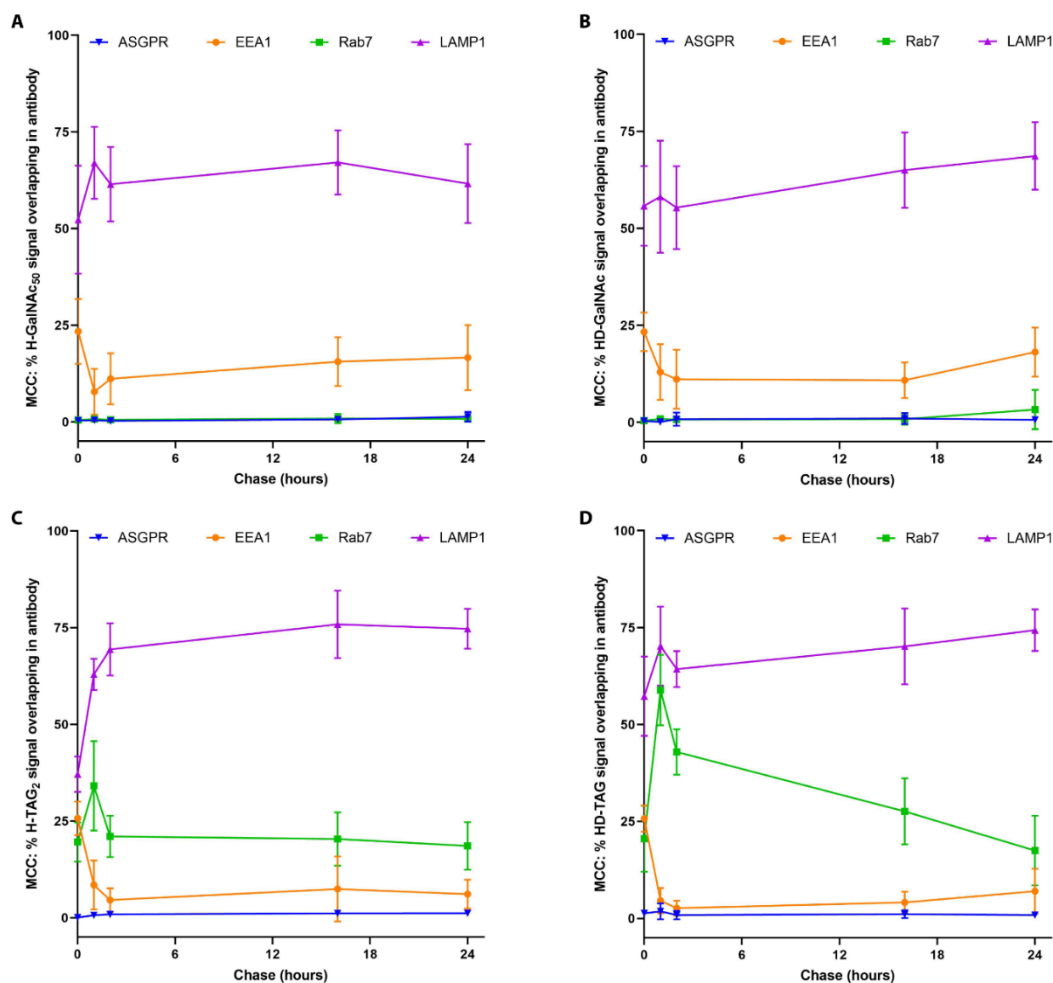
Figure 31. The kinetic investigation into the intracellular distribution of fluorescently labelled liver targeting systems and their chelator counterparts. Mander's Co-localization Coefficients (MCCs) were reported as a percentage of (A) H-GalNAc$_{50}$, (B) HD-GalNAc, (C) H-TAG$_2$, and (D) HD-TAG overlapping with immunostaining signal for the different antibodies used to trace the endocytic pathway. The endocytic pathway was traced using fluorescent immunostaining to asialoglycoprotein-receptors (ASGPR), early endosomes (EEA1), late endosomes (Rab7) and lysosomes (LAMP1). At least 100 cells were acquired using Leica SP5 confocal scanning laser microscopy. MCCs was calculated from 5 to 18 independent regions of interest. The error bars show standard deviations. A 2-way ANOVA with Tukey's multiple comparisons test was performed to compare the differences in signal overlap with endocytic markers within the same polymer treatments. A 2-way ANOVA with Dunnett's multiple comparisons test was performed to compare differences in signal overlap with endocytic markers between polymer treatments. All statistical analyses were performed using GraphPad Prism.

94

Next, distinct differences were observed between GalNAc decorated systems and TAG decorated systems when assessing the impact of DFO conjugation.

GalNAc decorated systems showed no statistical differences between the overlap of non-chelator H-GalNAc$_{50}$ and HD-GalNAc with any of the endocytic markers at all chase times, suggesting that DFO conjugation does not significantly influence the kinetics for its intracellular trafficking. GalNAc decorated systems showed overlap with either EEA1 or LAMP1; for EEA1 overlap, H-GalNAc$_{50}$ and HD-GalNAc showed 23% signal overlap at 0 h which decreased to 17% and 18% by 24 h respectively, and for LAMP1 overlap, H-GalNAc$_{50}$ and HD-GalNAc showed 52% and 56% overlap with LAMP1 at 0 h which increased to 62% and 69% at 24 h respectively. Minimal overlap was observed with Rab7 and ASGPR – only 0% and 3% signal overlap was measured at all chase times, respectively.

In contrast, TAG decorated systems showed statistical differences between the overlap of non-chelator H-TAG$_2$ and HD-TAG with Rab7 and LAMP1 antibodies within the first 2 h of chase. Unlike GalNAc decorated systems, DFO conjugation in TAG decorated systems influences the kinetics such that it speeds up its intracellular trafficking. For Rab7 overlap after 1 h chase, H-TAG$_2$ and HD-TAG showed 34% and 59% signal overlap after 1 h chase ($p < 0.0001$), and after 2 h chase, H-TAG$_2$ and HD-TAG showed 21% and 43% signal overlap ($p = 0.0008$). Similarly, for LAMP1 overlap after 0 h chase, H-TAG$_2$ and HD-TAG showed 37% and 57% signal overlap ($p < 0.0001$), and after 1 h chase, H-TAG$_2$ and HD-TAG showed 63% and 70% signal overlap ($p = 0.0462$). Similar to the GalNAc decorated systems, no significant differences were observed when comparing the overlap of H-TAG$_2$ and HD-TAG with EEA1 and ASGPR; for EEA1 overlap, H-TAG$_2$ and HD-TAG exhibited 26% signal overlap at 0 h which decreased to 6% by 24, and for ASGPR overlap, 0% to 2% of signal overlap was measured at all chase times. Notably, similar to GalNAc decorated systems, TAG decorated systems showed overlap with EEA1 and LAMP1, however only TAG decorated systems showed overlap with Rab7.
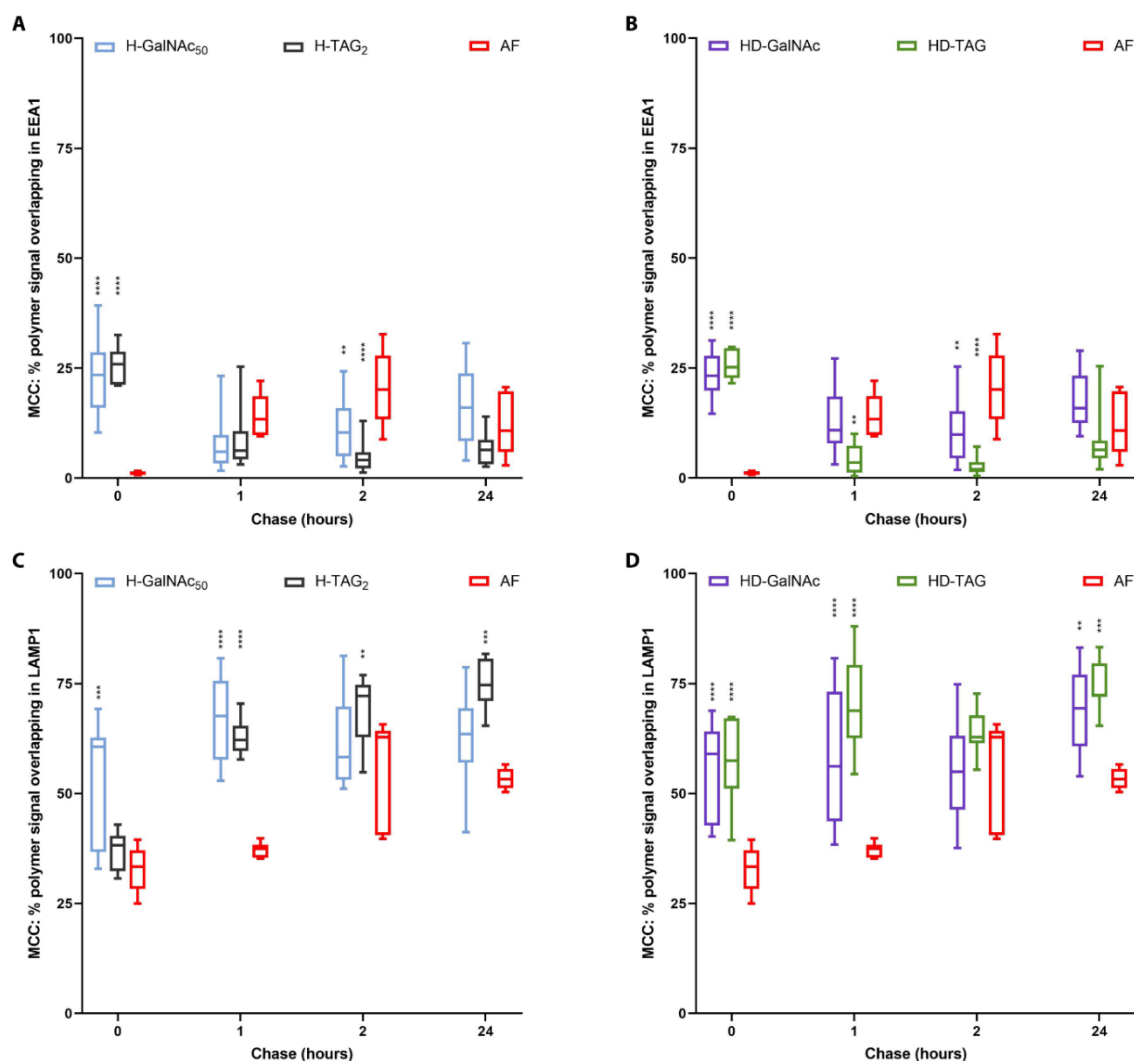
Figure 32. A comparative kinetic investigation into the intracellular distribution of fluorescently labelled liver targeting systems and their chelator counterparts against the endogenous ASGPR-specific protein, AF. Mander's Co-localization Coefficients (MCCs) were reported as a percentage of (A and C) H-GalNAc$_{50}$ and H-TAG$_2$ and (B and D) HD-GalNAc and HD-TAG polymer signal overlapping with immunostaining signal for (A and B) early endosomes (EEA1) and (C and D) lysosomes (LAMP1). At least 100 cells were acquired using Leica SP5 confocal scanning laser microscopy. MCCs was calculated from 5 to 18 independent regions of interest. The error bars show standard deviations. A 2-way ANOVA with Dunnett's multiple comparisons test was performed to compare the MCCs for all liver targeting polymers to AF. All statistical analyses were performed using GraphPad Prism. **** represents $p < 0.0001$, *** represents $p < 0.0010$, and ** represents $p < 0.0100$. Representative confocal micrographs were shown in **Appendix Figure 18** to **Appendix Figure 35.**

It is evident that both the ASGPR-specific ligand identity and DFO conjugation influenced the observed intracellular trafficking kinetics. To better contextualize these differences, similar pulse chase experiments were performed. The intracellular kinetics of liver targeting polymers were compared with asialofetuin (AF) with respect to EEA1 (**Figure 32A** and **B**) and LAMP1 (**Figure 32C** and **D**). AF is a natural ligand which exhibits high affinity for the ASGPR and is targeted to the lysosome for degradation.[223,413,414]

AF revealed significantly more EEA1 overlap from 0 h to 1 h (1% vs 14%; p = 0.0092). This increasing trend was observed over the first 2 h followed by a slight decrease after 24 h. When compared to all liver targeting polymers, AF exhibited a slower increase in the MCCs for EEA1 overlap. Immediately after a 30 min pulse, all liver targeting polymers showed significantly higher signal overlap when compared to AF (****p < 0.0001 for all comparisons). AF showed a 1% signal overlap whereas H-GalNAc$_{50}$, HD-GalNAc, H-TAG$_2$ and HD-TAG showed 23%, 23%, 26% and 26% signal overlap respectively. At 1 h of chase, only HD-TAG showed significantly lower signal overlap when compared to AF (5% HD-TAG vs 14% AF, **p = 0.0079). By 2 h of chase, all liver targeting polymers exhibited significantly lower signal overlap with EEA1 when compared to AF indicating the faster progression of these polymers through the early endosomes; 21% of AF signal vs 11% of H-GalNAc$_{50}$ (**p = 0.0074), 11% of HD-GalNAc (**p = 0.0065), 5% of H-TAG$_2$ (****p < 0.0001), and 3% of HD-TAG (****p < 0.0001). No significant differences were observed after 24 h chase.

AF revealed an increased trend in LAMP1 signal overlap which plateaued by 24 h. A significant increase in AF overlap was observed between 1 h and 2 h of chase (37% vs 56%; p = 0.0032). Similar patterns were observed for LAMP1 overlap. With the exception of H-TAG$_2$, H-GalNAc$_{50}$, HD-GalNAc and HD-TAG showed significantly higher MCCs for LAMP1 overlap when compared to AF (***p = 0.0003, ****p < 0.0001 and ****p < 0.0001, respectively). AF showed a 33% signal overlap and H-TAG$_2$ showed a 37% overlap whereas H-GalNAc$_{50}$, HD-GalNAc and HD-TAG exhibited 52%, 56% and 57% signal overlap. After 1 h chase, all liver targeting polymers had significantly higher signal overlap with LAMP1 (p < 0.0001 for all comparisons); 37% of AF signal vs 67% of H-GalNAc$_{50}$, 58% of HD-GalNAc, 63% of H-TAG$_2$, and 70% of HD-TAG. At 2 h of chase, H-GalNAc$_{50}$, HD-GalNAc and HD-TAG were not significantly different than AF when comparing their MCCs suggesting that these molecules have reached their final destination. Since the signal overlap of AF with LAMP1 was not significantly different between 2 h and 24 h (56% and 53% respectively), it is likely that the significant differences observed for H-TAG$_2$ at 2 h of chase and H-TAG$_2$, HD-GalNAc and HD-TAG at 24 h chase (**p = 0.0092, ***p = 0.0001, **p = 0.0037 and ***p = 0.0001, respectively) may be a constraint of this experiment.
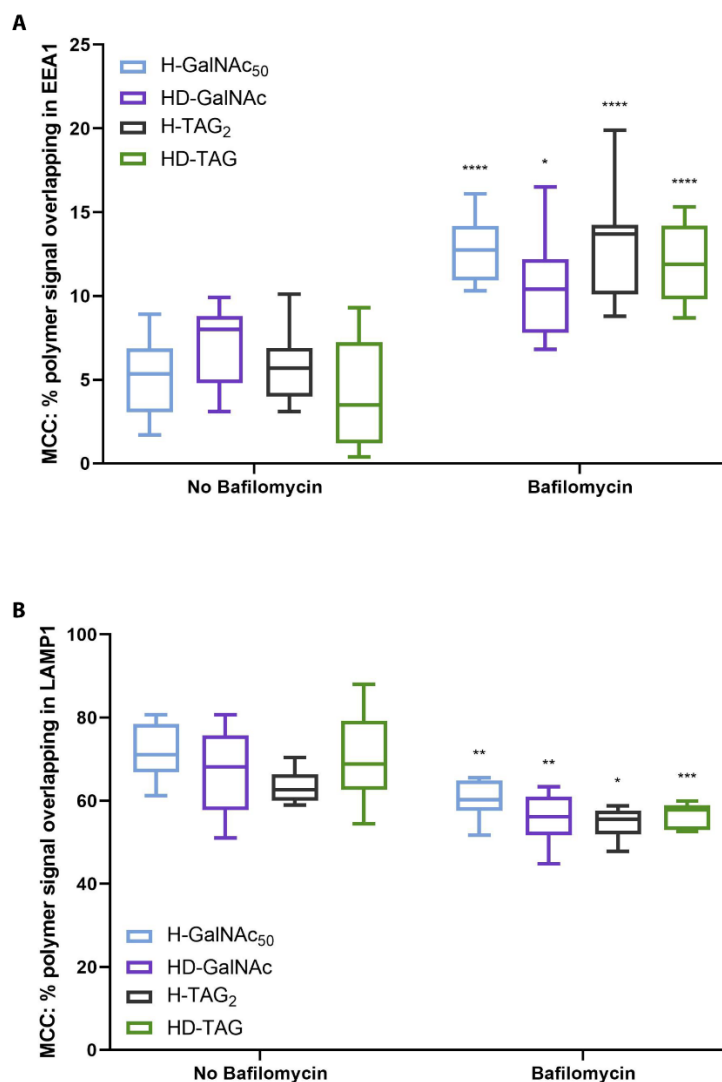
Figure 33. The influence of acidification of the intracellular distribution of liver targeting systems and their chelator counterparts. The intracellular translocation was perturbed with a 1 h pre-treatment of 10 nM bafilomycin, a proton pump inhibitor. HepG2 cells were then pulsed with fluorescently labelled polymers for 30 min and chased with fresh media for 1 h. Mander's Co-localization Coefficients (MCCs) were reported as a percentage of polymer signal overlapping with immunostaining signal for (A) early endosomes (EEA1) and (B) lysosomes (LAMP1). At least 100 cells were acquired using Leica SP5 confocal scanning laser microscopy. MCCs was calculated from 5 to 18 independent regions of interest. The error bars show standard deviations. A 2-way ANOVA with Dunnett's multiple comparisons test was performed to compare the MCCs for all liver targeting polymers with and without bafilomycin pre-treatment. All statistical analyses were performed using GraphPad Prism. **** represents p < 0.0001, *** represents p < 0.0010, and ** represents p < 0.0100.

All liver targeting systems accumulated in the lysosomes faster than the endogenous ligand, AF (**Figure 32**). To further explore why these systems exhibited rapid lysosomal accumulation, a similar pulse chase experiment was performed with 2 differences; (1) the endocytic pathway was perturbed by a pre-treatment with bafilomycin, a proton-pump inhibitor which prevents the maturation of the endosomes and the subsequent fusion with lysosomes[405,415], and (2) given the observations made previously, co-localization with EEA1 and LAMP1 was analyzed after only a chase of 1 h.

The observed MCCs for polymer signal overlapping with EEA1 signal were all significantly higher in cell pretreated with bafilomycin compared to cells without bafilomycin pre-treatment (**Figure 32A**); 13% vs 5% for H-GalNAc$_{50}$ (****$p < 0.0001$), 10% vs 7% for HD-GalNAc (*$p = 0.0239$), 13% vs 6% for H-TAG$_2$ (****$p < 0.0001$) and 12% vs 4% for HD-TAG (****$p < 0.0001$). Conversely, the observed MCCs for polymer signal overlapping with LAMP1 signal were all significantly lower in cells pretreated with bafilomycin compared to cells without bafilomycin pre-treatment (**Figure 32B**); 60% vs 72% for H-GalNAc$_{50}$ (**$p = 0.0013$), 56% vs 67% for HD-GalNAc (**$p = 0.0037$), 55% vs 63% for H-TAG$_2$ (*$p = 0.0492$) and 57% vs 70% for HD-TAG (***$p < 0.0006$).

3.5. Discussion

Nanomaterials, including polymer therapeutics, have been the subject of research for past several decades with enormous potential in diverse medical applications due to their unique properties and easily tunable surface chemistry.[373,390,416,417] In pursuit of developing materials with ideal properties that bypass biological barriers, extensive investigations revealed the importance of these systems' physical properties and their subsequent interaction with the reticuloendothelial systems. For instance, nanomaterials with minimal non-specific interaction with blood proteins and smaller than 5 nm are exclusively cleared through the kidneys because it is within the kidney clearance limit.[390,392] Whereas, nanomaterials above this size range are readily cleared by the reticuloendothelial system, which hampers the delivery of therapeutic cargo to intended target sites, and retained for extended periods within the body.[397,418,419]

Bypassing the resident macrophages and other non-parenchymal cells involved in the clearance and phagocytosis of these materials is imperative for the enhanced therapeutic index and the delivery of therapeutic cargo to its intended location. These strategies have been extensively sought after include surface modification of materials,[207] selective depletion of macrophages,[420] and alteration of particle size and shape, deformability[390,392,397]. The development of biodegradable nanomaterials has also been sought after, however, it degradation characteristics require particular attention since generated fragments may impart toxicity.[421] In addition, biodegradability is principally constrained to a limited subset of materials. Yet, these have resulted in poor translation.[419]

A major hurdle in the translation of nanomaterials beyond clinical trails is due to their poor excretion, prolonged unwanted retention and subsequent toxicities.[391,422] Thus, designing carrier systems with desired vascular residency to increase its therapeutic index whilst being cleared from systemic circulation without accumulating in organs still remains of great interest. Galactosylated macromolecules, including proteins, polymers, metal nanoparticles, and liposomes have attracted much attention as liver-specific drug delivery systems.[223,397,423] It is well known that various galactosylated proteins are internalized *via* ASGPR-mediated endocytosis, translocate to lysosomes for degradation in hepatocytes and the extent of galactosylation influences their excretion mechanisms.[424] The movement of proteins towards the apical membrane through microtubule-dependent movement result in hepato-biliary excretion.[425]

As such, ASGPR targeted HPG systems for the delivery of DFO were investigated because it offers the unique advantage of both delivering therapeutic cargo to liver whilst enabling its processing and elimination *via* the hepatobiliary tract. Herein, pharmacokinetic profiles of HD-GalNAc and HD-TAG were

investigated with particular attention to their excretion modalities and the underlying cellular processes involved. To the best of our knowledge, very limited data is available regarding the physical properties of ASGPR-targeted synthetic materials and how they correlate with cellular processing. The selection of the HD-GalNAc and HD-TAG has been detailed in **Chapter 2.**

A preliminary study was performed to assess the differences in biodistribution of HD-GalNAc and HD-Gluc after 2 h and 24 h of injection. Three key observations were made. First, this pilot investigation provided a proof-of-concept evidence for the *in vivo* translation of the previously discussed *in vitro* observations. HD-GalNAc was selected since it exhibited superior performance. When compared to its control, HD-GalNAc demonstrated significant differences as early as 2 h which were maintained after 24 h post injection (**Figure 23**). Second, given these differences, a detailed pharmacokinetic and biodistribution investigation to examine circulation times, liver accumulation, non-specific biodistribution and excretion were conducted accordingly with respect to the selection of an appropriate control and the time points of interest. HD-Gluc was designed as a control because glucose resembles the structure of GalNAc and it is readily taken up by hepatocytes *via* the glucose transporter but also interacts with ASGPR, albeit as a low affinity ligand.[223,426] Using the same synthetic approach, we anticipated that this control would provide similar surface properties. Given the significant differences observed between HD-GalNAc and HD-Gluc, HD-Gluc was replaced with HD as the non-targeted macromolecular chelator control. Since the global aim of this thesis was to design a novel class of liver targeted macromolecular iron chelators using HPG, HD served as a more appropriate control for both pharmacokinetic investigations in this chapter and iron chelation efficiency in the following chapters. This is because HPG-DFO systems have been heavily investigated previously.[182–184,198] Further, given the rapid liver accumulation, detail investigations focused on the profiles of HD-GalNAc and HD-TAG at earlier time point intervals. The behaviour of liver targeting chelating systems were compared to HD at 8 h and 24 h with respect to its biodistribution and excretion. Third, preliminary *in vitro* (**Figure 22**) and *in vivo* (**Figure 23**) studies confirm that radiolabelling of polymers, which required the methylation of hydroxyl groups *via* tritiated methyl iodide, did not perturb the ASGPR specificity observed through *in vitro* investigations. This is because the carbohydrate recognition domain on ASGPR exhibits high affinities for Gal and GalNAc based on the spatial arrangement between the ligand and lectin.[217,223]

Given this, detailed pharmacokinetic and biodistributions investigations (**Figure 24**) were performed over 144 h on liver targeting chelating systems with different ASGPR-specific ligands and densities – HD-GalNAc and HD-TAG. This work demonstrated that differences in vascular retention, liver targetability, excretion modalities and non-specific distribution were principally influenced by the targeting moieties.

The vascular retention of these systems was vastly different. After only 1 h of injection, HD-GalNAc showed 1.9% of the ID in plasma compared to HD-TAG which exhibited 49.8% of the ID ($p < 0.0001$). By 8 h post injection, 0.8% of HD-GalNAc was measured in circulation compared to 29.0% of HD-TAG ($p < 0.0001$). A two-compartment model analysis was performed to compare the distribution and elimination half-lives of these systems – in similar fashion to a recent publication that reported the development of renal clearable DFO nanoparticles[187]. The two-compartment model analyses were also significantly different ($p < 0.0001$).

Moreover, liver targeting chelating systems demonstrated significant liver accumulation when compared to the other excretory organ, the kidneys, as well as other vital organs including the heart, spleens and lungs (**Figure 24**). HD-GalNAc exhibited less than 3% of the ID present in other organs at 1h post injection, which decreased with time. On the other hand, HD-TAG exhibited less than 10% of the ID in other organs. Interestingly, splenic accumulation increased between 72 h and 144 h which may be due to redistribution or the involvement of the reticuloendothelial systems. Additional work will be needed to investigate this further. Remarkably, HD-GalNAc yielded significantly higher liver accumulation over the first 72 h when compared to HD-TAG. These observations were consistent with the vascular retention of these molecules. The selection of GalNAc or TAG as liver-targeting moieties resulted in significantly higher liver targetability, consistent with literature.[223,232,273,382,427]

When compared to the non-targeted control, HD, both HD-GalNAc and HD-TAG exhibited significantly higher liver targetability after 8 h (HD-GalNAc: 28.6% of ID, $p < 0.0001$. HD-TAG: 13.6% of ID, $p = 0.0124$) and 24 h (HD-GalNAc: 23.6% of ID, $p < 0.0001$. HD-TAG: 12.2% of ID, $p = 0.0015$) of injection (**Figure 25**). Despite HD exhibiting significantly more accumulation in the liver when compared to the kidneys, unlike HD-GalNAc and HD-TAG, HD uptake was less than 10%. This non-specific accumulation may be due to both the first pass elimination as well as systemic clearance mediated by the reticuloendothelial system. In order to assess the distribution of these molecules within the liver, further analysis was performed to assess the accumulation of fluorescently labelled polymers in either parenchymal hepatocytes or non-parenchymal Kupffer cells (**Figure 28**). HD-GalNAc and HD-TAG were almost exclusively observed in hepatocytes, although only a low percentage of hepatocytes stained positive; HD-GalNAc and HD-TAG

revealed between 0.4 to 1.2% and 0.2% to 5.7% whereas HD exhibited 2.1% to 21.6% in hepatocytes. No Kupffer cells stained positive for either HD-GalNAc or HD-TAG. This is likely due to the affinities associated with GalNAc and TAG sugars for the ASGPR and the galactose particle receptor found on Kupffer cells. The Gal particle receptor has a high affinity for Gal exposing particles but considerable low affinity for GalNAc moieties.[223,260,267,330,428] In contrast, HD exhibited increasing accumulation in the Kupffer cells by 8 h post injection (32.2% in Kupffer cells compared to 21.6% in hepatocytes, p = 0.0119), which suggests the involvement of the reticuloendothelial system in its clearance[420].

The differences between the high liver accumulation using tritiated macromolecules (**Figure 25**) and distribution of fluorescent macromolecules within the liver (**Figure 28**) maybe due to two reasons. First, it is possible that low percentages of hepatocytes stained positive for liver targeted polymers because these systems were transient and exocytosed by hepatocytes resulting rapid excretion *in vivo* (**Figure 26**). Second, there were technical differences between the detection of tritium-labelled and fluorescently-labelled polymers. The use of radioactive macromolecular systems allows for quantitative measurements of polymer in various compartments (organs, blood, excrement). The accumulation of radioactive polymers in the liver were determined by processing the entire liver and measuring scintillation counts. On the other hand, fluorescent macromolecular systems allows for the identification of cells containing signal. In other words, the presence of polymer was measured rather than the quantitative determination of intracellular polymer concentration. Additionally, at least 20,000 hepatocytes were analyzed to determine the percentage of cells staining positive for the fluorescent polymers – this is in direct contrast to the radioactivity measured from the entire organ.

In addition to the hepatocyte-specific accumulation of liver targeting chelating systems, these systems also demonstrated rapid excretion when compared to HD. Both HD-GalNAc and HD-TAG demonstrated a total excretion of 73.4% and 72.5% of the ID, respectively, compared to 51.1% observed for HD by 24 h (**Figure 27**). While the total excretion of both HD-GalNAc and HD-TAG were similar, the excretion modalities were significantly different. HD-GalNAc exhibited quicker and higher hepatocyte uptake yet excreted equally between the hepatobiliary and renal route. This was all the more interesting since HD-GalNAc has a higher particle size with respect to the kidney clearance limit. On the other hand, HD-TAG exhibited slower hepatocyte uptake yet excreted predominantly through the hepatobiliary route. These differences further support that hypothesis that the decorated sugars on HPG influence the pharmacokinetic behaviours and the excretion modalities in particular. The extent of galactosylation on a protein has been observed to govern its hepatobiliary excretion kinetics *via* altering the interactions

between ASGPR and their galactose ligands.[424] Notably, after 144 h, HD-GalNAc and HD-TAG exhibited a total excretion of 78.4% and 84.8% of the ID, respectively – an additional 5% of HD-GalNAc and 12% of HD-TAG were measured in the excrements. This suggests that most of the polymers were excreted by 24 h, supporting the observation of rapid excretion. It is important to highlight that while particle size influences the clearance the ASGPR-mediated systems, HPG based systems offer another advantage that facilitate ASGPR processing by being compact – all liver targeted systems (with or without chelator) have hydrodynamic sizes less than 25 nm.

To the best of our knowledge, total excretions of HD-GalNAc and HD-TAG exceeding 70% of the ID by 24 h is high when compared to other nanoparticle systems with sizes greater than 5 nm.[397,404,424,429] Lactosaminated N-succinyl-chitosan, a liver-specific carrier investigated in mice, exhibited less than 5% excretion by 24 h.[404] While limited literature is available on the excretion of ASGPR-targeted materials, to further substantiate the rapid excretion observation for HD-GalNAc and HD-TAG, the excretion profiles were compared to additional systems. For example, gold nanoparticles ranging from 5 nm to 60 nm demonstrated less than 20% were excreted within 24 h, silica nanoparticles ranging from 100 to 150 nm exhibited up to 40% excretion between 72 h and 96 h, and other manganese oxide or gadolinium nanoparticles revealed between 20 to 80% excretion between 5 days to 21 days.[397] Glycyrrhetinic acid microparticles revealed a total excretion of 30% by 24 h.[429]

In order to better understand the differences in excretion modalities, the kinetics pertaining to intracellular trafficking of these polymers were further investigated using confocal microscopy (**Figure 30**, **Figure 31**, **Figure 32**, and **Figure 33**). Mander's co-localization coefficients were quantitatively compared; raw images were converted into a binary mask[406,407] followed by Mander's analysis to determine the MCCs or the percentage of polymer signal overlap with antibody signal. In these kinetic investigations, MCC never reached a 100% – i.e. the polymer signal never overlapped entirely with antibody signal. This could be due to several reasons including the optical differences in the instrument set up, the parameters required to set a threshold in order to create a binary mask using MATLAB, and, in particular, the antibody selected for the endocytic compartment. To illustrate this further, **Appendix Figure 36** is a confocal micrograph which illustrates the polymer signal being encapsulated by the LAMP1 signal. Despite the percentage of overlap being less than 100%, the polymer is well within the lysosome.

The intracellular distribution of GalNAc decorated systems was first investigated because HD-GalNAc exhibited superior *in vivo* liver targeting and previous studies demonstrated differences in the cellular in

binding and uptake (**Chapter 2**). ASGPR specific ligands undergo ASGPR-mediated endocytosis and are trafficked to the lysosomes for subsequent processing.[217] Similar lysosomal accumulation was observed in HepG2 cells treated with either H-GalNAc$_{50}$ or HD-GalNAc for 2 h and 24 h (**Figure 30**). Notably, significant differences in the co-localization with early and recycling endosomal markers (EEA1 and TfR1, respectively) were observed between these two liver targeting polymers; HD-GalNAc migrated through the early endocytic vesicles slower than H-GalNAc$_{50}$ and exhibited greater co-localization with recycling endosomes. Recycling endosomes were traced because the ASGPR is recycled through the recycling endosomes back to cell surface.[223,258] Despite this, it is important to note that EEA1 and TfR1 are not mutually exclusive[430] so it is possible that the signal in TfR1 endocytic vesicles may be due to the EEA1 overlap. These observations suggest a role of DFO influencing endosomal maturation.

Furthermore, kinetics of intracellular trafficking revealed differences between GalNAc and TAG decorated polymers through pulse-chase experiments (**Figure 31** and **Figure 32**). No significant differences between H-GalNAc$_{50}$ and HD-GalNAc were observed, suggesting that the role of DFO conjugation may be secondary to GalNAc-ASGPR interaction. On the other hand, significant differences were observed between H-TAG$_2$ and HD-TAG at earlier time points which suggests that DFO hastens endocytic maturation and progression. The kinetics of these polymers were then compared to AF. AF is a natural high affinity ligand (K_i = 17 nM) for the ASGPR with 12 Gal and 3 GalNAc residues per mol of protein.[223,414] It is worthwhile to note that AF was selected in these analyses because it possessed GalNAc residues.

Remarkably, both GalNAc decorated polymers and HD-TAG exhibited significantly higher co-localization with early endosomes and lysosomes when compared to AF immediately after pulse. Similarly, after 1 h, both GalNAc and TAG decorated polymers showed significantly higher co-localization with lysosomes when compared to AF. The faster progression and maturation of these endocytic vesicles were also supported by the little to no overlap of liver targeting polymers with the ASGPR (**Figure 31**). This is consistent with ASGPR recycling kinetics observed in hepatoma cell lines; the ASGPR has been reported to take 20 minutes from internalization back to the cell surface for further interaction.[223,257] Additionally, bafilomycin studies, a proton pump inhibitor which prevents the acidification and maturation of these endosomes, demonstrated significant reductions in polymer signal overlap (**Figure 33**). This may suggest that the physical characteristics of these liver targeting systems enhance the maturation of these endocytic vesicles results in faster movement through the endocytic pathway. The rapid lysosomal accumulation may explain the rapid excretion observed for these systems *in vivo*. AF undergoes rapid clearance, degradation and biliary excretion in mice.[398] The expedited rate of translocation to the

lysosomes for HD-GalNAc and HD-TAG may reflect the movement of cargo towards the apical membrane, through microtubule-dependent movement, resulting in hepato-biliary excretion.[425]

Taken together, the data demonstrated that the chemistry and decoration of the ASPGR ligands contribute heavily to the *in vivo* pharmacokinetic behaviour with regards to the residence in plasma, liver accumulation, excretion, and processing of galactosylated nanomaterials. The work in this chapter illustrated the differences in internalization and intracellular trafficking of these systems. One hypothesis that may explain these differences is the interaction of either HD-GalNAc and HD-TAG, and the subsequent effect on ASGPRs recycling kinetics. HD-GalNAc may exhibit higher binding affinity to the ASGPR, as compared to HD-TAG, likely due to the cluster effect[241]. Upon internalization, this may result in slower dissociation of HD-GalNAc possibly resulting HD-GalNAc being recycled back to the cell surface with ASGPR, whereby it enters circulation and is further processed by the kidneys. Enterohepatic cycling may also be possible. On the other hand, the weaker interaction of HD-TAG with ASGPR may allow for faster dissociation once internalized followed by subsequent biliary excretion. The structure of triantennary N-acetyl galactosamine might be also key contributor in this rapid hepatic clearance process, since different TAG structures have been reported to influence cellular uptake[427]. While this work provided key insights into the observed difference, additional investigations are necessary to better understand the connection between the physical characteristics of these systems and the subsequent changes observed in key pharmacokinetic parameters. This will be imperative to shed light on designing optimum systems that yield desired liver targeting and excretion.

3.6. Conclusions

In summary, liver targeted chelating systems, HD-GalNAc and HD-TAG, were assessed for the pharmacokinetic, biodistribution and excretion properties. These polymers demonstrated significantly high liver specificity and were selectively internalized by hepatocytes as compared to the Kupffer cell dominant sequestration of HD, the non-targeted control system. These systems also exhibited rapid total excretion in mice, with almost three quarters of the ID eliminated within 24 h. The *in vivo* processing of these systems was influenced by the type of decorated sugars specific for the ASGPR, which resulted in different routes of excretion, vascular retention times and non-specific distribution. The role of the ligands was further supported by the *in vitro* kinetic analyses on the intracellular trafficking of HD-GalNAc and HD-TAG. The type of GalNAc, either monoantennary or tri-antennary seems to influence the kinetics of endocytosis and translocation which may translate into the systemic excretion. Taken together, the data illustrated that the chemistry and decoration of the ASGPR ligands strongly influence its residence in plasma, liver uptake, and excretion. The rapid excretion of these systems provides further support to investigate its iron chelation efficiency in the following chapters.

Chapter 4: Investigation of molecular and functional properties of liver specific iron chelators on iron excretion *in vivo*.

4.1. Overview

A novel class of liver targeting iron chelators have been designed and developed in previous chapters; HD-GalNAc and HD-TAG exhibited significant liver targeting and rapid excretion in mice. In this chapter, the translation of HD-GalNAc and HD-TAG were assessed with regards to chelation performance *in vivo*. In addition, to investigate the role of DFO density on chelation, HD_{40}-GalNAc were also synthesized and investigated. First, an iron overload model was optimized in C57Bl/6 mice by loading them with 3 doses of 300 mg/kg iron-dextran. In these mice, hepatic iron burden increased by 89-fold whilst minimizing signs of toxicity. Then, the colorimetric unified-ferene assay was validated for total iron quantification from mice samples using ICP-MS. The chelation efficiencies for all liver targeted iron chelators and their controls were then investigated in the optimized iron overload mouse model. Despite the rapid excretion displayed by HD-GalNAc and HD-TAG, these systems did not translate into significant rapid iron removal. However, HD_{40}-GalNAc demonstrated significant iron removal systemically and from the liver suggesting the role of DFO density on these liver targeting systems.

4.2. Background

Iron has a paradigmatic role in many key functions of mammalian organisms. Humans lack a specific iron excretion pathway. In order to maintain iron homeostasis, mammals have evolved highly specialized mechanisms that tightly regulate iron uptake, transport and utilization, recycling, and storage.[26,28,99] The liver plays a central role in coordinating iron homeostasis; all acquired iron enters the liver, 80% of which is comprised of hepatocytes, where it is either stored or utilized intracellularly, or mobilized for systemic demands.[211,214] Approximately 30% of the total amount iron in the body is stored in the liver. A perturbance in iron homeostasis can result in hepatic iron overload either through genetic or acquired disorders and also leads to iron deposits in other the organs including heart, spleen, and kidney.

Hepatic iron overload and subsequent damage is one of the major causes of mortality and morbidity in different pathogenesis, including hereditary hemochromatosis, transfusion-related iron overload, hepatitis C infection, alcoholic fatty liver disease, chronic hepatopathies, hepatic fibrosis and inflammation, and cirrhosis.[75,77–79,88,103–106] Under normal physiological conditions, liver iron content is usually less than 1 mg iron per gram of liver.[96] However, in patients suffering from iron overload, the liver iron content can exceed 15 to 20 mg iron per gram of liver.[97] Most commonly, the iron deposits in liver are found either in hepatocytes or Kupffer cells. The accumulation of bioactive redox iron triggers the generation of free ROS *via* the Haber-Weiss pathway and triggers oxidative stress-driven cell damage or signalling pathways involved in hepatic fibrogenesis and even carcinogenesis. Elevated levels of bioactive iron have been investigated for triggering metabolic pathogenesis such as insulin resistance, metabolic syndrome, and non-alcoholic fatty liver disease.[79,103,431] Further, it has been shown that iron can act as a comorbidity factor long with fat, hepatitis viruses and alcohol.[431] Liver dysfunction and failures, along with heart failures, account for over 75% of premature deaths in iron overload patients despite intensive treatment.[101,102]

Iron chelation therapy using small molecular chelators can attenuate the propensity of redox active iron to catalyze ROS and to reduce the iron burden in iron overloaded tissues. Small molecular chelators such as deferoxamine, deferiprone, and deferasirox, have shown some promise in reducing hepatic and myocardial iron burden in patients. However, these chelators are beset by limitations associated with their unfavorable pharmacokinetics and pharmacodynamics, systemic toxicity, nonspecific tissue distribution and suboptimal iron excretion.[94,137]

Macromolecular approaches circumvent these shortcomings, principally by increasing their molecular mass, and have been well documented in enhancing iron chelator's biological availability.[167–171] Despite the extensive research in using nanomaterials for the development of superior chelators, there are no active liver targeting strategies for the excretion of iron from liver. Since the liver is the primary storage organ and a key regulator in iron homeostasis, the selective removal of excess liver iron could be invaluable to protect the liver and to restore iron homeostasis. Additionally, by targeting and chelating the hepatic iron stores, this may allow for the redistribution of excess bioactive iron from other parts of the body to restore normal iron balance *via* existing iron transport and delivery mechanisms.

The design and development of liver targeted iron chelating systems have been described in previous chapters; **Chapter 2** outlined the screening and selection of appropriate systems for optimized liver targeting and **Chapter 3** investigated the pharmacokinetic, biodistribution and excretion properties for HD-GalNAc and HD-TAG and the underlying intracellular fate. HD-GalNAc and HD-TAG exhibited significant liver targeting, almost exclusively within the parenchymal cells, and displayed rapid elimination *in vivo*. Building on the previous observations, HD-GalNAc and HD-TAG were investigated for the chelation efficiencies in iron overloaded mice. HD_{40}-GalNAc was also investigated to assess the influence of DFO density on iron chelation and removal. We hypothesized that liver targeted macromolecular chelating systems will reduce the iron burden in iron overloaded mice, particularly from the liver.

In order to investigate this hypothesis, an iron overload model was first optimized in C57Bl/6 mice with respect to the dose of injected iron-dextran whilst minimizing toxicities. Iron loading was measured *via* changes in serum ferritin and liver iron content. Signs of toxicities were monitored by measuring changes in mice body weight, clinical signs, subsequent organ changes and alanine aminotransferase (ALT) activity. Next, the unified-ferene (*u*-ferene) assay was validated against ICP-MS for its total iron quantification from biological specimens obtained from mice. **Chapter 5** describes the development and validation of the unified-ferene assay for its labile and total iron quantification. The colorimetric *u*-ferene assay was designed with the intent to expedite data collection in a cost-effective manner. Then, the functional performance for these liver targeted chelating systems was investigated in the optimized iron overload mouse model for their iron excretion and reduction in iron burden.

Taken together, a novel class of liver targeted chelators were investigated for the removal systemic iron under iron overload conditions. These chelators potentially mitigate iron-mediated toxicity and protect the liver– a vital organ involved in iron homeostasis and implicated in various other disorders

4.3. Methods

4.3.1. Materials

Dulbecco's Phosphate Buffered Saline (PBS) was purchased from Thermo Fisher Scientific. Deferoxamine mesylate, ferric ammonium citrate (FAC), ammonium acetate, sodium L-ascorbate, ferene (3-(2-Pyridyl)-5,6-di(2-furyl)-1,2,4-triazine-5',5''-disulfonic acid disodium salt), ICP-MS grade iron standards, ICP-MS grade indium standards, 2 Dr glass vials, sodium chloride, iron dextran, 10% neutral buffered formalin, and concentrated nitric acid were obtained from Sigma-Aldrich. Fast-prep tubes (2 mL) were purchased from MP Biomedicals, LLC-Fisher. ICP-MS grade concentrated nitric acid was acquired from VWR. For cellular assay kits, both the alanine aminotransferase (ALT) activity and aspartate aminotransferase (AST) activity assay were purchased from Sigma-Aldrich. Mouse ferritin ELISA kits were obtained form Immunology Consultants Laboratory Inc.

4.3.2. Synthesis of liver targeting macromolecular iron chelators

All liver targeting macromolecular systems have been summarized in **Table 1** and **Table 2**. The synthesis protocols have been described in **Chapter 2.** In this chapter, HD_{40}-GalNAc was also synthesized to investigate the influence of DFO densities on iron chelation following the same synthetic protocols outlined previously.

4.3.3. *In vivo* iron chelation efficacy of liver targeting chelating systems

All the animal studies were carried out at the Experimental Therapeutics laboratory, B.C. Cancer Research Centre, Vancouver, BC, Canada. All the protocols were approved by the Institutional Animal Care Committee (IACC), UBC. For all studies, female C57Bl/6 mice between 6 to 9 weeks were used.

4.3.3.1. The development and validation of an *in vivo* iron overload model

In order to determine the appropriate iron loading conditions with iron-dextran (Fe-Dex), 3 treatment groups were investigated; 1. Saline group that received 5 injections, 2. 3 injection group that received 3 doses of 300 mg/kg of Fe-Dex, and 3. 5 injection groups that received 5 doses of 300 mg/kg of Fe-Dex. Each group had 3 mice. Mice were individually weighed three times per week. Mice were briefly restrained during tail vein injections and the injection volumes were 200 μL/20 g mouse. For groups 1 and 3, mice

were injected on days 1, 3, 5, 8 and 10. For group 2, mice were injected on days 5, 8 and 10. Mice were continually monitored for acute signs of toxicity for the first two hours after injection and daily for the duration of the experiment. After the last injection, mice were observed for an additional 7 days.

Mice were terminated by CO_2 asphyxiation. Whole blood and serum were collected and stored at 4°C. Feces and urine were collected from day 15 to 17 and stored at -80°C. Entire organs, including liver, spleen, kidneys, and heart, were rinsed in PBS, weighed, flash frozen in liquid nitrogen and stored at -80°C. Serum ferritin and ALT activity were measured, as described in section 4.3.5. and 4.3.6. respectively. Total iron was quantified using ICP-MS and the u-ferene assay, as described in section 4.3.4.

4.3.3.2. *In vivo* iron chelation efficiency for liver targeting chelating systems

The efficacy of liver targeted macromolecular chelators (HD-GalNAc, HD-TAG and HD_{40}-GalNAc) and their controls (non-targeted macromolecular chelator – HD, small molecule chelator – DFO, and no chelator treatment – saline) were investigated in iron overloaded mice. Each treatment group had 4 mice. Mice were first iron overloaded with 3 injections of 300 mg/kg of Fe-Dex on days 1, 3 and 5. After a 10 day observation period, mice were then treated with 50 mg/kg of DFO-equivalent chelators every 4 days for a total of 5 doses (i.e. treatments were made on days 15, 19, 23, 27 and 31). Mice were briefly restrained during tail vein injections and the injection volumes were 200 µL/20 g mouse. Body weights were recorded prior to injections and three times per week.

On day 35, mice were sacrificed *via* CO_2 asphyxiation. Whole blood and serum were collected and stored at 4°C. Serum ferritin were measured, as described in section 4.3.5. Feces and urine were collected from day 15 to 35 and stored at -80°C. Entire organs, including liver, spleen, kidneys, pancreas and heart, were rinsed in PBS, weighed, flash frozen in liquid nitrogen and stored at -80°C. Total iron in organs and excrements were quantified using u-ferene assay, as described in section 4.3.4.

For histological examinations, liver (25% by weight) and 1 kidney were washed in ice cold saline and then preserved in 10% neutral buffered formalin. Organs were paraffin embedded and stained for either hematoxylin & eosin or Prussian blue counter stained with nuclear fast. Histological processing was carried out by Wax-It Histology.

4.3.4. Total iron determination from tissue specimens

Biological specimens include organs, feces, urine and blood. These were first acid digested followed by quantification using the gold-standard, ICP-MS, and a novel unified-ferene (*u*-ferene) assay. Iron concentrations were interpolated from a standard curve.

In **Chapter 5**, the *u*-ferene assay was designed, developed and validated. For all pertinent details regarding the quantification of *in vitro* labile and total iron, please refer to **Chapter 5**. In this chapter, the *u*-ferene assay was used for total iron determination from *in vivo* biological samples and relevant details are provided below.

4.3.4.1. Acid digestion of biological specimens

Mice organs were weighed in Fast-Prep tubes and homogenized in 0.5 mL water (BioSpec Product 96+, Bartlesville, OK). Biological samples were transferred into acid-washed glass vials and dried at 100°C to 120°C. The evaporation of water hastens the digestion of organic samples with nitric acid (HNO_3). Then, all biological samples were digested with concentrated HNO_3 – samples were maintained at 100°C to 120°C and small volumes (0.5 to 1.0 mL) of concentrated HNO_3 were repeatedly added over the course of 5 days. All digested samples were dried at 120°C, then cooled to room temperature and weighed.

All the required dilutions were performed by mass. Acid-digested biological samples were resuspended in 4% HNO_3 (1 mL) and weighed again. All biological samples were further diluted in 2% HNO_3 for the quantification of iron, as outlined in the **Appendix Table 5**. 2% HNO_3 was used for final dilutions for the longevity of vacuum pumps required by ICP-MS.

4.3.4.2. Total iron quantification using inductively coupled plasma mass spectrometry (ICP-MS)

Biological samples were appropriately diluted in 2% HNO_3 with 10 ppb indium (Sigma Aldrich) as the internal standard, as outlined in **Appendix Table 5**. Iron standards were also prepared in 2% HNO_3 with 10 ppb indium, ranging from 0 ppb to 400 ppb, to generate a standard curve. Iron counts were measured on Agilent 7700 series ICP-MS and total iron concentrations were determined from the standard curve.

4.3.4.3. Total iron quantification using the *u*-ferene assay

The development of this assay for the measurement of both labile and total iron has been outlined and investigated in **Chapter 5**. In this chapter, the validation of *u*-ferene was investigated with respect to total iron determination from biological specimens.

Iron standards were prepared from ferric ammonium citrate in 2% HNO_3, ranging from 0 to 1000 μM. These standards are prepared by mass; mass of ferric ammonium citrate and mass of 2% nitric acid were taken into account to determine their concentrations.

The biological samples at its final dilutions (**Appendix Table 5**) (200 μL) and iron standards (200 μL) ranging from 0 to 1000 μM were transferred into different clean Eppendorf tubes. Ammonium acetate buffer (pH 4.5, 2.5 M) (200 μL) and total iron working solution (5 mM ferene and 1 M ascorbic acid prepared in ammonium acetate buffer pH 4.5, 2.5 M) (240 μL) were added to all Eppendorf tubes. This mixture was vortexed and left overnight at room temperature.

All mixtures of samples and standards with ferene-containing working solution were spun at 15,000 g for 5 minutes. Then, these were transferred (200 μL) into a 96 well plate for absorbance measurements. Absorbance was recorded at 595 nm using a SpectraMax 190 microplate reader from Molecular Devices. Iron concentrations were interpolated from the standard curve generated from the iron standards. These concentrations were normalized to the amount of protein analyzed (i.e., nmole of iron per mg of protein).

4.3.5. Serum ferritin determination

Serum ferritin level was assayed for each mouse within the group using a quantitative colorimetric ELISA kit (Immunology Consultants Laboratory, Inc., Portland OR.) following manufacturer's protocol. In brief, samples were diluted between 40 to 300 times and absorbance at 450 nm were analyzed using a 4-parameter logistic curve determined from standards.

4.3.6. ALT and AST Activity assay

Serum ALT activity was determined in C57Bl/6 mice optimized for iron overload. Serum ALT and AST activity were determined in healthy C57Bl/6 mice as an indicator of HD-GalNAc tolerability. Both ALT and AST activity were colorimetrically assayed using a commercially available kit (Sigma Aldrich) following

manufacturer's protocol. In short, samples were diluted at least 40 times and monitored in 5 minute intervals. Absorbance was measured at 570 nm and enzyme activity was calculated.

4.3.7. Statistical analysis

All experiments were performed in at least independent triplicates. Standard deviations were presented as error bars. Technical replicates were also performed, when stated. All statistical analyses were performed using GraphPad Prism 7 (Grahpad Software, San Diego, USA). The statistical tests and appropriate multiple comparison tests were outlined in the figure legends.

4.4. Results

4.4.1 The development and validation of an *in vivo* iron overload model

In order to investigate the functional capacities of the liver targeted chelating systems, an iron overload model was first developed in C57Bl/6 mice. In order to determine the appropriate iron loading conditions, mice were administered with parenteral iron-dextran (Fe-Dex) and observed for changes in iron status (**Figure 34**) and any physiological changes (**Figure 35** and **Figure 36**).

Mice were treated with either 3 injections or 5 injections of Fe-Dex at 300 mg/kg. Mice treated with 5 injections of saline served as a negative control. Serum ferritin and liver iron concentrations were measured as iron status markers for iron overloading (**Figure 34**). Despite the 3 injection group increasing the serum ferritin concentration to 176 μg/mL , compared to 1.2 μg/mL observed in the saline control group, no statistically significant difference was observed. Whereas, the 5 injection group had significantly elevated serum ferritin, a concentration of 971 μg/mL, when compared to the saline control group ($p = 0.0045$) and the 3 injection group ($p = 0.0130$). On the other hand, total liver iron content was elevated in both Fe-Dex treatment groups. Mice that received 3 doses of Fe-Dex exhibited a total hepatic iron of 8.9 mg and mice that received 5 doses of Fe-Dex exhibited a total hepatic iron of 10.3 mg. When compared to the total hepatic iron in the saline control group, 0.1 mg, both 3 injection and 5 injection groups were significantly higher ($p = 0.0003$ and $p = 0.0001$, respectively).
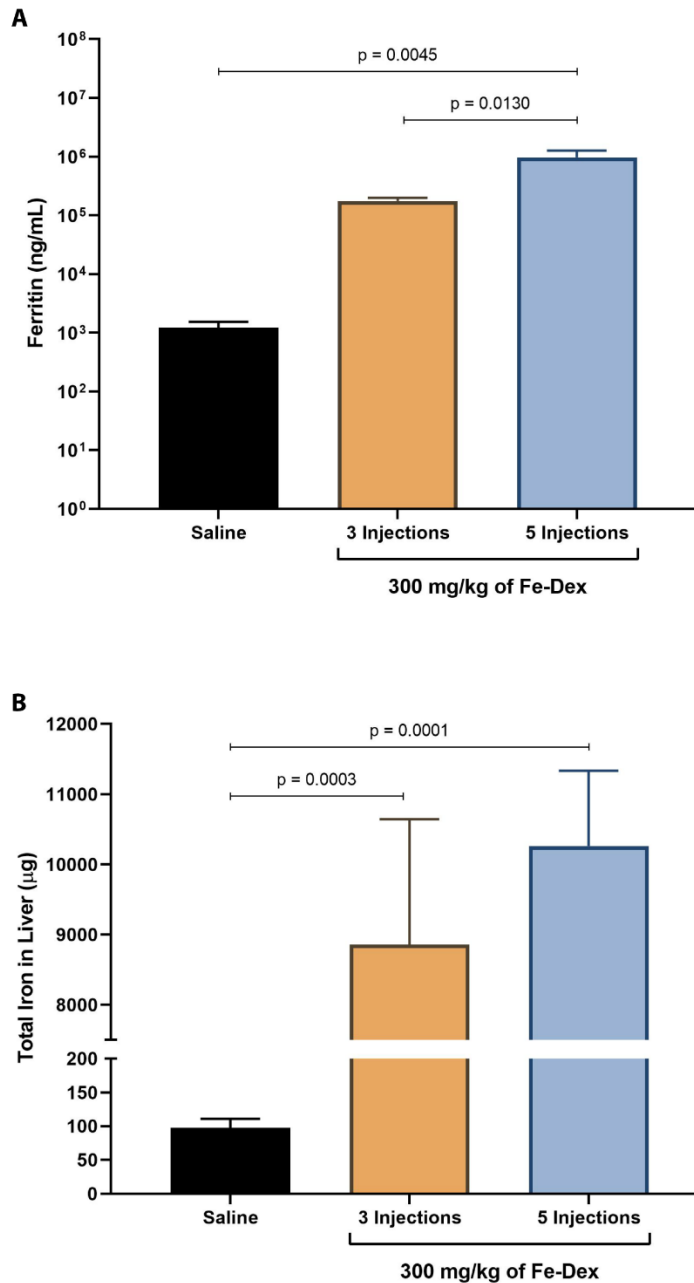
Figure 34. The development and validation of a secondary iron overload model *in vivo*. C57Bl/6 female mice were iron overloaded with either 3 injections or 5 injections of iron-dextran (Fe-Dex) at a dose 300 mg/kg. A control group was treated with saline for a total of 5 injections. (A) Serum ferritin concentrations were measured using an ELISA kit. (B) Total iron in the liver were quantified using ICP-MS. Error bars show standard deviations for 3 independent replicates. A 1-way ANOVA with Tukey's multiple comparisons test were performed to compare any differences between treatment groups using GraphPad Prism.

For the duration of the study, all mice were under observation for any clinically relevant changes (**Figure 35**). A similar weight gain was observed for mice treated with saline (8.6% ± 1.4%) and 3 injections of Fe-Dex (7.4% ± 1.9%). On the other hand, mice treated with 5 injections had minimal weight change (0.6% ± 2.1%) which was significantly lower than the saline group ($p = 0.0006$, Sidak's multiple comparison test). Notably, only mice treated with 5 doses of Fe-Dex exhibited a significant decrease in excrement output for both urine and feces (**$p = 0.0045$ and ***$p = 0.0005$, respectively).

With respect to signs of toxicity, no clinical signs were observed, however, serum ALT activity was markedly higher in mice receiving Fe-Dex (**Figure 36B**). ALT activity is a hepatic enzyme and serum ALT activity provides a measure of enzyme leakage due to liver insult. Mice that received either 3 or 5 injections had significantly elevated ALT activity when compared to the saline control group ($p = 0.0475$ and $p = 0.0003$, respectively). Further, mice treated with 5 injections exhibited significantly higher ALT activity when compared to 3 injections (p 0.0031). In addition to this, mice treated with Fe-Dex had markedly enlarged livers when compared to the saline control group ($p < 0.0001$ for both 3 injections and 5 injections groups); the 3 injection group revealed a 40% increase and the 5 injection group revealed a 20% increase in size. The 3 injection group had significantly larger livers than the 5 injection groups ($p < 0.0001$). No significant changes were observed for other organs, including heart, spleen, and kidneys.

Taken together, the 3 injection group yielded significant increases in iron status whilst exhibiting minimal toxicities when compared to the 5 injection group. Thus, the functional performance of liver targeted chelating systems was assessed in C57Bl/6 mice loaded with 3 doses of 300 mg/kg Fe-Dex.
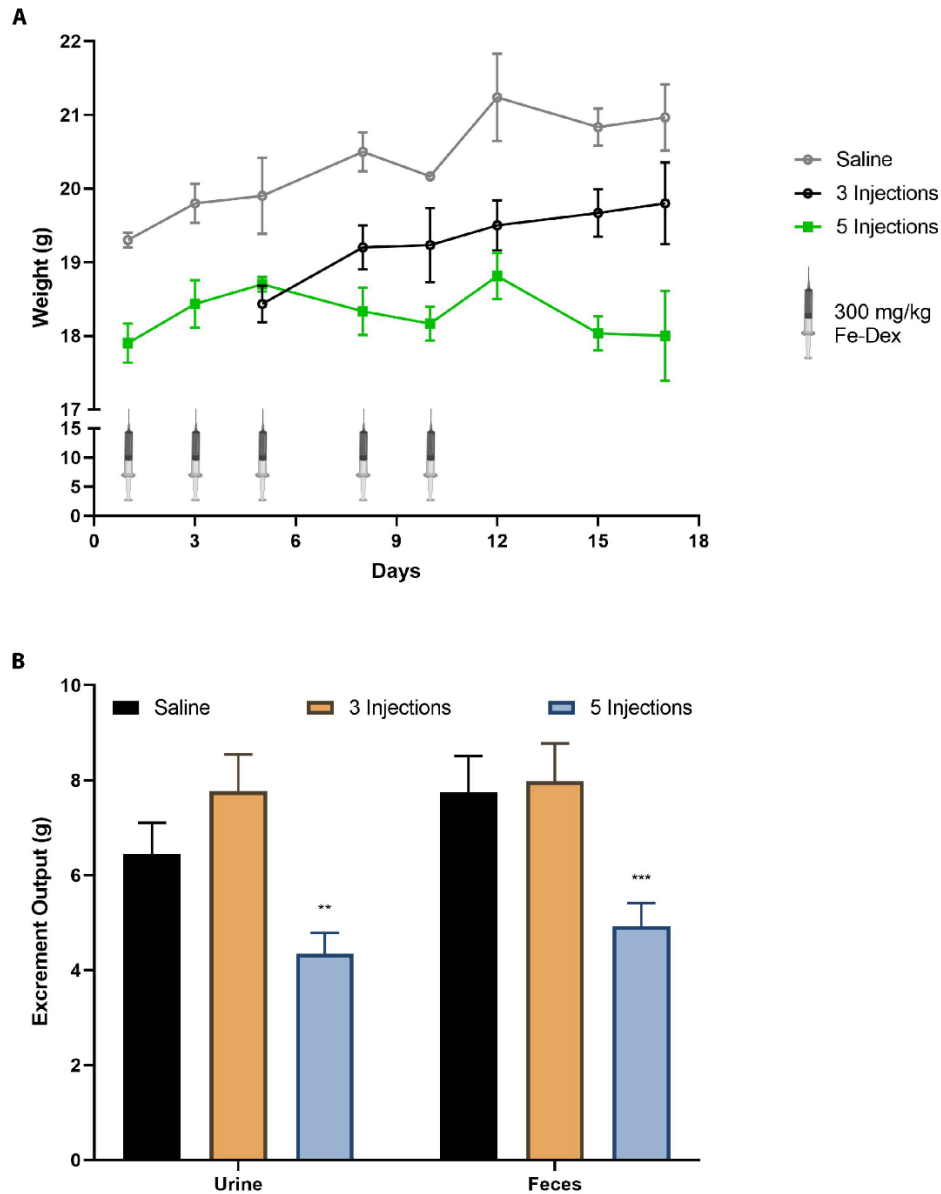
Figure 35. The schedule for iron overloading and the subsequent changes in body weight and excretion output. C57Bl/6 mice were treated with either 3 doses (on days 5, 8 and 10) or 5 doses (on days 1, 3, 5, 8 and 10) of Fe-Dex. The negative control group received saline instead. Mice were observed for an additional 7 days. (A) The schedule for treatment with iron-dextran (Fe-Dex) at 300 mg/kg and the changes in body weight. (B) Changes in their excretion output were also measured from day 15 to termination (day 17). Error bars show standard deviations from a sample size of 3 mice per group. A 2-way ANOVA with Sidak's multiple comparison test was performed to compare the changes in urine and feces output with respect to the saline control group. GraphPad Prism was used for statistical analyses. ** represents $p < 0.0100$ and *** represents $p < 0.0010$.
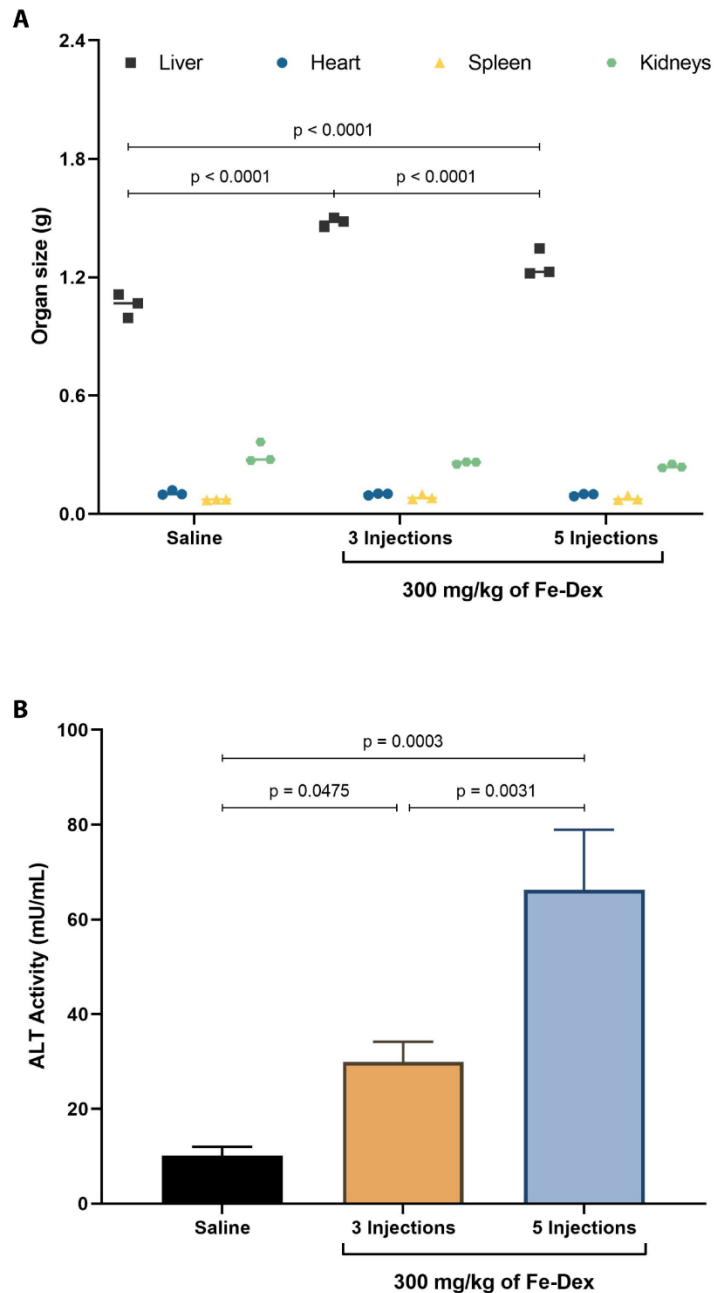
Figure 36. Toxicity evaluation of iron-dextran iron overloaded mice. (A) Changes in organ sizes were measured by weight (g). (B) Serum ALT activity was measured using a kit. Error bars show standard deviations from a sample size of 3 mice per group. A 2-way ANOVA with Tukey's multiple comparison tests were performed for the comparison of organ sizes. A 1-way ANOVA with Tukey's multiple comparison tests were performed for the comparison of ALT activities. All statistical analyses were performed using GraphPad Prism.

4.4.2. The quantification of total iron in various biological specimens using the *u*-ferene assay

The *u*-ferene assay has been optimized for the quantification of both labile and total iron from the same sample – this has been discussed in **Chapter 5** in great detail. Herein, the focus lies on the quantification of total iron using the *u*-ferene assay and its validation using ICP-MS in complex biological specimens – organs (liver, spleen, kidneys, heart), fluids (blood and urine), and solids (feces). The biological specimens from the optimization of an *in vivo* iron overload model were analyzed (**Figure 37**).

The total iron concentrations were almost identical between the *u*-ferene assay and ICP-MS irrespective of the complexities associated with tissue specimens. In the context of this experiment, accuracy of the *u*-ferene assay refers to the comparison of the iron concentrations determined from ICP-MS since ICP-MS is the current gold standard for elemental analysis.[432] For instance, the total iron concentrations in the liver for the saline control group was 102 µg ± 18 µg from the *u*-ferene assay compared to 98 µg ± 13 µg from ICP-MS. Similarly, the total iron concentrations in the spleen for the saline group was 46 µg ± 10 µg from the *u*-ferene assay compared to 46 µg ± 7 µg from ICP-MS. Additionally, the total iron concentrations in the kidneys for the 3 injection group 147 µg ± 21 µg from the *u*-ferene assay compared to 150 µg ± 21 µg from ICP-MS. Moreover, like ICP-MS, the *u*-ferene assay was able to measure a wide range of iron concentrations – from 12 µg iron found in the heart of mice treated with saline to 10.300 mg iron in the liver of mice treated with 5 doses of Fe-Dex.

Notably, by measuring the total iron concentrations in these specimens, the total iron concentrations in the spleen and kidneys significantly increased with increasing doses of Fe-Dex; splenic and renal iron significantly increased when comparing the saline group and the 3 injection group ($p < 0.0001$ for both organs) and when comparing 3 injection group and 5 injection group ($p < 0.0001$ for both organs). The total iron concentrations in the heart elevated mildly when comparing the saline group to the 3 injection group (12 µg vs 22 µg) and cardiac iron concentration increased significantly when comparing the saline group to the 5 injection group (12 µg vs 36 µg; $p = 0.0192$). No statistical difference in cardiac iron was observed between the 3 injection group and the 5 injection group. Moreover, no statistical differences were observed in the total iron concentrations from blood, urine and feces.
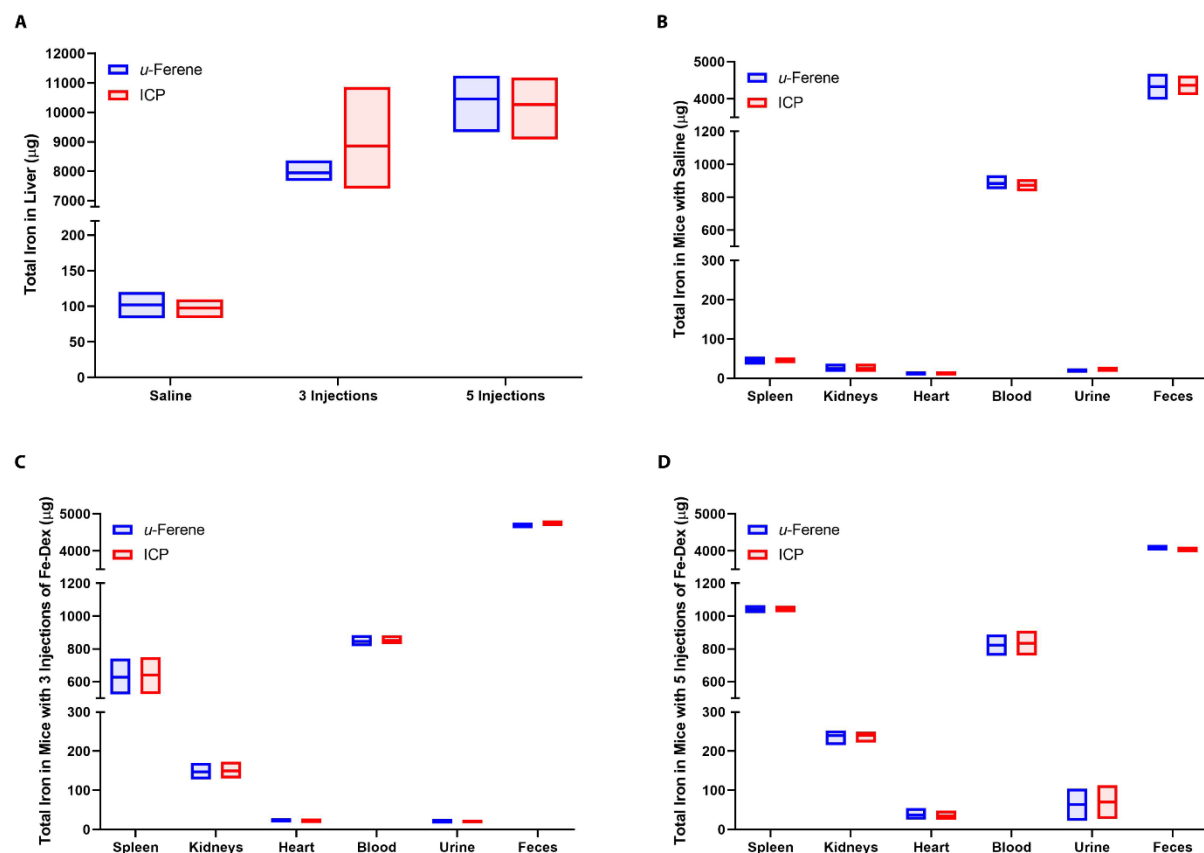
Figure 37. Quantification of total iron in various tissue specimens from iron overloaded mice. C57Bl/6 female mice were treated with either 3 injections or 5 injections of iron-dextran (Fe-Dex) at a dose 300 mg/kg. Total iron quantification was compared between the (blue) *u*-ferene assay and (red) ICP-MS. (A) The total iron in the livers of mice were compared. The agreement between the *u*-ferene assay and ICP-MS were investigated in mice that received (B) saline (a non-iron overloading control), (C) 3 injections of Fe-Dex and (D) 5 injections of Fe-Dex. The data from three biological replicates per group were shown as whisker box plots. A 2-way ANOVA with Sidak's multiple comparisons test were performed to compare the iron concentrations determined from the *u*-ferene assay and ICP-MS using GraphPad Prism.

4.4.3. Therapeutic efficacy and toxicity of liver targeting chelating systems *in vivo*

Before investigating the chelation efficacy of liver targeted chelating systems, the toxicity was first assessed *in vivo* (**Figure 38**). While both HD-GalNAc and HD-TAG preferentially accumulate within the liver as documented in **Chapter 4**, HD-GalNAc was used to investigate toxicity because of its higher hepatic accumulation. Alanine aminotransferase (ALT) are found primarily in the liver whereas aspartate aminotransferase (AST) are found in various tissues including the liver, pancreas and brain. ALT and AST are intracellular enzymes were are released into circulation from tissues typically during injury.[433] Hence, the activity of ALT and AST detected in serum were measured as a proxy of toxicity. Mice were treated with escalating doses of HD-GalNAc up to 100 mg/kg with respect to DFO equivalents.

The ALT activity for the saline control group was 45 mU/mL whereas the serum ALT activity measured ranged from 38 to 49 mU/mL for the escalating doses of HD-GalNAc. The AST activity for the saline control group was 70 mU/mL whereas the serum AST activity measured for the polymer ranged from 64 to 69 mU/mL. When compared to the saline control group, no significant differences were observed in serum ALT and AST activity for HD-GalNAc at different doses. Therefore, chelation efficiency of liver targeted chelating systems was explored at a dose of 50 mg/kg DFO equivalent.

Next, the iron chelation performance of liver targeted chelating systems and their controls were evaluated in the optimized iron overload mouse model. Mice were first loaded with 3 injections of 300 mg/kg Fe-Dex on alternating days, followed by a 10-day observation period. Following this, mice were then treated with 5 doses of 50 mg/kg of DFO equivalent chelators every 4 days. The dosing schedule has been summarized in **Figure 39**. Chelation efficiency of three different liver targeting chelating systems were evaluated, HD-GalNAc, HD-TAG and HD_{40}-GalNAc, and compared with non-targeted macromolecular chelator, HD, and small molecule chelators, DFO. HD_{40}-GalNAc was explored to investigate the influence of DFO density on its chelation efficiency *in vivo*.
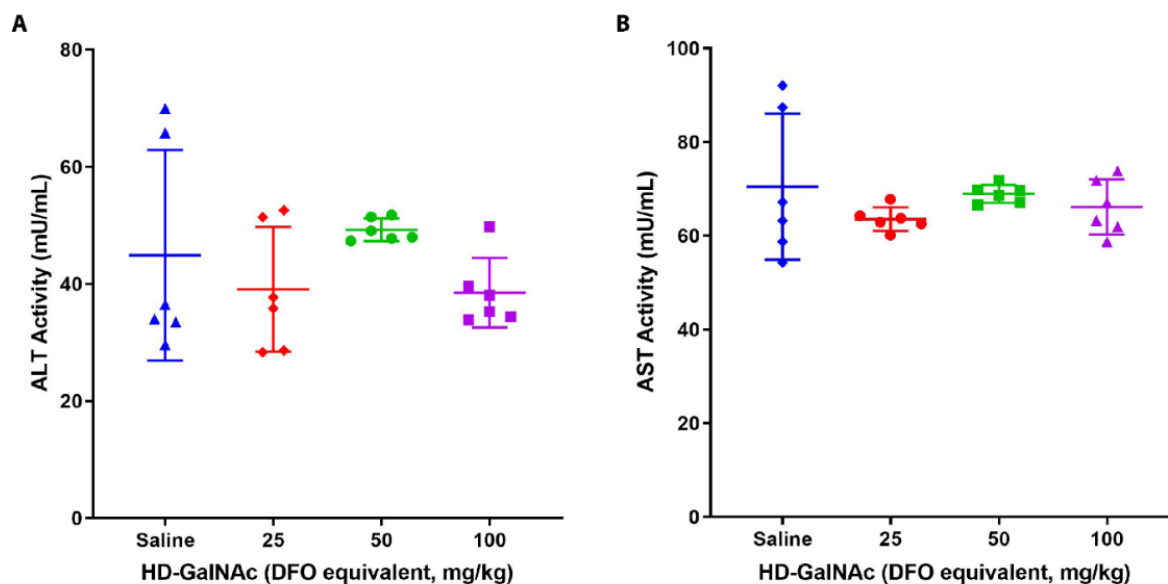
Figure 38. *In vivo* tolerance of liver targeting macromolecular chelator in healthy mice. The toxicity of HD-GalNAc were measured in C57Bl/6 mice treated with escalating DFO-equivalent doses (25, 50 and 100 mg/kg). Serum (A) ALT and (B) AST activities were measured as proxies of toxicity. The scatter dot plots show data from 3 independent replicates, each with an intraassay duplicate. A 1-way ANOVA with Dunnett's multiple comparisons test were performed to compare chelator treatment at varying doses to the saline control using GraphPad Prism.
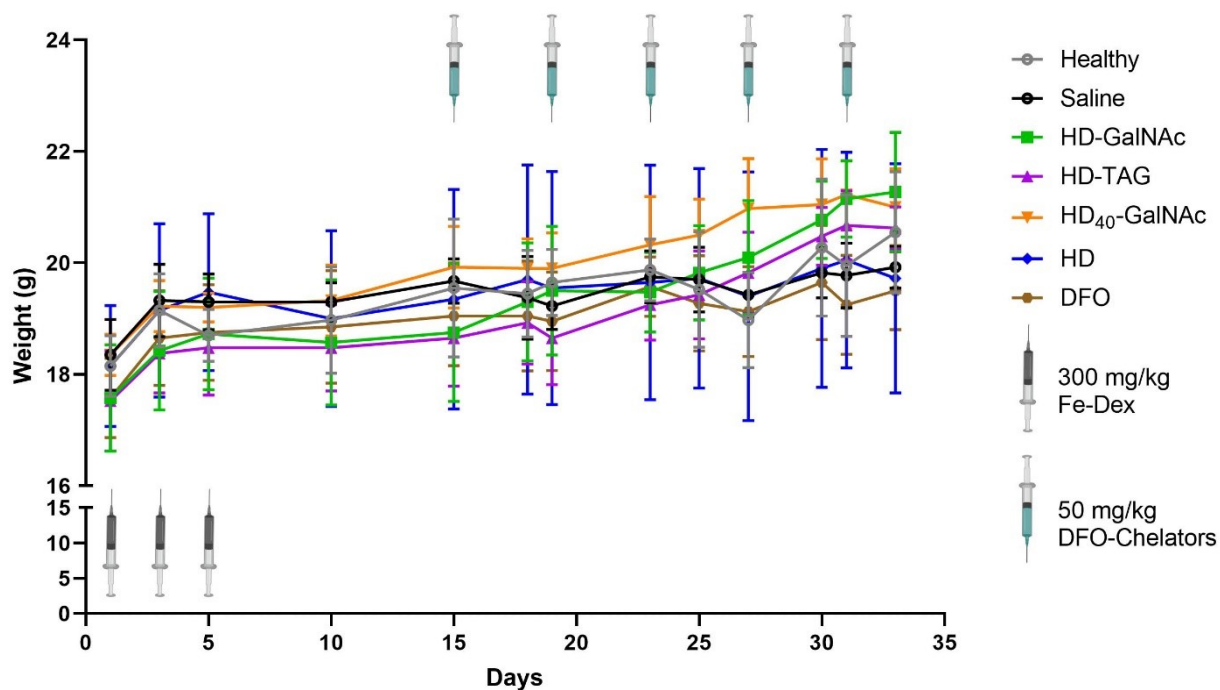
Figure 39. The treatment of iron overloaded mice with DFO-based chelators: A schedule of dosing and subsequent changes in body weight. C57Bl/6 female mice were iron overloaded with 3 injections of 300 mg/kg Fe-Dex on Days 1, 3 and 5. After a 10-day observation period, mice were treated with 50 mg/kg of DFO-equivalent chelators on Day 15 for every 4 days for a total of 5 injections (Day 15, 19, 23, 27 and 31). Excrements, both feces and urine, were collected during the treatment period. Organs and serum were collected at the end of the study. Error bars shows standard deviations from 4 mice per group. A 2-way ANOVA with Dunnett's multiple comparison tests were performed using GraphPad Prism.

Chelation efficacy was examined with respect to systemic iron removal (**Figure 40A** and **B**) as well as the iron burden (**Figure 40C** and **D**). In the feces (**Figure 40A**), the total iron excreted by mice treated with HD$_{40}$-GalNAc was significantly higher when compared to the saline (p < 0.0001), HD (p < 0.0001) or DFO treatment (p < 0.0001), removing approximately 5.12 mg of iron over the duration of the study. Whereas, mice treated with either HD-GalNAc, HD-TAG or HD exhibited a significant decrease in iron excretion (p = 0.0004, p = 0.0283 and p = 0.0005, respectively). No differences were observed the fecal excretion of iron when mice were treated with DFO alone.

On the other hand, all chelator treatments excreted significantly more iron *via* the urine when compared to the saline control group (**Figure 40B**); HD-GalNAc removed 42 μg of iron (p < 0.0001), HD-TAG removed 94 μg of iron (p < 0.0001), HD$_{40}$-GalNAc removed 138 μg of iron (p < 0.0001), HD removed 59 μg of iron (p < 0.0001), and DFO removed 30 μg of iron (p = 0.0081). HD-TAG systems resulted in a significant urinary excretion of iron when compared to HD or DFO treatments (p = 0.0040 and p < 0.0001, respectively. Similarly, HD$_{40}$-GalNAC also removed significantly more urinary iron when compared to HD and DFO treatment groups (p < 0.0001 for both comparisons).

Furthermore, the liver iron burden and serum ferritin concentrations were explored (**Figure 40C** and **D**). Remarkably, no significant differences were observed when comparing chelator treatments to the saline control, in either the liver iron content or serum ferritin concentrations. Despite removing over 5 mg of iron, HD$_{40}$-GalNAc decreased the total hepatic iron to 3147 μg when compared to total hepatic iron of 3581 μg measured in the saline control group. **Appendix Table 8** shows liver iron concentrations with respect to either wet or dried liver weight for the sake of comparison with other literature. However, the reduction in total hepatic iron by 521 μg was significant when compared to mice treated with DFO alone (p = 0.0227). No significant changes were observed in the iron burden of other organs, including the heart (**Appendix Figure 37**) and the total and labile iron concentrations (**Appendix Figure 38**).

Taken together, mice treated with 5 doses of HD$_{40}$-GalNAc removed an average of 5.26 mg of iron. The only chelating system that outperformed both non-targeted controls (HD and DFO) was HD-TAG with respect to urinary iron excretion.
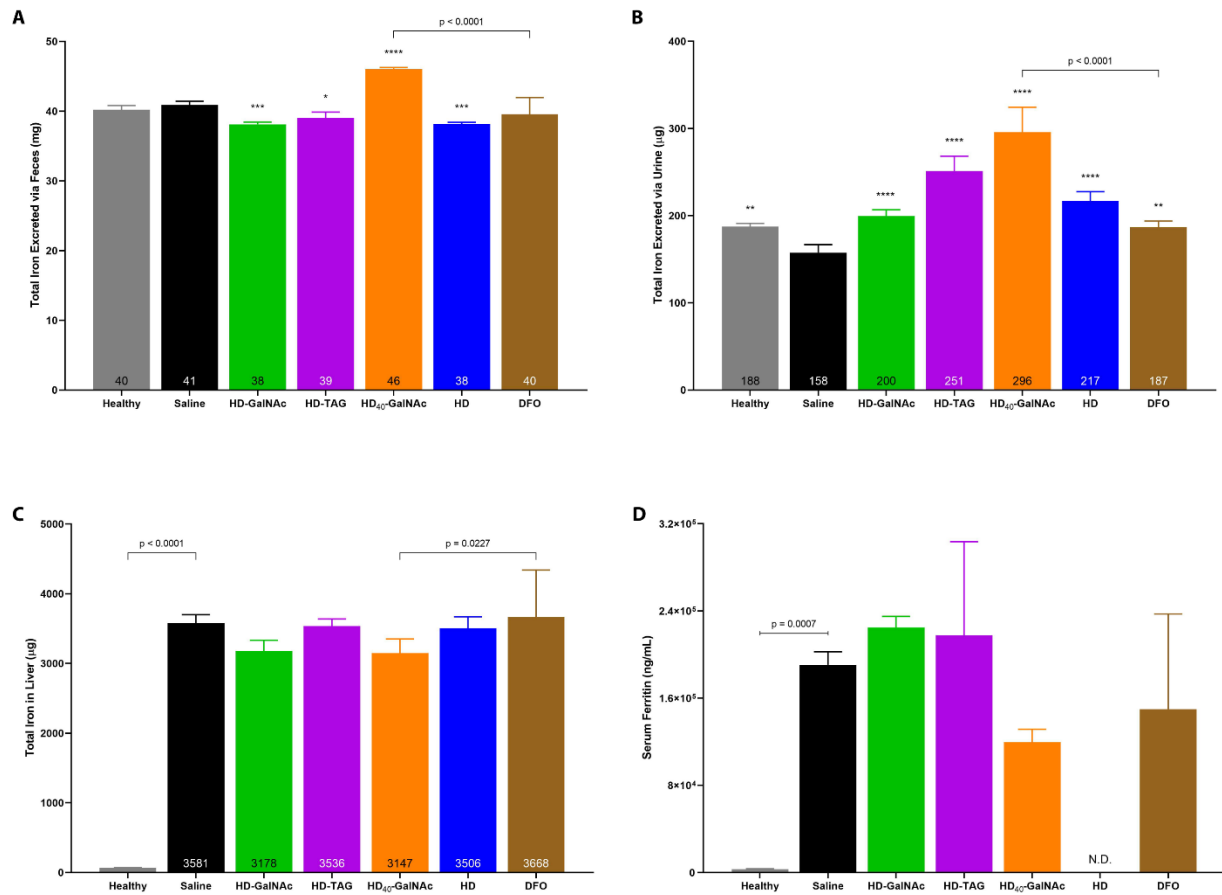
Figure 40. *In vivo* efficacy of liver targeting chelating systems using iron overloaded C57Bl/6 mice. The excretion of iron in (A) feces, (B) urine and (C) the liver was measured using the established *u*-ferene assay. (D) Serum ferritin was measured using an ELISA kit. Healthy mice represents non-iron overloaded C57Bl/6 mice treated with saline instead. Error bars show standard deviations from 4 mice in (A) feces, (B) urine and (D) serum ferritin. Error bars show standard deviations from 3 mice in (C) total liver iron. Intraassay duplicates were performed for all iron quantification assay using the *u*-ferene assay. A 1-way ANOVA with Sidak's multiple comparison tests were performed to compare the differences in treatment groups against iron overloaded saline group using GraphPad Prism.

Histological examination of liver sections (**Figure 40**) and kidney sections (**Appendix Figure 39**) revealed substantial iron deposits in all mice that were iron overloaded, depicted by the large and disperse blue staining from Prussian blue. Morphologically, the central veins were well defined and the sponge-like architecture was maintained. All iron overloaded treatment groups showed minimal signs of cellular injury, fibrosis or necrosis. Consistent with this, no changes in organ sizes were observed for all iron overloaded groups (**Appendix Figure 40**). Importantly, additional spaces in the cells' cytoplasm were observed in all iron overloaded mice, suggesting of potential damage, when compared to the healthy untreated group.
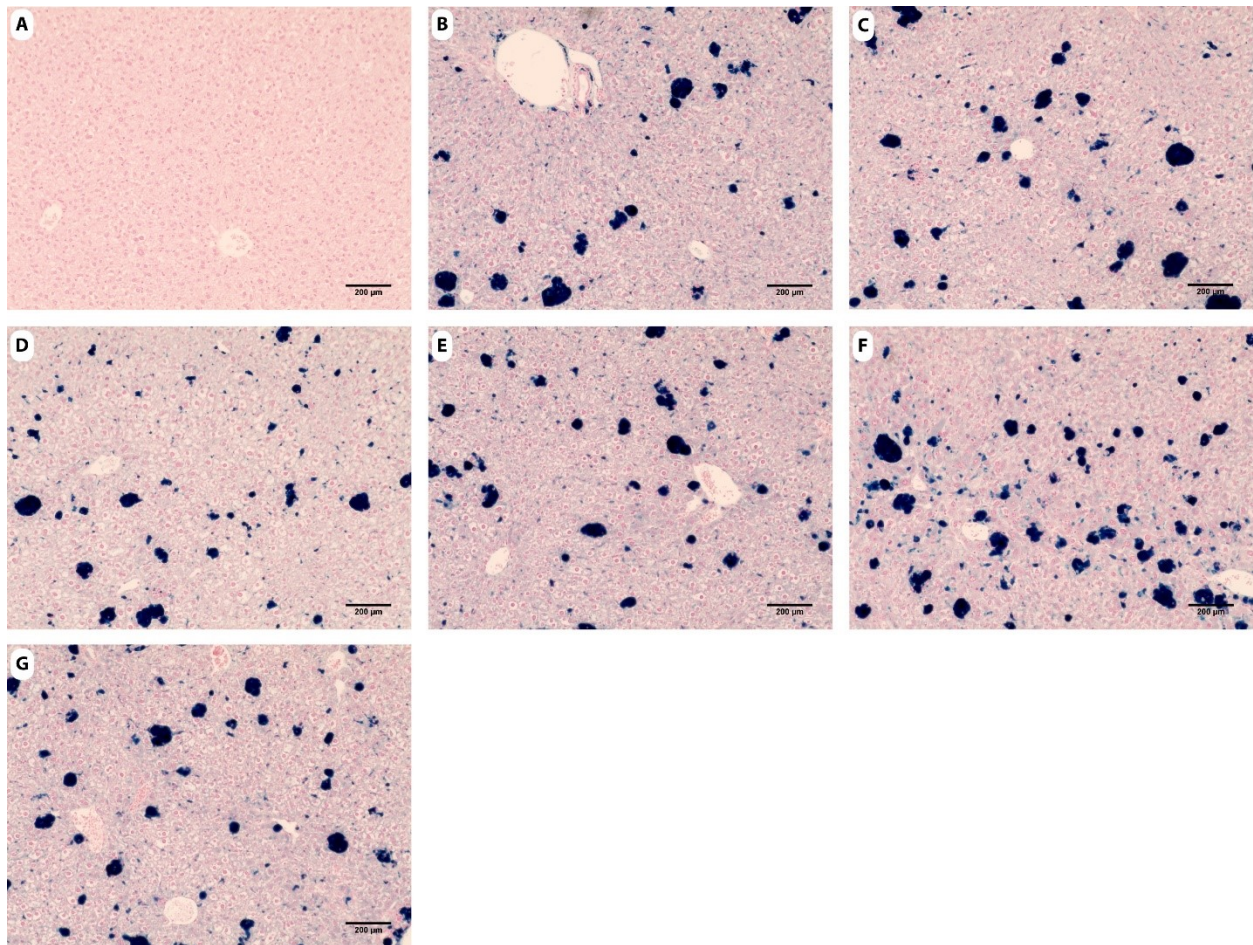
Figure 41. Histological examination of liver in iron overloaded C57Bl/6 mice. Liver sections were stained with Prussian blue to detect iron deposits, counter stained with nuclear fast red. Photomicrographs were acquired at 20X magnificent using EVOS XL Core imaging system. Representative micrographs were shown for (A) non-iron overload healthy control, (B) iron overload saline control, (C) HD-GalNAc, (D) HD-TAG, (E) HD_{40}-GalNAc, (F) HD, and (G) DFO treatment groups.

4.5. Discussion

Hepatic iron burden, along with cardiac iron overload, is a major clinical concern for patients suffering from primary and secondary iron overload as well as other iron induced pathogenesis.[101,102] Iron chelation therapy using Fe(III) specific small molecular chelators have demonstrated efficacy by reducing hepatic iron accumulation in patients over long-term and intense treatment.[131–133139,142131,133,151,152] Despite this, low molecular weight iron chelators are often associated with toxicities, including gastrointestinal discomfort, nausea, agranulocytosis and hepatic fibrosis, due to their non-specific distribution and off-site interactions. In addition, the efficacy of these chelators is undermined by a combination of their short circulation half-lives, mode of administration and patient non-compliance related issues.

Macromolecular approaches circumvent these shortcomings by safely increasing the circulation times for Fe(III) chelators and subsequently improve their chelation efficacy *in vivo*.[167–171] Such strategies use polymers either as polymeric iron chelators[172–174,179–181], small molecular iron chelators conjugated to polymers[182–186,190,197,198] or polymeric nanoparticle formulation of chelators[118,199–204]. The development of these systems focused on using DFO as the Fe(III) chelator because of its hexadentate ligand coordination which avoids the geometric constraints for stable chelation of iron. However, a major limitation for long circulating therapeutics is the non-specific organ accumulation, especially to treat chronic illnesses.[181,183,184,205,206] The clearance of nanoparticle formulations by the reticuloendothelial systems have been implicated in hepatic iron, however, the efficiency of such systems are low.[434] Thus, challenges remain in excretion of hepatic iron selectively because the liver a primary iron storage organ and a key regulator in iron homeostasis. The removal of excess hepatic redox active iron may to protect the liver and to restore iron homeostasis.

Currently, there are no liver targeting strategies for the delivery of DFO. The design and development of liver targeted DFO chelating systems have been detailed in previous chapters. Herein, the chelation efficiencies for these liver targeting DFO systems have been investigated in a mice model.

In order to investigate the chelation performance of liver targeted macromolecular chelators, an iron overload mouse model was optimized for the dose of Fe-Dex needed to induce hepatic iron overloading whilst minimizing toxicities. A parenteral Fe-Dex model was chosen for three reasons. Firstly, Fe-Dex has been used to establish various *in vivo* iron overload models.[435–443] Secondly, parenteral administration offered a convenient and cost-effective method to induce iron overload as compared to enteral

administration or genetic manipulations.[442,444–446] After parenteral administration, Fe-Dex undergoes phagocytosis by macrophages, which process the iron and either export it into circulation or store it within ferritin.[447–449] Fe-Dex has been shown to predominantly accumulate within Kupffer cells however, progressive increase in hepatocyte involvement has been observed; ferritin was mainly found in hepatocytes whereas non-heme non-ferritin complexes were elevated in Kupffer cells.[450,451] Histological examinations revealed periportal and centrilobular accumulation with a mixed pattern of parenchymal and mesenchymal iron deposits, consistent with the redistribution of iron.[450,452–454] Thirdly, parenteral Fe-Dex administrated has been well tolerated in mice with doses ranging from as little as 1 mg per mouse to as high as 200 mg per mouse.[437–440,442,443,454,455]

Given this, appropriate iron loading conditions in C57Bl/6 mice were investigated with respect to changes in the iron burden, in particular the liver iron content, whilst minimizing toxicities (**Figure 34** to **Figure 36**). Mice were treated with either 3 doses or 5 doses of 300 mg/kg Fe-Dex *via* the tail-vein, which meant a total injection of 18 mg or 30 mg of iron respectively. A healthy saline group served as a negative control group. Mice were terminated after 7 days from the last Fe-Dex injection. This was because of two reasons; first, iron redistribution from Kupffer cells to hepatocytes has been reported to occur over time[452,453] and second, Fe-Dex treated mice have been reported to excrete up to 15% of the iron within the first 2 days of iron loading.[455] Therefore, allowing for this additional time, which is also consistent with literature[182,183,187,206,442], may be sufficient to allow for the mice to stably iron overload.

First, changes in the iron burden were compared (**Figure 34** and **Figure 36**). In the liver, the 3 injection group revealed 8.9 mg of iron and the 5 injection group revealed 10.3 mg. In other words, between a third and a half of the injected materials was recovered in the liver, consistent with several other reports.[451] While most of the iron overload mouse models were established using intraperitoneal injections, the hepatic iron loading observed *via* intravenous injections through the tail-vein was higher. For instance, mice injected with a total of 28 mg of iron intraperitoneally resulted in 4 mg of iron / g of liver[437] whereas mice injected with a total of 30 mg of iron intravenously resulted in 8.6 mg of iron / g of liver. Similarly, mice treated with a total of 18 mg of iron intravenously resulted in 5.9 mg of iron / g of liver whereas mice injected with a total of 180 mg of iron intraperitoneally resulted in 15.6 mg of iron / g of liver[454] – despite a 10-fold increase in total iron treatment, the hepatic iron burden only increased 3 fold. On the other hand, other organs also had elevated iron burden. Splenic and renal iron burdens significantly increased in a dose-dependent fashion; the 5 injection treatment group had significantly higher iron burden when compared to the 3 injection treatment group and the saline group, and the 3 injection treatment group

had significantly higher iron contents when compared to saline group. Cardiac iron burden increased significantly only in mice that received 5 injections of Fe-Dex (35 µg) when compared to the saline group (12 µg). Although cardiac function was not imperative in this investigation, C57Bl/6 mice treated with a total of 180 mg of iron per 20 g mouse revealed no cardiac dysfunction or pathological ventricular remodelling, likely due to its genetic background which confers it cardio-protection.[456]

Next, toxicity was monitored by measuring changes in body weight, excrement output, changes in organ sizes and serum ALT activity (**Figure 35** and **Figure 36**). Mice that received a total of 30 mg of iron exhibited the most signs of toxicity. Based on gross observation, this treatment group exhibited a 0.6% change in body weight compared to the 8.7% of the saline group and the 7.4% of the 3 injection group, as well as having significantly reduced excrement output (**Figure 35**). Based on biochemical observations, the 5 injection treatment group showed a 6.6 fold increase in serum ALT activity which was significantly higher than both the saline group and the 3 injection treatment group (**Figure 36**). Notably, both Fe-Dex treatment group had liver hypertrophy which was consistent for Fe-Dex iron overload models.[454] Based on these observations, the 3 injection treatment group was selected as the protocol for iron overloading C57Bl/6 mice.

In conjunction with optimizing the iron overload model, a cost-saving colorimetric assay for the quantification of total iron, *u*-ferene assay, was validated against ICP-MS. **Chapter 5** details the development of this 2-in-1 assay that quantified both labile and total iron. In this chapter, the use of the *u*-ferene assay to the measurement of total iron biological specimens served two purposes; first, the applicability of analyzing more complex tissues by the *u*-ferene assay was compared to the gold standard of elemental analysis, ICP-MS, and second, to provide additional evidence for the feasibility and utility of the *u*-ferene assay (as covered in **Chapter 5**). For the sake of clarity, different biological specimens were loosely categorized in three groups; fluids (blood and urine), organs (liver, spleen, kidneys, and heart) and solid excrement (feces). The total iron determined from the *u*-ferene assay was almost identical to that determined from ICP-MS in all biological specimens (**Figure 37**) – the precision (i.e. standard deviations) of the *u*-ferene assay parallels that of ICP-MS. Additionally, it is worthwhile to note that similar level of sensitivity was achieved, as indicated by the wide range of iron concentrations measured (0 to 1000 µM), principally though acid-cleaned vials, sample manipulation and appropriate dilutions. Taken together, the *u*-ferene assay was utilized for the iron analysis when investigating chelation efficiencies.

Chelation efficacy for liver targeted chelating systems were investigated in the optimized iron overload mouse model. In addition to HD-GalNAc and HD-TAG, HD_{40}-GalNAc systems were synthesized in order to assess the influence of DFO density on its chelation capacity. Iron excretion and changes in the iron burden were quantified (**Figure 40**). Despite the significant liver targeting and the rapid excretion displayed by HD-GalNAc and HD-TAG, only HD-TAG removed 94 µg of iron *via* the urine which was significantly higher when compared to both non-targeted controls (HD and DFO). This may be due to the interplay of DFO density and rapid excretion, which may hinder iron chelation and subsequent removal. It is also possible that HD-GalNAc and HD-TAG may not sequester and reduce hepatic iron because Fe-Dex loading is cleared by Kupffer cells and histology photomicrographs revealed a mixed distribution.[450,451] Remarkably, by increasing the DFO density, HD_{40}-GalNAc significantly reduced the systemic iron burden when compared to both non-targeted controls by removing an average of 5.26 mg of iron. While the pharmacokinetic behaviour of HD_{40}-GalNAc were not investigated, this was the only system to also significantly reduce the hepatic iron burden, by 0.5 mg, when compared to the DFO control. Additional work should focus on the pharmacokinetic behaviour of HD_{40}-GalNAc.

Taken together, these studies provide compelling evidence for the design of liver targeted chelation strategies and suggest the utility of this approach for removing excess iron. Additional experiments are necessary to optimize the balance between DFO density and liver targetability, whilst maintaining relevant tolerability. This should include higher DFO equivalent concentrations for both escalating single dose tolerance as well as repeated dose tolerance. Given the pharmacokinetic behaviours, the liver, kidney and heart toxicity and function should be assayed. Whilst Fe-Dex C57Bl/6 mouse model served as an initial iron overload model, pharmacokinetic investigations and iron chelation in relevant disease mouse models would be invaluable to expand the current understanding as well as shedding light on treatment regimen for this novel class of chelators.

4.6. Conclusions

In summary, an iron overload model was optimized by treating C57Bl/6 mice with 3 doses of 300 mg/kg Fe-Dex on alternating days. The injection schedule and concentrations significantly elevated hepatic iron burden and minimal toxicity as examined by gross observations and biochemical assays. Iron quantification was also confirmed using a colorimetric u-ferene assay and validated by ICP-MS. These studies confirmed the accuracy of the u-ferene assay. Then, HD-GalNAc, HD-TAG and HD$_{40}$-GalNAc were examined for their *in vivo* chelation efficiency and compared with untreated control group as well as non-targeted control groups treated with HD and DFO. Only HD$_{40}$-GalNAc demonstrated significant iron removal and a reduction in the hepatic iron burden, suggesting the necessity to optimize for DFO density on these systems. The mechanism of action for iron chelation are investigated in **Chapter 5**. Taken together, the data supports the pursuit of this novel class of liver targeted chelators and requires additional investigations to better understand the relationship between the ASGPR-specific ligand and DFO densities in order to achieve ideal iron chelation performance *in vivo*.

Chapter 5: Investigation of chelation and mobilization of labile cellular iron using liver targeted macromolecular chelators.

5.1. Overview

The cellular targeting of DFO, using HPG as the polymer scaffold to assemble both ASGPR ligands and DFO, is novel. Previous chapters document important observations in the design and development of these liver targeting macromolecular systems with regards to the identity of ASGPR ligand and its density. Then, optimized systems were characterized for the intracellular trafficking and distribution - all liver targeting macromolecular systems rapidly localized within lysosomes, similar to the intracellular distribution of DFO alone. Moreover, these systems demonstrated improved tolerability, significant hepatic accumulation with improved iron chelation efficacy in mice.

In this chapter, the intracellular interaction of these systems within iron overloaded hepatocytes was examined. This was achieved by developing a novel unified-ferene assay for the colorimetric quantification of both labile and total iron, as well as an optimized iron overload model in HepG2 cells, a hepatocellular carcinoma cell line. Then, the uptake and cytotoxicity of liver targeting macromolecular chelating systems in iron overload HepG2 cells was analyzed and compared to non-iron overloaded cells. In addition, cellular responses to these systems with regards to iron status – both labile and total iron, iron-induced generation of reactive oxygen species (ROS), and subsequent changes in protein expressions, were monitored.

Liver targeting macromolecular chelating systems were well tolerated in both iron overload and non-iron overload HepG2 cells. Despite having a less pronounced uptake in iron overload HepG2 cells when compared to non-iron overload HepG2 cells, these systems reduced both the cellular iron burden as well as the generation of ROS similar to DFO alone. This suggests that liver targeting macromolecular systems gain access to the intracellular iron pool and mitigate iron-induced toxicity, as observed from the generation of ROS. Further, despite liver targeting macromolecular systems increasing the protein expression of transferrin receptor 1, an iron sensitive protein, these changes were milder than with DFO. Additional work is required to better understand the molecular players involved between iron status and the subsequent protein changes.

5.2. Background

Acquired iron, either TBI or NTBI under pathological conditions, enters a transient pool of redox-active iron referred to as the LIP.[53,60–62] This metabolically active iron serves as a cross-roads of metabolic pathways.[62] Our current understanding point to the fact that the pathogenesis of iron-induced diseases is attributed to the combination of increased iron along with prolonged exposure to the redox active LIP, which imparts oxidative damage through the generation of free ROS.[457–459]

The main objective of iron chelation is reduce the iron burden in iron overloaded tissues and subsequently to attenuate the propensity of redox active iron to catalyze ROS. Recently, the EUMDS and ALIVE trial document that LPI were linked to overall survival and non-relapse mortality in MDS and stem cell transplant settings.[460,461] This is achieved by the use of clinically approved chelators including DFO, DFX and DFP. DFO has been used since the 1960s and still remains the current gold standard for the treatment of transfusional iron overload. This chelator is effective in binding to endosomal and lysosomal iron, whereby it reduces the cytosolic labile iron pool and the subsequent generation of ROS.[462–464]

While the use of DFO significantly increased the life expectancy of iron overload patients, DFO suffers from poor pharmacokinetic properties with a narrow therapeutic index leading to severe toxicities and its subcutaneous mode of administrations leads to poor patient compliance, amongst others. Previous work showcase improved chelation efficiency for DFO when conjugated to polymers.[182,183,198]

We designed liver targeting macromolecular chelating systems that improved the pharmacokinetic properties of DFO. In **Chapters 2** and **3**, we demonstrated that these systems targeted to the liver with minimal extrahepatic accumulation, increased fecal elimination and documented its intracellular distribution. In **Chapter 4**, we demonstrated its improved chelation efficacy in an in vivo iron model. In this chapter, we investigated the intracellular chelation and its ability to protect hepatocytes from iron-induced toxicity. We hypothesize that liver targeting macromolecular chelating systems will mitigate the cellular responses to excess redox active iron by chelating intracellular labile iron. In order to do so, we also discuss the development of a method required for the measurement of cellular labile iron.

We first developed a unified-ferene (*u*-ferene) colorimetry assay to accurately quantify both labile and total iron concentrations from the same biological specimen because no such assay exists.

Currently used approaches to quantify total iron in biological samples are atomic absorption spectroscopy (AAS),[465–469] inductively coupled plasma mass spectrometry (ICP-MS),[432,470–472] electron paramagnetic resonance spectroscopy,[473,474] and colorimetric methods.[432,469,472,475–480] Both ICP-MS and AAS are highly sensitive, with ICP-MS enabling iron detection as low as parts per trillion. On the other hand, the quantification of the labile iron pool relies on fluorescent sensors, with an iron binding moiety, that can be investigated *via* confocal scanning laser microscopy or flow cytometry.[60,61,458,459,481–483] The fluorescent-based approaches offer a methodically defined quantification of labile iron which is often difficult to emulate under different circumstances.[70–72,481] Further, these redox active iron (Fe^{+2}) probes suffer from lack of metal ion selectivity,[484,485] requires additional chelators and specific reaction conditions such as acidic solution, and need to account for unwanted quenching of fluorescence in the presence of other metal ions.[486] Moreover, there is minimal to no overlap between total iron and labile iron quantification methodologies – i.e. requiring entirely separate protocols, techniques and instruments.

With the exception of colorimetric methods, all other techniques require special instrumentation, extensive sample manipulation and laborious methodologies. Several groups have made progress towards more accurate determination of iron.[469,472,480] However, most of these methods are handicapped by their application only to total iron, typically *in vitro* conditions. Thus, we developed a convenient and economical benchtop assay that can quantitatively measure labile and total iron content from cell lysates, as well as a wide variety of biological specimens.

Next, we optimized an *in vitro* iron overload cell model with a particular focus on the generation of ROS, and iron status with regards to labile and total iron. It is imperative that this cell model best resembles various cellular functions of unloaded cells in order to best capture its responses to liver targeting macromolecular chelating systems.

Within the literature, the *in vitro* iron overload models established are extremely diverse with regards to (a) hepatic cell lines, (b) iron source and (c) iron treatment conditions; A. Hirsh et al. eloquently highlight the differences in total iron concentrations in HepG2 and Hep3B cells in response to both TBI as well as NTBI,[487] B. various groups have used multiple sources of iron ranging from citrate-[57,487–496], nitriloacetate-[495,497–500] and sulfate-[501–505] complexes and C. various groups have used iron concentrations ranging from as low as 1 μM to as high as 2 mM for as short as 6 h to as long as 7 days.[57,487,489–496,498–504,506] Consequently, these inconsistencies can result in differences in measured outcomes. For instance, comparing the proteomic analysis performed in HepG2 cells loaded with different concentrations of ferrous sulfate by

Fang et al. 2012 and Petrak et al. 2006 yielded differential protein expressions that did not necessarily correlate to the iron concentrations used.[501,502]

Then, we investigated how liver targeting macromolecular chelating systems performed using the optimized iron overload model with regards to uptake, cytotoxicity, iron status – both redox active labile iron and total iron concentration, ROS generation and any subsequent changes in protein expression.

5.3. Methods

5.3.1. Materials

Eagle's Minimum Essential Media (EMEM), Dulbecco's Phosphate Buffered Saline (PBS), Pierce RIPA Lysis Buffer, Trypan blue, 2 mg/mL bovine serum albumin (BSA) standards, cell scrapers, and Pierce Coomasie (BCA) protein assay kit was purchased from Thermo Fisher Scientific. Deferoxamine mesylate, Fetal bovine serum, tissue culture treated 6-well and 48-well cell culture plates, tissue culture treated T25 flasks, ferric ammonium citrate (FAC), calcein acetoxymethyl ester (Cal-AM), ammonium acetate, sodium L-ascorbate, ferene (3-(2-Pyridyl)-5,6-di(2-furyl)-1,2,4-triazine-5',5''-disulfonic acid disodium salt), ICP-MS grade iron standards, and concentrated nitric acid were obtained from Sigma-Aldrich. Fast-prep tubes (2 mL) were purchased from MP Biomedicals, LLC-Fisher. ICP-MS grade concentrated nitric acid was acquired from VWR. 7-AAD solution was acquired from BioLegends. For cellular assay kits, both the DCFDA/H2DCFDA ROS generation kit (ab113851) and the JC-10 mitochondrial membrane potential assay kit (ab112134) were purchased from Abcam, while the MTT assay kit was purchased from ATCC (20-1010K).

5.3.2. Synthesis of liver targeting macromolecular iron chelators

DFO, GalNAc and TAG were conjugated to HPG as outlined in the protocol described in **Chapter 2**. Several conjugates were screened for optimal *in vitro* cellular uptake and binding. These were then selected for DFO conjugation. The properties of these liver targeting macromolecular systems have been outlined in **Table 1** and **Table 2**.

5.3.3. Absorbance measurements

For ferene-based iron detection, all mixtures of samples and standards with ferene-containing working solution were spun at 15,000 G for 5 minutes. Then, the supernatant (200 μL) was transferred into a 96 well plate for absorbance measurements. Absorbance was recorded at 595 nm using a SpectraMax 190 microplate reader from Molecular Devices. Iron concentrations were interpolated from the standard curve generated from the iron standards. These concentrations were normalized to the amount of protein analyzed (i.e., nmole of iron per mg of protein).

5.3.4. Acid digestion of cell lysates

Acid digestions of cell lysates were only performed for the quantification of total iron, as outlined in section 5.3.5.3., to release all iron from stable stores and proteins.[507]

Cell lysates (typically 200 μL, unless specified otherwise) and biological samples were transferred into acid-washed glass vials and dried at 100°C to 120°C. The evaporation of water hastens the digestion of organic samples with nitric acid. Then, all biological samples were digested with concentrated nitric acid (HNO_3) – samples were maintained at 100°C to 120°C and small volumes (0.5 to 1.0 mL) of concentrated nitric acid were repeatedly added over the course of 5 days. All digested samples were dried at 120°C, then cooled to room temperature and weighed. All the required dilutions were performed by mass. Cell lysates were resuspended in 4% HNO_3 (200 μL).

5.3.5. The development of a ferene-based assay for the measurement of iron

A modified ferene assay was developed to analyze the labile and total iron content by manipulating ascorbic acid concentration. This section outlines three subsequent methods for the development of this assay: i) determining iron concentrations in buffer conditions; ii) distinguishing total and labile iron in cell lysates; and iii) distinguishing labile and chelatable iron in cell lysates.

5.3.5.1. Buffers and standards

Preparation of ammonium acetate buffer:

Ammonium acetate buffer (pH 4.5, 2.5M) was prepared using ammonium acetate and glacial acetic acid.

Preparation of iron standards:

Iron standards were prepared from ferric ammonium citrate in 2% nitric acid, ranging from 0 to 1000 μM. These standards are prepared by mass; mass of ferric ammonium citrate and mass of 2% nitric acid are taken into account to determine the concentrations.

5.3.5.2. Determining iron concentrations in buffer conditions

Preparation of analytes and working solution:

Three analytes were prepared with desired concentrations in distilled water;

- (Fe) 100 μM of free iron.

- (DFO-Fe) 100 μM of iron pre-chelated with 2 mM deferoxamine. 100 μM of iron solution in distilled water was incubated with 2 mM DFO for 48 h.

- (DFO) 2 mM free deferoxamine.

Nine working solutions were prepared, each with 5 mM ferene in ammonium acetate buffer (pH 4.5, 2.5 M) with varying concentration of ascorbic acid (0, 1, 5, 10, 25, 50 100, 250, and 1000 mM). All the solutions were filtered (0.2 μm PVDF syringe filter) before use.

Determination of iron concentration:

Iron content of the three analytes was measured in nine different sets of working solutions. A fresh calibration curve was generated using iron standards ranging from 0 to 400 μM for each set of working solution. This has been conveniently outlined in the **Appendix Table 6**.

Each set has analyte (either Fe, DFO-Fe, or DFO) (100 μL) and iron standards (eight samples) (100 μL) in separate Eppendorf tubes. To each Eppendorf tube, ammonium acetate buffer (pH 4.5, 2.5 M) (100 μL) and working solution (100 μL) were added. The resultant solution was vortexed and left overnight at room temperature.

Iron concentrations in different analytes in the presence of varying ascorbic acid concentrations were determined by interpolating from the standard curve generated using iron standards (**Appendix Figure 41**). Calibration curves were generated for nine different ascorbic acid concentrations.

5.3.5.3. Distinguishing total and labile iron in iron overload HepG2 cell lysates

In the context of this, labile iron was defined as iron chelated and detected by ferene using a working solution with a particular ascorbic concentration from undigested samples. Similarly, total iron was

defined as iron chelated and detected by ferene using a working solution with a particular ascorbic concentration from nitric acid digested samples. In order to distinguish labile and total iron, different working solutions with varying ascorbic acid concentrations were investigated

Iron loading cells:

Hepatocarcinoma cell line, HepG2 (ATCC HB-8065) cells with passage numbers between 4 to 9, were seeded at 500,000 cells per well in a 12 well-plate and grown for 2 days. Cells were then loaded with iron; cells were treated with media (0.5 mL) containing 200 μM iron from ferric ammonium citrate (18 mole % iron) each day for 2 days. After 2 days of iron loading, cells were maintained for an additional day in media (0.5 mL) without iron. Prior to any analysis, cells were washed with 2-3 times PBS (0.5 mL).

Cell lysate preparation:

HepG2 cells were scraped, pelleted and washed with PBS (1 mL) thrice at 500 G for 5 minutes. The supernatant was aspirated and cells were lysed in Pierce RIPA buffer (Thermo Fisher Scientific) (at least 300 μL) with intermittent sonication for 20 minutes. After lysis, cell debris was pelleted by centrifuging at 21,000 G for 10 mins. The supernatant was quantitatively transferred into a clean Eppendorf tube for further analysis. Samples were kept at $-80°$C prior to any further analysis.

Protein measurement:

Protein content in cell lysates were measured using the BCA assay, following manufacturer's protocol. Working solution was prepared using reagent A and B at a 50:1 ratio, respectively. BSA standards (10 μL) and cell lysates (10 μL) were added into a 96 well plate. Then, BCA working solution (200 μL) was added to each well. This was kept at 37°C for 30 minutes, then cooled to room temperature for 5 minutes. Absorbance was read at 562 nm. Protein concentrations in cell lysates were interpolated using the standard curve generated.

Measurement of ferene-bound iron:

A set of four working solutions were prepared, each with 5 mM ferene in ammonium acetate buffer (pH 4.5, 2.5 M) with four varying ascorbic acid concentrations (10, 50, 250, and 1000 mM). For labile iron measurements, cell lysates (100 μL) were transferred into separate Eppendorf tubes. For total iron

measurements, nitric acid (100 µL) digested cell lysates (as outlined in section 5.3.4.) were aliquoted into separate Eppendorf tubes. Iron standards (100 µL) were also aliquoted into separate Eppendorf tubes.

Ammonium acetate buffer (pH 4.5, 2.5 M) (100 µL) and working solution (120 µL) were added to all tubes. The samples were vortexed and left overnight at room temperature. The absorbance was measured in the resultant solution (200 µL), as outlined in section 5.3.3.

5.3.5.4. Distinguishing labile and chelatable iron in iron overload HepG2 cell lysates

Cell lysates for both non-iron treated and iron overloaded HepG2 cells were prepared as outlined in section 5.3.5.3. For the purpose of this investigation, chelatable iron is defined as the portion of labile iron that is chelated by iron chelators and subsequently prevents the ferene-based detection of iron using a working solution at a particular concentration of ascorbic acid.

Chelator treatment of iron overloaded cell lysates:

Deferoxamine (DFO), deferiprone (DFP), and deferasirox (DFX) at 50 µM were prepared in PBS. Iron overloaded cell lysates were treated with chelators; iron loaded HepG2 cell lysates (250 µL) were transferred into a clean Eppendorf tube followed by 50 µM chelator (50 µL) – either DFO, DFP or DFX. As negative controls, non-iron loaded and iron loaded HepG2 cell lysates (250 µL) were also transferred into clean Eppendorf tubes followed by PBS (50 µL) only. These were left overnight at room temperature.

Measurement of ferene-based iron:

For labile and chelatable iron: Working solution was prepared with 5 mM ferene in ammonium acetate buffer (pH 4.5, 2.5 M) with 10 mM of ascorbic acid. Cell lysates (100 µL) and iron standards (100 µL) were transferred into separate Eppendorf tubes. ammonium acetate buffer (pH 4.5, 2.5 M) (100 µL) and working solution (120 µL) were added to each tube.

For total iron: Working solution was prepared with 5 mM ferene in ammonium acetate buffer (pH 4.5, 2.5 M) with 1 M of ascorbic acid. Acid digested cell lysates (as outlined in section 5.3.4.) (100 µL) and iron standards (100 µL) were transferred into separate Eppendorf tubes. Ammonium acetate buffer (pH 4.5, 2.5 M) (100 µL) and working solution (120 µL) were added to each tube.

For iron quantification: These tubes were vortexed and left overnight. Absorbance was measured as described in section 5.3.3.

5.3.6. The unified-ferene (*u*-ferene) assay for the measurement of both labile and total iron – the final protocol

A unified-ferene (*u*-ferene) assay was developed to enable a 2-in-1 quantification of both labile iron and total iron in biological samples. In this assay, labile and total iron were defined by their experimental parameters; labile iron was defined as iron detected in undigested biological samples using 10 mM ascorbic acid in the working solution, and total iron was defined as iron detected in nitric acid digested biological samples using 1 M ascorbic acid in the working solution.

This assay has five components, 1. working solution, 2. ammonium acetate buffer (pH 4.5, 2.5 M), 3. iron standards, 4. cell lysates, and 5. absorbance measurements. Section 5.3.6.1. outlines the measurement of labile iron and section 5.3.6.2. outlines the measurement of total iron.

The working solutions:

The working solution is composed of ferene (5 mM) and ascorbic acid (either 10 mM for labile iron measurements or 1 M for total iron measurements) in ammonium acetate buffer. This is summarized in the **Appendix Table 7**. The volume of working solution is determined by a 1:6 molar ratio between iron in the highest standard to ferene at 5 mM in working solution – i.e. when using 100 μL of sample, the working solution is calculated such that there is 6 times more moles of ferene than the moles of iron present in 100 μL of 1000 μM iron standard. Hence, this assay is applicable for investigations requiring larger sample volumes.

Ammonium acetate buffer (see also section 5.3.5.1.):

Ammonium acetate buffer was added at a 1:1 volume equivalence to all biological samples and iron standards, i.e. when using 100 μL samples, 100 μL of buffer was added.

Iron standards (see also section 5.3.5.1.):

When using iron standards for *u*-ferene assay, 1000 μM was used at the highest iron standard. However, the absorbance for this standard exceeded SpectraMax 190 microplate reader's limit of detection and was not accounted for in the analysis.

Cell lysates (see also section 5.3.5.3.):

It is important to highlight that cell lysates were handled differently to quantify labile or total iron. Labile iron measurements in samples do not require nitric acid digestion, whereas total iron measurements require this digestion to release iron from all stores and proteins.

Absorbance measurements: Details are given in section 5.3.3.

5.3.6.1 Labile iron measurement with the *u*-ferene assay

Labile iron concentrations were determined in cell lysates. Samples (100 μL) and iron standards (100 μL) with concentrations ranging from 0 to 1000 μM were transferred into different clean Eppendorf tubes. Ammonium acetate buffer (pH 4.5, 2.5 M) (100 μL) and labile iron working solution (5 mM ferene and 10 mM ascorbic acid prepared in ammonium acetate buffer pH 4.5, 2.5 M) (120 μL) were added to all Eppendorf tubes. This mixture was vortexed and left overnight at room temperature. Absorbance was measured as described earlier in section 5.3.3.

5.3.6.2. Total iron measurement with the *u*-ferene assay

Total iron concentrations were determined in cell lysates. The nitric acid digested samples after their final dilution (200 μL) and iron standards (200 μL) ranging from 0 to 1000 μM were transferred into different clean Eppendorf tubes. 200 μL of ammonium acetate buffer (pH 4.5, 2.5 M) and 240 μL of total iron working solution (5 mM ferene and 1 M ascorbic acid prepared in ammonium acetate buffer pH 4.5, 2.5 M) were added to all Eppendorf tubes. This mixture was vortexed and left overnight at room temperature. Absorbance was measured as described in section 5.3.3.

5.3.6.3. Validation and support for the *u*-ferene assay

Validation of total iron concentrations using inductively coupled plasma mass spectrometry:

Cell samples were nitric acid-digested, as described in section in 5.3.4., and resuspended in 2% HNO_3 with 10 ppb indium (Sigma Aldrich) as the internal standard. Iron standards were also prepared in 2% HNO3 with 10 ppb indium, ranging from 0 ppb to 400 ppb, to generate a standard curve. Iron counts were measured on Agilent 7700 series ICPMS and total iron concentrations were determined from the standard curve. HNO_3 (2%) is used for final dilutions for the longevity of vacuum pumps required by ICP-MS.

Support for changes in the labile iron using Calcein-based labile iron sensor:

Intracellular labile iron was measured using calcein acetoxymethyl ester (Cal-AM), described elsewhere.[508] This is a non-fluorescent dye that readily permeates the cell membrane and becomes fluorescent after intracellular enzymatic modification.[509,510] This fluorophore binds to iron stoichiometrically, which quenches its green fluorescence. [509,510] Cells were washed, trypsinized and pelleted at 500 G for 5 mins. Then, the cells were resuspended in PBS (0.5 mL) with 0.2 μM of Cal-AM for 20 minutes at room temperature. Cellular calcein fluorescence was measured using Beckman Coulter's flow cytometry. At least 10,000 cells were analyzed and fluorescence was measured by the 488 nm laser and the FITC emission filter (530/20 nm).

5.3.7. The optimization of an iron overload HepG2 model

An iron overload HepG2 model was optimized with regards to its iron status and iron-induced toxicity, as measured by the generation of reactive oxygen species (ROS), whilst maintaining cellular functions that most closely resemble non-iron overload HepG2 cells. This protocol was optimized for iron treatment conditions – concentration and duration of loading, using ferric ammonium citrate as the source of NTBI.

5.3.7.1. Cell culture and treatment with ferric ammonium citrate

HepG2 cells with passage numbers between 3 to 10 were used for all experiments. Cells were maintained in EMEM with media changed every 1-2 days. For all iron treatments, ferric ammonium citrate (FAC) was used as the source of iron (18 mole % iron). All concentrations were prepared with respect to iron in EMEM.

For iron loading conditions, HepG2 cells were seeded in 6 wells plates at a density of 400,000 cells per well and grown for 2 days. Cells were treated with media (1 mL) containing either 0, 50, 100, 200, 500 or 1000 µM iron from FAC each day for either 1 or 2 days. After iron loading, cells were washed with PBS (1 mL) thrice. Cell lysates and subsequent total iron analysis were performed, as outlined in section 5.3.6.1.

For iron retention conditions, HepG2 cells were seeded in 6 well plates at a density of 400,000 cells per well and grown for 2 days. Cells were then iron loaded; cells were treated with 200 µM iron in media (1 mL) each day for 2 days. Then, cells were maintained for an additional 0, 1, 2 or 3 days in fresh media (1 mL) without iron with the media replaced daily. Cells were washed with PBS (1 mL) thrice. Cell lysates and subsequent total iron analysis were performed, as outlined in section 5.3.6.2.

5.3.7.2. Optimized protocol to establish an iron overload HepG2 model

The final protocol for establishing an iron overload model in HepG2 was followed; cells were treated with iron-containing media each day for 2 days, followed by maintaining the cells in media without iron for 1 day. To characterize changes in iron-dependent parameters and cellular functions, HepG2 cells were loaded with either 50, 100 or 200 µM.

Characterization of iron-dependent parameters in an iron overload HepG2 model:

For changes in total and labile iron, HepG2 cells were cultured at a density of 500,000 cells per well in a T25 tissue culture flask. After loading cells with iron, cells were washed thrice with PBS (5 mL). Cell lysates were prepared and iron was quantified, as outlined in section 5.3.6.1. and 5.3.6.2.

For changes in ROS generation and calcein-based labile iron, HepG2 cells were cultured in 6 well plates at a density of 400,000 cells per well. After loading cells with iron, cells were washed thrice with PBS (1 mL). Cells were stained and analyzed *via* flow cytometry, as described in section 5.3.7.3.

Characterization of cellular functions in an iron overload HepG2 model:

After being iron overloaded, HepG2 cells were also characterized for their cellular functions including metabolic activity (see MTT assay), mitochondrial membrane potential (see JC-10 assay), membrane integrity (see Trypan Blue assay), and cell viability (see 7-AAD assay), as described in section 5.3.7.3. For the MTT and JC-10 assay, cells were seeded in a 48 well plate at a density of 50,000 cells per well while

for the Trypan blue and the 7-AAD assay, cells were cultured in 6 well plates at a density of 400,000 cells per well.

5.3.7.3. Characterization of cellular functions

ROS generation:

Cellular ROS generation measured using a DCFDA / H2DCFDA kit (Abcam 113851) on Beckman Coulters CytoFLEX Flow Cytometer. Manufacturer's protocol was followed. DCFDA (2',7' –dichlorofluorescein diacetate), a fluorogenic cell permeable dye, undergoes deacetylation by cellular esterases to a non-fluorescent dye. Cellular ROS oxidize this into DCF (2',7' –dichlorofluorescein) which is highly fluorescent, detected in the FITC channel. After washing cells with PBS (1 mL) thrice, cells were stained with 5 μM DCFDA in EMEM and incubated for 20 minutes at 37°C. Then, cells were washed with PBS, trypsinized and pelleted at 500 G for 5 mins. At least 10,000 cells were analyzed *via* flow cytometry and DCF was measured by the 488 nm laser and the FITC emission filter (530/20 nm).

Calcein-based labile iron measurements: Details are given in section 5.3.6.3.

Metabolic activity by MTT Assay:

The MTT (3-(4,5-dimethylthiazolyl-2)-2,5-diphenyltetrazolium bromide) assay (ATCC 20-1010K) was performed according to manufacturer's protocol to investigate changes in metabolic activity. After iron loading, cells were treated with a 10% MTT solution in media (0.5 mL) for 2 h followed by detergent-induced (1 mL) lysis for overnight. Absorbance was measured at 570 nm on SpectraMax 190 Microplate Reader from Molecular Devices. Cell viability was determined; (mean570 nm treated cells / mean570 nm untreated cells) x 100%.

Mitochondrial membrane potential by JC-10 Assay:

The JC-10 mitochondrial membrane potential assay kit (Abcam 112134) was performed to investigate changes in mitochondrial membrane potential. When excited by a 488 nm laser, JC-10 monomers emit at 520 nm whereas JC-10 aggregates emit at 580 nm. JC-10 monomers localize in the mitochondria and aggregate as the membrane potential increases. However, in apoptotic and necrotic cells with perturbed mitochondrial potential, JC-10 does not aggregate. The manufacturer's protocol was followed. Iron

overload HepG2 cells were treated with JC-10 for 30 minutes at 37°C and fluorescence was measured at 490/525 and 540/590 (excitation/emission nm) on a SpectraMax 190 Microplate Reader from Molecular Devices. Mitochondrial membrane potential was determined as follows ((ratio of 520 nm / 590 nm in treated cells) / (ratio of 520 nm / 590 nm in control cells)) x 100%.

Membrane integrity by Trypan blue exclusion assay:

Membrane integrity was investigated using the trypan blue exclusion method, as described elsewhere.[511] Iron overloaded cells were scraped and pelleted, then resuspended in media (1 mL). Cell suspension (10 μL) was gently mixed with trypan blue (HyClone Trypan Blue Stain – Fisher) (10 μL). Live and dead cells were counted using a hemocytometer and percentages were reported; (number of live cells / number of total cells) x 100%.

Cell viability by 7-AAD Assay:

Cell viability was determined with a membrane impermeable 7-AAD (7-amino-actinomycin D, at 50 μg/mL) solution (BioLegend) that fluoresces upon binding to DNA indicative of membrane damage. Manufacturer's protocol was followed. Iron overload cells were scraped, pelleted, and resuspended in PBS (0.5 mL). Cells were incubated with 7-AAD solution (5 μL) per sample for 15 minutes at room temperature. Cells were then analyzed by flow cytometry; at least 10,000 cells were analyzed and dead cells were gated in the APC channel (660/10 nm). Cell viabilities were reported as percentage of live cells (i.e. 7-AAD negative cells).

5.3.8. Uptake and cytotoxicity of liver targeting macromolecular iron chelators

The uptake and cytotoxicity of liver targeting macromolecular chelating systems were investigated in the optimized iron overload HepG2 model. In this model, HepG2 cells were treated with 50 μM of iron-containing media each day for 2 days, followed by maintaining the cells in media without iron for 1 day. In all experiments, untreated non-iron overload and untreated iron overload HepG2 cells were used as negative controls.

5.3.8.1. Binding and uptake of liver targeted polymers in iron overload HepG2 cells

HepG2 cells were seeded at a density of 50,000 cells per well in a 48 well plate and allowed to adhere for 48 h. Media (0.5 mL) was replaced. The next day, cells were iron loaded. Then, cells were treated with fluorescent carboxyrhodamine-tagged liver targeting macromolecular systems (HD-GalNAc and HD-TAG) (0.25 mL) for 2 h at 37°C at varying concentrations ranging from 10 μM to 0.1 nM. After 2 h, cells were washed with PBS (0.5 mL) thrice, trypsinized and pellet at 500 G for 5 mins. Cells were resuspended and incubated in PBS (0.5 mL) with 7-AAD solution (5 μL of 50 μg/mL) for 15 mins at room temperature to identify dead cells. Flow cytometry was used to analyze at least 10,000 cells; carboxyrhodamine positive cells were gated using the FITC emission filter (530/20 nm) and dead cells were gated using the APC emission filter (660/10 nm).

5.3.8.2. Cytotoxicity in iron overload HepG2 cells

HepG2 cells were seeded at a density of 20,000 cells per well in a 96 well plate. Media (200 μL) was replaced on the 3rd day, allowing cells to adhere for 48 h. Cells were then iron loaded. Following this, cells were treated with either liver targeting macromolecular chelating systems (HD, HD-GalNAc, HD-TAG) (200 μL) or small molecular weight chelators (DFO, DFX and DFP) (200 μL) at varying concentrations ranging from 50 μM to 1 nM for 24 h at 37°C. The MTT assay was performed, as described in section 5.3.7.3. Absorbance was measured at 570 nm on SpectraMax 190 Microplate Reader from Molecular Devices. Metabolic activity was reported as absorbance units to showcase the metabolic activity of untreated non-iron overload and untreated iron-overload HepG2 cells.

5.3.9. Mobilization of labile cellular iron and subsequent changes in protein expression

Using the newly developed *u*-ferene assay, cellular responses to liver targeting macromolecular chelating systems were measured in the optimized iron overload HepG2 model. These include changes in labile and total iron, generation of ROS and change in protein expression.

5.3.9.1. Cell culture and iron loading

HepG2 cells were seeded at a density of 500,000 cells per T25 flasks and allowed 48 h to adhere. The next day, media (5 mL) was replaced. Cells were then iron loaded with 50 μM of iron-containing media (5 mL) each day for 2 days, followed by maintaining the cells in fresh media (5 mL) for 1 day. Before treatment,

cells were washed with PBS (5 mL) once. Negative controls included untreated non-iron overload and untreated iron overload HepG2 cells. These experiments were done in triplicate.

5.3.9.2. Chelator treatment

Iron overloaded HepG2 cells were treated with 15 μM chelators (5 mL) prepared in media for 48 h; HD, HD-GalNAc, HD-TAG, deferoxamine (DFO), deferiprone (DFP) and deferasirox (DFX). Untreated non-iron overloaded and untreated iron overloaded HepG2 cells were used as negative controls. Cells were washed thrice with PBS (5 mL) and analyzed for ROS generation, changes in labile and total iron, and changes in transferrin receptor 1 expression – as outlined below. After treatment, cells were washed thrice with PBS (5 mL), scraped and pelleted at 500 G for 5 mins.

5.3.9.3. Iron measurement using the *u*-ferene assay:

Labile and total iron concentrations were quantified using the unified-ferene assay. Cell lysates were prepared and protein concentrations were determined as described in section 5.3.5.3. There were a total of eight cell lysates and these include two controls (non-iron and iron overload HepG2 cells), three macromolecular systems (HD, HD-GalNAc and HD-TAG) and three small molecular weight (DFO, DFP, and DFX). Iron standards were also prepared from FAC in 4% nitric acid, ranging from 0 to 1000 μM, as described in section 5.3.5.1. Labile iron and total iron in the cells were measured as described previously (section 5.3.6.1. and 5.3.6.2.)

5.3.9.4. Generation of ROS: (See also section 5.3.7.3.)

After pelleting cells, cells were resuspended in media (1 mL) 5 μM DCFDA and incubated for 15 minutes at room temperature. Then, cells were washed with PBS at 500 G for 5 mins. At least 10,000 cells were analyzed *via* flow cytometry and DCF was measured by the 488 nm laser and the FITC emission filter (530/20 nm).

5.3.9.5. Changes in protein expression using Western Blots

Similar to iron measurements, transferrin receptor 1 (TfR1) and asialoglycoprotein receptor (ASGPR) expressions were investigated in all lysates through western blots, as described elsewhere.[512] GAPDH protein expression was also investigated because this is a house-keeping protein and serves as a protein-

loading control. Proteins were separated in a 10% sodium dodecyl sulfate polyacrylamide gel and transferred to a nitrocellulose membrane, using Bio-Rad's vertical electrophoresis cell. The membrane was blocked in 10% skim milk to prevent non-specific adsorption of proteins.

A two-step fluorescent immunostaining approach was used. First, monoclonal mouse anti-human TfR1 antibody (H68.4 Thermofischer), anti-human ASGPR antibody (Santa Cruz) and anti- human GAPDH antibody (Cell Signalling Technology) were incubated at 3 μg/mL overnight at 4°C overnight. Then, donkey anti-mouse IgG antibody tagged with an infrared dye 700 (LI-COR) was incubated at 1:10,000 dilution for 4 h at room temperature.

The nitrocellulose membranes were imaged using LI-COR at the following settings; resolution was set at 169 μm, medium image quality, 700 nm channel at intensity of 5, and scan area large enough to cover the membrane. The western blot was analyzed using LI-COR's Odyssey Application Software 3.0. Data was first normalized to the house keeping protein GAPDH, and then represented relative to the control cells; (ratio of TfR1:GAPDH in treated cells) / (ratio of TfR1:GAPDH in control cells). ASGPR was not normalized because the signal to noise ratio was not adequate.

5.3.10. Statistical analyses

All data were performed in at least independent triplicate and presented with error bars that correspond to standard deviation. Technical replicates were also performed, but only independent triplicates were used for statistical analysis. All statistical analyses were performed using GraphPad Prism 7 (Grahpad Software, San Diego, USA). The statistical tests and appropriate multiple comparison tests were outlined in the figure legends.

5.4. Results

5.4.1 The development of the *u*-ferene assay for labile and total iron determination

5.4.1.1 The role of ascorbic acid in iron content measurement by the ferene assay

In order to measure iron using the ferene assay, Fe(III) should be reduced to Fe(II), typically by ascorbic acid, followed by the bidentate chelation of Fe(II) by ferene to form a stable blue complex between pH 3 to 6, with a molar absorptivity of 34,500 L cm^{-1} mol^{-1}.[480,513] In addition to ascorbic acid being a potent reducing agent, the concentration of ascorbic acid has strong influence on the decomplexation iron complexes in the analyte (DFO-Fe). DFO is a hexadentate iron chelator with a pFe^{3+} of 26 and was used to investigate the significance of ascorbic acid in iron content measurement by the ferene assay.[514–516] First, the ascorbic acid concentration was optimized in both buffer and *in vitro* conditions; iron was measured in three analytes – 100 µM of free iron (Fe), 2000 µM DFO only (DFO), and 100 µM iron pre-chelated with 2000 µM DFO (DFO-Fe) – using a working solution composed of 5 mM ferene in ammonium acetate buffer and varying concentrations of ascorbic acid **(Figure 42A)**.

At concentrations of ascorbic acid lower than 10 mM, there is a significant difference between iron concentrations measured in Fe analyte and DFO-Fe analyte, $p < 0.0001$ at all concentrations. In other words, there is a significant difference between the iron measured in the two analytes. Interestingly, at ascorbic acid concentrations of 50 mM and above, the iron concentrations measured by ferene in Fe and DFO-Fe are not significantly different. DFO only samples show no detection of iron, as expected. It is evident that the concentration of ascorbic acid plays a strong role on the removal of iron from DFO-Fe complex. This observation is of particular interest because it warrants further investigation into the utility of ascorbic acid concentration to discern between labile and total iron with the biological context – labile iron is redox active iron and total iron is all iron, both redox active and inactive.
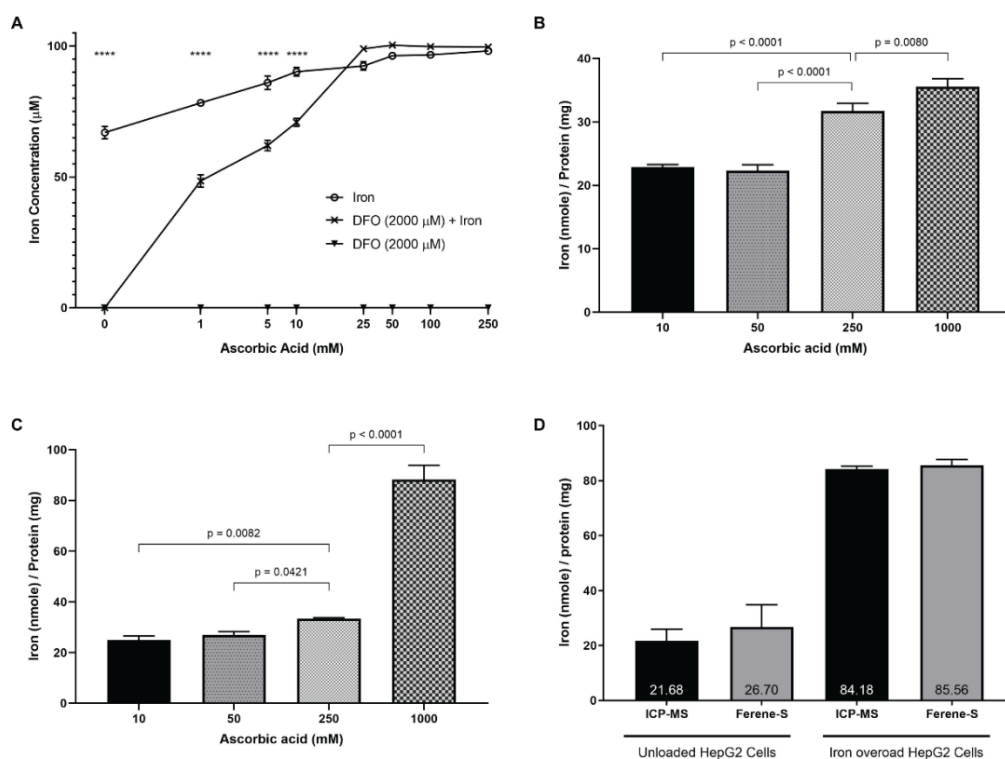
Figure 42. The effect of changing the working solution's ascorbic acid concentration on the measurement of ferene-chelatable iron. (A) Changes in OD 595nm were measured for three analytes, 100 μM of iron, either free or pre-chelated with 2000 μM deferoxamine (DFO), when changing ascorbic acid. A concentration dependent increase in iron concentration was observed for iron pre-chelated with DFO. A two-way ANOVA was performed with Dunnett's correction, using GraphPad Prism. **** represents $p < 0.0001$ (B) Labile iron pool, "LIP", was quantified in iron overload HepG2 cell lysates. Ascorbic acid concentrations in the working solution were varied from 10 mM to 1 M. In LIP measurements, there was a significant increase in the detection of labile iron when using 250 mM ($p < 0.0001$) and 1 M ($p = 0.0080$). (C) Total iron was quantified in the same cell lysates after digestion with nitric acid. Ascorbic acid concentrations also varied form 10 mM to 1 M. In total iron measurements, there was a significant increase in iron concentration when using 250 mM ($p = 0.0421$) and 1 M ($p < 0.0001$) ascorbic acid. One-way ANOVA was performed with Dunnett's correction using GraphPad Prism. (D) Total iron was quantified using both ICP-MS and the *u*-ferene assay in unloaded and iron overloaded HepG2 cells. Similar results were obtained for both ICP-MS and the *u*-ferene assay; no significant difference was observed between either the control or the iron overload cells. All experiments were done in at least triplicate. Error bars show standard deviation. Statistical analyses were performed using GraphPad Prism.

5.4.1.2. The role of ascorbic acid in labile and total iron content measurement by the ferene assay

Next, the role of ascorbic acid was investigated to distinguish the measurement of labile and total iron from cell lysates using the ferene assay. HepG2 cells were iron loaded and lysates were prepared. Labile and total iron was measured in cell lysates before **(Figure 42B)** and after **(Figure 42C)** nitric acid digestion, respectively, since nitric acid digestion is required to release all stably stored iron.[507] Four different working solutions were used to measure iron content, constituting of 5 mM ferene and varying ascorbic acid concentrations (10, 50, 250 and 1000 mM). It is important to highlight two things; first, only iron that is chelated by ferene enables iron measurement and that ferene chelatable iron is dependent on the ascorbic acid concentration present in the working solution, and second, cellular iron concentration is reported as a ratio of iron concentration to protein concentration rather than iron concentration alone[503,517,518] or relative to the number of cells[472,498,519–521]. We anticipate that protein concentrations better accounts for fluctuations associated with handling cells and reflect changes due to cell death.

In iron overload cell lysates without nitric acid digestion, no difference was observed in the ferene-based iron detection from working solutions with 10 mM or 50 mM ascorbic acid. However, significantly more iron was quantified as ascorbic acid concentration increased from 50 mM to 250 mM and then from 250 mM to 1000 mM ($p < 0.0001$ and $p = 0.0080$, respectively). This increase is suggestive of iron being released from other iron complexes in the undigested cell lysates. Therefore, accounting for the observations made from **Figure 42A** – 10 mM yields a significant difference in iron detection when comparing free iron and pre-chelated DFO iron, while not being significantly different in iron overloaded cell lysates **– we can define labile iron as iron measured in undigested samples by 5 mM ferene using a working solution with 10 mM ascorbic acid.**

In iron overload cell lysates that underwent nitric acid digestion, total iron concentration significantly increased when comparing working solutions with 50 mM and 250 mM ascorbic acid, and again when comparing 250 mM and 1000 mM ascorbic acid ($p = 0.0421$ and $p < 0.0001$). The requirement for high ascorbic acid concentration is likely due to two reason; first, more iron is available after acid-digestion, and second, more of this iron is present in the ferric form which needs to be reduced. Taken together, we can define total iron as iron measured in acid-digested samples by 5 mM ferene using a working solution with 1 M ascorbic acid. This is further corroborated by ICP-MS analysis of these samples, which shows no significant differences in the total iron measurements **(Figure 42D)**.

5.4.1.3. Distinguishing "labile" and "chelatable" iron using a 2-in-1 *u*-ferene assay

To investigate the measurement of labile iron and chelatable labile iron, iron overload HepG2 cells lysates were prepared, followed by treatment with clinically approved iron chelators – DFO, DFP and DFX – at 50 µM, in excess of the labile iron concentration, overnight **(Figure 43)**. Chelatable labile iron is defined as the portion of the labile iron that is chelated by the iron chelators. Labile iron in cell lysates was measured using the labile iron protocol (described in section 5.3.5.4.). DFO and DFP treatment displayed a significant decrease in labile iron when compared to the untreated iron overloaded cell lysates ($p < 0.0001$ and $p = 0.0431$, respectively) **(Figure 43A)**. Total iron was measured using the total iron protocol (described in section 5.3.5.4.) and, as expected, no significant changes were observed **(Figure 43B)**. Further, there is reproducibility of the total iron content with previous experiments, as shown in **(Figure 42C)**, and ICP-MS, **(Figure 42D)**. Of great importance, the data highlighted the importance of ascorbic acid concentration to differentiate between total and labile iron, as well as chelatable iron with respect to different chelators (**Appendix Figure 42**).
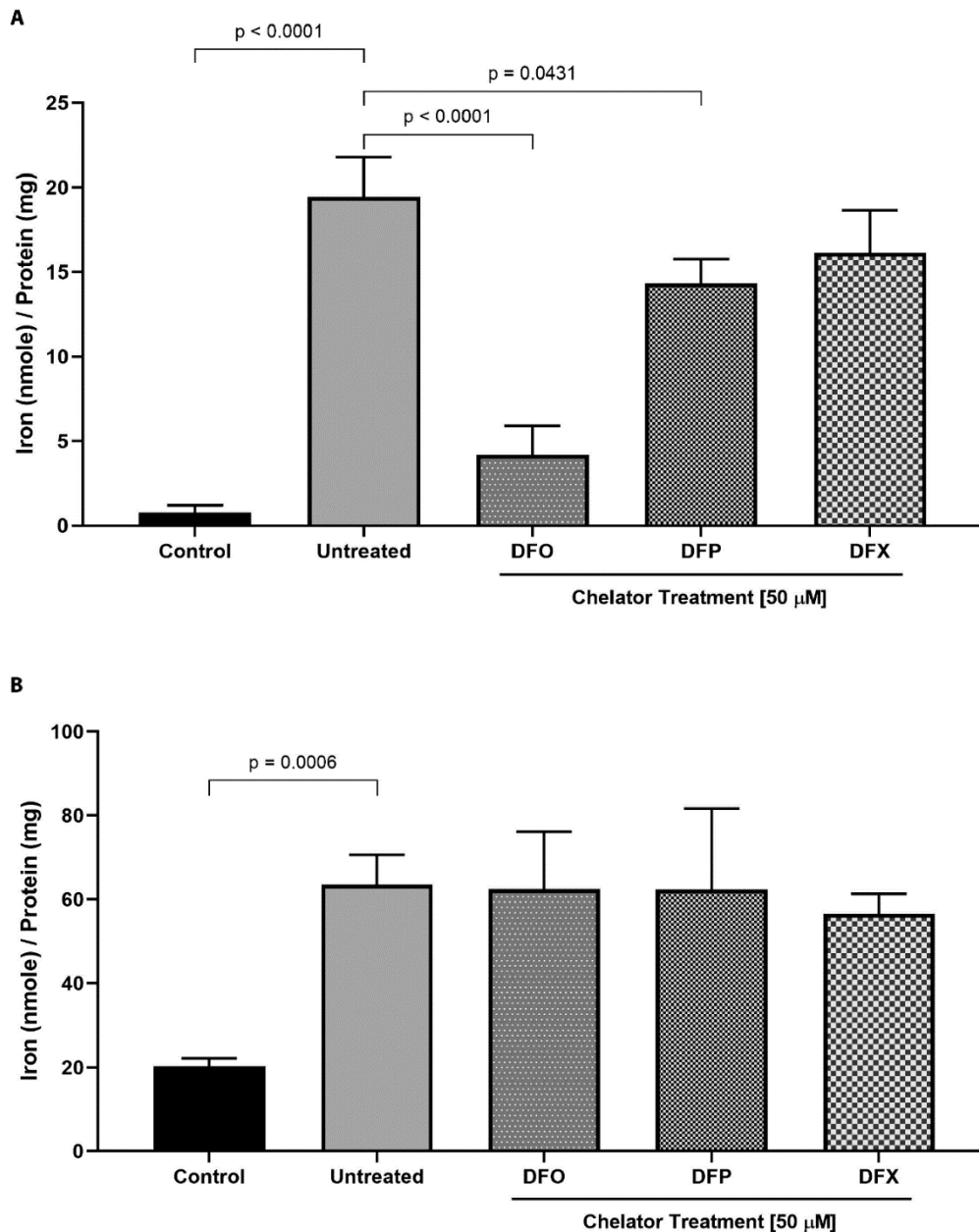
Figure 43. The confirmation of measuring chelatable labile iron *in vitro*. HepG2 cells were loaded with 200 μM of iron using FAC. Cells were lysed and these lysates were treated with either deferoxamine (DFO), deferiprone (DFP) or deferasirox (DFX) at 50 μM overnight. (A) LIP was measured using 5 mM ferene and 10 mM ascorbic acid in lysates. (B) In total iron measurements, cell lysates were first digested with concentrated nitric acid at 100°C to 120°C followed by the ferene-based assay for total iron (5 mM ferene and 1 M ascorbic acid). One-way ANOVA was performed with Tukey's correction using GraphPad Prism.

5.4.2. The development and validation of the iron overload HepG2 cell model

5.4.2.1. Establishing an iron overload HepG2 model:

A protocol to establish an iron overload model in hepatocytes, using HepG2 cells and FAC as the source of NTBI, was optimized. The *u*-ferene assay was extensively utilized to quantitate cellular iron status for both labile and total iron. First, the experimental conditions required to iron load HepG2 cells was explored **(Figure 44A and B)**. Cells were treated with varying concentrations of iron every 24 h for either 24 h or 48 h. HepG2 cells treated with iron, for either 24 or 48 h, had significantly higher total iron concentration when compared to non-iron treated cells; 24 h iron treatment resulted in $p = 0.0005$, $p = 0.0009$ and $p = 0.0009$ for 100, 200 and 1000 μM respectively, and 48 h iron treatment resulted in $p < 0.0001$ at all concentrations.

Iron loading was dependent on the duration of treatment rather than iron loading concentration. When comparing the different iron loading concentrations at either 24 h or 48 h, no significant difference was observed between 100, 200 or 1000 μM iron containing media. However, cells treated with 100, 200 and 1000 μM for 48 h yielded significantly higher total iron concentration than the cells treated for 24 h ($p < 0.0001$, $p < 0.0001$ and $p < 0.0001$, respectively). For instance, HepG2 cells had a total iron concentration of 46.3 nmole per mg protein after 24 h compared to 83.7 nmole per mg protein after 48 h.

Then, the duration of iron retention was investigated **(Figure 44C)**. HepG2 cells were loaded with 200 μM every 24 h for 48 h. Then, these cells were maintained in fresh media for up to 3 days with media being replaced every day. Total iron concentration did not change even up to 72-h post-loading.

The final protocol to establish an iron overload HepG2 cell model required the cells to be loaded with iron every 24 h for 48 h followed by 24 h of maintenance in fresh media.
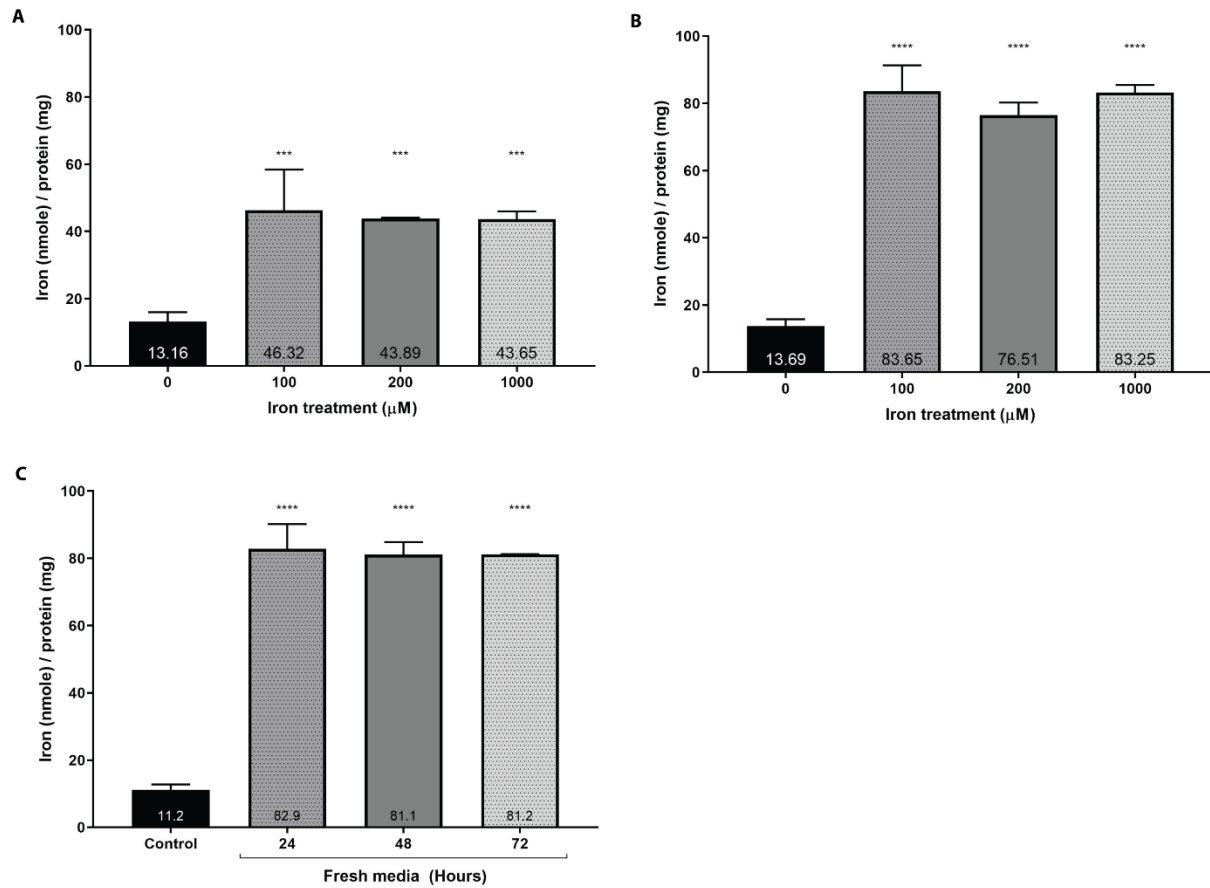
Figure 44. The effect of iron concentration and treatment time on establishing an iron overload HepG2 cell model. (A & B) HepG2 cells were treated with varying concentrations of iron (100 to 1000 µM) either once in 24 h (A) or twice in 48 h (B). (C) HepG2 cells were first treated with 200 µM every 24 h for 48 h. Then, these cells were maintained in fresh media without iron for up 72 h with media being changed every 24 h. Total iron was analyzed using u-ferene assay described previously. Error bars show standard deviation from 3 independent replicates. One-way ANOVA with Dunnett's correction method were performed to compare differences against the control or unloaded cells. One-way ANOVA with Sidak's correction method was performed to compare the iron loading with 24 h or 48 h treatment. **** represent $p < 0.0001$ and *** represents $p < 0.0010$. All statistical analyses were performed using GraphPad Prism.

5.4.2.2. The effect of iron concentrations on cellular iron responses:

Iron overload HepG2 cells were established using different iron loading concentrations (50, 100 and 200 μM) using the optimized protocol to investigate changes in iron response **(Figure 45)** and cellular functions **(Figure 46)**. Cellular iron responses were examined for changes in labile iron concentration **(Figure 45A and B)**, total iron concentration **(Figure 45C)**, and ROS generation **(Figure 45D)**. Iron treated cells showed a concentration-dependent increase in the labile iron pool (LIP). There was a significant increase in the LIP quantified by the *u*-ferene assay when comparing unloaded cells to cells loaded with 50 μM iron or cells loaded with 50 μM iron compared to 200 μM iron (p = 0.0066 and p = 0.0010, respectively). This dose-dependent increase in the LIP was further corroborated by the calcein-based fluorescent assay; calcein fluorescence reduced as it bound to labile or redox active iron. The significant reduction in calcein-based fluorescence between control cells and 50 μM iron overloaded cells and between 50 μM and 200 μM iron overloaded cells (p = 0.0001 and p < 0.0001, respectively) supports the observation of increasing labile iron concentration.

Similar to iron loading investigations **(Figure 44A)**, there was an increase in total iron concentration when cells were treated with 50, 100 and 200 μM of iron-containing media compared to controls (p = 0.0165, p = 0.0030 and p = 0.0006, respectively). Further, there was no appreciable differences in total iron loading amongst iron treated cells treated with different concentrations, highlighting the reproducibility of establishing a HepG2-based iron overload cell model.

Interestingly, the concentration-dependent trend in labile iron concentration was not observed for ROS generation **(Figure 45D)**. There was a significant increase in ROS mediated median fluorescence intensity when comparing non-loaded cells to iron loaded cells – p = 0.0010, p = 0.0006 and p = 0.0006 for cells loaded with 50, 100 and 200 μM iron, respectively. However, there was no significant difference when comparing iron overloaded cells at any loading concentration tested. Despite increasing labile iron concentration, ROS generation did not increase with respect to increasing iron loading concentrations.
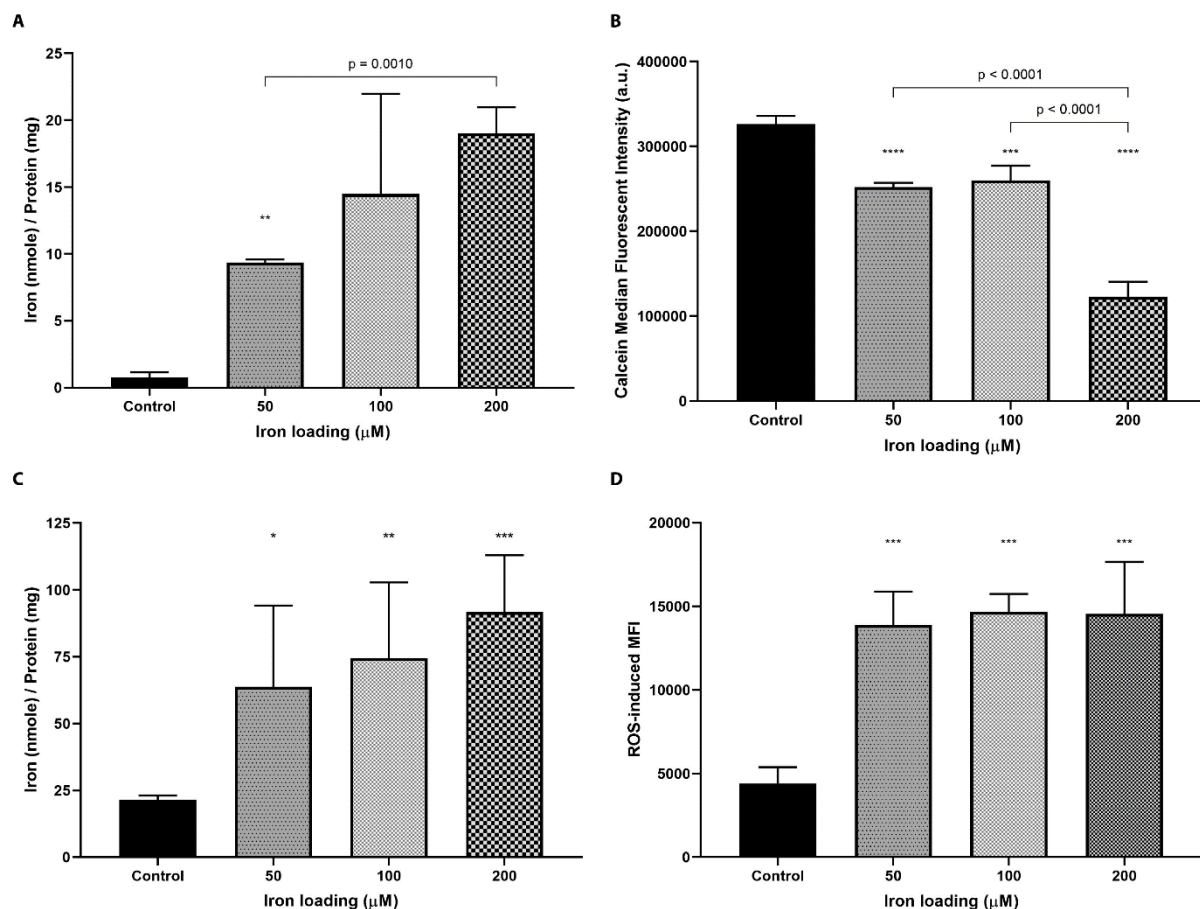
Figure 45. The effect of varying iron loading concentrations (50 to 200 μM) on labile iron, total iron and the generation of reactive oxidative species (ROS) in HepG2 cells. (A) Labile iron was quantified using the *u*-ferene assay. One-way ANOVA with Sidak's correction method was used to compare iron-loaded cells with control cells. (B) Changes in the intracellular labile iron pool was monitored *via* fluorescence. Calcein fluorescence is quenched in the presence of iron. One-way ANOVA with either Sidak's or Dunnett's correction method was used to compare iron loaded cells with control cells. (C) Total iron was quantified using the *u*-ferene assay. One-way ANOVA with Dunnett's correction method was used to compare iron loaded cells with control cells. (D) ROS generation was measured using a DCFDA/DCF ROS kit in at least 10,000 HepG2 cells *via* flow cytometry. One-way ANOVA with Dunnett's correction method was used to compare iron loaded cells with control cells. Error bars show standard deviations for 3 independent replicates. Statistical analyses were performed using GraphPad Prism. **** represent $p < 0.0001$, *** represents $p < 0.0010$, ** represents $p < 0.0100$ and * represents $p < 0.05$.

5.4.2.3. Characterization of cellular function in response to varying iron loading concentration.

Measures of cellular function were characterized in iron overloaded HepG2 cells. Cell viability was measured as a function of either nuclear or plasma membrane integrity **(Figure 46A and B)**. In both cell viability assays, HepG2 cells loaded with 50 μM iron showed no significant differences when compared to control (non-iron loaded cells). Any iron loading concentration above 100 μM yielded a significant increase in either nuclear or plasma membrane permeability when compared to controls ($p < 0.0001$ for all comparisons). Mitochondrial membrane potential was measured through the JC-10 assay, which takes advantage of the different fluorescent emissions when cells become apoptotic **(Figure 46C)**. HepG2 cells loaded with iron at 500 μM or 1000 μM had significantly perturbed the mitochondrial membrane potential when compared to control ($p < 0.0001$ for both). No significant alterations in cells loaded with 50, 100 or 200 μM iron were observed. Metabolic activity was observed through the MTT assay which measures the rate of MTT conversion to formazan salt by intracellular enzymes, including dehydrogenase enzymes **(Figure 46D)**. All iron overloaded HepG2 cells yielded significantly lower metabolic activities when compared to the control ($p < 0.0001$ for all comparisons). Taken together, HepG2 cells loaded with 50 μM were similar to control cells with respect to nuclear membrane integrity, plasma membrane integrity and mitochondrial membrane potential. As iron loading concentration increased, particularly at 200 μM or higher, cellular functions were significantly different to iron overload cells loaded with lower iron concentrations.

Iron overload HepG2 cells treated with 50 μM of iron from FAC has been well characterized; there are significant increases in iron-dependent parameters whilst maintaining cellular function comparable to that of untreated HepG2 cells. The cellular responses to liver targeting macromolecular chelating systems were investigated in this model. First, uptake and cytotoxicity were investigated, followed by changes in iron-dependent parameters including mobilization of intracellular iron and the mitigation of iron overload response.
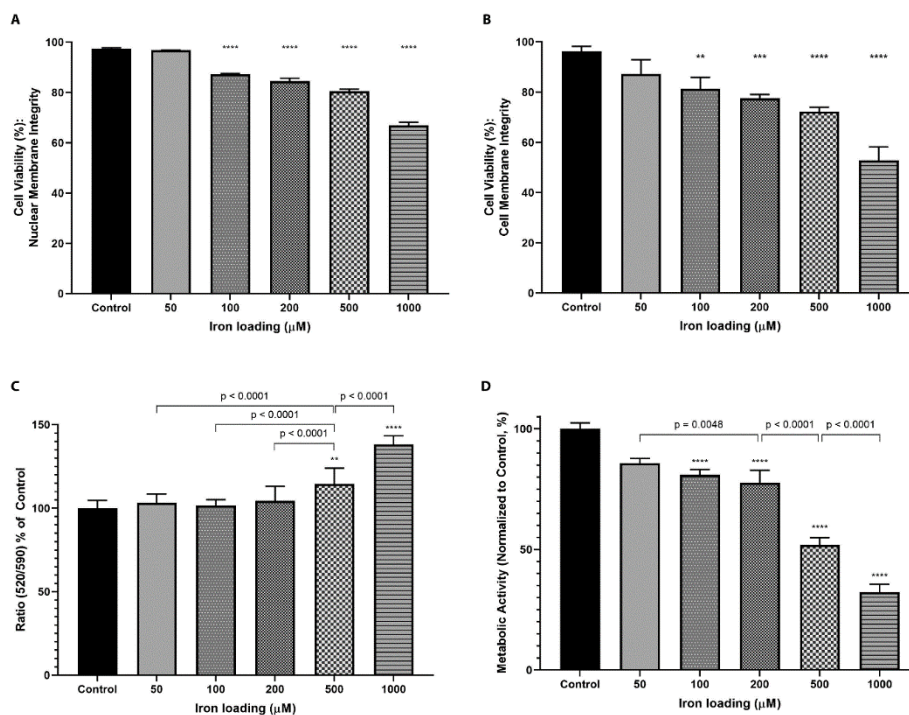
Figure 46. Characterization of cellular functions of HepG2 cells loaded with varying iron concentrations (50 to 200 μM). (A) Cell viability was measured using a membrane impermeable 7-aminoactinomycin D (7-AAD) *via* a flow cytometry, analyzing at least 10,000 cells. 7-AAD binds to DNA and the fluorescence is detected in PC5.5 channel (710/50 nm). One-way ANOVA with Dunnett's correction method were performed to compare iron loaded cells with control cells. (B) Cell membrane integrity was measured using the Trypan blue (TB) exclusion assay. This dye is membrane impermeable. Cells with or without TB uptake were counted using a hemocytometer. One-way ANOVA with Dunnett's correction method was performed to compare iron-loaded cells with control cells. (C) Mitochondrial membrane potential was measured using the JC-10 assay kit using a plate reader. The ratio of fluorescence emitted at 590 nm and 540 nm were normalized to control cells. One-way ANOVA with Dunnett's correction method were performed to compare iron loaded cells with control cells. Similarly, one-way ANOVA with Dunnett's correction method was performed to compare iron loaded cells with cells loaded with 500 μM. (D) Metabolic activity was measured using the MTT assay using a plate reader. One-way ANOVA with Dunnett's correction method was performed to compare iron loaded cells with control cells. One way ANOVA with Tukey's correction was also performed to compare different iron loaded cells with each other. Error bars show standard deviations for 3 – 6 independent replicates. All statistical analyses were performed using GraphPad Prism. **** represents p < 0.0001, *** represents p < 0.0010, and ** represents p < 0.0100.

5.4.3. Application of the *u*-ferene to evaluate iron chelation efficiency.

5.4.3.1. The uptake and cytotoxicity of liver targeting macromolecular chelating systems in the iron overload HepG2 model

The uptake of liver targeting macromolecular chelating systems was examined in iron overload HepG2 cells, loaded with 50 μM iron, and compared to non-iron overloaded HepG2 cells **(Figure 47A)**. The uptake of HD-GalNAc and HD-TAG was less in the iron overloaded HepG2 cells compared to normal cells; there was significantly higher uptake of HD-GalNAc starting at 0.2 μM (****$p < 0.0001$) and HD-TAG at 10 μM (####$p < 0.0001$) in non-iron overloaded HepG2 cells.

Further, changes in metabolic activity were measured in iron overloaded HepG2 cells treated with either macromolecular chelators (HD, HD-GalNAc and HD-TAG) **(Figure 47B)** or small molecular weight chelators (DFO, DFX and DFP) **(Figure 47C)** over a range of chelator-equivalent concentrations. With the exception of DFP, all chelators were well tolerated by iron overloaded HepG2 cells such that the metabolic activity remained at 80% or above (equivalent to 0.75 arbitrary absorbance units) up to a chelator concentration of 1.4 μM. At 8.3 μM of chelators, DFO and DFX showed a significant decrease in metabolic activity when compared to macromolecular chelators ($p < 0.0001$ for both), which remained at 80% or above. At 50 μM, all chelator-treated cells showed a decrease in metabolic activity; HD-GalNAc and HD-TAG had an average of 50% metabolic activity whereas HD, DFO, DFX and DFP had less than 1% of metabolic activity. Liver targeting macromolecular chelators (HD-GalNAc and HD-TAG) were significantly better than HD and small molecular weight chelators ($p < 0.0001$ for all comparisons). DFP had metabolic activity below 80% at all concentrations, with a concentration dependent decline. It is worthwhile to mention that there was a decrease in metabolic activity when HepG2 cells become iron overloaded, and that chelator treatment did not reverse this.
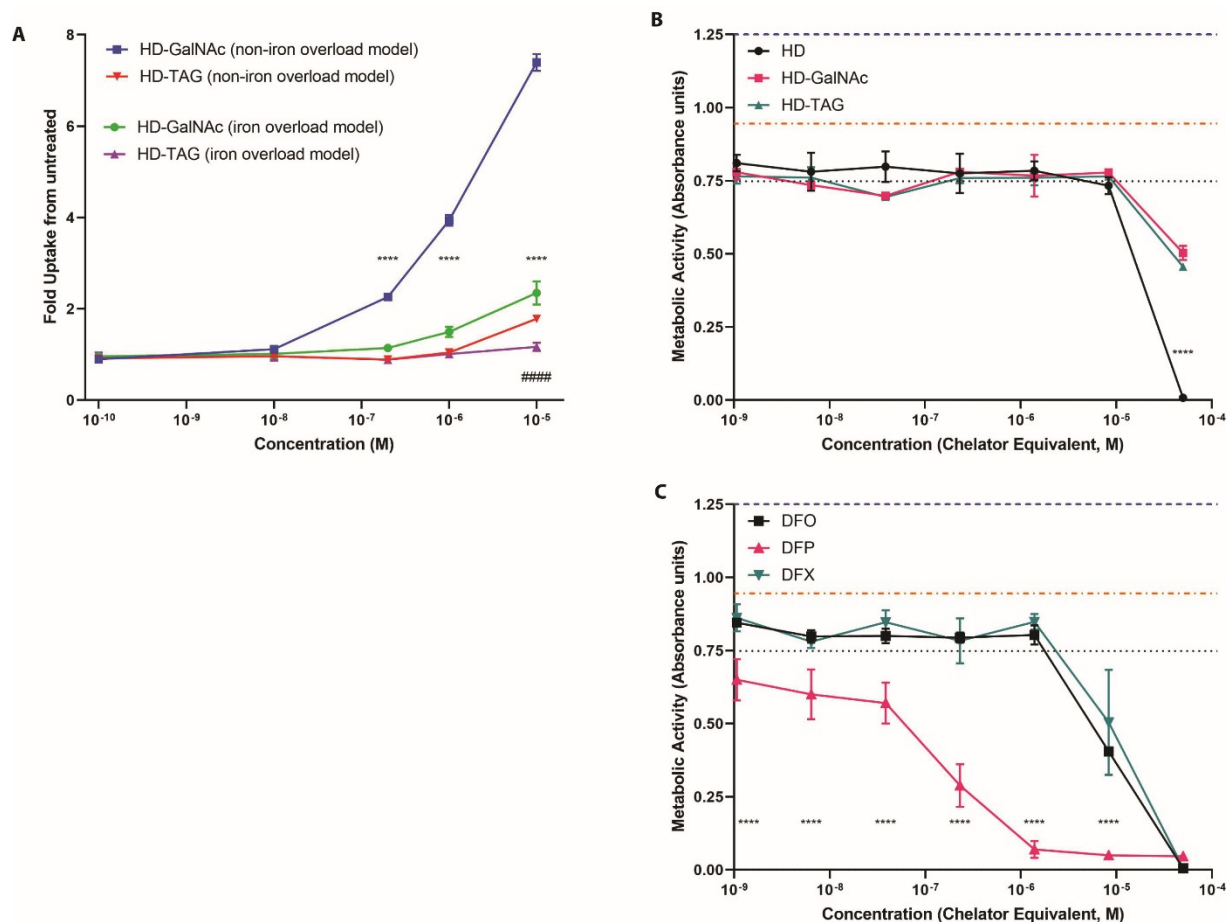
Figure 47. The uptake and cytotoxicity of liver targeting macromolecular chelating systems in iron overloaded HepG2 cells. (A) The uptake of fluorescently tagged liver targeting macromolecular systems was analyzed in at least 10,000 cells *via* flow cytometry. The metabolic activity was measured by the MTT assay using a plate reader in iron overloaded cells treated with either macromolecular chelators (B) or small molecular weight chelators (C). The blue dashed line at 1.25 absorbance units refer to the metabolic activity in untreated non-iron overload HepG2 cells. The orange speckled line at 0.94 absorbance units refer to the metabolic activity in untreated iron overload HepG2 cells. The black dotted line at 0.75 absorbance units refers to the metabolic activity at 80% of untreated iron overload HepG2 cells. HepG2 cells were loaded with 50 µM of iron following the established protocol. Error bars show standard deviation of 3 independent replicates. Two-way ANOVA with Sidak's correction method was performed to compare either uptake or metabolic activity at a particular concentration between iron overloaded cells and non-iron overloaded cells. Statistical analyses were preformed using GraphPad Prism. **** and #### represents $p < 0.0001$.

5.4.3.2. Iron-dependent cellular responses to iron chelation in the iron overload HepG2 model

Iron overloaded HepG2 cells were treated with 15 μM of small molecular weight chelators – DFO, DFX or DFP, or with 15 μM chelator equivalent of macromolecular systems - HD, HD-GalNAc, or HD-TAG. The reported clinically-relevant steady state concentration of DFO is between 10 to 28 μM and therefore, a concentration of 15 μM was used.[463,522–524]

When comparing to untreated iron overload cells, all chelators showed a significant reduction in iron concentration **(Figure 48A and B)**. HD-TAG and DFO treated cells had a significant reduction in both LIP (p = 0.0001 and p = 0.0124, respectively) and total iron concentration (p = 0.0001 and p = 0.0028, respectively). HD, HD-GalNAc and DFX treated cells only had a significant reduction in LIP concentration (p = 0.0006, p = 0.0028 and p = 0.0270, respectively). DFP treated cells only had a significant reduction in total iron concentration (p = 0.0350).

Further, HD, HD-TAG, DFO and DFP showed a significant reduction in intracellular ROS generation **(Figure 48C)** when compared to untreated iron overload cells (p < 0.0001, p < 0.0001, p < 0.0001, and p = 0.0325, respectively). Interestingly, HD-TAG and DFO treated cells showed ROS levels comparable to the non-iron loaded control cells. HD-GalNAc and DFX showed no significant changes in ROS.

In addition, TfR1 expression was measured as a cellular response to iron overload **(Figure 48D)**. Under iron overload conditions, TfR1 expression decreased when compared to control and iron overloaded HepG2 cells (p < 0.0001). Upon treatment with iron chelators, TfR1 expression significantly increased when compared untreated iron overload cells; while HD, HD-GalNAc, HD-TAG and DFP had significant elevation in TfR1 (p = 0.0014, p < 0.0001, p < 0.0001, and p < 0.0001, respectively), DFO and DFX increased expression beyond the non-iron overload control cells (p < 0.0001 and p < 0.0001, respectively).
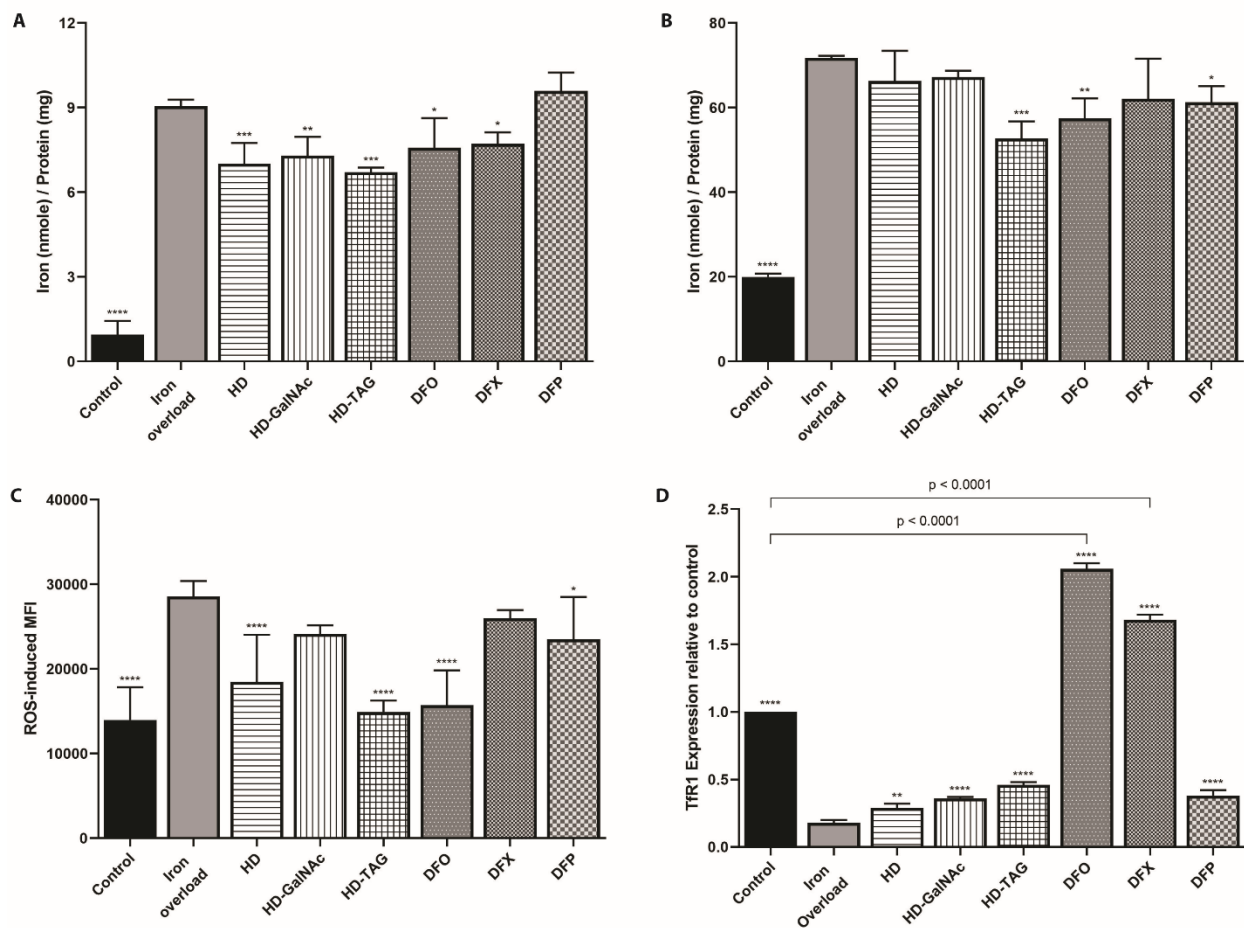
Figure 48. Effect of iron chelation in iron overload HepG2 cells. Labile iron (A) and total iron (B) were quantified using the *u*-ferene assay. (C) ROS generation was measured using a DCFDA/DCF ROS kit in at least 10,000 cells *via* flow cytometry. (D) Relative expression of TfR1, normalized to control cells, were measured using western blot and quantified using LI-COR's Odyssey Software Application. HepG2 cells were loaded with 50 µM following the established protocol. Error bars show standard deviations for 3 independent replicates. One-way ANOVA with Dunnett's correction method was performed to compared iron overloaded cells with either control or chelator treated cells. Statistical analyses were preformed using GraphPad Prism. **** represents $p < 0.0001$, *** represents $p < 0.0010$, ** represents $p < 0.0100$ and * represents $p < 0.0500$.

5.5. Discussion

Liver targeting macromolecular systems have shown improved pharmacokinetic and pharmacodynamic properties, especially with regards to hepatocyte uptake and intracellular distribution of these systems. In this chapter, we investigated these systems for their mode of intracellular action to chelate iron and subsequently prevent iron-induced toxicity.

In order to do this, we first developed a novel colorimetric unified-ferene assay that enables a 2-in-1 quantification of labile and total iron as a means to directly measure the iron status. Then, we optimized an *in vitro* iron overload HepG2 model with elevated iron burden, both labile and total iron, and ROS generation whilst maintaining various cellular functions similar to that of unloaded cells. With these in place, we then probed how liver targeting macromolecular chelating systems performed with regards to their uptake and cytotoxicity, intracellular iron chelation and the potential to mitigate iron-mediated toxicity.

Robust and accessible methods are required to measure iron levels, both labile and total iron, in different tissue specimens. Current approaches to quantitate iron exist, however they require specialised methodologies, extensive sample preparation and costly equipment.[432,465–474] Colorimetric methods are accessible, economic and are routinely refined for better sensitivities, convenient sample preparation and robust application. Several chromogenic substrates, specific for chelatable ferrous iron, absorb strongly in the UV/Vis region, including bathophenanthroline sulfonate, ferrozine or ferene.[469,472,476,477,525–527] Reimer et al. developed a common assay for quantification of iron in astrocytes, using permanganate-mediated digestion and ferrozine-based colorimetric iron determination.[469] Hedayati et al. then improved Reimer et al. assay's sensitivity by using nitric acid-mediated digestion and ferene-based colorimetric iron determination.[472] Ferene binds to iron with an affinity of $\sim 10^{14.9}$.[513] However, the quantification of both labile and total iron from the same biological sample is yet to be reported. It is worthwhile to mention that the quantification of labile iron pool is often tied to the specific fluorescent sensor, environmental variations within cells, and solvent systems used for calibration.[71] As such, it is difficult to directly translate these concentrations to other modes of analysis.

The labile iron pool is critical for cellular iron metabolism and exists in dynamic equilibrium between different organelles.[457,458,528] Current methods to trace and quantitate labile iron concentration measure changes in fluorescence from iron sensors, which either turn-on (fluorescence signal enhances) or turn-

off (fluorescence signal quenches) in the presence of iron.[458,481] These fluorescence techniques to measure metals is a rapidly growing approach offering spatial and temporal resolution. However, the use of fluorescence sensors is greatly hindered by limited commercially available probes, poor metal selectivity, mediocre signal-to-noise ratio, and it requires specialized instruments (fluorescence microscopy or flow cytometry).[458,481] Taken together, this limits the absolute quantification of labile iron pool.

We began with the development of a unified-ferene assay (*u*-ferene) that enables a 2-in-1 detection of both total and labile iron in biological samples, by varying ascorbic acid concentrations. Ascorbic acid is one of the low-molecular ligands that reduces ferric iron to ferrous iron, which then enables ferene, a bidentate chelator with a pFe^{2+} of 15, to chelate ferrous iron.[3,513,529] Moreover, this reducing agent also has the potential to interrupt stably chelated iron. To assess the ferene-based detection of iron, DFO was used as our model chelator to compete and stably chelate iron because it has been extensively investigated and has a high affinity for iron.[514–516] Based on our preliminary screening experiments, it was confirmed that ascorbic acid concentration has a central role in these measurements; significant release of iron from the DFO-Fe coordination sphere was observed with a concentration of ascorbic acid above 10 mM **(Figure 42A)**. In other words, ascorbic acid above 10 mM is sufficient to reduce all iron pre-chelated with DFO. Therefore, we chose 10 mM ascorbic concentration for the determination of labile iron. This is because the iron measured at 10 mM ascorbic sufficiently discerns between the iron only analyte and the iron pre-chelated with DFO analyte ($p < 0.0001$). It is important to note that these working concentrations may change when using other iron chelators. Within a biological context, DFO bound iron serves as an indicator of stably bound iron, and at 10 mM ascorbic acid, we can conservatively discern between chelatable and unchelatable iron.

Therefore, we defined labile iron as chelatable redox active ferrous iron quantified using 5 mM ferene and 10 mM ascorbic acid from a biological sample. The labile iron concentration in non-iron loaded HepG2 cells was found to be 0.8 ± 0.2 nmole of labile iron per mg of protein (4 μM) **(Figure 45A)** by the *u*-ferene assay. This is similar to the reported values using fluorescent based labile iron determination methods; it has been reported that there is an average of 2 to 5 μM (equivalent to 0.3 to 0.9 nmole) of intracellular chelatable iron within normal rat hepatocytes.[71,72,530] Moreover, the increase in labile iron after iron loading HepG2 cells was also shown using calcein as a metallosensor for intracellular labile iron (**Figure 45B)**. While there is agreement in the labile iron concentrations determined from two different techniques in two different hepatocytes, it is important to note that these diversities pose a challenge to validate labile iron concentrations thoroughly.

On the other hand, total iron is defined as all iron, redox active and unchelatable stored iron, quantified using 5 mM ferene and 1 M ascorbic acid after nitric acid digestion in a biological sample. We noticed 10 mM ascorbic acid concentration was not enough to completely reduce the iron following acid digestion of cell lysates **(Figure 42C)** and ferene-based iron detection increased with ascorbic acid concentration. We hypothesized that this is due to the equilibrium between Fe^{3+} and Fe^{2+} under acidic conditions requiring more ascorbic acid to reduce the iron, since all the stable and otherwise unchelated iron had been released *via* nitric acid digestion. At 1000 mM ascorbic acid concentration, the total iron measurements agreed with ICP-MS analysis **(Figure 42D)**. Thus, by optimizing the ascorbic acid concentration needed to sufficiently reduce iron for detection by ferene, we were able to quantitate both labile iron and total iron **(Figure 42)**.

To further validate this assay's capacity to quantify chelatable iron in cell lysates, the labile iron pool was perturbed by the introduction of high-affinity iron chelators with stability constants above log(20) and the iron content was determined by the *u*-ferene assay **(Figure 43)**. The monitoring of different cellular iron pools is of utmost importance, especially within the field of hereditary and transfusion-dependent iron overload, since the production of reactive oxygen species has been correlated to changes in the labile iron pool.[62,531] Cell lysates were used for two reasons; first, it ensured changes in the labile iron pool without affecting the total iron and second, it demonstrated the use of the same lysate for both labile and total iron determination. Upon treatment with DFO and DFP, the labile iron pool is significantly lowered because these chelators strongly bind to intracellular ferric iron hence reducing the measurable labile iron pool **(Figure 43A)**. DFX treatment showed only a slight decrease in the labile iron pool. This may speak to the tunability of this assay, with respect to ascorbic acid concentration, for other chelators (**Appendix Figure 42**). Of note, total iron concentration was not different across treatments since only the lysates were manipulated.

Next, total iron was quantified using the same *u*-ferene assay with two modifications; first, biological samples underwent nitric acid digestion to release all iron[472] and second, 1 M ascorbic acid concentration in working solution was used. Total iron concentrations loaded within HepG2 cells were in the range of 3.5 to 5.0 μg iron per mg protein (70 to 90 nmole iron per mg protein across the different iron loading concentrations), which has been validated by ICP-MS, a gold standard approach, **(Figure 42D)** and is in agreement with earlier reports.[487,496,532] Moreover, the total iron content did not change despite increasing iron loading concentration. This pattern of iron accumulation has been observed to be unique in HepG2 cells **(Figure 44B)**.[487]

Taken together, this *u*-ferene assay enables quantification of both labile and total iron using defined ascorbic acid concentrations as well as nitric acid treatment to release all iron. Next, an *in vitro* iron overload HepG2 model was optimized. *In vitro* hepatic iron overload models provide an invaluable tool to better understand pathogenesis whilst enabling the progression of treatment development. All acquired iron, either TBI or NTBI, enters the liver where it is either stored, utilized or mobilized for systemic use.[35] As such, the liver is critical for coordinating iron homeostasis. An imbalance in this maintenance can result in iron overload where excess free iron results in hepatic toxicity and damage giving rise to a variety of disorders including hepatic insulin resistance,[533,534] fibrosis and cirrhosis,[535,536] and an increased risk for hepatocellular carcinoma.[537,538]

Such models exist, yet their utility is undermined by extreme diversity; (1) different hepatic cell lines, such has HepG2 versus Hep3B respond differently to NTBI, (2) various sources of NTBI are used, most commonly including citrate-[57,487–496], nitriloacetate-[495,497–500] and sulfate-[501–505] complexes, as well as other preparations[495,502,506,539], and (3) iron treatment vary greatly with vastly different concentrations and durations, ranging from as low as 1 µM to as high as 2 mM for as short as 6 h to as long as 7 days.[487,490–496,498–500,503,504,506] This lack of consensus within the field can produce conflicting outcomes as highlighted in a proteomic study that investigated protein alterations in HepG2 cells loaded with two different iron concentrations; HepG2 cells treated with 10 µM resulted in 25 proteins being up-regulated and 5 proteins being down-regulated whereas HepG2 cells treated with 1000 µM resulted in 19 proteins being up-regulated and 8 proteins being down-regulated.[501,502] Interestingly, two down-regulated proteins at 10 µM became up-regulated at 1000 µM.[501,502] Thus, in this chapter, the process needed to develop and establish a consistent iron overload *in vitro* model was optimized with the intention to enable reproducible findings.

HepG2 cells were loaded with iron from ferric ammonium citrate, a common complex in NTBI, to mimic iron accumulation in patients suffering from iron overload.[540–542] Whilst the uptake of NTBI has not been completely elucidated, NTBI is rapidly internalized by hepatocytes *via* the DMT1 or the ZIP14 transmembrane metal-ion transporter.[53,54,57–59] Since iron treatment conditions vary greatly, HepG2 cells were first screened for a changes in total iron with respect to concentration and duration of iron loading. Total iron in cells increased with time of incubation rather than iron loading concentration **(Figure 44)**; total iron concentration was significantly more elevated in cells treated for 48 h compared to 24 h at the same concentration, however, there was no significant difference between cells treated with different

concentrations for a given time. Total iron concentration in loaded HepG2 cells was in the range of 75 to 85 nmole per mg protein (3.5 to 5.0 μg iron per mg protein) after 48 h incubation, which is in agreements with earlier reports.[487,496,532] Taken together, a 48 h treatment period was more than sufficient to induce iron overload, which is maintained for at least 3 days, providing ample time to conduct further studies.

Next, we investigated the impact of iron loading concentrations using the established time stamps – load every 24 h for 48 h, followed by 24 h of fresh media. Intracellularly, a small fraction of redox labile iron is maintained in dynamic equilibrium such that it accounts for ∼ 3-5% of the total iron.[457] This is observed using the *u*-ferene assay in control cells with 3.7% LIP (0.8 nmole of labile iron per mg of protein out of the 21.5 nmole of total iron per mg of protein). Similar to **Figure 42,** HepG2 cells loaded with iron, irrespective of iron loading concentration, showed no significant differences when comparing their total iron, highlighting the reproducibility of this iron overload model.

Moreover, similar to hepatic iron overload diseases, iron overloaded HepG2 cells demonstrate significantly elevated labile iron concentration as iron loading concentration increased. The labile iron concentration, using the *u*-ferene assay, was significantly increased when comparing control cells to iron overload HepG2 cells. This pattern was further corroborated with the calcein assay as well as in the literature.[499,500,504] Elevated labile iron catalyzes the generation of ROS through the Haber-Weiss reaction, which imparts oxidative damage to lipids, proteins and DNA.[5–7,10,11] Intracellular ROS levels were measured and a significant increase was observed for iron overloaded cells. This increase in ROS has been documented in earlier reports.[489,497,499,501,503] Similar to total iron concentrations, ROS generation was not significantly different between cells treated with different iron loading concentration. Huang et al. reports a linear correlation between lipid peroxidation and total iron concentrations, which might rationalize our findings.[503] It is also possible that intracellular catalases mitigate the generation of ROS, making it difficult to identify possible correlations with intracellular labile iron concentration.[543] Further work would need to validate this. In addition, iron overload cells treated with hydrogen peroxide further increased ROS generation (p = 0.0024) (**Appendix Figure 43**) demonstrating that the cells are susceptible to further ROS generation and that ROS generation is still within the assay's limit of detection. Taken together, using the established time stamps to develop an iron overload model with different iron loading concentrations (50, 100 and 200 μM) only labile iron concentrations significantly changed.

Next, toxicity indices were measured as a function of iron loading concentration **(Figure 46)**; lower iron loading concentration better resembled non-iron loaded control cells in the measured cellular functions.

As iron loading concentration increased, iron overloaded HepG2 cells showed exacerbated decline in these parameters – as exemplified by HepG2 cells loaded with 1000 μM. Of importance, cytotoxicity indices vary greatly within the literature. Abalea et al. report elevated LDH in HepG2 cells treated with iron at 10 and 100 μM for 24 h whilst Fang et al. report unchanged HepG2 cell proliferation for concentrations as high as 1000 μM treated for up to 5 days.[499,502] It is important to note that both Abalea et al. and Fang et al. used nitriloacetate complexed iron, as different NTBI sources yield different kinetic parameters with regard to NTBI uptake.[495] Previous publications, using ferric ammonium citrate to treat HepG2 cells, also report varying toxicities. Parkes et al. report that nuclear membrane integrity changes at concentrations higher than 200 μM while LDH levels remain unchanged at concentrations as high as 1.4 mM.[495] In addition, Popovic et al. report that metabolic activity, measured by MTT, decreases below 80% of control only at concentrations exceeding 2 mM.[496] Given this variability and that many reports aim to investigate the treatment of iron overload or the reversal of ROS-mediated damage, it is essential that cytotoxic indices are thoroughly documented and account for different cellular parameters. Adopting this practice will empower reproducibility within the field. Our data showed that iron loading concentrations of 50 μM yield an iron overload model closest to control cells and that any concentrations above 200 μM iron show significant alterations to cellular function. Additional mechanistic studies are required to provide insight into the molecular signal causing these changes.

With this established iron overload HepG2 model, we then assessed the response of cells when treated with chelators with regards to uptake, metabolic activity, iron status, ROS generation and TfR1 expression (**Figure 47** and **Figure 48**). A less pronounced uptake was observed for liver targeting macromolecular systems in iron overloaded HepG2 cells. This is likely due to decreased ASGPR expression observed through western blot analysis (**Appendix Figure 44**). Despite this, liver targeted macromolecular chelators were well tolerated when compared to either their non-liver targeted counterparts or to the small molecular weight chelators (**Figure 47**). Moreover, a reduction in iron concentration was observed, consistent with earlier reports.[495,503] Similarly, generation of intracellular ROS (**Figure 48**) was also reduced with chelator treatment suggesting a protective action which is in accordance with Huang et al.'s report. Moreover, TfR1 expression was also modulated by changes in cellular iron status.[501,502,512] TfR1 expression is regulated by iron regulatory proteins by binding to iron-responsive elements in the 3'-untranslated region of TfR1 mRNA transcripts such that there is decreased expression under iron overload conditions.[26] As such, TfR1 expression was reduced upon iron loading followed by a subsequent increase with chelator treatment. Such intracellular changes are observed elsewhere with both TfR1 and intracellular ferritin.[493]

It is interesting to note that TfR1 expression were significantly higher for DFO and DFX treated cells when compared to non-iron overload control cells ($p < 0.0001$ for both chelators), as observed by Chenoufi et al.[493] This was not observed for any of the other chelators.

Taken together, the mobilization of iron and the mitigation of iron-induced toxicity through the generation of ROS suggest that macromolecular chelators, whether liver targeted or not, operate similarly to DFO alone. However, only HD-TAG performed as well as DFO in reducing both labile and total iron concentrations as well as ROS generation, despite its decreased uptake when compared to either HD-GalNAc or in iron overloaded HepG2 cells. A notable difference was observed with the modulation of TfR1 protein expression for macromolecular chelators compared to DFO alone; all chelators significantly increased TfR1 expression when compared to iron overload HepG2 cells, however only DFO significantly increased TfR1 expression beyond that of untreated non-iron overloaded HepG2 cells. The underlying mechanisms for this remains unclear and this requires further analyses to elucidate these interactions.

5.6. Conclusions

Herein, the development of an economic and readily accessible alternative assay for the measurement of both labile and total iron using the unified-ferene (*u*-ferene) assay was outlined. This assay was validated using other currently available and widely accepted techniques, including ICP-MS and flow cytometry, as well as being supported by iron concentration reported within literature. Further, this method provides adequate quantification of both chelatable and labile iron as well.

Moreover, the optimization of iron treatment conditions and duration to establish an iron overload HepG2 cell model was thoroughly documented because of the apparent lack of consensus within the literature. This model had increased iron-dependent measured outcomes – ROS generation, labile and total iron concentrations, whilst being non-toxic and maintained cellular functions that closely resembled unloaded HepG2 cells.

Then, the mobilization of iron and mitigation of iron-mediated toxicity through the generation of ROS were investigated in the optimized iron overload HepG2 cell model using both macromolecular chelators and small molecular weight chelators. Differences were observed between the two liver targeting macromolecular systems, which points to the importance of understanding the design of these systems.

Chapter 6: Concluding remarks and Future directions

6.1. Significance of Thesis

Iron chelation therapy is the current standard of care to manage the iron burden in patients who suffer from hemoglobinopathies or myelodysplastic syndromes. Iron chelators are small organic molecules that stably bind to iron (III), preventing their redox activity[5,7,60,112–114], and are readily excreted through either the feces or the urine thereby decreasing the iron burden.[76,77,94,111] Iron chelators have been extensively investigated as a potential therapy in different diseases including cancer, neurodegenerative diseases, diabetes, and infections.[115–127]

So far, only three chelators are approved by the FDA for iron chelation therapy; deferiprone, deferasirox, and deferoxamine.[4,128] Numerous other chelators have been in different stages of clinical trials.[115,116,156–166] However, these low molecular weight iron chelators are greatly limited by relatively short circulation half-lives that limit its efficacy and are often associated with toxicities, due to non-specific distribution and off-site interactions. Macromolecular approaches circumvent these shortcomings by increasing their molecular mass and safely increasing their circulation times. These have been well documented in enhancing iron chelator's biological activity in both *in vitro* and *in vivo* models.

These works are at the forefront of designing novel systems with ideal properties; these systems must have a high therapeutic index with minimal toxicity to allow for the mobilization and elimination of labile iron, from the plasma as well as intracellularly, such that it offers hepatic and cardiac protection from iron-induced toxicity. In addition, the mode of administration and dosage will impact patient compliance and the subsequent economic burden.

A major limitation for long circulating therapeutics is non-specific organ accumulation, especially to treat chronic illnesses.[181,183,184,205,206] The challenge lies in maintaining its pharmacokinetic properties whilst preventing bioaccumulation. The work described in this thesis begins to develop a novel class of liver targeted iron chelators that offers two unique advantages; first, a critical organ involved in iron homeostasis can be protected from iron mediated toxicity, and second, these systems can be eliminated through the hepatic-biliary route minimizing non-specific accumulation.

Currently, no liver targeting strategies for the delivery of DFO exist. The presented thesis describes the synthesis and characterization of this novel class of liver targeted chelators (**Chapter 2**). Further, the targeting ability and intracellular processing of these systems were correlated with its design parameters (**Chapter 3**). Lastly, the translation of these liver targeted chelators were investigated in both *in vivo* and *in vitro* models to discern its mechanism of action (**Chapter 4** and **Chapter 5**).

The design and development of liver targeting systems was described in **Chapter 2**. HPG served as a multi-functional macromolecule carrier. A library of targeting systems was developed to optimize for the identity and density of ASGPR specific ligands – GalNAc and TAG units, on hepatocyte binding and uptake. H-GalNAc$_{50}$ demonstrated maximum binding and uptake responses and H-TAG$_2$ exhibited superior binding whilst offering a synthetic advantage for additional polymer modification. Both H-GalNac$_{50}$ and H-TAG$_2$ were carried forward for DFO conjugation (HD-GalNAc and HD-TAG, respectively). These liver targeting chelating systems still elicited cellular binding and uptake, though lower than their non-DFO parent systems. The intracellular distribution of these systems was confirmed by confocal laser scanning microscopy. In addition, HD-GalNAc and HD-TAG were well tolerated *in vitro*.

The *in vivo* pharmacokinetic behavior and intracellular processing of liver targeting chelators were investigated and described in **Chapter 3**. ASGPR-specific polymers, HD-GalNAc and HD-TAG, resulted in significant and rapid liver specificity when compared to the non-targeted control, HD. In addition, both HD-GalNAc and HD-TAG were selectively internalized by hepatocytes as compared to the Kupffer cell dominant sequestration of HD. Notably, almost 75% of both HD-GalNAc and HD-TAG was rapidly excreted within the first 24 h, which highlights the utility of these systems for systemic clearance. Remarkably, this is one of the first studies that demonstrates that the *in vivo* processing of these systems was influenced by selection of the ligands (HD-GalNAc vs HD-TAG). HD-GalNAc demonstrated significantly higher liver uptake and minimal vascular residency when compared to HD-TAG. Further, HD-GalNAc was eliminated equally between the hepatobiliary and renal routes whereas HD-TAG was excreted predominantly through the hepatobiliary route. The role of the ligands was further supported by the *in vitro* kinetic analyses on the intracellular trafficking of HD-GalNAc and HD-TAG. Whilst the intracellular fate for both HD-GalNAc and HD-TAG revealed rapid lysosomal accumulation, the type of GalNAc, either monoantennary or tri-antennary seemed to influence the kinetics of endocytosis and translocation which may translate into different modes of systemic excretion. Taken together, the data illustrated that the chemistry and decoration of the ASGPR ligands strongly influences its residence in plasma, liver uptake, and, most notably, the time and route of excretion.

The *in vivo* performance of a novel class of liver targeted iron chelators was assessed in iron overloaded mice, as described in **Chapter 4**. An iron overload model was first optimized in C57Bl/6 mice by loading them with 3 doses of 300 mg/kg iron-dextran. In these mice, hepatic iron burden increased by 89 fold whilst minimizing signs of toxicity. The chelation efficiencies for HD-GalNAc and HD-TAG and their controls was then investigated in the optimized iron overload mouse model. Despite the rapid excretion displayed by HD-GalNAc and HD-TAG, these systems did not translate into significant iron removal. However, HD-GalNAc polymers with higher DFO units, HD_{40}-GalNAc, demonstrated significant iron removal and a reduction in hepatic iron burden, suggesting the necessity to optimize for DFO density on these systems. Taken together, this work supports the utility of liver targeted chelators.

The intracellular mechanism of iron chelation was investigated in iron overloaded hepatocytes, as documented in **Chapter 5**. In this chapter, a novel unified-ferene assay for the colorimetric quantification of both labile and total iron was validated using other currently available and widely accepted techniques, including ICP-MS and flow cytometry, as well as being supported by iron concentration reported within the literature. Additionally, an optimized iron overload model in a hepatocellular carcinoma cell line was thoroughly documented and developed due to the apparent lack of consensus regarding iron loading protocols within the literature. Liver targeting macromolecular chelating systems were well tolerated in both iron overload and non-iron overload HepG2 cells. Despite having a less pronounced uptake in iron overload cells when compared to non-iron overload cells, these systems reduced both the cellular iron burden as well as the generation of ROS similar to DFO alone. This suggests that both HD-GalNAc and HD-TAG interact with the intracellular iron pool whilst being trafficked in endosomes, which subsequently mitigate iron-induced generation of ROS.

Overall, the combined observation of immediate hepatocyte targeting, subsequent rapid excretion and the clinical translation of HD-GalNAc and HD-TAG in iron overload mice demonstrate that this novel class of liver targeted chelators are potential candidates for the removal of systemic and hepatic iron in iron overload disorders. This thesis investigates the synthetic design strategy and its biological evaluation under both *in vitro* and *in vivo* condition.

6.2. Limitations

The development of liver targeting chelating systems offers tremendous value to current iron chelation therapy; the selective removal of excess hepatic iron could protect the liver, a key storage organ and iron homeostasis regulator, from iron mediated toxicity as well as improving the current iron excretion efficiencies which may elicit systemic iron redistribution and reduce iron burden in other organs. In this thesis, a novel class of liver targeted, high molecular weight iron chelators was developed and assessed for their liver specificity, tolerability and efficacy. This work sheds light on synthetic design parameters and its translation to both *in vitro* and *in vivo* models. These preliminary investigations are imperative and provide the groundwork required in the area of organ-specific chelation. Substantial work is required to address the limitations in the presented thesis as well as important consideration in the development of liver specific iron chelators.

Chapter 2 investigated the design of HPG-based polymers to achieve ideal liver targeting. This chapter can be expanded in at least two directions. First, in addition to screening the library of polymers through cellular binding and uptake, their ASGPR binding constants should be quantified using either surface plasmon resonance or isothermal titration calorimetry assays. This will allow for a quantitative comparison of the library of polymers screened as well as elucidating the observed differences in cellular responses to these liver targeting systems. While the conjugation of DFO resulted in a decrease in cellular binding and uptake, the IC_{50} values were higher for HD-GalNAc when compared to H-GalNAc$_{50}$. These measured cellular responses are due to the combination of ASGPR binding, subsequent internalization and dissociation of ASGPR-specific cargo, and the recycling of ASGPR back to cell surface for further receptor mediated endocytic events. Therefore, the determination equilibrium constants for ASGPR association and dissociation will better delineate the influence of DFO conjugation on cellular responses. Second, in addition to the library of polymers decorated with ASGPR-specific ligands and based on the observations in Chapter 4, the investigation of DFO densities on binding and uptake *in vitro* would be imperative to correlate cellular responses as well as chelation capacities for these systems. DFO density is a significant variable that influences iron chelation *in vivo*. Therefore, another library with varying DFO units should be screened to understand changes in both ASGPR binding kinetics, as measured through surface plasmon resonance, and *in vitro* cellular responses. Lastly, it is important to note that if DFO conjugation significantly and negatively hampers ASGPR and cellular binding, the synthetic protocol utilized should be reconsidered. Click chemistry was used because of its convenience. Alternatively,

previous HPG-DFO conjugation strategies utilized Schiff-base chemistry.[183,184,198] This can be explored, if required.

Chapter 3 assessed pharmacokinetic profiles as well as investigating the relationship between rapid excretion and subsequent intracellular processing and trafficking of HD-GalNAc and HD-TAG. Detailed pharmacokinetic profiles were determined for HD-GalNAc and HD-TAG over 144 h in healthy mice. This chapter would benefit from expanding the scope of the *in vivo* pharmacokinetic analyses and the *in vitro* kinetic analyses in order to answer four main questions. **First, how does DFO conjugation influence the *in vivo* processing of these polymers?** Both HD-GalNAc and HD-TAG exhibited significant liver targeting with minimal non-specific biodistribution. These studies would greatly benefit by assessing and comparing the pharmacokinetic profiles to non-DFO conjugated polymers (H-GalNAc$_{50}$ and H-TAG$_2$) as well as liver targeting polymers with increasing DFO densities. This would highlight the role of DFO conjugation on vascular retention and hepatic targeting. **Second, why is there a difference in excretion modalities for HD-GalNAc and HD-TAG despite both displaying significant liver targeting and rapid excretion?** HD-GalNAc and HD-TAG exhibited rapid excretion, with almost 75% of the polymers excreted within the first 24 h of injection. This is a novel observation for synthetic macromolecular systems. The underlying cellular mechanisms were investigated; *in vivo* cellular distribution revealed a predominantly hepatocyte specific uptake and kinetic analyses revealed rapid lysosomal accumulation. Taken together, these experiments suggest that the rapid translocation of HD-GalNAc and HD-TAG to lysosomes in the hepatocytes result in the rapid excretion. To confirm this connection, additional experiments are required. This could entail advancing *in vivo* cellular distribution studies by separating Kupffer cells and hepatocytes and performing confocal analysis to identify the intracellular distribution of HD-GalNAc and HD-TAG. Moreover, significant differences were observed for HD-GalNAc and HD-TAG systems in their excretion modalities; HD-GalNAc was excreted equally *via* feces and urine whereas HD-TAG was excreted predominantly *via* the feces. To elucidate these differences, pharmacokinetic studies would benefit from the examination of polymer concentration in the hepatobiliary route (i.e. polymer content in bile, gall bladder, intestines and feces) and the renal route (i.e. polymer content in kidneys, urinary bladder and urine). This might uncover a role of enterohepatic cycling in the case of HD-GalNAc, which could explain its renal excretion. **Third, what happens to these polymers over longer periods of time?** The pharmacokinetic profile of HD-TAG suggested splenic redistribution between 72 h and 144 h after injection. Therefore, evaluation of *in vivo* processing of these polymers over longer periods of time would be of particular interest to assess changes in hepatic accumulation and the possibility of redistribution to other organs. Further, these studies might

highlight implications for chronic accumulation of liver targeted polymers which may justify the need to investigate alternate strategies including biodegradable polymeric systems as well as small molecular liver specific adducts (**Appendix** – sections A.3.1 and A.3.2.). **Fourth, how do these pharmacokinetic profile change in diseased models?** In addition to this, the pharmacokinetic profiles in an iron overload model would be critical because it would highlight any changes in the distribution and excretion of liver targeted chelating systems as a consequence of iron overloading. This would also provide valuable insights to optimize the dosing regimen for *in vivo* iron chelation assessment. The frequency and concentration of liver specific polymeric iron chelators were determined from investigation in healthy mice. This a major assumption and it should be challenged. This would be of great value for the wider scientific community, since many reports also make this assumption.

In chapter 4, the chelation efficiency of HD-GalNAc and HD-TAG was analyzed in an iron overload mouse model and we identified that DFO density is a key consideration in the design of liver targeted iron chelators. Additional work can be done in three directions. First, the iron overload mouse model was optimized with respect to frequency and concentration of intravenous iron dextran. Given this, the optimization of this model would benefit further by assessing the consistency and reproducibility of iron loading. This can be done by quantifying the total iron content in mice and compared to the total injected dose in several independent experiments. This is important because this model is used to gauge the success of these systems. Second, this chapter would benefit from a more robust investigation of the safety and success of iron chelation. Liver targeting iron chelators were well tolerated with minimal signs of acute toxicity in mice that received a single dose of HD-GalNAc and HD-TAG. Despite this, the safety of these polymers could be further investigated to assess signs of chronic toxicities, liver function tests and kidney function tests following repeated chelator administration. Moreover, the therapeutic efficacy of liver targeted iron chelators should be expanded to measure protection of the liver from iron-induced toxicity, such as lipid peroxidation and markers of fibrosis. Third, this chapter highlights the value of iron-dextran iron overload mouse model which offers an economical model to assess the functional translation of liver targeted chelating systems. This model should be used to screen for liver targeted iron chelators that vary in DFO units to identify ideal candidates. These ideal candidates should then be investigated in clinically relevant mouse models, such as hemochromatosis mouse models or β-thalassemic mouse models.

Chapter 5 investigated the mobilization of cellular iron and the subsequent changes in protein expression. Differences were observed in the decrease of labile iron, total iron and the reduction of ROS generation

between HD-GalNAc and HD-TAG in iron overloaded HepG2 cells. This chapter can be expanded to identify accessibility to the different intracellular pools, using compartment specific metallosensors. This would be valuable and can shed light on the mechanism of intracellular chelation. High-throughput analysis can identify intracellular compartments influenced by this class of chelators. Detailed confocal microscopy studies can quantitate the magnitude of iron chelation in different compartments.[71,458,481,483] In addition to this, treatment with all chelators demonstrated a significant increase in TfR1 expression when compared to untreated iron overload cells. Since only TfR1 was assessed, this work can be expanded to examine changes in other iron sensitive proteins including DMT1, ferritin and ferroportin. Lastly, the beneficial effect on reducing oxidative stress was observed in vitro. It would be worthwhile to investigate whether this translate *in vivo* by measuring lipid oxidation, DNA damage or alterations to the mitochondrial respiratory chain.

6.3. Future Directions

The work described in this thesis provides the foundation to expand on current HPG-based liver targeting chelating systems. This is central to this thesis and is discussed in great detail in section 6.2. In addition to this, this thesis also provides two exciting new directions for this novel class of liver targeted iron chelators.

First, a biodegradable polymeric carrier (BHPG) can be utilized to circumvent limitations associated with prolong hepatic accumulation of non-degradable polymers. The design and development of liver targeting BHPG systems have been documented in the **Appendix** (section A.3.1.). In short, BHPG-based systems demonstrated similar trends as HPG-based systems with respect to cellular binding and uptake, intracellular trafficking and kinetic analyses *in vitro*, as well as pharmacokinetic properties *in vivo*. These highlight the influence on the polymeric backbone in the translation of liver targeted macromolecular chelators. Remarkably, after 24 h of injection, the hepatic accumulation begins to decrease suggestive of either elimination or degradation followed by elimination. This work should be expanded and compared to HPG-based systems over a long duration to investigate whether the biodegradability of the BHPG polymer offers any advantages over non-degradable HPG polymers. Additionally, both HPG and BHPG liver targeted chelators would benefit from further analyses of DFO density and subsequent iron chelation efficacy *in vivo*.

Second, a small molecular approach using TAG adducts can offer a unique advantage to directly modulate DFO's pharmacokinetic properties independent and free of the polymeric backbone. The design and development of small molecule TAG linkers have been documented in **Appendix** (A.3.2.). In short, the density of TAG required to achieve hepatocyte targetability *in vitro* was investigated and 1 TAG linker was carried for DFO conjugation. Confocal laser scanning microscopy confirmed the intracellular presence of TAG-DFO, suggestive of rapid lysosomal accumulation – similar to HPG-based systems. This work should be expanded to better delineate its cellular binding, uptake and intracellular trafficking kinetics *in vitro* as well as its pharmacokinetic properties. Small molecule systems offer an exciting avenue for clinical translation due to well defined structures. Such systems have gained momentum, especially after the FDA approval of Onpattro (patisiran) and Givlaari (givosiran).

It is important to note that the design and development of liver targeting carriers offers interesting new opportunities beyond the field of iron chelation. This thesis offers a blueprint to expand liver targeted carriers, whether polymeric based or small molecule, into various other applications. It would be exciting to see these systems investigated for applications requiring rapid liver targeting as well as systemic clearance.

Bibliography

1. Zhang, C. Essential functions of iron-requiring proteins in DNA replication, repair and cell cycle control. *Protein Cell* **5**, 750–760 (2014).

2. Sheftel, A. D. *et al.* Human ind1, an iron-sulfur cluster assembly factor for respiratory complex I. *Mol. Cell. Biol.* **29**, 6059–6073 (2009).

3. Lane, D. J. R. *et al.* Cellular iron uptake, trafficking and metabolism: Key molecules and mechanisms and their roles in disease. *Biochim. Biophys. Acta* **1853**, 1130–1144 (2015).

4. Heli, H., Mirtorabi, S. & Karimian, K. Advances in iron chelation: an update. *Expert Opin. Ther. Pat.* **21**, 819–856 (2011).

5. Koppenol, W. H. The Haber-Weiss cycle--70 years later. *Redox Rep. Commun. Free Radic. Res.* **6**, 229–234 (2001).

6. Kehrer, J. P. The Haber–Weiss reaction and mechanisms of toxicity. *Toxicology* **149**, 43–50 (2000).

7. Anderson, G. J. Mechanisms of iron loading and toxicity. *Am. J. Hematol.* **82**, 1128–1131 (2007).

8. Nurtjahja-Tjendraputra, E., Fu, D., Phang, J. M. & Richardson, D. R. Iron chelation regulates cyclin D1 expression via the proteasome: a link to iron deficiency-mediated growth suppression. *Blood* **109**, 4045–4054 (2007).

9. Kempe, D. S. *et al.* Enhanced programmed cell death of iron-deficient erythrocytes. *FASEB J. Off. Publ. Fed. Am. Soc. Exp. Biol.* **20**, 368–370 (2006).

10. Eaton, J. W. & Qian, M. Molecular bases of cellular iron toxicity. *Free Radic. Biol. Med.* **32**, 833–840 (2002).

11. Richardson, D. R. Molecular mechanisms of iron uptake by cells and the use of iron chelators for the treatment of cancer. *Curr. Med. Chem.* **12**, 2711–2729 (2005).

12. Anderson, C. P., Shen, M., Eisenstein, R. S. & Leibold, E. A. Mammalian iron metabolism and its control by iron regulatory proteins. *Biochim. Biophys. Acta BBA - Mol. Cell Res.* **1823**, 1468–1483 (2012).

13. Sharp, P. A. Intestinal Iron Absorption: Regulation by Dietary & Systemic Factors. *Int. J. Vitam. Nutr. Res.* **80**, 231–242 (2010).

14. Andrews, N. C. Disorders of Iron Metabolism. *N. Engl. J. Med.* **341**, 1986–1995 (1999).

15. McKie, A. T. The role of Dcytb in iron metabolism: an update. *Biochem. Soc. Trans.* **36**, 1239–1241 (2008).

16. Gunshin, H. *et al.* Cloning and characterization of a mammalian proton-coupled metal-ion transporter. *Nature* **388**, 482–488 (1997).

17. McKie, A. T. *et al.* An iron-regulated ferric reductase associated with the absorption of dietary iron. *Science* **291**, 1755–1759 (2001).

18. West, A. R. & Oates, P. S. Mechanisms of heme iron absorption: Current questions and controversies. *World J. Gastroenterol. WJG* **14**, 4101–4110 (2008).

19. Gräsbeck, R., Kouvonen, I., Lundberg, M. & Tenhunen, R. An intestinal receptor for heme. *Scand. J. Haematol.* **23**, 5–9 (1979).

20. Tenhunen, R., Gräsbeck, R., Kouvonen, I. & Lundberg, M. An intestinal receptor for heme: Its partial characterization. *Int. J. Biochem.* **12**, 713–716 (1980).

21. Rajagopal, A. *et al.* Haem homeostasis is regulated by the conserved and concerted functions of HRG-1 proteins. *Nature* **453**, 1127–1131 (2008).

22. White, C. *et al.* HRG1 is essential for heme transport from the phagolysosome of macrophages during erythrophagocytosis. *Cell Metab.* **17**, 261–270 (2013).

23. Abboud, S. & Haile, D. J. A novel mammalian iron-regulated protein involved in intracellular iron metabolism. *J. Biol. Chem.* **275**, 19906–19912 (2000).

24. McKie, A. T. *et al.* A Novel Duodenal Iron-Regulated Transporter, IREG1, Implicated in the Basolateral Transfer of Iron to the Circulation. *Mol. Cell* **5**, 299–309 (2000).

25. Donovan, A. *et al.* Positional cloning of zebrafish ferroportin1 identifies a conserved vertebrate iron exporter. *Nature* **403**, 776–781 (2000).

26. Hentze, M. W., Muckenthaler, M. U., Galy, B. & Camaschella, C. Two to Tango: Regulation of Mammalian Iron Metabolism. *Cell* **142**, 24–38 (2010).

27. Papanikolaou, G. & Pantopoulos, K. Systemic iron homeostasis and erythropoiesis. *IUBMB Life* **69**, 399–413 (2017).

28. Coffey, R. & Ganz, T. Iron Homeostasis--an Anthropocentric Perspective. *J. Biol. Chem.* jbc.R117.781823 (2017) doi:10.1074/jbc.R117.781823.

29. Chiabrando, D., Vinchi, F., Fiorito, V., Mercurio, S. & Tolosano, E. Heme in pathophysiology: a matter of scavenging, metabolism and trafficking across cell membranes. *Front. Pharmacol.* **5**, 61 (2014).

30. Richardson, D. R. *et al.* Mitochondrial iron trafficking and the integration of iron metabolism between the mitochondrion and cytosol. *Proc. Natl. Acad. Sci. U. S. A.* **107**, 10775–10782 (2010).

31. Ajioka, R. S., Phillips, J. D. & Kushner, J. P. Biosynthesis of heme in mammals. *Biochim. Biophys. Acta* **1763**, 723–736 (2006).

32. Lill, R. *et al.* The role of mitochondria in cellular iron–sulfur protein biogenesis and iron metabolism. *Biochim. Biophys. Acta BBA - Mol. Cell Res.* **1823**, 1491–1508 (2012).

33. Knutson, M. D. Iron transport proteins: Gateways of cellular and systemic iron homeostasis. *J. Biol. Chem.* **292**, 12735–12743 (2017).

34. Arosio, P., Ingrassia, R. & Cavadini, P. Ferritins: A family of molecules for iron storage, antioxidation and more. *Biochim. Biophys. Acta BBA - Gen. Subj.* **1790**, 589–599 (2009).

35. Anderson, E. R. & Shah, Y. M. Iron homeostasis in the liver. *Compr. Physiol.* **3**, 315–330 (2013).

36. Arosio, P. & Levi, S. Cytosolic and mitochondrial ferritins in the regulation of cellular iron homeostasis and oxidative damage. *Biochim. Biophys. Acta BBA - Gen. Subj.* **1800**, 783–792 (2010).

37. Itkonen, O. *et al.* Binding of Hepcidin to Plasma Proteins. *Clin. Chem.* **58**, 1158–1160 (2012).

38. Krause, A. *et al.* LEAP-1, a novel highly disulfide-bonded human peptide, exhibits antimicrobial activity. *FEBS Lett.* **480**, 147–150 (2000).

39. Park, C. H., Valore, E. V., Waring, A. J. & Ganz, T. Hepcidin, a Urinary Antimicrobial Peptide Synthesized in the Liver. *J. Biol. Chem.* **276**, 7806–7810 (2001).

40. Peslova, G. *et al.* Hepcidin, the hormone of iron metabolism, is bound specifically to α-2-macroglobulin in blood. *Blood* **113**, 6225–6236 (2009).

41. Pigeon, C. *et al.* A New Mouse Liver-specific Gene, Encoding a Protein Homologous to Human Antimicrobial Peptide Hepcidin, Is Overexpressed during Iron Overload. *J. Biol. Chem.* **276**, 7811–7819 (2001).

42. Zhang, A.-S., Xiong, S., Tsukamoto, H. & Enns, C. A. Localization of iron metabolism–related mRNAs in rat liver indicate that HFE is expressed predominantly in hepatocytes. *Blood* **103**, 1509–1514 (2004).

43. Bekri, S. *et al.* Increased Adipose Tissue Expression of Hepcidin in Severe Obesity Is Independent From Diabetes and NASH. *Gastroenterology* **131**, 788–796 (2006).

44. Ganz, T. Systemic Iron Homeostasis. *Physiol. Rev.* **93**, 1721–1741 (2013).

45. Zumerle, S. *et al.* Targeted disruption of hepcidin in the liver recapitulates the hemochromatotic phenotype. *Blood* **123**, 3646–3650 (2014).

46. Sangkhae, V. & Nemeth, E. Regulation of the Iron Homeostatic Hormone Hepcidin. *Adv. Nutr.* **8**, 126–136 (2017).

47. Qiao, B. *et al.* Hepcidin-Induced Endocytosis of Ferroportin Is Dependent on Ferroportin Ubiquitination. *Cell Metab.* **15**, 918–924 (2012).

48. Nemeth, E. *et al.* Hepcidin Regulates Cellular Iron Efflux by Binding to Ferroportin and Inducing Its Internalization. *Science* **306**, 2090–2093 (2004).

49. Ross, S. L. *et al.* Molecular Mechanism of Hepcidin-Mediated Ferroportin Internalization Requires Ferroportin Lysines, Not Tyrosines or JAK-STAT. *Cell Metab.* **15**, 905–917 (2012).

50. De Domenico, I. *et al.* The Molecular Mechanism of Hepcidin-mediated Ferroportin Down-Regulation. *Mol. Biol. Cell* **18**, 2569–2578 (2007).

51. Gkouvatsos, K., Papanikolaou, G. & Pantopoulos, K. Regulation of iron transport and the role of transferrin. *Biochim. Biophys. Acta BBA - Gen. Subj.* **1820**, 188–202 (2012).

52. Ohgami, R. S. *et al.* Identification of a ferrireductase required for efficient transferrin-dependent iron uptake in erythroid cells. *Nat. Genet.* **37**, 1264–1269 (2005).

53. Le Lan, C. *et al.* Redox active plasma iron in C282Y/C282Y hemochromatosis. *Blood* **105**, 4527–4531 (2005).

54. Brissot, P., Wright, T. L., Ma, W. L. & Weisiger, R. A. Efficient clearance of non-transferrin-bound iron by rat liver. Implications for hepatic iron loading in iron overload states. *J. Clin. Invest.* **76**, 1463–1470 (1985).

55. Singh, A. *et al.* Prion protein (PrP) knock-out mice show altered iron metabolism: a functional role for PrP in iron uptake and transport. *PloS One* **4**, e6115 (2009).

56. Tripathi, A. K. *et al.* Prion protein functions as a ferrireductase partner for ZIP14 and DMT1. *Free Radic. Biol. Med.* **84**, 322–330 (2015).

57. Nam, H. *et al.* ZIP14 and DMT1 in the liver, pancreas, and heart are differentially regulated by iron deficiency and overload: implications for tissue iron uptake in iron-related disorders. *Haematologica* **98**, 1049–1057 (2013).

58. Pinilla-Tenas, J. J. *et al.* Zip14 is a complex broad-scope metal-ion transporter whose functional properties support roles in the cellular uptake of zinc and nontransferrin-bound iron. *Am. J. Physiol. Cell Physiol.* **301**, C862-871 (2011).

59. Randell, E. W., Parkes, J. G., Olivieri, N. F. & Templeton, D. M. Uptake of non-transferrin-bound iron by both reductive and nonreductive processes is modulated by intracellular iron. *J. Biol. Chem.* **269**, 16046–16053 (1994).

60. Jacobs, A. An intracellular transit iron pool. *Ciba Found. Symp.* 91–106 (1976) doi:10.1002/9780470720325.ch5.

61. Jacobs, A. Low molecular weight intracellular iron transport compounds. *Blood* **50**, 433–439 (1977).

62. Cabantchik, Z. I. Labile iron in cells and body fluids: physiology, pathology, and pharmacology. *Front. Pharmacol.* **5**, (2014).

63. Ponka, P., Borová, J., Neuwirt, J. & Fuchs, O. Mobilization of iron from reticulocytes. Identification of pyridoxal isonicotinoyl hydrazone as a new iron chelating agent. *FEBS Lett.* **97**, 317–321 (1979).

64. Philpott, C. C. & Ryu, M.-S. Special delivery: distributing iron in the cytosol of mammalian cells. *Front. Pharmacol.* **5**, (2014).

65. Philpott, C. C. Coming into View: Eukaryotic Iron Chaperones and Intracellular Iron Delivery. *J. Biol. Chem.* **287**, 13518–13523 (2012).

66. Rouhier, N., Couturier, J., Johnson, M. K. & Jacquot, J.-P. Glutaredoxins: roles in iron homeostasis. *Trends Biochem. Sci.* **35**, 43 (2010).

67. Leidgens, S. *et al.* Each member of the poly-r(C)-binding protein 1 (PCBP) family exhibits iron chaperone activity toward ferritin. *J. Biol. Chem.* **288**, 17791–17802 (2013).

68. Shi, H., Bencze, K. Z., Stemmler, T. L. & Philpott, C. C. A cytosolic iron chaperone that delivers iron to ferritin. *Science* **320**, 1207–1210 (2008).

69. Yanatori, I., Yasui, Y., Tabuchi, M. & Kishi, F. Chaperone protein involved in transmembrane transport of iron. *Biochem. J.* **462**, 25–37 (2014).

70. Petrat, F., de Groot, H., Sustmann, R. & Rauen, U. The chelatable iron pool in living cells: a methodically defined quantity. *Biol. Chem.* **383**, 489–502 (2002).

71. Petrat, F., de Groot, H. & Rauen, U. Subcellular distribution of chelatable iron: a laser scanning microscopic study in isolated hepatocytes and liver endothelial cells. *Biochem. J.* **356**, 61–69 (2001).

72. Petrat, F., de Groot, H. & Rauen, U. Determination of the Chelatable Iron Pool of Single Intact Cells by Laser Scanning Microscopy. *Arch. Biochem. Biophys.* **376**, 74–81 (2000).

73. Hentze, M. W. & Kühn, L. C. Molecular control of vertebrate iron metabolism: mRNA-based regulatory circuits operated by iron, nitric oxide, and oxidative stress. *Proc. Natl. Acad. Sci. U. S. A.* **93**, 8175–8182 (1996).

74. Muckenthaler, M. U., Galy, B. & Hentze, M. W. Systemic iron homeostasis and the iron-responsive element/iron-regulatory protein (IRE/IRP) regulatory network. *Annu. Rev. Nutr.* **28**, 197–213 (2008).

75. Fleming, R. E. & Ponka, P. Iron Overload in Human Disease. *N. Engl. J. Med.* **366**, 348–359 (2012).

76. Brittenham, G. M. Iron-Chelating Therapy for Transfusional Iron Overload. *N. Engl. J. Med.* 11 (2011).

77. Hershko, C., Link, G., Konijn, A. M. & Cabantchik, Z. I. Objectives and mechanism of iron chelation therapy. *Ann. N. Y. Acad. Sci.* **1054**, 124–135 (2005).

78. Batts, K. P. Iron overload syndromes and the liver. *Mod. Pathol.* **20**, S31–S39 (2007).

79. Sachinidis, A. *et al.* Dysmetabolic Iron Overload in Metabolic Syndrome. *Curr. Pharm. Des.* **26**, 1019–1024 (2020).

80.   Whittington, C. A. & Kowdley, K. V. Haemochromatosis. *Aliment. Pharmacol. Ther.* **16**, 1963–1975 (2002).

81.   Brandhagen, D. J., Fairbanks, V. F. & Baldus, W. Recognition and Management of Hereditary Hemochromatosis. *Am. Fam. Physician* **65**, 853 (2002).

82.   Ganz, T. & Nemeth, E. Iron imports. IV. Hepcidin and regulation of body iron metabolism. *Am. J. Physiol. Gastrointest. Liver Physiol.* **290**, G199-203 (2006).

83.   Brissot, P. *et al.* Haemochromatosis. *Nat. Rev. Dis. Primer* **4**, 1–15 (2018).

84.   Fleming, R. E., Britton, R. S., Waheed, A., Sly, W. S. & Bacon, B. R. Pathophysiology of Hereditary Hemochromatosis. *Semin. Liver Dis.* **25**, 411–419 (2005).

85.   Hanson, E. H., Imperatore, G. & Burke, W. HFE gene and hereditary hemochromatosis: a HuGE review. Human Genome Epidemiology. *Am. J. Epidemiol.* **154**, 193–206 (2001).

86.   Silvestri, L., Nai, A., Pagani, A. & Camaschella, C. The extrahepatic role of TFR2 in iron homeostasis. *Front. Pharmacol.* **5**, (2014).

87.   Sabelli, M. *et al.* Human macrophage ferroportin biology and the basis for the ferroportin disease. *Hepatol. Baltim. Md* **65**, 1512–1525 (2017).

88.   Siddique, A. & Kowdley, K. V. Review article: the iron overload syndromes. *Aliment. Pharmacol. Ther.* **35**, 876–893 (2012).

89.   Taher, A. T., Weatherall, D. J. & Cappellini, M. D. Thalassaemia. *The Lancet* **391**, 155–167 (2018).

90.   Herbert L. Muncie, J. & Campbell, J. S. Alpha and Beta Thalassemia. *Am. Fam. Physician* **80**, 339–344 (2009).

91.   Zeidan, A. M., Shallis, R. M., Wang, R., Davidoff, A. & Ma, X. Epidemiology of myelodysplastic syndromes: Why characterizing the beast is a prerequisite to taming it. *Blood Rev.* **34**, 1–15 (2019).

92.   Gattermann, N. The Treatment of Secondary Hemochromatosis. *Dtsch. Ärztebl. Int.* **106**, 499–504 (2009).

93. Tanhehco, Y. C. & DeSimone, R. A. Chapter 29 - Errors and adverse effects of blood transfusion. in *Accurate Results in the Clinical Laboratory (Second Edition)* (eds. Dasgupta, A. & Sepulveda, J. L.) 439–447 (Elsevier, 2019). doi:10.1016/B978-0-12-813776-5.00029-7.

94. Hoffbrand, A. V., Taher, A. & Cappellini, M. D. How I treat transfusional iron overload. *Blood* **120**, 3657–3669 (2012).

95. Fillet, G., Beguin, Y. & Baldelli, L. Model of reticuloendothelial iron metabolism in humans: abnormal behavior in idiopathic hemochromatosis and in inflammation. *Blood* **74**, 844–851 (1989).

96. Bassett, M. L., Halliday, J. W. & Powell, L. W. Value of hepatic iron measurements in early hemochromatosis and determination of the critical iron level associated with fibrosis. *Hepatol. Baltim. Md* **6**, 24–29 (1986).

97. Wood, J. C. Estimating Tissue Iron Burden: Current Status and Future Prospects. *Br. J. Haematol.* **170**, 15–28 (2015).

98. Wallace, D. F. The Regulation of Iron Absorption and Homeostasis. *Clin. Biochem. Rev.* **37**, 51–62 (2016).

99. Bogdan, A. R., Miyazawa, M., Hashimoto, K. & Tsuji, Y. Regulators of Iron Homeostasis: New Players in Metabolism, Cell Death, and Disease. *Trends Biochem. Sci.* **41**, 274–286 (2016).

100. Mentzer, W. C. & Kan, Y. W. Prospects for research in hematologic disorders: sickle cell disease and thalassemia. *JAMA* **285**, 640–642 (2001).

101. Davis, B. A. & Porter, J. B. Long-term outcome of continuous 24-hour deferoxamine infusion via indwelling intravenous catheters in high-risk beta-thalassemia. *Blood* **95**, 1229–1236 (2000).

102. Díez-López, C., Comín-Colet, J. & González-Costello, J. Iron overload cardiomyopathy: from diagnosis to management. *Curr. Opin. Cardiol.* **33**, 334–340 (2018).

103. Milic, S. *et al.* The Role of Iron and Iron Overload in Chronic Liver Disease. *Med. Sci. Monit. Int. Med. J. Exp. Clin. Res.* **22**, 2144–2151 (2016).

104. Basaranoglu, M., Basaranoglu, G. & Sentürk, H. From fatty liver to fibrosis: a tale of 'second hit'. *World J. Gastroenterol.* **19**, 1158–1165 (2013).

105. Ramachandran, P. & Iredale, J. P. Liver fibrosis: a bidirectional model of fibrogenesis and resolution. *QJM Mon. J. Assoc. Physicians* **105**, 813–817 (2012).

106. Liu, Y. *et al.* Animal models of chronic liver diseases. *Am. J. Physiol. Gastrointest. Liver Physiol.* **304**, G449-468 (2013).

107. Kim, Y. *et al.* Temporal trends in population-based death rates associated with chronic liver disease and liver cancer in the United States over the last 30 years. *Cancer* **120**, 3058–3065 (2014).

108. Moon, A. M., Singal, A. G. & Tapper, E. B. Contemporary Epidemiology of Chronic Liver Disease and Cirrhosis. *Clin. Gastroenterol. Hepatol.* (2019) doi:10.1016/j.cgh.2019.07.060.

109. James, S. L. *et al.* Global, regional, and national incidence, prevalence, and years lived with disability for 354 diseases and injuries for 195 countries and territories, 1990–2017: a systematic analysis for the Global Burden of Disease Study 2017. *The Lancet* **392**, 1789–1858 (2018).

110. Asrani, S. K., Devarbhavi, H., Eaton, J. & Kamath, P. S. Burden of liver diseases in the world. *J. Hepatol.* **70**, 151–171 (2019).

111. Olivieri, N. F. *et al.* Long-term safety and effectiveness of iron-chelation therapy with deferiprone for thalassemia major. *N. Engl. J. Med.* **339**, 417–423 (1998).

112. Morehouse, L. A., Thomas, C. E. & Aust, S. D. Superoxide generation by NADPH-cytochrome P-450 reductase: the effect of iron chelators and the role of superoxide in microsomal lipid peroxidation. *Arch. Biochem. Biophys.* **232**, 366–377 (1984).

113. Link, G., Athias, P., Grynberg, A., Pinson, A. & Hershko, C. Effect of iron loading on transmembrane potential, contraction, and automaticity of rat ventricular muscle cells in culture. *J. Lab. Clin. Med.* **113**, 103–111 (1989).

114. Porter, J. B. & Garbowski, M. The pathophysiology of transfusional iron overload. *Hematol. Oncol. Clin. North Am.* **28**, 683–701, vi (2014).

115. Angus, D. *et al.* Safety, tolerability, and efficacy of PBT2 in Huntington's disease: a phase 2, randomised, double-blind, placebo-controlled trial. *Lancet Neurol.* **14**, 39–47 (2015).

116. Avramovich-Tirosh, Y. *et al.* Neurorescue Activity, APP Regulation and Amyloid-β Peptide Reduction by Novel Multi-Functional Brain Permeable Iron- Chelating- Antioxidants,M-30 and Green Tea Polyphenol, EGCG. *Curr. Alzheimer Res.* **4**, 403–411 (2007).

117. Islam, S. *et al.* Anti-inflammatory and anti-bacterial effects of iron chelation in experimental sepsis. *J. Surg. Res.* **200**, 266–273 (2016).

118. Qiao, J., Purro, M., Liu, Z. & Xiong, M. P. Terpyridine-Micelles for Inhibiting Bacterial Biofilm Development. *ACS Infect. Dis.* **4**, 1346–1354 (2018).

119. Farmaki, K. *et al.* Effect of enhanced iron chelation therapy on glucose metabolism in patients with β-thalassaemia major. *Br. J. Haematol.* **134**, 438–444 (2006).

120. Pieper, G. M. & Siebeneich, W. Diabetes-induced endothelial dysfunction is prevented by long-term treatment with the modified iron chelator, hydroxyethyl starch conjugated-deferoxamine. *J. Cardiovasc. Pharmacol.* **30**, 734–738 (1997).

121. Torti, S. V. & Torti, F. M. Iron and cancer: more ore to be mined. *Nat. Rev. Cancer* **13**, 342–355 (2013).

122. Long-term Deferiprone Treatment in Patients With Pantothenate Kinase-Associated Neurodegeneration - Full Text View - ClinicalTrials.gov. https://clinicaltrials.gov/ct2/show/NCT02174848.

123. Klopstock, T. *et al.* Safety and efficacy of deferiprone for pantothenate kinase-associated neurodegeneration: a randomised, double-blind, controlled trial and an open-label extension study. *Lancet Neurol.* **18**, 631–642 (2019).

124. Knox, J. J. *et al.* Phase II study of Triapine® in patients with metastatic renal cell carcinoma: a trial of the National Cancer Institute of Canada Clinical Trials Group (NCIC IND.161). *Invest. New Drugs* **25**, 471–477 (2007).

125. Mody, K. *et al.* A phase I study of the safety and tolerability of VLX600, an Iron Chelator, in patients with refractory advanced solid tumors. *Invest. New Drugs* **37**, 684–692 (2019).

126. Focal Accumulation of Iron in Cerebral Regions in Early ALS (Amyotrophic Lateral Sclerosis) Patients - Full Text View - ClinicalTrials.gov. https://clinicaltrials.gov/ct2/show/NCT02164253.

127. Ferrochelating Treatment in Patients Affected by Neurodegeneration With Brain Iron Accumulation (NBIA) - Full Text View - ClinicalTrials.gov. https://clinicaltrials.gov/ct2/show/NCT00907283.

128. Porter, J., Viprakasit, V. & Kattamis, A. *IRON OVERLOAD AND CHELATION*. (Thalassaemia International Federation, 2014).

129. Lee, P. *et al.* Intravenous infusion pharmacokinetics of desferrioxamine in thalassaemic patients. *Drug Metab. Dispos. Biol. Fate Chem.* **21**, 640–644 (1993).

130. Porter, J. B. *et al.* A trial to investigate the relationship between DFO pharmacokinetics and metabolism and DFO-related toxicity. *Ann. N. Y. Acad. Sci.* **850**, 483–487 (1998).

131. Cappellini, M. D. *et al.* A phase 3 study of deferasirox (ICL670), a once-daily oral iron chelator, in patients with beta-thalassemia. *Blood* **107**, 3455–3462 (2006).

132. Pennell, D. J. *et al.* A 1-year randomized controlled trial of deferasirox vs deferoxamine for myocardial iron removal in β-thalassemia major (CORDELIA). *Blood* **123**, 1447–1454 (2014).

133. Cohen, A. R., Glimm, E. & Porter, J. B. Effect of transfusional iron intake on response to chelation therapy in beta-thalassemia major. *Blood* **111**, 583–587 (2008).

134. Borgna-Pignatti, C. *et al.* Survival and complications in patients with thalassemia major treated with transfusion and deferoxamine. *Haematologica* **89**, 1187–1193 (2004).

135. Kaplinsky, C. *et al.* Deferoxamine (Desferal)-induced ocular toxicity. *Pediatr. Hematol. Oncol.* **5**, 293–297 (1988).

136. Levine, J. E., Cohen, A., MacQueen, M., Martin, M. & Giardina, P. J. Sensorimotor neurotoxicity associated with high-dose deferoxamine treatment. *J. Pediatr. Hematol. Oncol.* **19**, 139–141 (1997).

137. Brissot, P., Troadec, M.-B., Loréal, O. & Brissot, E. Pathophysiology and classification of iron overload diseases; update 2018. *Transfus. Clin. Biol. J. Soc. Francaise Transfus. Sang.* **26**, 80–88 (2019).

138. Hider, R. C. & Hoffbrand, A. V. The Role of Deferiprone in Iron Chelation. *N. Engl. J. Med.* **379**, 2140–2150 (2018).

139. Pennell, D. J. *et al.* Randomized controlled trial of deferiprone or deferoxamine in beta-thalassemia major patients with asymptomatic myocardial siderosis. *Blood* **107**, 3738–3744 (2006).

140. Viprakasit, V. *et al.* Deferiprone (GPO-L-ONE(®)) monotherapy reduces iron overload in transfusion-dependent thalassemias: 1-year results from a multicenter prospective, single arm, open label, dose escalating phase III pediatric study (GPO-L-ONE; A001) from Thailand. *Am. J. Hematol.* **88**, 251–260 (2013).

141. Cohen, A. R. *et al.* Safety profile of the oral iron chelator deferiprone: a multicentre study. *Br. J. Haematol.* **108**, 305–312 (2000).

142. Maggio, A. *et al.* Deferiprone versus deferoxamine in patients with thalassemia major: a randomized clinical trial. *Blood Cells. Mol. Dis.* **28**, 196–208 (2002).

143. Ha, S.-Y. *et al.* A randomized controlled study evaluating the safety and efficacy of deferiprone treatment in thalassemia major patients from Hong Kong. *Hemoglobin* **30**, 263–274 (2006).

144. Comparison of Deferiprone Delayed Release Tablets and Deferiprone Oral Solution in Healthy Volunteers - Full Text View - ClinicalTrials.gov. https://clinicaltrials.gov/ct2/show/NCT02442310.

145. Pilot Study of the Pharmacokinetic Profile of Deferiprone Sustained-Release Formulation in Healthy Volunteers - Full Text View - ClinicalTrials.gov. https://clinicaltrials.gov/ct2/show/NCT02189941.

146. Zhou, T., Ma, Y., Kong, X. & Hider, R. C. Design of iron chelators with therapeutic application. *Dalton Trans.* **41**, 6371–6389 (2012).

147. Liu, Z. D. *et al.* Synthesis of 2-amido-3-hydroxypyridin-4(1H)-ones: novel iron chelators with enhanced pFe3+ values. *Bioorg. Med. Chem.* **9**, 563–573 (2001).

148. Kontoghiorghes, G. J. *et al.* Effective chelation of iron in beta thalassaemia with the oral chelator 1,2-dimethyl-3-hydroxypyrid-4-one. *Br. Med. J. Clin. Res. Ed* **295**, 1509–1512 (1987).

149. Shirley, M. & Plosker, G. L. Deferasirox: A Review of Its Use for Chronic Iron Overload in Patients with Non-Transfusion-Dependent Thalassaemia. *Drugs* **74**, 1017–1027 (2014).

150. Waldmeier, F. *et al.* Pharmacokinetics, metabolism, and disposition of deferasirox in beta-thalassemic patients with transfusion-dependent iron overload who are at pharmacokinetic steady state. *Drug Metab. Dispos. Biol. Fate Chem.* **38**, 808–816 (2010).

151. Porter, J. B. & Shah, F. T. Iron Overload in Thalassemia and Related Conditions: Therapeutic Goals and Assessment of Response to Chelation Therapies. *Hematol. Oncol. Clin. North Am.* **24**, 1109–1130 (2010).

152. Porter, J. *et al.* Health-Related Quality of Life, Treatment Satisfaction, Adherence and Persistence in β-Thalassemia and Myelodysplastic Syndrome Patients with Iron Overload Receiving Deferasirox: Results from the EPIC Clinical Trial. *Anemia* https://www.hindawi.com/journals/anemia/2012/297641/ (2012) doi:https://doi.org/10.1155/2012/297641.

153. Xia, S., Zhang, W., Huang, L. & Jiang, H. Comparative Efficacy and Safety of Deferoxamine, Deferiprone and Deferasirox on Severe Thalassemia: A Meta-Analysis of 16 Randomized Controlled Trials. *PLoS ONE* **8**, (2013).

154. Piga, A. *et al.* High-Dose Desferrioxamine as a Cause of Growth Failure in Thalassemic Patients. *Eur. J. Haematol.* **40**, 380–381 (1988).

155. Kontoghiorghes, G. J. A record number of fatalities in many categories of patients treated with deferasirox: loopholes in regulatory and marketing procedures undermine patient safety and misguide public funds? *Expert Opin. Drug Saf.* **12**, 605–609 (2013).

156. Nuñez, T. M. & Chana-Cuevas, P. New Perspectives in Iron Chelation Therapy for the Treatment of Neurodegenerative Diseases. *Pharmaceuticals* **11**, (2018).

157. Crichton, R. R., Ward, J. R. & Hider, C. R. The Efficacy of Iron Chelators for Removing Iron from Specific Brain Regions and the Pituitary—Ironing out the Brain. *Pharmaceuticals* **12**, (2019).

158. Reznichenko, L. *et al.* Reduction of iron-regulated amyloid precursor protein and beta-amyloid peptide by (-)-epigallocatechin-3-gallate in cell cultures: implications for iron chelation in Alzheimer's disease. *J. Neurochem.* **97**, 527–536 (2006).

159. Kuang, Y. & Wang, Q. Iron and lung cancer. *Cancer Lett.* **464**, 56–61 (2019).

160. Das, B. *et al.* A Novel Iron(II) Preferring Dopamine Agonist Chelator as Potential Symptomatic and Neuroprotective Therapeutic Agent for Parkinson's Disease. *ACS Chem. Neurosci.* **8**, 723–730 (2017).

161. Safety and Pharmacodynamic Study of an Oral Iron Chelator Given for 6 Months to Patients With Iron Overload - Full Text View - ClinicalTrials.gov.

162. Neufeld, E. J. *et al.* A phase 2 study of the safety, tolerability, and pharmacodynamics of FBS0701, a novel oral iron chelator, in transfusional iron overload. *Blood* **119**, 3263–3268 (2012).

163. Rienhoff, H. Y. *et al.* A phase 1 dose-escalation study: safety, tolerability, and pharmacokinetics of FBS0701, a novel oral iron chelator for the treatment of transfusional iron overload. *Haematologica* **96**, 521 LP – 525 (2011).

164. Grady, R. W. & Hershko, C. HBED: a potential oral iron chelator. *Ann. N. Y. Acad. Sci.* **612**, 361–368 (1990).

165. Zhou, T., Kong, X.-L. & Hider, R. C. Synthesis and iron chelating properties of hydroxypyridinone and hydroxypyranone hexadentate ligands. *Dalton Trans.* **48**, 3459–3466 (2019).

166. Ferrer, P., Vega-Rodriguez, J., Tripathi, A. K., Jacobs-Lorena, M. & Sullivan, D. J. Antimalarial Iron Chelator FBS0701 Blocks Transmission by Plasmodium falciparum Gametocyte Activation Inhibition. *Antimicrob. Agents Chemother.* **59**, 1418–1426 (2015).

167. Duncan, R. The dawning era of polymer therapeutics. *Nat. Rev. Drug Discov.* **2**, 347–360 (2003).

168. Kopeček, J. Polymer-drug conjugates: origins, progress to date and future directions. *Adv. Drug Deliv. Rev.* **65**, 49–59 (2013).

169. Larson, N. & Ghandehari, H. Polymeric conjugates for drug delivery. *Chem. Mater. Publ. Am. Chem. Soc.* **24**, 840–853 (2012).

170. Pelegri-O'Day, E. M., Lin, E.-W. & Maynard, H. D. Therapeutic protein-polymer conjugates: advancing beyond PEGylation. *J. Am. Chem. Soc.* **136**, 14323–14332 (2014).

171. Shu, J. Y., Panganiban, B. & Xu, T. Peptide-polymer conjugates: from fundamental science to application. *Annu. Rev. Phys. Chem.* **64**, 631–657 (2013).

172. Zhou, Y. J. *et al.* Novel 3-hydroxypyridin-4-one hexadentate ligand-based polymeric iron chelator: Synthesis, characterization and antimicrobial evaluation. *MedChemComm* **6**, 1620–1625 (2015).

173. Qian, J. & Berkland, C. Conformational Stability Effect of Polymeric Iron Chelators. *iScience* **21**, 124–134 (2019).

174. Ang, M. T. C. *et al.* DIBI, a 3-hydroxypyridin-4-one chelator iron-binding polymer with enhanced antimicrobial activity. *MedChemComm* **9**, 1206–1212 (2018).

175. Johann, T., Kemmer-Jonas, U., Barent, R. D. & Frey, H. Multifunctional Fe(III)-Binding Polyethers from Hydroxamic Acid-Based Epoxide Monomers. *Macromol. Rapid Commun.* **41**, 1900282 (2020).

176. Islam, S. *et al.* Anti-inflammatory and anti-bacterial effects of iron chelation in experimental sepsis. *J. Surg. Res.* **200**, 266–273 (2015).

177. Holbein, B. E. & Mira De Orduña, R. Effect of trace iron levels and iron withdrawal by chelation on the growth of Candida albicans and Candida vini. *FEMS Microbiol. Lett.* **307**, 19–24 (2010).

178. Parquet, M. del C., Savage, K. A., Allan, D. S., Davidson, R. J. & Holbein, B. E. Novel iron-chelator DIBI inhibits Staphylococcus aureus growth, suppresses experimental MRSA infection in mice and enhances the activities of diverse antibiotics in vitro. *Front. Microbiol.* **9**, 1–11 (2018).

179. Winston, A., Varaprasad, D. V., Metterville, J. J. & Rosenkrantz, H. Evaluation of polymeric hydroxamic acid iron chelators for treatment of iron overload. *J. Pharmacol. Exp. Ther.* **232**, 644–649 (1985).

180. Zhou, T., Kong, X. L., Liu, Z. D., Liu, D. Y. & Hider, R. C. Synthesis and iron(III)-chelating properties of novel 3-hydroxypyridin-4-one hexadentate ligand-containing copolymers. *Biomacromolecules* **9**, 1372–1380 (2008).

181. Qian, J., Sullivan, B. P., Peterson, S. J. & Berkland, C. Nonabsorbable Iron Binding Polymers Prevent Dietary Iron Absorption for the Treatment of Iron Overload. *ACS Macro Lett.* **6**, 350–353 (2017).

182. Abbina, S. *et al.* Design of Safe Nanotherapeutics for the Excretion of Excess Systemic Toxic Iron. *ACS Cent. Sci.* acscentsci.9b00284-acscentsci.9b00284 (2019) doi:10.1021/acscentsci.9b00284.

183. Imran Ul-Haq, M. *et al.* Design of long circulating nontoxic dendritic polymers for the removal of iron in vivo. *ACS Nano* **7**, 10704–10716 (2013).

184. Hamilton, J. L. *et al.* In vivo efficacy, toxicity and biodistribution of ultra-long circulating desferrioxamine based polymeric iron chelator. *Biomaterials* **102**, (2016).

185. Abbina, S. *et al.* Hyperbranched polyglycerols: recent advances in synthesis, biocompatibility and biomedical applications. *J. Mater. Chem. B* **5**, 9249–9277 (2017).

186. Rossi, N. A. A. *et al.* In vitro chelating, cytotoxicity, and blood compatibility of degradable poly(ethylene glycol)-based macromolecular iron chelators. *Biomaterials* **30**, 638–648 (2009).

187. Kang, H. *et al.* Renal clearable nanochelators for iron overload therapy. *Nat. Commun.* **10**, 1–11 (2019).

188. Mahoney, J. R., Hallaway, P. E., Hedlund, B. E. & Eaton, J. W. Acute iron poisoning. Rescue with macromolecular chelators. *J. Clin. Invest.* **84**, 1362–1366 (1989).

189. Donneys, A. *et al.* Implantable hyaluronic acid-deferoxamine conjugate prevents nonunions through stimulation of neovascularization. *Npj Regen. Med.* **4**, 1–9 (2019).

190. Hallaway, P. E., Eaton, J. W., Panter, S. S. & Hedlund, B. E. Modulation of deferoxamine toxicity and clearance by covalent attachment to biocompatible polymers. *Proc. Natl. Acad. Sci. U. S. A.* **86**, 10108–10112 (1989).

191. Tian, M. *et al.* Long-term and oxidative-responsive alginate–deferoxamine conjugates with a low toxicity for iron overload. *RSC Adv.* **6**, 32471–32479 (2016).

192. Guo, S. *et al.* Polymeric Nanoparticles Enhance the Ability of Deferoxamine To Deplete Hepatic and Systemic Iron. *Nano Lett.* **18**, 5782–5790 (2018).

193. Liu, Z., Qiao, J., Nagy, T. & Xiong, M. P. ROS-triggered degradable iron-chelating nanogels: Safely improving iron elimination in vivo. *J. Control. Release Off. J. Control. Release Soc.* **283**, 84–93 (2018).

194. Kong, L. *et al.* Bioactive Injectable Hydrogels Containing Desferrioxamine and Bioglass for Diabetic Wound Healing. *ACS Appl. Mater. Interfaces* **10**, 30103–30114 (2018).

195. Tyagi, P., Kumar, A., Gupta, D. & Singh, H. Decorporation of Iron Metal Using Dialdehyde Cellulose-Deferoxamine Microcarrier. *AAPS PharmSciTech* **18**, 156–165 (2017).

196. Harmatz, P. *et al.* Phase Ib clinical trial of starch-conjugated deferoxamine (40SD02): a novel long-acting iron chelator. *Br. J. Haematol.* **138**, 374–381 (2007).

197. Wilms, D., Stiriba, S.-E. & Frey, H. Hyperbranched polyglycerols: from the controlled synthesis of biocompatible polyether polyols to multipurpose applications. *Acc. Chem. Res.* **43**, 129–141 (2010).

198. Hamilton, J. L., ul-haq, M. I., Creagh, A. L., Haynes, C. A. & Kizhakkedathu, J. N. Iron Binding and Iron Removal Efficiency of Desferrioxamine Based Polymeric Iron Chelators: Influence of Molecular Size and Chelator Density. *Macromol. Biosci.* **17**, 1–12 (2017).

199. You, L. *et al.* Targeted Brain Delivery of Rabies Virus Glycoprotein 29-Modified Deferoxamine-Loaded Nanoparticles Reverses Functional Deficits in Parkinsonian Mice. *ACS Nano* **12**, 4123–4139 (2018).

200. Liu, Z., Purro, M., Qiao, J. & Xiong, M. P. Multifunctional Polymeric Micelles for Combining Chelation and Detection of Iron in Living Cells. *Adv. Healthc. Mater.* **6**, (2017).

201. Yan, J. *et al.* Melanin nanoparticles as an endogenous agent for efficient iron overload therapy. *J. Mater. Chem. B* **4**, 7233–7240 (2016).

202. Lazaridou, M. *et al.* Formulation and In-Vitro Characterization of Chitosan-Nanoparticles Loaded with the Iron Chelator Deferoxamine Mesylate (DFO). *Pharmaceutics* **12**, (2020).

203. Rassu, G. *et al.* Solid microparticles based on chitosan or methyl-β-cyclodextrin: a first formulative approach to increase the nose-to-brain transport of deferoxamine mesylate. *J. Control. Release Off. J. Control. Release Soc.* **201**, 68–77 (2015).

204. Huang, X. *et al.* From small deferiprone to macromolecular micelles: Self-assembly enhances iron chelation. *J. Colloid Interface Sci.* **533**, 375–384 (2019).

205. Liu, Z., Wang, Y., Purro, M. & Xiong, M. P. Oxidation-Induced Degradable Nanogels for Iron Chelation. *Sci. Rep.* **6**, 1–9 (2016).

206. Liu, Z., Lin, T.-M., Purro, M. & Xiong, M. P. Enzymatically Biodegradable Polyrotaxane-Deferoxamine Conjugates for Iron Chelation. *ACS Appl. Mater. Interfaces* **8**, 25788–25797 (2016).

207. Alexis, F., Pridgen, E., Molnar, L. K. & Farokhzad, O. C. Factors affecting the clearance and biodistribution of polymeric nanoparticles. *Mol. Pharm.* **5**, 505–515 (2008).

208. Shenoi, R. A. *et al.* Branched Multifunctional Polyether Polyketals: Variation of Ketal Group Structure Enables Unprecedented Control over Polymer Degradation in Solution and within Cells. *J. Am. Chem. Soc.* **134**, 14945–14957 (2012).

209. Shenoi, R. A., Lai, B. F. L., Imran ul-haq, M., Brooks, D. E. & Kizhakkedathu, J. N. Biodegradable polyglycerols with randomly distributed ketal groups as multi-functional drug delivery systems. *Biomaterials* **34**, 6068–6081 (2013).

210. Kovacs, E. J. Wheater's Functional Histology: A Text and Colour Atlas. *Arch. Pathol. Lab. Med.* **125**, 708–708 (2001).

211. Mulaikal, T. A. & Emond, J. C. Physiology and Anatomy of the Liver. in *Liver Anesthesiology and Critical Care Medicine* (ed. Wagener, G.) 3–20 (Springer, 2012). doi:10.1007/978-1-4614-5167-9_1.

212. Kalra, A. & Tuma, F. Physiology, Liver. in *StatPearls* (StatPearls Publishing, 2019).

213. Reynaert, H., Thompson, M. G., Thomas, T. & Geerts, A. Hepatic stellate cells: role in microcirculation and pathophysiology of portal hypertension. *Gut* **50**, 571–581 (2002).

214. Racanelli, V. & Rehermann, B. The liver as an immunological organ. *Hepatol. Baltim. Md* **43**, S54-62 (2006).

215. Trefts, E., Gannon, M. & Wasserman, D. H. The liver. *Curr. Biol.* **27**, R1147–R1151 (2017).

216. Spiess, M. The asialoglycoprotein receptor: a model for endocytic transport receptors. *Biochemistry* **29**, 10009–10018 (1990).

217. Stockert, R. J. The asialoglycoprotein receptor: relationships between structure, function, and expression. *Physiol. Rev.* **75**, 591–609 (1995).

218. Pricer, W. E., Hudgin, R. L., Ashwell, G., Stockert, R. J. & Morell, A. G. A membrane receptor protein for asialoglycoproteins. *Methods Enzymol.* **34**, 688–691 (1974).

219. Roggenbuck, D., Mytilinaiou, M. G., Lapin, S. V., Reinhold, D. & Conrad, K. Asialoglycoprotein receptor (ASGPR): a peculiar target of liver-specific autoimmunity. *Auto-Immun. Highlights* **3**, 119–125 (2012).

220. Ii, M., Kurata, H., Itoh, N., Yamashina, I. & Kawasaki, T. Molecular cloning and sequence analysis of cDNA encoding the macrophage lectin specific for galactose and N-acetylgalactosamine. *J. Biol. Chem.* **265**, 11295–11298 (1990).

221. Pacifico, F. *et al.* The RHL-1 subunit of the asialoglycoprotein receptor of thyroid cells: cellular localization and its role in thyroglobulin endocytosis. *Mol. Cell. Endocrinol.* **208**, 51–59 (2003).

222. Seow, Y. T., Tan, M. G. K. & Woo, K. T. Expression of a functional asialoglycoprotein receptor in human renal proximal tubular epithelial cells. *Nephron* **91**, 431–438 (2002).

223. D'Souza, A. A. & Devarajan, P. V. Asialoglycoprotein receptor mediated hepatocyte targeting — Strategies and applications. *J. Controlled Release* **203**, 126–139 (2015).

224. Li, Y., Huang, G., Diakur, J. & Wiebe, L. I. Targeted delivery of macromolecular drugs: asialoglycoprotein receptor (ASGPR) expression by selected hepatoma cell lines used in antiviral drug development. *Curr. Drug Deliv.* **5**, 299–302 (2008).

225. Bon, C., Hofer, T., Bousquet-Mélou, A., Davies, M. R. & Krippendorff, B.-F. Capacity limits of asialoglycoprotein receptor-mediated liver targeting. *mAbs* **9**, 1360–1369 (2017).

226. Stokmaier, D. *et al.* Design, synthesis and evaluation of monovalent ligands for the asialoglycoprotein receptor (ASGP-R). *Bioorg. Med. Chem.* **17**, 7254–7264 (2009).

227. Henis, Y. I., Katzir, Z., Shia, M. A. & Lodish, H. F. Oligomeric structure of the human asialoglycoprotein receptor: nature and stoichiometry of mutual complexes containing H1 and H2 polypeptides assessed by fluorescence photobleaching recovery. *J. Cell Biol.* **111**, 1409–1418 (1990).

228. Yik, J. H. N., Saxena, A. & Weigel, P. H. The minor subunit splice variants, H2b and H2c, of the human asialoglycoprotein receptor are present with the major subunit H1 in different hetero-oligomeric receptor complexes. *J. Biol. Chem.* **277**, 23076–23083 (2002).

229. Bider, M. D., Wahlberg, J. M., Kammerer, R. A. & Spiess, M. The Oligomerization Domain of the Asialoglycoprotein Receptor Preferentially Forms 2:2 Heterotetramers in Vitro. *J. Biol. Chem.* **271**, 31996–32001 (1996).

230. Ishibashi, S., Hammer, R. E. & Herz, J. Asialoglycoprotein receptor deficiency in mice lacking the minor receptor subunit. *J. Biol. Chem.* **269**, 27803–27806 (1994).

231. Tozawa, R. *et al.* Asialoglycoprotein receptor deficiency in mice lacking the major receptor subunit. Its obligate requirement for the stable expression of oligomeric receptor. *J. Biol. Chem.* **276**, 12624–12628 (2001).

232. Wu, J., Nantz, M. H. & Zern, M. A. Targeting hepatocytes for drug and gene delivery: emerging novel approaches and applications. *Front. Biosci. J. Virtual Libr.* **7**, d717-725 (2002).

233. Lee, R. T. Binding site of the rabbit liver lectin specific for galactose/N-acetylgalactosamine. *Biochemistry* **21**, 1045–1050 (1982).

234. D'Souza, A. A. *et al.* Comparative in silico-in vivo evaluation of ASGP-R ligands for hepatic targeting of curcumin Gantrez nanoparticles. *AAPS J.* **15**, 696–706 (2013).

235. Wong, T. C., Townsend, R. R. & Lee, Y. C. Synthesis of D-galactosamine derivatives and binding studies using isolated rat hepatocytes. *Carbohydr. Res.* **170**, 27–46 (1987).

236. Meier, M., Bider, M. D., Malashkevich, V. N., Spiess, M. & Burkhard, P. Crystal structure of the carbohydrate recognition domain of the H1 subunit of the asialoglycoprotein receptor. *J. Mol. Biol.* **300**, 857–865 (2000).

237. Connolly, D. T., Townsend, R. R., Kawaguchi, K., Bell, W. R. & Lee, Y. C. Binding and endocytosis of cluster glycosides by rabbit hepatocytes. Evidence for a short-circuit pathway that does not lead to degradation. *J. Biol. Chem.* **257**, 939–945 (1982).

238. Kolatkar, A. R. *et al.* Mechanism of N-acetylgalactosamine binding to a C-type animal lectin carbohydrate-recognition domain. *J. Biol. Chem.* **273**, 19502–19508 (1998).

239. Ruiz, N. I. & Drickamer, K. Differential ligand binding by two subunits of the rat liver asialoglycoprotein receptor. *Glycobiology* **6**, 551–559 (1996).

240. Lee, Y. C. *et al.* Binding of synthetic oligosaccharides to the hepatic Gal/GalNAc lectin. Dependence on fine structural features. *J. Biol. Chem.* **258**, 199–202 (1983).

241. Rensen, P. C. *et al.* Determination of the upper size limit for uptake and processing of ligands by the asialoglycoprotein receptor on hepatocytes in vitro and in vivo. *J. Biol. Chem.* **276**, 37577–37584 (2001).

242. Biessen, E. A. L. *et al.* Synthesis of Cluster Galactosides with High Affinity for the Hepatic Asialoglycoprotein Receptor. *J. Med. Chem.* **38**, 1538–1546 (1995).

243. Rensen, P. C. N. *et al.* Recombinant lipoproteins: lipoprotein-like lipid particles for drug targeting. *Adv. Drug Deliv. Rev.* **47**, 251–276 (2001).

244. Rice, K. G., Weisz, O. A., Barthel, T., Lee, R. T. & Lee, Y. C. Defined geometry of binding between triantennary glycopeptide and the asialoglycoprotein receptor of rat heptocytes. *J. Biol. Chem.* **265**, 18429–18434 (1990).

245. Lee, Y. C. Biochemistry of carbohydrate-protein interaction. *FASEB J. Off. Publ. Fed. Am. Soc. Exp. Biol.* **6**, 3193–3200 (1992).

246. Joziasse, D. H. *et al.* alpha3-galactosylated glycoproteins can bind to the hepatic asialoglycoprotein receptor. *Eur. J. Biochem.* **267**, 6501–6508 (2000).

247. Pearse, B. M. & Bretscher, M. S. Membrane recycling by coated vesicles. *Annu. Rev. Biochem.* **50**, 85–101 (1981).

248. Wall, D. A., Wilson, G. & Hubbard, A. L. The galactose-specific recognition system of mammalian liver: the route of ligand internalization in rat hepatocytes. *Cell* **21**, 79–93 (1980).

249. Geuze, H. J., Slot, J. W., Strous, G. J., Lodish, H. F. & Schwartz, A. L. Intracellular site of asialoglycoprotein receptor-ligand uncoupling: double-label immunoelectron microscopy during receptor-mediated endocytosis. *Cell* **32**, 277–287 (1983).

250. McAbee, D. D., Jiang, X. & Walsh, K. B. Lactoferrin binding to the rat asialoglycoprotein receptor requires the receptor's lectin properties. *Biochem. J.* **348 Pt 1**, 113–117 (2000).

251. Grant, B. D. & Donaldson, J. G. Pathways and mechanisms of endocytic recycling. *Nat. Rev. Mol. Cell Biol.* **10**, 597–608 (2009).

252. Xie, S. *et al.* The endocytic recycling compartment maintains cargo segregation acquired upon exit from the sorting endosome. *Mol. Biol. Cell* **27**, 108–126 (2016).

253. Sahay, G., Alakhova, D. Y. & Kabanov, A. V. Endocytosis of nanomedicines. *J. Control. Release Off. J. Control. Release Soc.* **145**, 182–195 (2010).

254. Tanabe, T., Pricer, W. E. & Ashwell, G. Subcellular membrane topology and turnover of a rat hepatic binding protein specific for asialoglycoproteins. *J. Biol. Chem.* **254**, 1038–1043 (1979).

255. Varga, C. M., Wickham, T. J. & Lauffenburger, D. A. Receptor-mediated targeting of gene delivery vectors: insights from molecular mechanisms for improved vehicle design. *Biotechnol. Bioeng.* **70**, 593–605 (2000).

256. Warren, R. & Doyle, D. Turnover of the surface proteins and the receptor for serum asialoglycoproteins in primary cultures of rat hepatocytes. *J. Biol. Chem.* **256**, 1346–1355 (1981).

257. Schwartz, A. L., Fridovich, S. E. & Lodish, H. F. Kinetics of internalization and recycling of the asialoglycoprotein receptor in a hepatoma cell line. *J. Biol. Chem.* **257**, 4230–4237 (1982).

258. Schwartz, A. L., Bolognesi, A. & Fridovich, S. E. Recycling of the asialoglycoprotein receptor and the effect of lysosomotropic amines in hepatoma cells. *J. Cell Biol.* **98**, 732–738 (1984).

259. Popielarski, S. R., Pun, S. H. & Davis, M. E. A nanoparticle-based model delivery system to guide the rational design of gene delivery to the liver. 1. Synthesis and characterization. *Bioconjug. Chem.* **16**, 1063–1070 (2005).

260. Biessen, E. A., Vietsch, H. & Van Berkel, T. J. Cholesterol derivative of a new triantennary cluster galactoside directs low- and high-density lipoproteins to the parenchymal liver cell. *Biochem. J.* **302**, 283–289 (1994).

261. Kuiper, J., Bakkeren, H. F., Biessen, E. A. & Van Berkel, T. J. Characterization of the interaction of galactose-exposing particles with rat Kupffer cells. *Biochem. J.* **299 (Pt 1)**, 285–290 (1994).

262. Soenen, S. J. H. *et al.* The labeling of cationic iron oxide nanoparticle-resistant hepatocellular carcinoma cells using targeted magnetoliposomes. *Biomaterials* **32**, 1748–1758 (2011).

263. Biessen, E. A., Beuting, D. M., Vietsch, H., Bijsterbosch, M. K. & Van Berkel, T. J. Specific targeting of the antiviral drug 5-iodo 2'-deoxyuridine to the parenchymal liver cell using lactosylated poly-L-lysine. *J. Hepatol.* **21**, 806–815 (1994).

264. Managit, C., Kawakami, S., Nishikawa, M., Yamashita, F. & Hashida, M. Targeted and sustained drug delivery using PEGylated galactosylated liposomes. *Int. J. Pharm.* **266**, 77–84 (2003).

265. Naicker, K., Ariatti, M. & Singh, M. PEGylated galactosylated cationic liposomes for hepatocytic gene delivery. *Colloids Surf. B Biointerfaces* **122**, 482–490 (2014).

266. Longmuir, K. J., Robertson, R. T., Haynes, S. M., Baratta, J. L. & Waring, A. J. Effective targeting of liposomes to liver and hepatocytes in vivo by incorporation of a Plasmodium amino acid sequence. *Pharm. Res.* **23**, 759–769 (2006).

267. Schlepper-Schäfer, J. *et al.* Endocytosis via galactose receptors in vivo: Ligand size directs uptake by hepatocytes and/or liver macrophages. *Exp. Cell Res.* **165**, 494–506 (1986).

268. Nishikawa, M., Takemura, S., Takakura, Y. & Hashida, M. Targeted delivery of plasmid DNA to hepatocytes in vivo: optimization of the pharmacokinetics of plasmid DNA/galactosylated poly(L-lysine) complexes by controlling their physicochemical properties. *J. Pharmacol. Exp. Ther.* **287**, 408–415 (1998).

269. Arangoa, M. A., Düzgüneş, N. & Tros de Ilarduya, C. Increased receptor-mediated gene delivery to the liver by protamine-enhanced-asialofetuin-lipoplexes. *Gene Ther.* **10**, 5–14 (2003).

270. Maitani, Y., Kawano, K., Yamada, K., Nagai, T. & Takayama, K. Efficiency of liposomes surface-modified with soybean-derived sterylglucoside as a liver targeting carrier in HepG2 cells. *J. Controlled Release* **75**, 381–389 (2001).

271. Shimizu, K., Maitani, Y., Takayama, K. & Nagai, T. Formulation of liposomes with a soybean-derived sterylglucoside mixture and cholesterol for liver targeting. *Biol. Pharm. Bull.* **20**, 881–886 (1997).

272. Kawakami, S. & Hashida, M. Glycosylation-mediated targeting of carriers. *J. Controlled Release* **190**, 542–555 (2014).

273. Nishikawa, M. Development of cell-specific targeting systems for drugs and genes. *Biol. Pharm. Bull.* **28**, 195–200 (2005).

274. Tsuchiya, S., Aramaki, Y., Hara, T., Hosoi, K. & Okada, A. Preparation and disposition of asialofetuin-labelled liposome. *Biopharm. Drug Dispos.* **7**, 549–558 (1986).

275. Kara, T., Ishihara, H., Aramaki, Y. & Tsuchiya, S. Specific uptake of asialofetuin-labeled liposomes by isolated hepatocytes. *Int. J. Pharm.* **42**, 69–75 (1988).

276. Detampel, P., Witzigmann, D., Krähenbühl, S. & Huwyler, J. Hepatocyte targeting using pegylated asialofetuin-conjugated liposomes. *J. Drug Target.* **22**, 232–241 (2014).

277. Wu, J., Liu, P., Zhu, J. L., Maddukuri, S. & Zern, M. A. Increased liver uptake of liposomes and improved targeting efficacy by labeling with asialofetuin in rodents. *Hepatol. Baltim. Md* **27**, 772–778 (1998).

278. Motoyama, K. *et al.* In Vitro Gene Delivery Mediated by Asialofetuin-Appended Cationic Liposomes Associated with γ-Cyclodextrin into Hepatocytes. *Journal of Drug Delivery* vol. 2011 e476137 https://www.hindawi.com/journals/jdd/2011/476137/ (2011).

279. Díez, S., Navarro, G. & de ILarduya, C. T. In vivo targeted gene delivery by cationic nanoparticles for treatment of hepatocellular carcinoma. *J. Gene Med.* **11**, 38–45 (2009).

280. Yang, D. Y., Ouyang, C. H., Lu, F. G., Liu, X. W. & Huang, L. Q. Targeting specificity and pharmacokinetics of asialoorosomucoid, a specific ligand for asialglycoprotein receptor on hepatocyte. *J. Dig. Dis.* **8**, 89–95 (2007).

281. Peng, D.-J. *et al.* Inhibition of hepatocarcinoma by systemic delivery of Apoptin gene via the hepatic asialoglycoprotein receptor. *Cancer Gene Ther.* **14**, 66–73 (2007).

282. Cutone, A. *et al.* Lactoferrin's Anti-Cancer Properties: Safety, Selectivity, and Wide Range of Action. *Biomolecules* **10**, (2020).

283. Bennatt, D. J., Ling, Y. Y. & McAbee, D. D. Isolated rat hepatocytes bind lactoferrins by the RHL-1 subunit of the asialoglycoprotein receptor in a galactose-independent manner. *Biochemistry* **36**, 8367–8376 (1997).

284. Oh, S. T. *et al.* Lactoferrin as a gene delivery vehicle to hepatocytes. *Exp. Mol. Med.* **29**, 111–116 (1997).

285. Wei, M. *et al.* Hepatocellular carcinoma targeting effect of PEGylated liposomes modified with lactoferrin. *Eur. J. Pharm. Sci. Off. J. Eur. Fed. Pharm. Sci.* **46**, 131–141 (2012).

286. Wei, M. *et al.* Lactoferrin-modified PEGylated liposomes loaded with doxorubicin for targeting delivery to hepatocellular carcinoma. *Int. J. Nanomedicine* **10**, 5123–5137 (2015).

287. Nishikawa, M. *et al.* Synthesis and pharmacokinetics of a new liver-specific carrier, glycosylated carboxymethyl-dextran, and its application to drug targeting. *Pharm. Res.* **10**, 1253–1261 (1993).

288. Joshi, V. M. & Devarajan, P. V. Receptor-mediated hepatocyte-targeted delivery of primaquine phosphate nanocarboplex using a carbohydrate ligand. *Drug Deliv. Transl. Res.* **4**, 353–364 (2014).

289. Wu, D.-Q. *et al.* Galactosylated fluorescent labeled micelles as a liver targeting drug carrier. *Biomaterials* **30**, 1363–1371 (2009).

290. Liu, X. *et al.* Asialoglycoprotein receptor-targeted liposomes loaded with a norcantharimide derivative for hepatocyte-selective targeting. *Int. J. Pharm.* **520**, 98–110 (2017).

291. Chen, S. *et al.* Development of lipid nanoparticle formulations of siRNA for hepatocyte gene silencing following subcutaneous administration. *J. Control. Release Off. J. Control. Release Soc.* **196**, 106–112 (2014).

292. Kim, I.-S. & Kim, S.-H. Development of polymeric nanoparticulate drug delivery systems: evaluation of nanoparticles based on biotinylated poly(ethylene glycol) with sugar moiety. *Int. J. Pharm.* **257**, 195–203 (2003).

293. Hosseinkhani, H., Aoyama, T., Ogawa, O. & Tabata, Y. Liver targeting of plasmid DNA by pullulan conjugation based on metal coordination. *J. Control. Release Off. J. Control. Release Soc.* **83**, 287–302 (2002).

294. Narainpersad, N., Singh, M. & Ariatti, M. Novel neo glycolipid: formulation into pegylated cationic liposomes and targeting of DNA lipoplexes to the hepatocyte-derived cell line HepG2. *Nucleosides Nucleotides Nucleic Acids* **31**, 206–223 (2012).

295. Naicker, K., Ariatti, M. & Singh, M. PEGylated galactosylated cationic liposomes for hepatocytic gene delivery. *Colloids Surf. B Biointerfaces* **122**, 482–490 (2014).

296. Di Stefano, G., Busi, C., Camerino, A., Nardo, B. & Fiume, L. Enhanced liver blood concentrations of adenine arabinoside accomplished by lactosaminated poly-L-lysine coupling: implications for regional chemotherapy of hepatic micrometastases. *Biochem. Pharmacol.* **59**, 301–304 (2000).

297. Di Stefano, G. *et al.* Ribavirin conjugated with lactosaminated poly-L-lysine: selective delivery to the liver and increased antiviral activity in mice with viral hepatitis. *Biochem. Pharmacol.* **54**, 357–363 (1997).

298. Hashida, M., Takemura, S., Nishikawa, M. & Takakura, Y. Targeted delivery of plasmid DNA complexed with galactosylated poly(L-lysine). *J. Control. Release Off. J. Control. Release Soc.* **53**, 301–310 (1998).

299. Fiume, L. *et al.* Hepatotropic conjugate of adenine arabinoside monophosphate with lactosaminated poly-L-lysine. Synthesis of the carrier and pharmacological properties of the conjugate. *J. Hepatol.* **26**, 253–259 (1997).

300. Fiume, L. *et al.* Galactosylated poly(L-lysine) as a hepatotropic carrier of 9-beta-D-arabinofuranosyladenine 5'-monophosphate. *FEBS Lett.* **203**, 203–206 (1986).

301. Zheng, S.-J. *et al.* Distribution and anti-HBV effects of antisense oligodeoxynu-cleotides conjugated to galactosylated poly-L-lysine. *World J. Gastroenterol. WJG* **9**, 1251–1255 (2003).

302. Hashida, M., Akamatsu, K., Nishikawa, M., Yamashita, F. & Takakura, Y. Design of polymeric prodrugs of prostaglandin E(1) having galactose residue for hepatocyte targeting. *J. Control. Release Off. J. Control. Release Soc.* **62**, 253–262 (1999).

303. Akamatsu, K., Yamasaki, Y., Nishikawa, M., Takakura, Y. & Hashida, M. Development of a hepatocyte-specific prostaglandin E(1) polymeric prodrug and its potential for preventing carbon tetrachloride-induced fulminant hepatitis in mice. *J. Pharmacol. Exp. Ther.* **290**, 1242–1249 (1999).

304. Hirabayashi, H., Nishikawa, M., Takakura, Y. & Hashida, M. Development and pharmacokinetics of galactosylated poly-L-glutamic acid as a biodegradable carrier for liver-specific drug delivery. *Pharm. Res.* **13**, 880–884 (1996).

305. Tomiya, N. *et al.* Liver-targeting of primaquine-(poly-γ-glutamic acid) and its degradation in rat hepatocytes. *Bioorg. Med. Chem.* **21**, 5275–5281 (2013).

306. Jiang, H.-L. *et al.* Galactosylated poly(ethylene glycol)-chitosan-graft-polyethylenimine as a gene carrier for hepatocyte-targeting. *J. Control. Release Off. J. Control. Release Soc.* **131**, 150–157 (2008).

307. Ma, J. *et al.* Inhibition of hepatitis B virus and induction of hepatoma cell apoptosis by ASGPR-directed delivery of shRNAs. *PloS One* **7**, e46096 (2012).

308. Zanta, M. A., Boussif, O., Adib, A. & Behr, J. P. In vitro gene delivery to hepatocytes with galactosylated polyethylenimine. *Bioconjug. Chem.* **8**, 839–844 (1997).

309. Fumoto, S. *et al.* Analysis of hepatic disposition of native and galactosylated polyethylenimine complexed with plasmid DNA in perfused rat liver. *Drug Metab. Pharmacokinet.* **18**, 230–237 (2003).

310. Morimoto, K. *et al.* Molecular weight-dependent gene transfection activity of unmodified and galactosylated polyethyleneimine on hepatoma cells and mouse liver. *Mol. Ther. J. Am. Soc. Gene Ther.* **7**, 254–261 (2003).

311. Sagara, K. & Kim, S. W. A new synthesis of galactose-poly(ethylene glycol)-polyethylenimine for gene delivery to hepatocytes. *J. Control. Release Off. J. Control. Release Soc.* **79**, 271–281 (2002).

312. Bettinger, T., Remy, J. S. & Erbacher, P. Size reduction of galactosylated PEI/DNA complexes improves lectin-mediated gene transfer into hepatocytes. *Bioconjug. Chem.* **10**, 558–561 (1999).

313. Cheng, M. *et al.* Synthesis and efficient hepatocyte targeting of galactosylated chitosan as a gene carrier in vitro and in vivo. *J. Biomed. Mater. Res. B Appl. Biomater.* **99**, 70–80 (2011).

314. Jain, N., Rajoriya, V., Jain, P. K. & Jain, A. K. Lactosaminated-N-succinyl chitosan nanoparticles for hepatocyte-targeted delivery of acyclovir. *J. Nanoparticle Res.* **16**, 2136 (2013).

315. Wei, W. *et al.* Galactosylated nanocrystallites of insoluble anticancer drug for liver-targeting therapy: an in vitro evaluation. *Nanomed.* **5**, 589–596 (2010).

316. Villa, R. *et al.* Targeted doxorubicin delivery by chitosan-galactosylated modified polymer microbubbles to hepatocarcinoma cells. *Colloids Surf. B Biointerfaces* **110**, 434–442 (2013).

317. Zhu, X. L. *et al.* Galactosylated Chitosan Oligosaccharide Nanoparticles for Hepatocellular Carcinoma Cell-Targeted Delivery of Adenosine Triphosphate. *Int. J. Mol. Sci.* **14**, 15755–15766 (2013).

318. Jain, N. K. & Jain, S. K. Development and in vitro characterization of galactosylated low molecular weight chitosan nanoparticles bearing doxorubicin. *AAPS PharmSciTech* **11**, 686–697 (2010).

319. Guan, M. *et al.* Uptake and transport of a novel anticancer drug-delivery system: lactosyl-norcantharidin-associated N-trimethyl chitosan nanoparticles across intestinal Caco-2 cell monolayers. *Int. J. Nanomedicine* **7**, 1921–1930 (2012).

320. Wang, Q. *et al.* Norcantharidin-associated galactosylated chitosan nanoparticles for hepatocyte-targeted delivery. *Nanomedicine Nanotechnol. Biol. Med.* **6**, 371–381 (2010).

321. Yousef, S., Alsaab, H. O., Sau, S. & Iyer, A. K. Development of asialoglycoprotein receptor directed nanoparticles for selective delivery of curcumin derivative to hepatocellular carcinoma. *Heliyon* **4**, (2018).

322. Cao, Y. *et al.* Targeted CT imaging of human hepatocellular carcinoma using low-generation dendrimer-entrapped gold nanoparticles modified with lactobionic acid. *J. Mater. Chem. B* **3**, 286–295 (2014).

323. Wada, K., Arima, H., Tsutsumi, T., Hirayama, F. & Uekama, K. Enhancing effects of galactosylated dendrimer/alpha-cyclodextrin conjugates on gene transfer efficiency. *Biol. Pharm. Bull.* **28**, 500–505 (2005).

324. Liu, H. *et al.* Lactobionic Acid-Modified Dendrimer-Entrapped Gold Nanoparticles for Targeted Computed Tomography Imaging of Human Hepatocellular Carcinoma. *ACS Appl. Mater. Interfaces* **6**, 6944–6953 (2014).

325. Medina, S. H. *et al.* Enzyme-activated nanoconjugates for tunable release of doxorubicin in hepatic cancer cells. *Biomaterials* **34**, 4655–4666 (2013).

326. Medina, S. H. *et al.* N-acetylgalactosamine-functionalized dendrimers as hepatic cancer cell-targeted carriers. *Biomaterials* **32**, 4118–4129 (2011).

327. Kuruvilla, S. P., Tiruchinapally, G., Kaushal, N. & ElSayed, M. E. H. Effect of N-acetylgalactosamine ligand valency on targeting dendrimers to hepatic cancer cells. *Int. J. Pharm.* **545**, 27–36 (2018).

328. Kuruvilla, S. P., Tiruchinapally, G., ElAzzouny, M. & ElSayed, M. E. H. N-Acetylgalactosamine-Targeted Delivery of Dendrimer-Doxorubicin Conjugates Influences Doxorubicin Cytotoxicity and Metabolic Profile in Hepatic Cancer Cells. *Adv. Healthc. Mater.* **6**, (2017).

329. Kim, E.-M. *et al.* Asialoglycoprotein-receptor-targeted hepatocyte imaging using 99mTc galactosylated chitosan. *Nucl. Med. Biol.* **33**, 529–534 (2006).

330. Seymour, L. W. *et al.* Hepatic drug targeting: phase I evaluation of polymer-bound doxorubicin. *J. Clin. Oncol. Off. J. Am. Soc. Clin. Oncol.* **20**, 1668–1676 (2002).

331. Suo, A., Qian, J., Yao, Y. & Zhang, W. Galactosylated poly(ethylene glycol)-b-poly (l-lactide-co-β-malic acid) block copolymer micelles for targeted drug delivery: preparation and in vitro characterization. *Int. J. Nanomedicine* **5**, 1029–1038 (2010).

332. Wang, Z. *et al.* Amphiphilic Diblock Terpolymer PMAgala-b-P(MAA-co-MAChol)s with Attached Galactose and Cholesterol Grafts and Their Intracellular pH-Responsive Doxorubicin Delivery. *Biomacromolecules* **17**, 98–110 (2016).

333. Wang, Y., Jiang, G., Qiu, T. & Ding, F. Preparation and evaluation of paclitaxel-loaded nanoparticle incorporated with galactose-carrying polymer for hepatocyte targeted delivery. *Drug Dev. Ind. Pharm.* **38**, 1039–1046 (2012).

334. Varshosaz, J., Hassanzadeh, F., Sadeghi, H. & Khadem, M. Galactosylated nanostructured lipid carriers for delivery of 5-FU to hepatocellular carcinoma. *J. Liposome Res.* **22**, 224–236 (2012).

335. Ong, Z. Y. *et al.* Galactose-functionalized cationic polycarbonate diblock copolymer for targeted gene delivery to hepatocytes. *Macromol. Rapid Commun.* **34**, 1714–1720 (2013).

336. Kim, T. H., Park, I. K., Nah, J. W., Choi, Y. J. & Cho, C. S. Galactosylated chitosan/DNA nanoparticles prepared using water-soluble chitosan as a gene carrier. *Biomaterials* **25**, 3783–3792 (2004).

337. Hopewel, J. W., Duncan, R., Wilding, D. & Chakrabarti, K. Preclinical evaluation of the cardiotoxicity of PK2: a novel HPMA copolymer-doxorubicin-galactosamine conjugate antitumour agent. *Hum. Exp. Toxicol.* **20**, 461–470 (2001).

338. Julyan, P. J. *et al.* Preliminary clinical study of the distribution of HPMA copolymers bearing doxorubicin and galactosamine. *J. Control. Release Off. J. Control. Release Soc.* **57**, 281–290 (1999).

339. Hu, H., Zhang, X., Zhong, N. & Pan, S. Study on galactose-poly(ethylene glycol)-poly(L-lysine) as novel gene vector for targeting hepatocytes in vitro. *J. Biomater. Sci. Polym. Ed.* **23**, 677–695 (2012).

340. Hashida, M., Hirabayashi, H., Nishikawa, M. & Takakura, Y. Targeted delivery of drugs and proteins to the liver via receptor-mediated endocytosis. *J. Controlled Release* **46**, 129–137 (1997).

341. Li, X., Wu, Q., Chen, Z., Gong, X. & Lin, X. Preparation, characterization and controlled release of liver-targeting nanoparticles from the amphiphilic random copolymer. *Polymer* **49**, 4769–4775 (2008).

342. Tao, Y. *et al.* Galactosylated biodegradable poly(ε-caprolactone-co-phosphoester) random copolymer nanoparticles for potent hepatoma-targeting delivery of doxorubicin. *Polym. Chem.* **5**, 3443–3452 (2014).

343. Chen, W. *et al.* Glyco-Nanoparticles with Sheddable Saccharide Shells: A Unique and Potent Platform for Hepatoma-Targeting Delivery of Anticancer Drugs. *Biomacromolecules* **15**, 900–907 (2014).

344. Pujol, A. M. *et al.* Hepatocyte targeting and intracellular copper chelation by a thiol-containing glycocyclopeptide. *J. Am. Chem. Soc.* **133**, 286–296 (2011).

345. Wang, W. *et al.* Galactosylated solid lipid nanoparticles with cucurbitacin B improves the liver targetability. *Drug Deliv.* **17**, 114–122 (2010).

346. Chen, G. *et al.* Targeted delivery of doxorubicin by lactobionic acid-modified laponite to hepatocarcinoma cells. *J. Control. Release Off. J. Control. Release Soc.* **213**, e34 (2015).

347. Lv, Y. *et al.* Targeted delivery and controlled release of doxorubicin into cancer cells using a multifunctional graphene oxide. *Mater. Sci. Eng. C Mater. Biol. Appl.* **59**, 652–660 (2016).

348. Fu, F. *et al.* Multifunctional lactobionic acid-modified dendrimers for targeted drug delivery to liver cancer cells: investigating the role played by PEG spacer. *ACS Appl. Mater. Interfaces* **6**, 16416–16425 (2014).

349. Janas, M. M. *et al.* Selection of GalNAc-conjugated siRNAs with limited off-target-driven rat hepatotoxicity. *Nat. Commun.* **9**, 1–10 (2018).

350. Hai, L., Zhang, Z.-R., Wang, S., Xiao, X. & Wu, Y. Synthesis of Multivalent Galactosides as Targeting Ligand for Gene Delivery. *Synth. Commun.* **40**, 1802–1811 (2010).

351. Zimmermann, T. S. *et al.* Clinical Proof of Concept for a Novel Hepatocyte-Targeting GalNAc-siRNA Conjugate. *Mol. Ther.* **25**, 71–78 (2017).

352. Zhang, X. *et al.* Patisiran Pharmacokinetics, Pharmacodynamics, and Exposure-Response Analyses in the Phase 3 APOLLO Trial in Patients With Hereditary Transthyretin-Mediated (hATTR) Amyloidosis. *J. Clin. Pharmacol.* **60**, 37–49 (2020).

353. APOLLO: The Study of an Investigational Drug, Patisiran (ALN-TTR02), for the Treatment of Transthyretin (TTR)-Mediated Amyloidosis - Full Text View - ClinicalTrials.gov. https://clinicaltrials.gov/ct2/show/NCT01960348.

354. Sardh, E. *et al.* Phase 1 Trial of an RNA Interference Therapy for Acute Intermittent Porphyria. *N. Engl. J. Med.* **380**, 549–558 (2019).

355. ENVISION: A Study to Evaluate the Efficacy and Safety of Givosiran (ALN-AS1) in Patients With Acute Hepatic Porphyrias (AHP) - Study Results - ClinicalTrials.gov. https://clinicaltrials.gov/ct2/show/results/NCT03338816.

356. Daar, S. & Pathare, A. V. Combined therapy with desferrioxamine and deferiprone in beta thalassemia major patients with transfusional iron overload. *Ann. Hematol.* **85**, 315–319 (2006).

357. Hamilton, J. L. & Kizhakkedathu, J. N. Polymeric nanocarriers for the treatment of systemic iron overload. *Mol. Cell. Ther.* **3**, (2015).

358. Sheth, S. Iron chelation: an update. *Curr. Opin. Hematol.* **21**, 179 (2014).

359. Galey, J. B. Recent advances in the design of iron chelators against oxidative damage. *Mini Rev. Med. Chem.* **1**, 233–242 (2001).

360. Sezaki, H. & Hashida, M. Macromolecule-drug conjugates in targeted cancer chemotherapy. *Crit. Rev. Ther. Drug Carrier Syst.* **1**, 1–38 (1984).

361. Takakura, Y. & Hashida, M. Macromolecular carrier systems for targeted drug delivery: pharmacokinetic considerations on biodistribution. *Pharm. Res.* **13**, 820–831 (1996).

362. Poelstra, K., Prakash, J. & Beljaars, L. Drug targeting to the diseased liver. *J. Controlled Release* **161**, 188–197 (2012).

363. Schlepper-Schäfer, J., Kolb-Bachofen, V. & Kolb, H. Analysis of lectin-dependent recognition of desialylated erythrocytes by Kupffer cells. *Biochem. J.* **186**, 827 (1980).

364. Kolb, H., Vogt, D. & Kolb-Bachofen, V. Does the D-galactose receptor on Kupffer cells recycle? *Biochem. J.* **200**, 445 (1981).

365. Kolb-Bachofen, V., Schlepper-Schäfer, J., Vogell, W. & Kolb, H. Electron microscopic evidence for an asialoglycoprotein receptor on kupffer cells: Localization of lectin-mediated endocytosis. *Cell* **29**, 859–866 (1982).

366. Coombs, P. J., Taylor, M. E. & Drickamer, K. Two categories of mammalian galactose-binding receptors distinguished by glycan array profiling. *Glycobiology* **16**, 1C-7C (2006).

367. Hillaireau, H. & Couvreur, P. Nanocarriers' entry into the cell: relevance to drug delivery. *Cell. Mol. Life Sci.* **66**, 2873–2896 (2009).

368. Park, J.-H., Cho, E.-W., Shin, S. Y., Lee, Y.-J. & Kim, K. L. Detection of the Asialoglycoprotein Receptor on Cell Lines of Extrahepatic Origin. *Biochem. Biophys. Res. Commun.* **244**, 304–311 (1998).

369. Tomoda, H., Kishimoto, Y. & Lee, Y. C. Temperature effect on endocytosis and exocytosis by rabbit alveolar macrophages. *J. Biol. Chem.* **264**, 15445–15450 (1989).

370. Kainthan, R. K., Hester, S. R., Levin, E., Devine, D. V. & Brooks, D. E. In vitro biological evaluation of high molecular weight hyperbranched polyglycerols. *Biomaterials* **28**, 4581–4590 (2007).

371. Kainthan, R. K. & Brooks, D. E. In vivo biological evaluation of high molecular weight hyperbranched polyglycerols. *Biomaterials* **28**, 4779–4787 (2007).

372. Kainthan, R. K., Janzen, J., Levin, E., Devine, D. V. & Brooks, D. E. Biocompatibility testing of branched and linear polyglycidol. *Biomacromolecules* **7**, 703–709 (2006).

373. Akinc, A. *et al.* The Onpattro story and the clinical translation of nanomedicines containing nucleic acid-based drugs. *Nat. Nanotechnol.* **14**, 1084–1087 (2019).

374. Mishra, N. *et al.* Efficient Hepatic Delivery of Drugs: Novel Strategies and Their Significance. *BioMed Res. Int.* **2013**, (2013).

375. Doshi, N. *et al.* Flow and adhesion of drug carriers in blood vessels depend on their shape: a study using model synthetic microvascular networks. *J. Control. Release Off. J. Control. Release Soc.* **146**, 196–200 (2010).

376. Decuzzi, P. *et al.* Size and shape effects in the biodistribution of intravascularly injected particles. *J. Control. Release Off. J. Control. Release Soc.* **141**, 320–327 (2010).

377. Nakamura, K., Funakoshi, H., Miyamoto, K., Tokunaga, F. & Nakamura, T. Molecular cloning and functional characterization of a human scavenger receptor with C-type lectin (SRCL), a novel member of a scavenger receptor family. *Biochem. Biophys. Res. Commun.* **280**, 1028–1035 (2001).

378. Harashima, H. & Kiwada, H. Liposomal targeting and drug delivery: kinetic consideration. *Adv. Drug Deliv. Rev.* **19**, 425–444 (1996).

379. Managit, C., Kawakami, S., Yamashita, F. & Hashida, M. Effect of galactose density on asialoglycoprotein receptor-mediated uptake of galactosylated liposomes. *J. Pharm. Sci.* **94**, 2266–2275 (2005).

380. Hirabayashi, H., Nishikawa, M., Takakura, Y. & Hashida, M. Development and Pharmacokinetics of Galactosylated Poly-L-Glutamic Acid as a Biodegradable Carrier for Liver-Specific Drug Delivery. *Pharm. Res.* **13**, 880–884 (1996).

381. Nishikawa, M., Miyazaki, C., Yamashita, F., Takakura, Y. & Hashida, M. Galactosylated proteins are recognized by the liver according to the surface density of galactose moieties. *Am. J. Physiol.* **268**, G849-856 (1995).

382. Dalal, C. & Jana, N. R. Galactose Multivalency Effect on the Cell Uptake Mechanism of Bioconjugated Nanoparticles. *J. Phys. Chem. C* **122**, 25651–25660 (2018).

383. Sanhueza, C. A. *et al.* Efficient Liver Targeting by Polyvalent Display of a Compact Ligand for the Asialoglycoprotein Receptor. *J. Am. Chem. Soc.* **139**, 3528–3536 (2017).

384. Hatcher, H. C., Singh, R. N., Torti, F. M. & Torti, S. V. Synthetic and natural iron chelators: therapeutic potential and clinical use. *Future Med. Chem.* **1**, (2009).

385. Huang, X., Leroux, J.-C. & Castagner, B. Well-Defined Multivalent Ligands for Hepatocytes Targeting via Asialoglycoprotein Receptor. *Bioconjug. Chem.* **28**, 283–295 (2017).

386. Youle, R. J., Murray, G. J. & Neville, D. M. Studies on the galactose-binding site of ricin and the hybrid toxin Man6P-ricin. *Cell* **23**, 551–559 (1981).

387. Bosmann, H. B., Hagopian, A. & Eylar, E. H. Glycoprotein biosynthesis: The characterization of two glycoprotein: Fucosyl transferases in HeLa cells. *Arch. Biochem. Biophys.* **128**, 470–481 (1968).

388. Liu, L., Ruan, Z., Li, T., Yuan, P. & Yan, L. Near infrared imaging-guided photodynamic therapy under an extremely low energy of light by galactose targeted amphiphilic polypeptide micelle encapsulating BODIPY-Br2. *Biomater. Sci.* **4**, 1638–1645 (2016).

389. Thapa, B., Kumar, P., Zeng, H. & Narain, R. Asialoglycoprotein Receptor-Mediated Gene Delivery to Hepatocytes Using Galactosylated Polymers. *Biomacromolecules* **16**, 3008–3020 (2015).

390. Blanco, E., Shen, H. & Ferrari, M. Principles of nanoparticle design for overcoming biological barriers to drug delivery. *Nat. Biotechnol.* **33**, 941–951 (2015).

391. Hua, S., de Matos, M. B. C., Metselaar, J. M. & Storm, G. Current Trends and Challenges in the Clinical Translation of Nanoparticulate Nanomedicines: Pathways for Translational Development and Commercialization. *Front. Pharmacol.* **9**, 790 (2018).

392. Liu, J., Yu, M., Zhou, C. & Zheng, J. Renal clearable inorganic nanoparticles: a new frontier of bionanotechnology. *Mater. Today* **16**, 477–486 (2013).

393. Choi, H. S. *et al.* Renal clearance of quantum dots. *Nat. Biotechnol.* **25**, 1165–1170 (2007).

394. Braet, F. *et al.* Contribution of high-resolution correlative imaging techniques in the study of the liver sieve in three-dimensions. *Microsc. Res. Tech.* **70**, 230–242 (2007).

395. Chen, L. T. & Weiss, L. The role of the sinus wall in the passage of erythrocytes through the spleen. *Blood* **41**, 529–537 (1973).

396. Tsoi, K. M. *et al.* Mechanism of hard-nanomaterial clearance by the liver. *Nat. Mater.* **15**, 1212–1221 (2016).

397. Zhang, Y.-N., Poon, W., Tavares, A. J., McGilvray, I. D. & Chan, W. C. W. Nanoparticle-liver interactions: Cellular uptake and hepatobiliary elimination. *J. Control. Release Off. J. Control. Release Soc.* **240**, 332–348 (2016).

398. Furumoto, K. *et al.* Biliary excretion of polystyrene microspheres depends on the type of receptor-mediated uptake in rat liver. *Biochim. Biophys. Acta* **1526**, 221–226 (2001).

399. Renaud, G., Hamilton, R. L. & Havel, R. J. Hepatic metabolism of colloidal gold-low-density lipoprotein complexes in the rat: evidence for bulk excretion of lysosomal contents into bile. *Hepatol. Baltim. Md* **9**, 380–392 (1989).

400. Seo, H. J. *et al.* Rapid Hepatobiliary Excretion of Micelle-Encapsulated/Radiolabeled Upconverting Nanoparticles as an Integrated Form. *Sci. Rep.* **5**, 15685 (2015).

401. Souris, J. S. *et al.* Surface charge-mediated rapid hepatobiliary excretion of mesoporous silica nanoparticles. *Biomaterials* **31**, 5564–5574 (2010).

402. Moghimi, S. M., Hunter, A. C. & Murray, J. C. Long-circulating and target-specific nanoparticles: theory to practice. *Pharmacol. Rev.* **53**, 283–318 (2001).

403. Zhang, L. *et al.* Softer zwitterionic nanogels for longer circulation and lower splenic accumulation. *ACS Nano* **6**, 6681–6686 (2012).

404. Kato, Y., Onishi, H. & Machida, Y. Biological characteristics of lactosaminated N-succinyl-chitosan as a liver-specific drug carrier in mice. *J. Control. Release Off. J. Control. Release Soc.* **70**, 295–307 (2001).

405. Bayer, N. *et al.* Effect of bafilomycin A1 and nocodazole on endocytic transport in HeLa cells: implications for viral uncoating and infection. *J. Virol.* **72**, 9645–9655 (1998).

406. Bolger-Munro, M. *et al.* Arp2/3 complex-driven spatial patterning of the BCR enhances immune synapse formation, BCR signaling and B cell activation. *eLife* **8**, e44574 (2019).

407. Bolger-Munro, M. *et al. Arp2/3 complex-driven spatial patterning of the BCR enhances immune synapse formation, BCR signaling and cell activation*. http://biorxiv.org/lookup/doi/10.1101/490698 (2018) doi:10.1101/490698.

408. Bolte, S. & Cordelières, F. P. A guided tour into subcellular colocalization analysis in light microscopy. *J. Microsc.* **224**, 213–232 (2006).

409. Manders, E. M. M. *et al.* Four-dimensional imaging of chromatin dynamics during the assembly of the interphase nucleus. *Chromosome Res.* **11**, 537–547 (2003).

410. Manders, E. M. M., Verbeek, F. J. & Aten, J. A. Measurement of co-localization of objects in dual-colour confocal images. *J. Microsc.* **169**, 375–382 (1993).

411. Zhou, H. *et al.* Dense and Dynamic Polyethylene Glycol Shells Cloak Nanoparticles from Uptake by Liver Endothelial Cells for Long Blood Circulation. *ACS Nano* **12**, 10130–10141 (2018).

412. Black, M. RBC Lysing Solutions and Cell Lysing Procedure.

413. Dunn, W. A., LaBadie, J. H. & Aronson, N. N. Inhibition of 125I-asialofetuin catabolism by leupeptin in the perfused rat liver and in vivo. *J. Biol. Chem.* **254**, 4191–4196 (1979).

414. Shi, B., Abrams, M. & Sepp-Lorenzino, L. Expression of Asialoglycoprotein Receptor 1 in Human Hepatocellular Carcinoma. *J. Histochem. Cytochem.* **61**, 901–909 (2013).

415. Huotari, J. & Helenius, A. Endosome maturation. *EMBO J.* **30**, 3481–3500 (2011).

416. Anselmo, A. C. & Mitragotri, S. Nanoparticles in the clinic. *Bioeng. Transl. Med.* **1**, 10–29 (2016).

417. Giardiello, M. *et al.* Accelerated oral nanomedicine discovery from miniaturized screening to clinical production exemplified by paediatric HIV nanotherapies. *Nat. Commun.* **7**, 13184 (2016).

418. Wang, B., He, X., Zhang, Z., Zhao, Y. & Feng, W. Metabolism of nanomaterials in vivo: blood circulation and organ clearance. *Acc. Chem. Res.* **46**, 761–769 (2013).

419. Gustafson, H. H., Holt-Casper, D., Grainger, D. W. & Ghandehari, H. Nanoparticle Uptake: The Phagocyte Problem. *Nano Today* **10**, 487–510 (2015).

420. Tavares, A. J. *et al.* Effect of removing Kupffer cells on nanoparticle tumor delivery. *Proc. Natl. Acad. Sci. U. S. A.* **114**, E10871–E10880 (2017).

421. Marin, E., Briceño, M. I. & Caballero-George, C. Critical evaluation of biodegradable polymers used in nanodrugs. *Int. J. Nanomedicine* **8**, 3071–3090 (2013).

422. Singh, D., Dilnawaz, F. & Sahoo, S. K. Challenges of moving theranostic nanomedicine into the clinic. *Nanomed.* **15**, 111–114 (2020).

423. Nair, J. K. *et al.* Multivalent N-acetylgalactosamine-conjugated siRNA localizes in hepatocytes and elicits robust RNAi-mediated gene silencing. *J. Am. Chem. Soc.* **136**, 16958–16961 (2014).

424. Staud, F., Nishikawa, M., Takakura, Y. & Hashida, M. Liver uptake and hepato-biliary transfer of galactosylated proteins in rats are determined by the extent of galactosylation. *Biochim. Biophys. Acta BBA - Gen. Subj.* **1427**, 183–192 (1999).

425. Boyer, J. L. Bile Formation and Secretion. *Compr. Physiol.* **3**, 1035–1078 (2013).

426. Kim, S.-H., Goto, M. & Akaike, T. Specific Binding of Glucose-derivatized Polymers to the Asialoglycoprotein Receptor of Mouse Primary Hepatocytes. *J. Biol. Chem.* **276**, 35312–35319 (2001).

427. Lai, C.-H. *et al.* Galactose Encapsulated Multifunctional Nanoparticle for HepG2 Cell Internalization. *Adv. Funct. Mater.* **20**, 3948–3958 (2010).

428. Kolatkar, A. R. & Weis, W. I. Structural basis of galactose recognition by C-type animal lectins. *J. Biol. Chem.* **271**, 6679–6685 (1996).

429. Takahashi, H., Onishi, H. & Machida, Y. Glycyrrhetic acid-loaded microparticles: liver-specific delivery and therapeutic potential against carbon tetrachloride-induced hepatitis. *J. Pharm. Pharmacol.* **56**, 437–444 (2004).

430. Mu, F.-T. *et al.* EEA1, an Early Endosome-Associated Protein. EEA1 IS A CONSERVED α-HELICAL PERIPHERAL MEMBRANE PROTEIN FLANKED BY CYSTEINE "FINGERS" AND CONTAINS A CALMODULIN-BINDING IQ MOTIF. *J. Biol. Chem.* **270**, 13503–13511 (1995).

431. Pietrangelo, A. Iron in NASH, chronic liver diseases and HCC: How much iron is too much? *J. Hepatol.* **50**, 249–251 (2009).

432. Jenner, G. A., Longerich, H. P., Jackson, S. E. & Fryer, B. J. ICP-MS — A powerful tool for high-precision trace-element analysis in Earth sciences: Evidence from analysis of selected U.S.G.S. reference samples. *Chem. Geol.* **83**, 133–148 (1990).

433. Giannini, E. G., Testa, R. & Savarino, V. Liver enzyme alteration: a guide for clinicians. *CMAJ Can. Med. Assoc. J. J. Assoc. Medicale Can.* **172**, 367–379 (2005).

434. Guo, S. *et al.* Polymeric Nanoparticles Enhance the Ability of Deferoxamine To Deplete Hepatic and Systemic Iron. *Nano Lett.* **18**, 5782–5790 (2018).

435. Svoboda, M., Vaňhara, J. & Berlinská, J. Parenteral iron administration in suckling piglets – a review. *Acta Vet. Brno* **86**, 249–261 (2017).

436. Dabbagh, A. J., Shwaery, G. T., Keaney, J. F. & Frei, B. Effect of iron overload and iron deficiency on atherosclerosis in the hypercholesterolemic rabbit. *Arterioscler. Thromb. Vasc. Biol.* **17**, 2638–2645 (1997).

437. Kidd, J. M., Abdelraouf, K. & Nicolau, D. P. Development of Neutropenic Murine Models of Iron Overload and Depletion To Study the Efficacy of Siderophore-Antibiotic Conjugates. *Antimicrob. Agents Chemother.* **64**, (2019).

438. Guenancia, C. *et al.* Paradoxically, iron overload does not potentiate doxorubicin-induced cardiotoxicity in vitro in cardiomyocytes and in vivo in mice. *Toxicol. Appl. Pharmacol.* **284**, 152–162 (2015).

439. Kidd, J. M., Abdelraouf, K. & Nicolau, D. P. Efficacy of Humanized Cefiderocol Exposure Is Unaltered by Host Iron Overload in the Thigh Infection Model. *Antimicrob. Agents Chemother.* **64**, (2019).

440. Marques, V. B. *et al.* Chronic iron overload intensifies atherosclerosis in apolipoprotein E deficient mice: Role of oxidative stress and endothelial dysfunction. *Life Sci.* **233**, 116702 (2019).

441. Frýdlová, J. *et al.* Effect of stimulated erythropoiesis on liver SMAD signaling pathway in iron-overloaded and iron-deficient mice. *PLoS One San Franc.* **14**, e0215028 (2019).

442. Simchick, G., Liu, Z., Nagy, T., Xiong, M. & Zhao, Q. Assessment of MR-based and quantitative susceptibility mapping for the quantification of liver iron concentration in a mouse model at 7T. *Magn. Reson. Med.* **80**, 2081–2093 (2018).

443. Cavey, T. *et al.* Spleen iron, molybdenum, and manganese concentrations are coregulated in hepcidin-deficient and secondary iron overload models in mice. *FASEB J. Off. Publ. Fed. Am. Soc. Exp. Biol.* **33**, 11072–11081 (2019).

444. Vidal, R. *et al.* Expression of a Mutant Form of the Ferritin Light Chain Gene Induces Neurodegeneration and Iron Overload in Transgenic Mice. *J. Neurosci.* **28**, 60–67 (2008).

445. Zhou, X. Y. *et al.* HFE gene knockout produces mouse model of hereditary hemochromatosis. *Proc. Natl. Acad. Sci.* **95**, 2492–2497 (1998).

446. Huang, F. W., Pinkus, J. L., Pinkus, G. S., Fleming, M. D. & Andrews, N. C. A mouse model of juvenile hemochromatosis. *J. Clin. Invest.* **115**, 2187–2191 (2005).

447. Daba, A., Gkouvatsos, K., Sebastiani, G. & Pantopoulos, K. Differences in activation of mouse hepcidin by dietary iron and parenterally administered iron dextran: compartmentalization is critical for iron sensing. *J. Mol. Med.* **91**, 95–102 (2013).

448. Richter, G. W. The iron-loaded cell--the cytopathology of iron storage. A review. *Am. J. Pathol.* **91**, 362–404 (1978).

449. Muir, A. R. & Golberg, L. Observations on subcutaneous macrophages. Phago-cytosis of iron-dextran and ferritin synthesis. *Q. J. Exp. Physiol. Cogn. Med. Sci.* **46**, 289–298 (1961).

450. Shoden, A. & Sturgeon, P. Iron Storage. *Am. J. Pathol.* **40**, 671–683 (1962).

451. Wyk, C. P. V., Linder-Horowitz, M. & Munro, H. N. Effect of Iron Loading on Non-Heme Iron Compounds in Different Liver Cell Populations. *J. Biol. Chem.* **246**, 1025–1031 (1971).

452. Bloomer, S. A. & Brown, K. E. Iron-Induced Liver Injury: A Critical Reappraisal. *Int. J. Mol. Sci.* **20**, (2019).

453. Greaves, P. Chapter 9 - Liver and Pancreas. in *Histopathology of Preclinical Toxicity Studies (Fourth Edition)* (ed. Greaves, P.) 433–535 (Academic Press, 2012). doi:10.1016/B978-0-444-53856-7.00009-9.

454. Yatmark, P. *et al.* Iron distribution and histopathological characterization of the liver and heart of β-thalassemic mice with parenteral iron overload: Effects of deferoxamine and deferiprone. *Exp. Toxicol. Pathol.* **66**, 333–343 (2014).

455. Musumeci, M. *et al.* Iron excretion in iron dextran-overloaded mice. *Blood Transfus. Trasfus. Sangue* **12**, 485–490 (2014).

456. Musumeci, M. *et al.* The C57BL/6 genetic background confers cardioprotection in iron-overloaded mice. *Blood Transfus.* **11**, 88–93 (2013).

457. Kruszewski, M. Labile iron pool: the main determinant of cellular response to oxidative stress. *Mutat. Res.* **531**, 81–92 (2003).

458. Kakhlon, O. & Cabantchik, Z. I. The labile iron pool: characterization, measurement, and participation in cellular processes. *Free Radic. Biol. Med.* **33**, 1037–1046 (2002).

459. Chutvanichkul, B., Vattanaviboon, P., Mas-Oodi, S., U-Pratya, Y. & Wanachiwanawin, W. Labile iron pool as a parameter to monitor iron overload and oxidative stress status in β-thalassemic erythrocytes. *Cytometry B Clin. Cytom.* **94**, 631–636 (2018).

460. Swart, L. de *et al.* Labile plasma iron levels predict survival in patients with lower-risk myelodysplastic syndromes. *Haematologica* **103**, 69–79 (2018).

461. Wermke, M. *et al.* Enhanced labile plasma iron and outcome in acute myeloid leukaemia and myelodysplastic syndrome after allogeneic haemopoietic cell transplantation (ALLIVE): a prospective, multicentre, observational trial. *Lancet Haematol.* **5**, e201–e210 (2018).

462. Glickstein, H., Ben El, R., Shvartsman, M. & Cabantchik, Z. I. Intracellular labile iron pools as direct targets of iron chelators: a fluorescence study of chelator action in living cells. *Blood* **106**, 3242–3250 (2005).

463. De Domenico, I., Ward, D. M. & Kaplan, J. Specific iron chelators determine the route of ferritin degradation. *Blood* **114**, 4546–4551 (2009).

464. Hoyes, K. P. & Porter, J. B. Subcellular distribution of desferrioxamine and hydroxypyridin-4-one chelators in K562 cells affects chelation of intracellular iron pools. *Br. J. Haematol.* **85**, 393–400 (1993).

465. Kimber, C. L., Mukherjee, T. & Deller, D. J. In vitro iron attachment to the intestinal brush border. *Am. J. Dig. Dis.* **18**, 781–791 (1973).

466. Slavin, W. Atomic absorption spectrometry. in *Methods in Enzymology* vol. 158 117–145 (Academic Press, 1988).

467. Bosscher, D. *et al.* In Vitro Availability of Calcium, Iron, and Zinc from First-Age Infant Formulae and Human Milk. *J. Pediatr. Gastroenterol. Nutr.* **32**, 54–58 (2001).

468. Felice, M. R. *et al.* Post-transcriptional Regulation of the Yeast High Affinity Iron Transport System. *J. Biol. Chem.* **280**, 22181–22190 (2005).

469. Riemer, J., Hoepken, H. H., Czerwinska, H., Robinson, S. R. & Dringen, R. Colorimetric ferrozine-based assay for the quantitation of iron in cultured cells. *Anal. Biochem.* **331**, 370–375 (2004).

470. Patil, U. S. *et al.* In Vitro/In Vivo Toxicity Evaluation and Quantification of Iron Oxide Nanoparticles. *Int. J. Mol. Sci.* **16**, 24417–24450 (2015).

471. Xue, Y. *et al.* Endoplasmic reticulum-mitochondria junction is required for iron homeostasis. *J. Biol. Chem.* jbc.M117.784249 (2017) doi:10.1074/jbc.M117.784249.

472. Hedayati, M. *et al.* An optimised spectrophotometric assay for convenient and accurate quantitation of intracellular iron from iron oxide nanoparticles. *Int. J. Hyperth. Off. J. Eur. Soc. Hyperthermic Oncol. North Am. Hyperth. Group* **34**, 373–381 (2018).

473. Stadler Nadina, Lindner Robyn A. & Davies Michael J. Direct Detection and Quantification of Transition Metal Ions in Human Atherosclerotic Plaques: Evidence for the Presence of Elevated Levels of Iron and Copper. *Arterioscler. Thromb. Vasc. Biol.* **24**, 949–954 (2004).

474. Woodmansee, A. N. & Imlay, J. A. Quantitation of intracellular free iron by electron paramagnetic resonance spectroscopy. in *Methods in Enzymology* vol. 349 3–9 (Academic Press, 2002).

475. Viollier, E., Inglett, P. W., Hunter, K., Roychoudhury, A. N. & Van Cappellen, P. The ferrozine method revisited: Fe(II)/Fe(III) determination in natural waters. *Appl. Geochem.* **15**, 785–790 (2000).

476. Derman, D. P. *et al.* A systematic evaluation of bathophenanthroline, ferrozine and ferene in an ICSH-based method for the measurement of serum iron. *Ann. Clin. Biochem.* **26 (Pt 2)**, 144–147 (1989).

477. Artiss, J. D., Vinogradov, S. & Zak, B. Spectrophotometric study of several sensitive reagents for serum iron. *Clin. Biochem.* **14**, 311–315 (1981).

478. Carter, P. Spectrophotometric determination of serum iron at the submicrogram level with a new reagent (ferrozine). *Anal. Biochem.* **40**, 450–458 (1971).

479. Eskelinen, S., Haikonen, M. & Räisänen, S. Ferene-S as the chromogen for serum iron determinations. *Scand. J. Clin. Lab. Invest.* **43**, 453–455 (1983).

480. Jeitner, T. M. Optimized ferrozine-based assay for dissolved iron. *Anal. Biochem.* **454**, 36–37 (2014).

481. Lv, H. & Shang, P. The significance, trafficking and determination of labile iron in cytosol, mitochondria and lysosomes. *Metallomics* **10**, 899–916 (2018).

482. Prus, E. & Fibach, E. Flow cytometry measurement of the labile iron pool in human hematopoietic cells. *Cytom. Part J. Int. Soc. Anal. Cytol.* **73**, 22–27 (2008).

483. Espósito, B. P., Epsztejn, S., Breuer, W. & Cabantchik, Z. I. A Review of Fluorescence Methods for Assessing Labile Iron in Cells and Biological Fluids. *Anal. Biochem.* **304**, 1–18 (2002).

484. Praveen, L., Reddy, M. L. P. & Varma, R. L. Dansyl-styrylquinoline conjugate as divalent iron sensor. *Tetrahedron Lett.* **51**, 6626–6629 (2010).

485. Petrat, F., Rauen, U. & Groot, H. de. Determination of the chelatable iron pool of isolated rat hepatocytes by digital fluorescence microscopy using the fluorescent probe, phen green SK. *Hepatology* **29**, 1171–1179 (1999).

486. Au-Yeung, H. Y., Chan, J., Chantarojsiri, T. & Chang, C. J. Molecular Imaging of Labile Iron(II) Pools in Living Cells with a Turn-On Fluorescent Probe. *J. Am. Chem. Soc.* **135**, 15165–15173 (2013).

487. Hirsh, M., Konijn, A. M. & Iancu, T. C. Acquisition, storage and release of iron by cultured human hepatoma cells. *J. Hepatol.* **36**, 30–38 (2002).

488. Parkes, J. G. & Templeton, D. M. Modulation of stellate cell proliferation and gene expression by rat hepatocytes: effect of toxic iron overload. *Toxicol. Lett.* **144**, 225–233 (2003).

489. Barisani, D., Meneveri, R., Ginelli, E., Cassani, C. & Conte, D. Iron overload and gene expression in HepG2 cells: analysis by differential display. *FEBS Lett.* **469**, 208–212 (2000).

490. Guillemot, J., Asselin, M.-C., Susan-Resiga, D., Essalmani, R. & Seidah, N. G. Deferoxamine stimulates LDLR expression and LDL uptake in HepG2 cells. *Mol. Nutr. Food Res.* **60**, 600–608 (2016).

491. Cragg, L. *et al.* The iron chelator L1 potentiates oxidative DNA damage in iron-loaded liver cells. *Blood* **92**, 632–638 (1998).

492. Rakba, N. *et al.* Antiproliferative and apoptotic effects of O-Trensox, a new synthetic iron chelator, on differentiated human hepatoma cell lines. *Carcinogenesis* **21**, 943–951 (2000).

493. Chenoufi, N. *et al.* Antiproliferative effect of deferiprone on the Hep G2 cell line. *Biochem. Pharmacol.* **56**, 431–437 (1998).

494. Barnum-Huckins, K. & Adrian, G. S. IRON REGULATION OF TRANSFERRIN SYNTHESIS IN THE HUMAN HEPATOMA CELL LINE HEPG2. *Cell Biol. Int.* **24**, 71–77 (2000).

495. Parkes, J. G., Randell, E. W., Olivieri, N. F. & Templeton, D. M. Modulation by iron loading and chelation of the uptake of non-transferrin-bound iron by human liver cells. *Biochim. Biophys. Acta* **1243**, 373–380 (1995).

496. Popovic, Z. & Templeton, D. M. Iron accumulation and iron-regulatory protein activity in human hepatoma (HepG2) cells. *Mol. Cell. Biochem.* **265**, 37–45 (2004).

497. Sekine, S. *et al.* Mitochondrial iron accumulation exacerbates hepatic toxicity caused by hepatitis C virus core protein. *Toxicol. Appl. Pharmacol.* **282**, 237–243 (2015).

498. Gao, J., Zhao, N., Knutson, M. D. & Enns, C. A. The Hereditary Hemochromatosis Protein, HFE, Inhibits Iron Uptake via Down-regulation of Zip14 in HepG2 Cells. *J. Biol. Chem.* **283**, 21462–21468 (2008).

499. Abalea, V. *et al.* Iron-induced oxidative DNA damage and its repair in primary rat hepatocyte culture. *Carcinogenesis* **19**, 1053–1059 (1998).

500. Lymboussaki, A. *et al.* The role of the iron responsive element in the control of ferroportin1/IREG1/MTP1 gene expression. *J. Hepatol.* **39**, 710–715 (2003).

501. Petrak, J. *et al.* Proteomic analysis of iron overload in human hepatoma cells. *Am. J. Physiol.-Gastrointest. Liver Physiol.* **290**, G1059–G1066 (2006).

502. Fang, C., Zhao, C., Liu, X., Yang, P. & Lu, H. Protein alteration of HepG2.2.15 cells induced by iron overload. *PROTEOMICS* **12**, 1378–1390 (2012).

503. Huang, X. *et al.* Ferrous ion autoxidation and its chelation in iron-loaded human liver HepG2 cells. *Free Radic. Biol. Med.* **32**, 84–92 (2002).

504. Ali, A., Zhang, Q., Dai, J. & Huang, X. Calcein as a fluorescent iron chemosensor for the determination of low molecular weight iron in biological fluids. *Biometals* **16**, 285–293 (2003).

505. Teixeira, J. *et al.* Development of a Mitochondriotropic Antioxidant Based on Caffeic Acid: Proof of Concept on Cellular and Mitochondrial Oxidative Stress Models. *J. Med. Chem.* **60**, 7084–7098 (2017).

506. Sturm, B., Goldenberg, H. & Scheiber-Mojdehkar, B. Transient increase of the labile iron pool in HepG2 cells by intravenous iron preparations. *Eur. J. Biochem.* **270**, 3731–3738 (2003).

507. Van Wyck, D. B., Schifman, R. B., Stivelman, J. C., Ruiz, J. & Martin, D. Rapid sample preparation for determination of iron in tissue by closed-vessel digestion and microwave energy. *Clin. Chem.* **34**, 1128–1130 (1988).

508. Breuer, W., Epsztejn, S. & Cabantchik, Z. I. Iron Acquired from Transferrin by K562 Cells Is Delivered into a Cytoplasmic Pool of Chelatable Iron(II). *J. Biol. Chem.* **270**, 24209–24215 (1995).

509. Tenopoulou, M., Kurz, T., Doulias, P.-T., Galaris, D. & Brunk, U. T. Does the calcein-AM method assay the total cellular 'labile iron pool' or only a fraction of it? *Biochem. J.* **403**, 261–266 (2007).

510. Thomas, F. *et al.* Calcein as a Fluorescent Probe for Ferric Iron Application to Iron Nutrition in Plant Cells. *J. Biol. Chem.* **274**, 13375–13383 (1999).

511. Strober, W. Trypan Blue Exclusion Test of Cell Viability. *Curr. Protoc. Immunol.* **21**, A.3B.1-A.3B.2 (1997).

512. Hubert, N. *et al.* Regulation of ferritin and transferrin receptor expression by iron in human hepatocyte cultures. *J. Hepatol.* **18**, 301–312 (1993).

513. Hennessy, D. J., Reid, G. R., Smith, F. E. & Thompson, S. L. Ferene — a new spectrophotometric reagent for iron. *Can. J. Chem.* **62**, 721–724 (1984).

514. Hider, R. C. & Kong, X. Chemistry and biology of siderophores. *Nat. Prod. Rep.* **27**, 637 (2010).

515. Spasojević, I., Armstrong, S. K., Brickman, T. J. & Crumbliss, A. L. Electrochemical Behavior of the Fe(III) Complexes of the Cyclic Hydroxamate Siderophores Alcaligin and Desferrioxamine E. *Inorg. Chem.* **38**, 449–454 (1999).

516. Ma, Y., Zhou, T. & Hider, R. C. pFe3+ determination of multidentate ligands by a fluorescence assay. *Analyst* **140**, 3603–3606 (2015).

517. Zanninelli, G. *et al.* Chelation and Mobilization of Cellular Iron by Different Classes of Chelators. *Mol. Pharmacol.* **51**, 842–852 (1997).

518. Briley-Saebo, K. *et al.* Hepatic cellular distribution and degradation of iron oxide nanoparticles following single intravenous injection in rats: implications for magnetic resonance imaging. *Cell Tissue Res.* **316**, 315–323 (2004).

519. Ge, Y. *et al.* Effect of surface charge and agglomerate degree of magnetic iron oxide nanoparticles on KB cellular uptake in vitro. *Colloids Surf. B Biointerfaces* **73**, 294–301 (2009).

520. Spira, D. *et al.* Labeling Human Melanoma Cells With SPIO: In Vitro Observations. *Mol. Imaging* **15**, 1536012115624915 (2016).

521. Soenen, S. J. H., Nuytten, N., Meyer, S. F. D., Smedt, S. C. D. & Cuyper, M. D. High Intracellular Iron Oxide Nanoparticle Concentrations Affect Cellular Cytoskeleton and Focal Adhesion Kinase-Mediated Signaling. *Small* **6**, 832–842 (2010).

522. Porter, J. B. Deferoxamine pharmacokinetics. *Semin. Hematol.* **38**, 63–68 (2001).

523. Bourdon, S., Houzé, P. & Bourdon, R. Quantification of desferrioxamine in blood plasma by inductively coupled plasma atomic emission spectrometry. *Clin. Chem.* **33**, 132–134 (1987).

524. Llados i Vallory, E. A. *et al.* Studies of variations of subcutaneously infused desferrioxamine and iron movements in thalassaemia children. *Eur. J. Pediatr.* **148**, 503–506 (1989).

525. Pieroni, L. *et al.* Comparison of bathophenanthroline sulfonate and ferene as chromogens in colorimetric measurement of low hepatic iron concentration. *Clin. Chem.* **47**, 2059–2061 (2001).

526. Ceriotti, F. & Cerlotti, G. Improved Direct Specific Determination of Serum Iron and Total Iron-BindingCapacity. 6.

527. Iron Panel of the International Committee for Standardization in Haematology. Revised recommendations for the measurements of the serum iron in human blood. *Br. J. Haematol.* **75**, 615–616 (1990).

528. Hider, R. C. & Kong, X. Iron speciation in the cytosol: an overview. *Dalton Trans.* **42**, 3220–3229 (2013).

529. Sherman, H. G. *et al.* New Perspectives on Iron Uptake in Eukaryotes. *Front. Mol. Biosci.* **5**, (2018).

530. Ma, Y., de Groot, H., Liu, Z., Hider, R. C. & Petrat, F. Chelation and determination of labile iron in primary hepatocytes by pyridinone fluorescent probes. *Biochem. J.* **395**, 49–55 (2006).

531. Zanninelli, G. *et al.* The labile iron pool of hepatocytes in chronic and acute iron overload and chelator-induced iron deprivation. *J. Hepatol.* **36**, 39–46 (2002).

532. Ternes, N., Scheiber-Mojdehkar, B., Landgraf, G., Goldenberg, H. & Sturm, B. Iron availability and complex stability of iron hydroxyethyl starch and iron dextran—a comparative in vitro study with liver cells and macrophages. *Nephrol. Dial. Transplant.* **22**, 2824–2830 (2007).

533. Britton, L. *et al.* Hepatic iron concentration correlates with insulin sensitivity in nonalcoholic fatty liver disease. *Hepatol. Commun.* **2**, 644–653 (2018).

534. Fargion, S. *et al.* Iron and insulin resistance. *Aliment. Pharmacol. Ther.* **22**, 61–63 (2005).

535. Pietrangelo, A. *et al.* Enhanced hepatic collagen type I mRNA expression into fat-storing cells in a rodent model of hemochromatosis. *Hepatol. Baltim. Md* **19**, 714–721 (1994).

536. Ramm, G. A. & Ruddell, R. G. Hepatotoxicity of Iron Overload: Mechanisms of Iron-Induced Hepatic Fibrogenesis. *Semin. Liver Dis.* **25**, 433–449 (2005).

537. Borgna-Pignatti, C. *et al.* Hepatocellular carcinoma in the thalassaemia syndromes. *Br. J. Haematol.* **124**, 114–117 (2004).

538. Bradbear, R. A. *et al.* Cohort study of internal malignancy in genetic hemochromatosis and other chronic nonalcoholic liver diseases. *J. Natl. Cancer Inst.* **75**, 81–84 (1985).

539. Lewandowska, H. *et al.* LDL dinitrosyl iron complex: A new transferrin-independent route for iron delivery in hepatocytes. *BioFactors Oxf. Engl.* **44**, 192–201 (2018).

540. Faller, B. & Nick, H. Kinetics and Mechanism of Iron(III) Removal from Citrate by Desferrioxamine B and 3-Hydroxy-1,2-Dimethyl-4-Pyridone. *J. Am. Chem. Soc.* **116**, 3860–3865 (1994).

541. Grootveld, M. *et al.* Non-transferrin-bound iron in plasma or serum from patients with idiopathic hemochromatosis. Characterization by high performance liquid chromatography and nuclear magnetic resonance spectroscopy. *J. Biol. Chem.* **264**, 4417–4422 (1989).

542. Evans, R. W. *et al.* Nature of non-transferrin-bound iron: studies on iron citrate complexes and thalassemic sera. *JBIC J. Biol. Inorg. Chem.* **13**, 57–74 (2008).

543. Bai, J. & Cederbaum, A. I. Catalase protects HepG2 cells from apoptosis induced by DNA-damaging agents by accelerating the degradation of p53. *J. Biol. Chem.* **278**, 4660–4667 (2003).

Appendix

A.1. Tables

Appendix Table 1. Leica SP5 inverted confocal scanning laser microscope settings for Chapter 2.

		Nucleus	Polymers	Early & recycling endosomes	Late endosomes & lysosomes
Marker		Hoescht	Carboxyrhodamine-110	Transferrin-647	Lysotracker Red DND-99
Laser	Wavelength (nm)	405	488	633	561
Laser	Voltage (V)	30	30	30	30
PMT Detector	Bandwidth (nm)	414-480	494-567	643-795	574-737
PMT Detector	Voltage (V)	550	670	625	625

Appendix Table 2. The list of primary and secondary antibodies and the intracellular compartment identified.

Primary			Secondary			Intracellular compartment identified
Species	Antibody	Fluorophore	Species	Antibody	Fluorophore	
Single antibody staining (ASGPR staining)						
Mouse	Anti-human ASGPR	Alexa 647	N/A			ASGPR
Double antibody staining (The endocytic pathway staining)						
Mouse	Anti-human EEA1	None	Goat	Anti-mouse	Alexa 568	Early endosomes
Rabbit	Anti-human TfR1	None	Goat	Anti-rabbit	Alexa 568	Recycling endosomes
Mouse	Anti-human Rab7	None	Goat	Anti-mouse	Alexa 568	Late endosomes
Mouse	Anti-human LAMP	None	Goat	Anti-mouse	Alexa 568	Lysosomes

Appendix Table 3. Leica SP5 Inverted confocal scanning laser microscope settings in Chapter 3.

		Nucleus	Polymer	Early endosomes	Recycling endosomes	Late endosomes	Lysosomes	ASGPR
Marker		Hoescht	Carboxy rhodamine 110	EEA1	TfR1	Rab7	LAMP	ASGPR
Laser	Wavelength (nm)	405	488	561	561	561	561	633
Laser	Voltage (V)	30	30	30	30	30	30	30
PMT Detector	Bandwidth (nm)	414-480	494-567	574-737	574-737	574-737	574-737	643-795
PMT Detector	Voltage (V)	550	670	625	625	625	625	625

Appendix Table 4. Parameters used in the MATLAB script to obtain binary masks.

Fluorescent markers		Sigmas			Threshold
Compartment	Markers	Smallest	Largest	Step-wise increments	
Polymer	Polymers	0.20	2.00	0.40	12
AF	AF	0.20	2.00	0.40	12
Early endosomes	EEA1	0.10	1.50	0.10	10
Recycling endosomes	TfR1	0.25	3.00	0.25	10
Late endosomes	Rab7	0.10	1.50	0.10	10
Lysosomes	LAMP	0.25	2.00	0.25	4
ASGPR	ASGPR	0.10	1.50	0.10	10

Appendix Table 5. A list of dilutions used for the analysis of total iron in biological samples using the u-ferene assay and ICP-MS

Biological sample	Dilution factors	
	u-ferene assay	ICP-MS
Cell lysates	1	3
Plasma	1	3
Liver	40	5000
Spleen	20	1000
Heart	1	40
Kidneys	8	250
Urine	1	10
Feces	80	4000
Blood	10	1500

Appendix Table 6. The template for running the ferene assay to determine the effect of ascorbic acid on iron quantification.

		working solution (5 mM ferene in ammonium acetate buffer) with varying ascorbic acid concentrations (0-1000 mM)								
		0	1	5	10	25	50	100	250	1000
Analytes	Fe Fe-DFO DFO									
Iron standards (µM)	0									
	5									
	10									
	25									
	50									
	100									
	200									
	400									
	1000									

Appendix Table 7. The components in the u-ferene assay's working solution.

Working solution components	Labile iron	Total iron
Ferene	5 mM	5 mM
Ascorbic acid	10 mM	1 M
Prepared in ammonium acetate buffer (pH 4.5, 2.5 M)		

Appendix Table 8. Liver iron concentration represented in different units. Errors represent standard deviations from 3 mice.

	Total iron (μg)	Iron (μg) per wet liver weight (g)	Iron (μg) per dry liver weight (g)
Health	69 ± 2	60 ± 6	253 ± 29
Saline	3581 ± 121	2272 ± 219	9501 ± 794
HD-GalNAc	3178 ± 156	1825 ± 113	7666 ± 460
HD-TAG	3536 ± 102	2204 ± 177	9062 ± 739
HD$_{40}$-GalNAc	3147 ± 204	2072 ± 562	8635 ± 2441
HD	3506 ± 165	1996 ± 139	8313 ± 600
DFO	3668 ± 673	2604 ± 528	11086 ± 2206

A.2. Figures
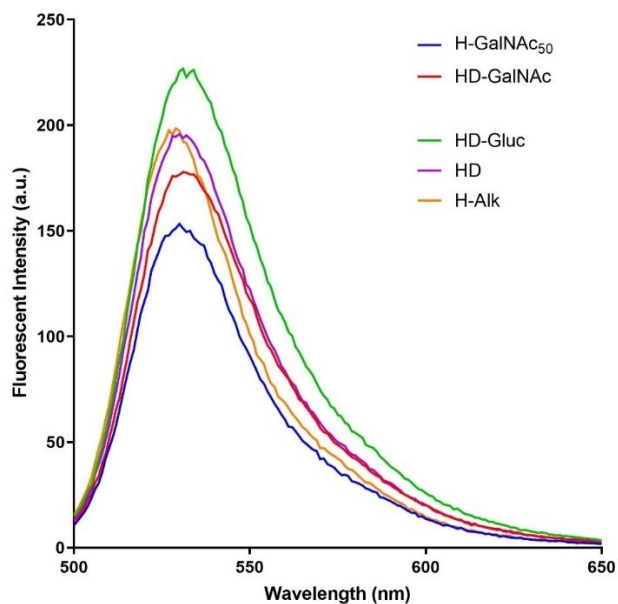
Appendix Figure 1. Fluorescent emission spectrums of liver targeting systems and their controls. All polymers (1 μM) were excited at 490 nm and emission spectrums were scanned at a scan rate of 60 nm/min and a detector PMT set at 910 V.

$\varepsilon = 74,000\ M^{-1}cm^{-1}$

Excitation Maximum = 501 nm

Emission Maximum = 523 nm
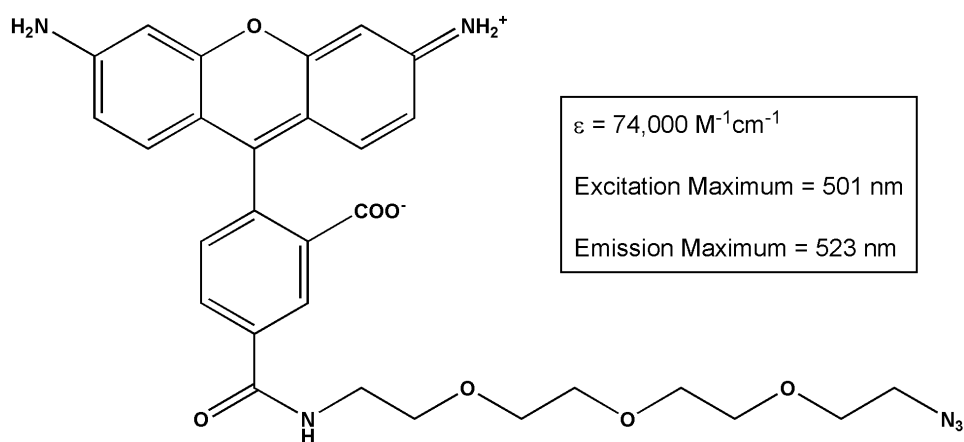
Appendix Figure 2. The structure of carboxyrhodamine-110 azide. This dye has a terminal azide to facilitate conjugation via copper-catalyzed click chemistry.
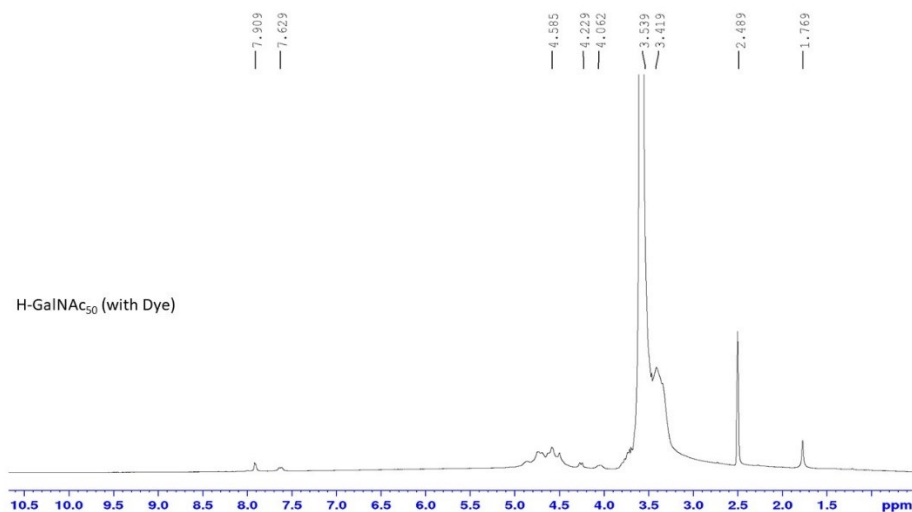
Appendix Figure 3. NMR spectrum of fluorescently labelled H-GalNAc₅₀. ^{1}H NMR (400 MHz, D2O) δ 7.91 (br, 1H, triazole ring protons), 7.62 (br, 1H, NHCO-, GalNAc amide protons), 4.58 (m, 1H, -OH), 3.90-3.41 (m, protons from HPG and GalNAc), 1.75 (br, 1H, -NH(CO)-CH3)
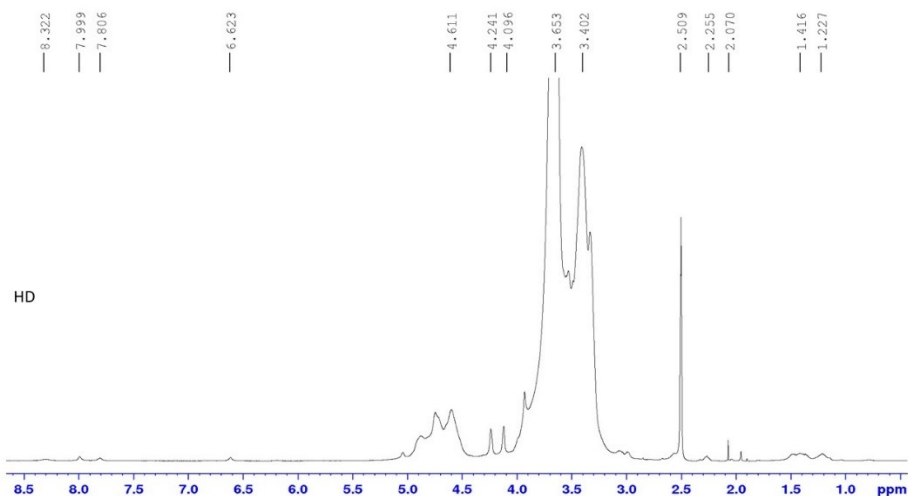
Appendix Figure 4. NMR spectrum of HD. ^{1}H NMR (400 MHz, D2O) δ 8.32 (br, OH protons from DFO), 8.00 (br, 1H, -NHCO-, DFO amide protons), 7.80 (br, 1H, -C=CH, triazole ring protons), 6.62 (br, 1H, -NHCO), 4.61 (m, H,-OH), 3.92-3.41 (m, protons from HPG and DFO), 2.25 (br, 3H, DFO protons), 1.41-1.00 (br, 18H, DFO protons).
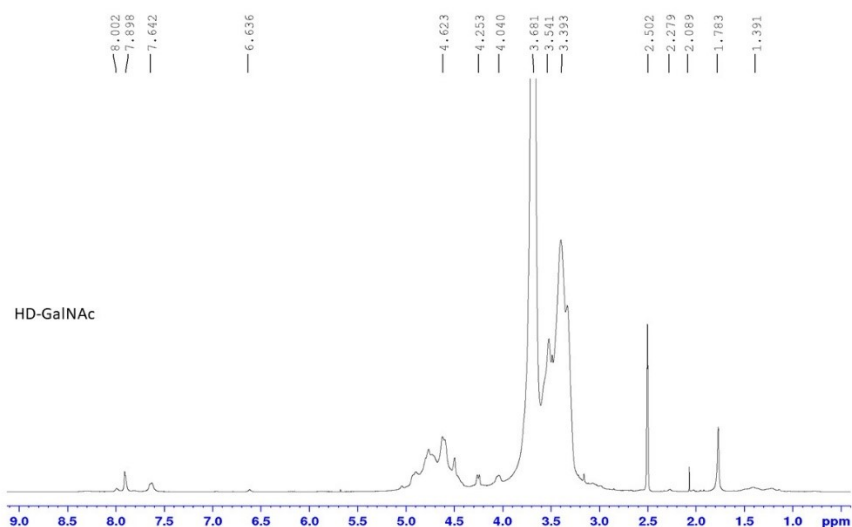
Appendix Figure 5. ¹H-NMR spectrum of HD-GalNAc. ^{1}H NMR (400 MHz, D2O) δ 8.00 (br, 1H, -NHCO-, DFO amide protons), 7.89 (br, 1H, -C=CH, triazole ring protons), 7.64 (br, 1H, NHCO-, GalNAc amide protons), 6.36 (br, 1H, -NHCO), 4.61 (m, H,-OH), 3.91-3.43 (m, protons from HPG, GalNAc, and DFO), 2.09 (br, 3H, DFO protons), 1.78 (br, 1H, -NH(CO)-CH3), 1.39-1.00 (br, 18H, DFO protons).
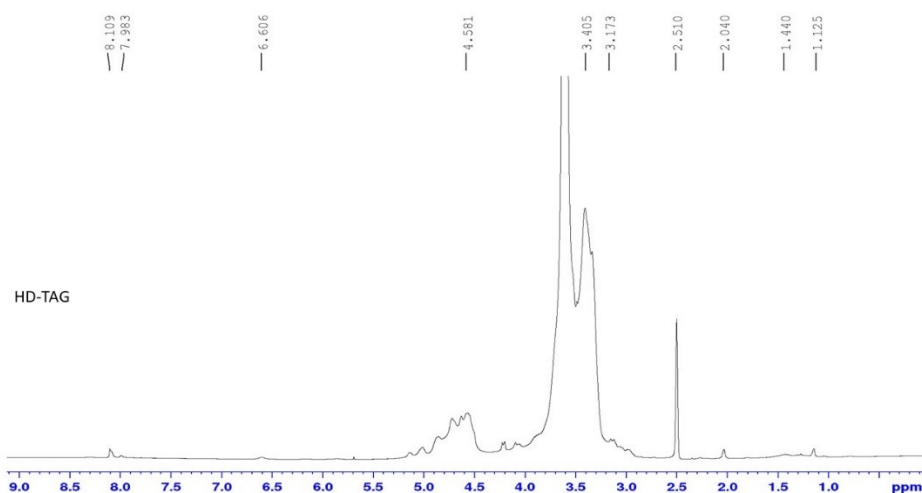
Appendix Figure 6. ¹H-NMR spectrum of HD-TAG. ^{1}H NMR (400 MHz, D2O) δ 8.10 (br, 1H, -NHCO-, DFO amide protons), 7.98 (br, 1H, -C=CH, triazole ring protons), 7.64 (br, 1H, NHCO-, TAG amide protons), 6.60 (br, 1H, -NHCO), 4.58 (m, H,-OH), 4.01-3.38 (m, protons from HPG, TAG, and DFO), 2.04 (br, 3H, DFO protons), 1.78 (br, 1H, -NH(CO)-CH3), 1.40-1.00 (br, 18H, DFO protons).

242
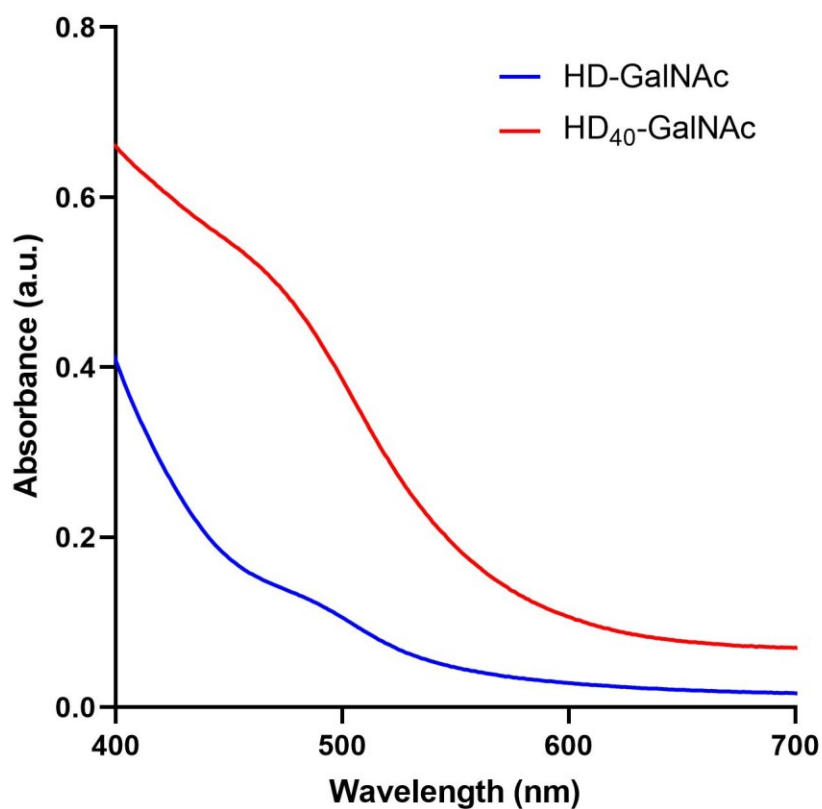
Appendix Figure 7. The quantification of the number of DFO units on the HPG backbone. The UV-VIS spectrum was measured for DFO conjugated polymers complexed with iron. The absorbance at 540 nm was used to quantify the concentration of DFO. The number of DFO units were confirmed using thermogravimetry to determine polymer mass.
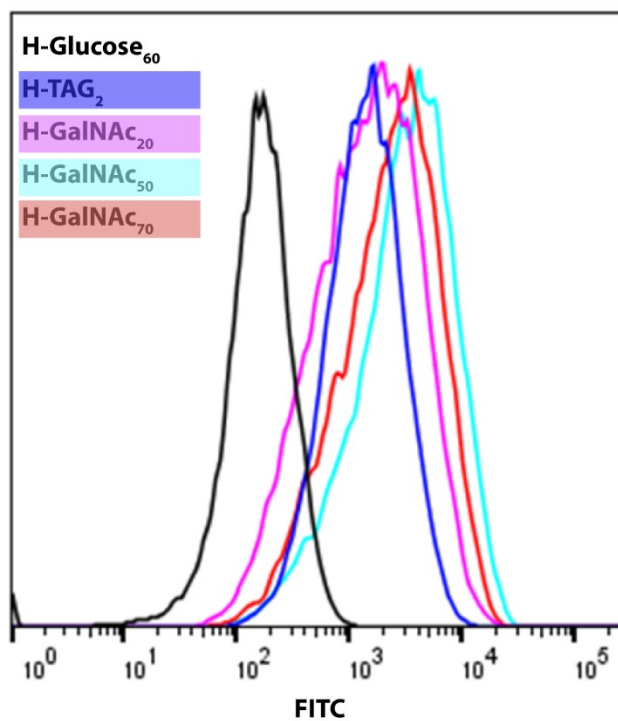
Appendix Figure 8. The histogram distribution of fluorescently-labelled liver targeting macromolecules at 10 μM after a 2 hour incubation at 37°C. All polymers were carboxyrhodamine-tagged. At least 10,000 cells were analyzed using the 488 nm laser and the FITC emission filter (530/20 nm). HPG-Glucose60 is in black. HPG-TAG2 is in dark blue. HPG-GalNAc20 is in pink. HPG-GalNAc50 is in cyan. HPG-GalNAc70 is in red.
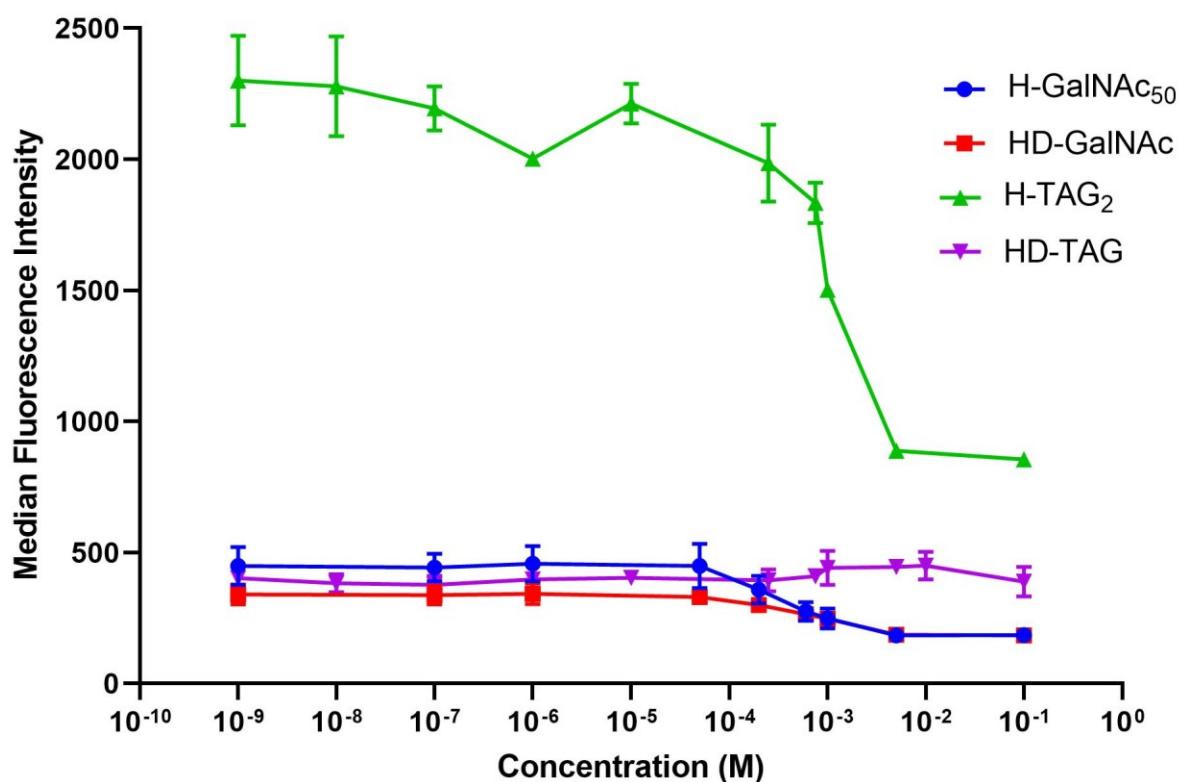
Appendix Figure 9. The IC$_{50}$ profiles of liver targeting macromolecular systems. An inhibition in the binding and uptake response was observed through the dose-dependent reduction in median fluorescence intensity as the concentration of GalNAc increased. All polymers were fluorescently tagged and at least 10,000 cells were analyzed using the FITC emission filter (530/20 nm). HPG-DFO$_{15}$-TAG$_2$ does not show any decrease and therefore its IC$_{50}$ concentration was not determined. Error bars show standard deviations for a sample size of 3 independent replicates.
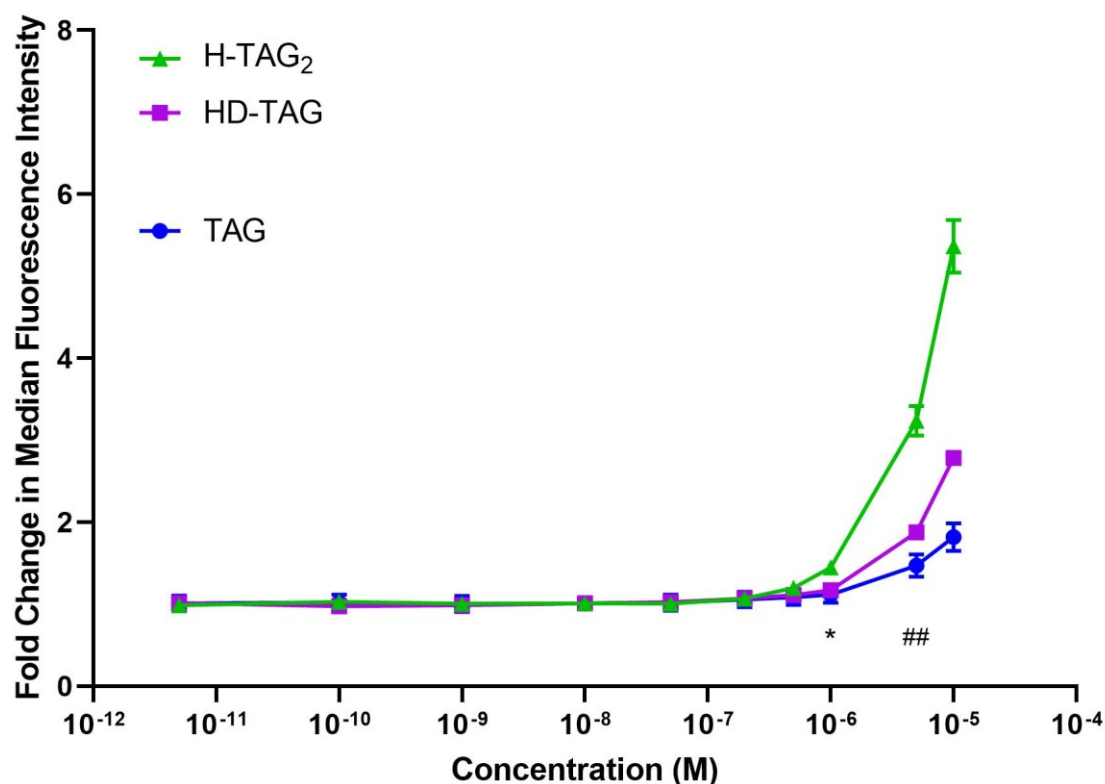
Appendix Figure 10. The binding and uptake of TAG based systems in HeLa. The response of all carboxyrhodamine-tagged molecules were measured over a range of concentrations. At least 10,000 cells were analyzed using the 488 nm laser and the FITC emission filter (530/20 nm). HeLa cells have been used as ASGPR negative cells. TAG represents the unmodified TAG sugar prior to conjugation. Error bars show standard deviations for a sample size of 3 independent replicates. A 2-way ANOVA with Dunnett's multiple comparison tests were performed to compare the uptake of all systems against TAG using Graphpad Prism. TAG vs H-TAG$_2$ had a *p = 0.0313 at 1 μM and TAG vs HD-TAG $^{\#\#}$p = 0.0077 at 5 μM.
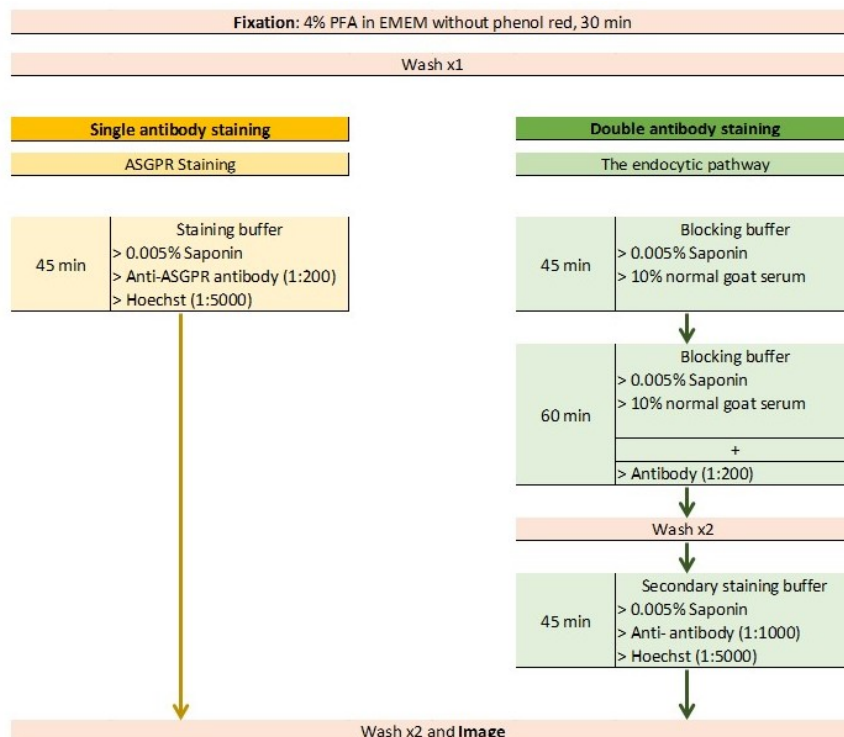
Appendix Figure 11. The work-flow for immunostaining HepG2 cells, as described in section 3.3.5.4. All buffers were prepared in PBS. All washes were performed with PBS. All incubations were performed at room temperature. The details of the antibodies have been outlined in **Appendix Table 2**.
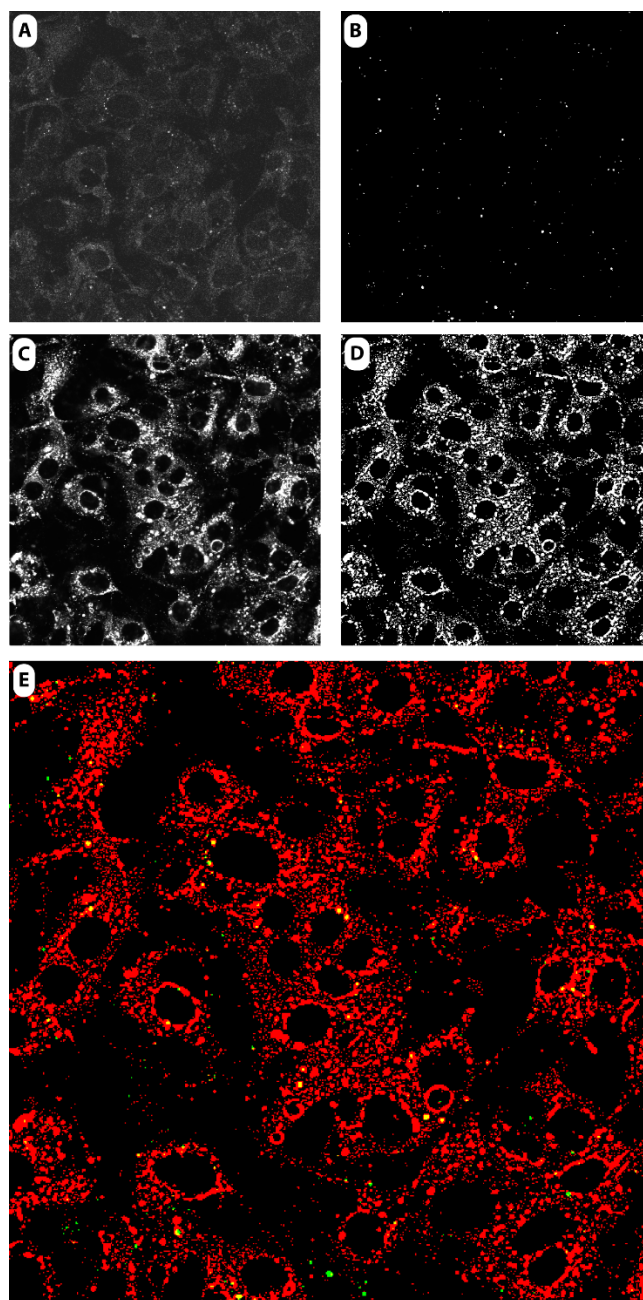
Appendix Figure 12. The step-wise processing of raw images into binary masks for Mander's Co-localization Coefficient determination. (A and C) Images were acquired from the Leica SP5 inverted confocal scanning laser microscope. Raw images were then converted into (B and D) binary masks using the MATLAB scripts and optimized sigma and threshold parameters – outlined in **Appendix Table 4**. Then, (E) Mander's Co-localization Coefficients (MCCs) were determined using JACoP (Just Another Co-localization Plug-in) in ImageJ. The percentage of polymer signal overlap into the antibody signal was determined (M1).
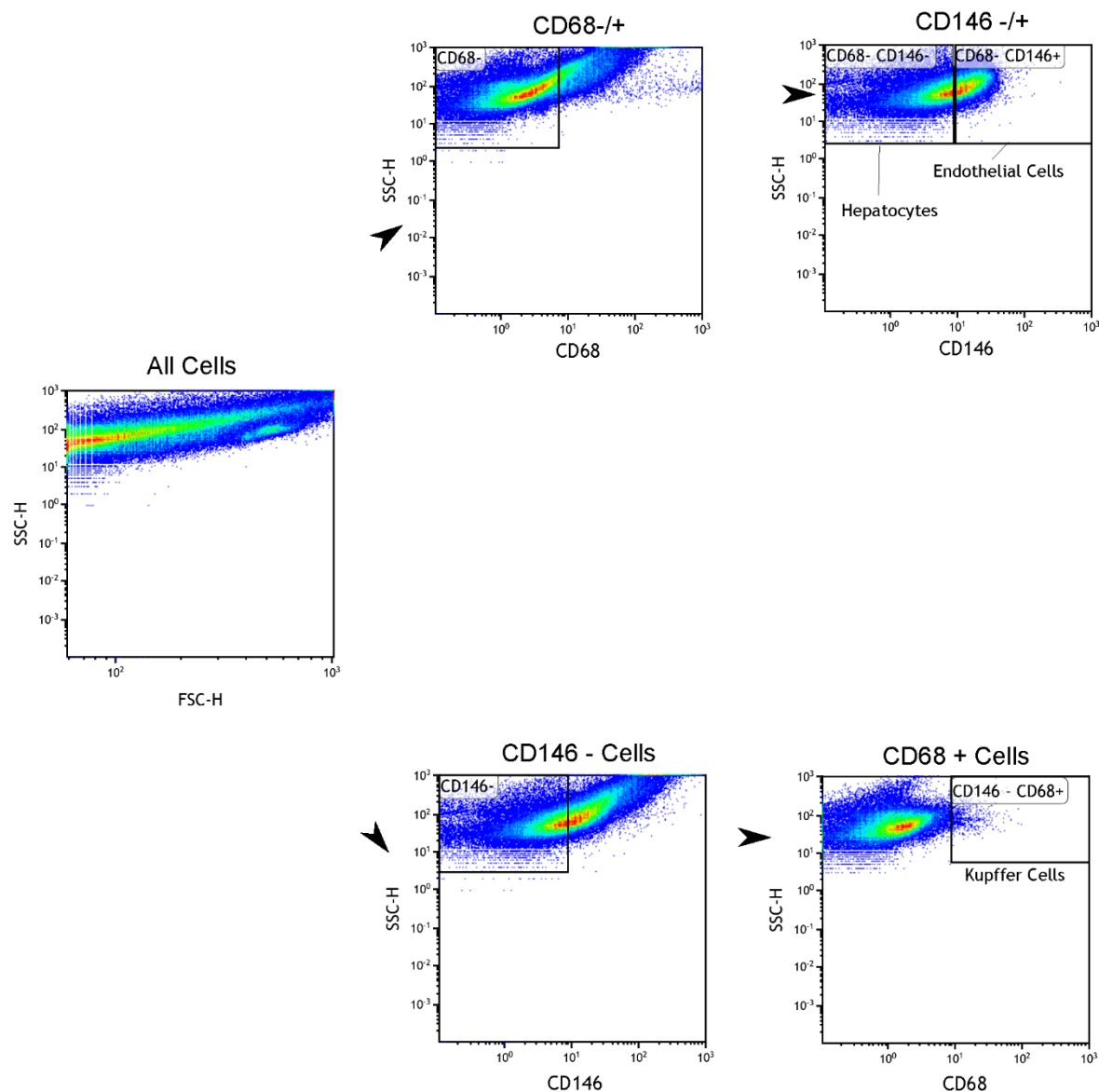
Appendix Figure 13. The gating for different cellular populations from the liver. Liver cells were isolated and analyzed by flow cytometry. At least 10,000 cells were analyzed. Data was represented as the percentage of cells positive for polymers. Kupffer cells were identified as CD68 positive and CD146 negative cell populations. Hepatocytes were identified as CD68 negative and CD146 negative cell populations. Endothelial cells were identified as CD68 negative and CD146 positive cells.
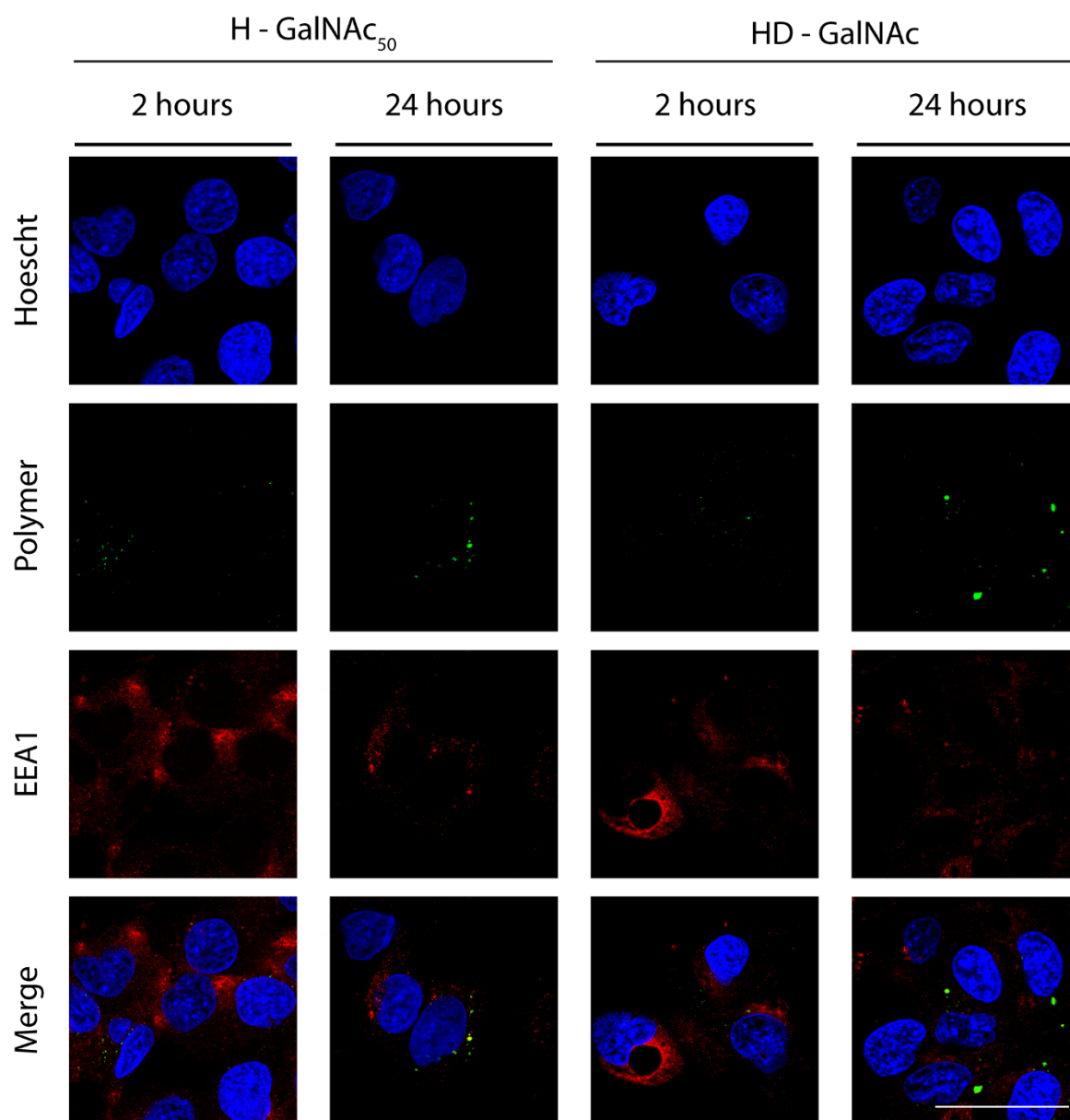
Appendix Figure 14. The intracellular distribution of H-GalNAc$_{50}$ and HD-GalNAc incubated for either 2 or 24 h with early endosomes (EEA1). Images were acquired using Leica SP5 confocal scanning laser microscopy using a 63X objective with a 2X zoom. Early endosomes (EEA1) and the nuclei (Hoescht) were stained. Scale bar represents 1 μm. Representative images were shown.
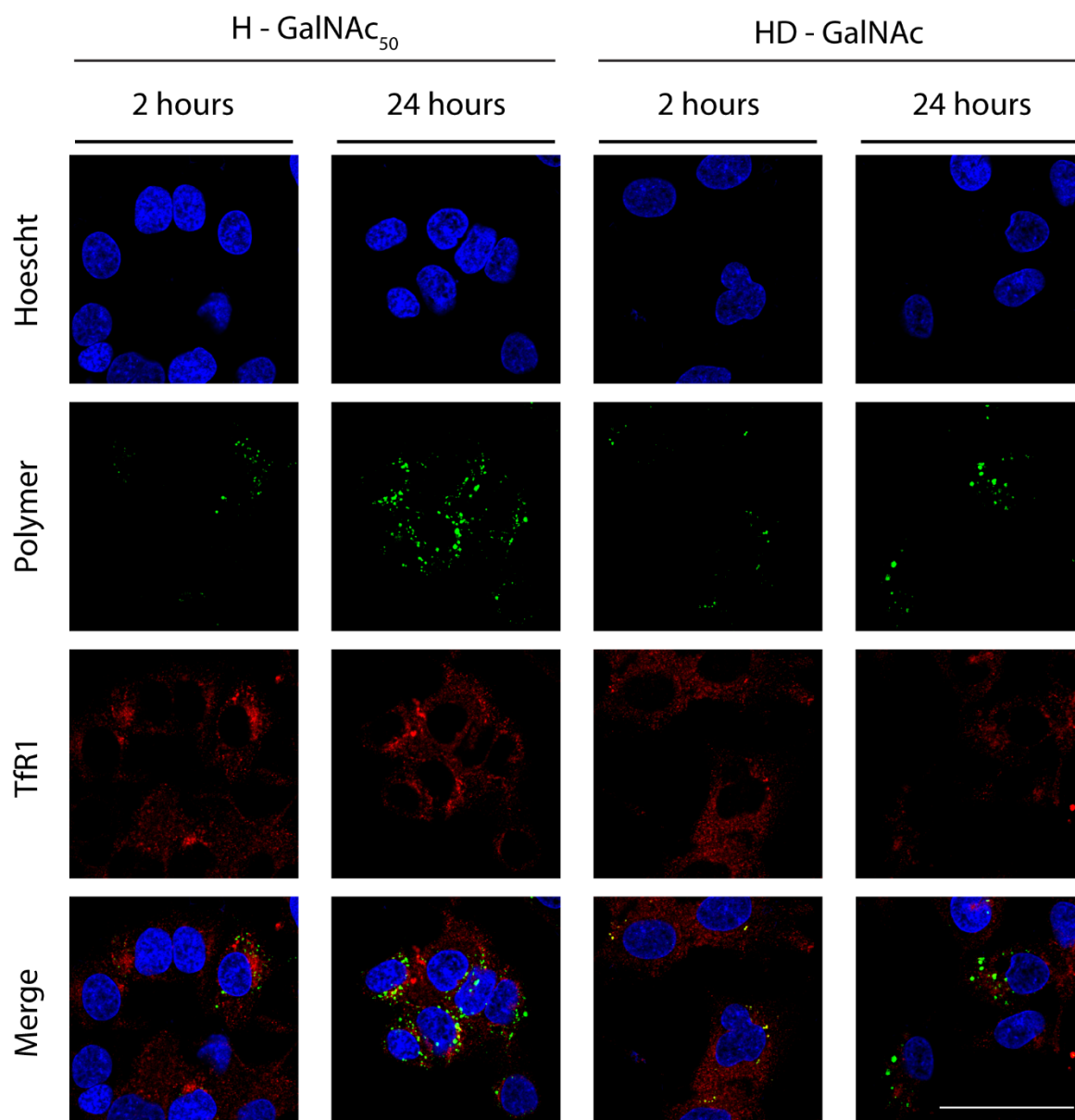
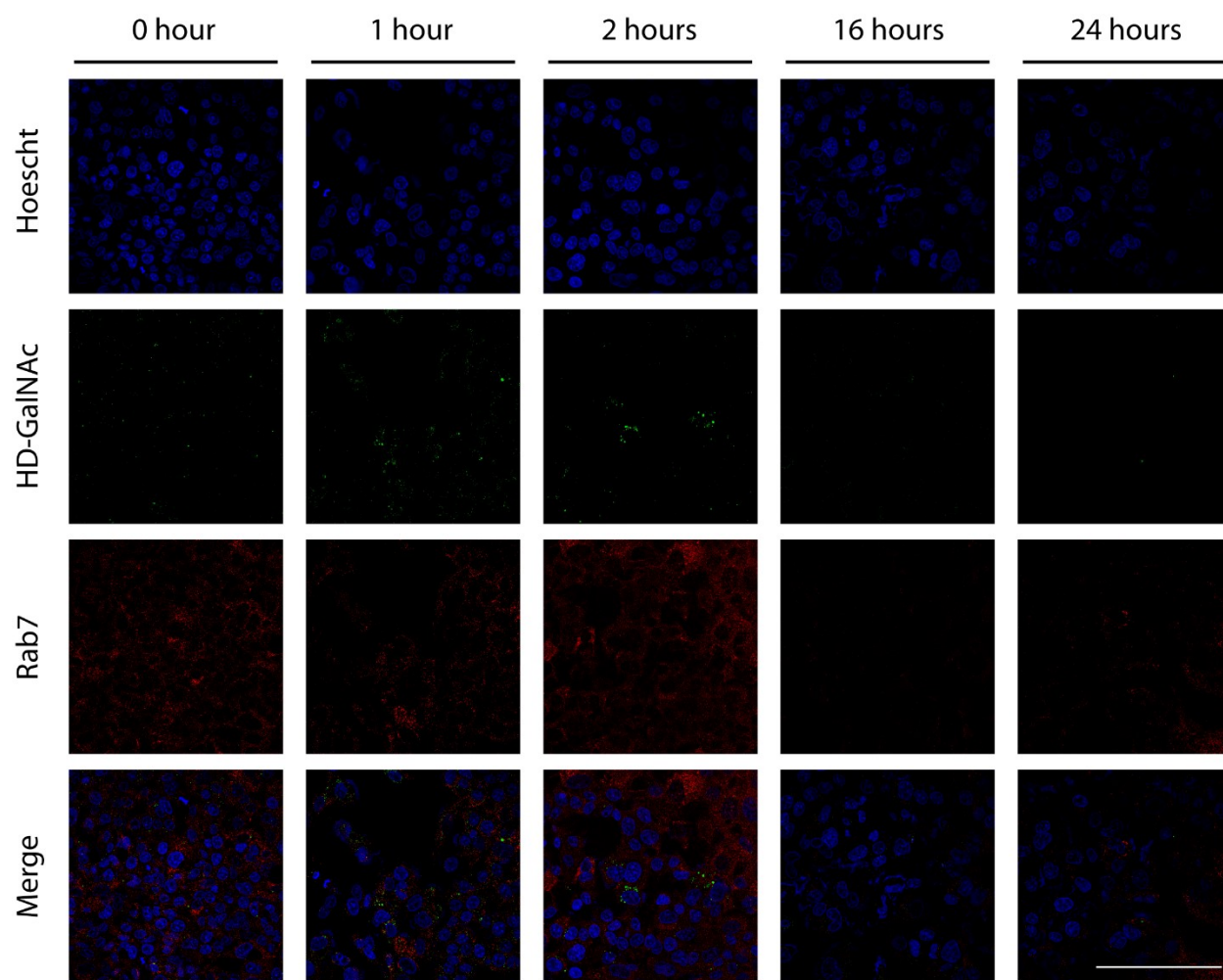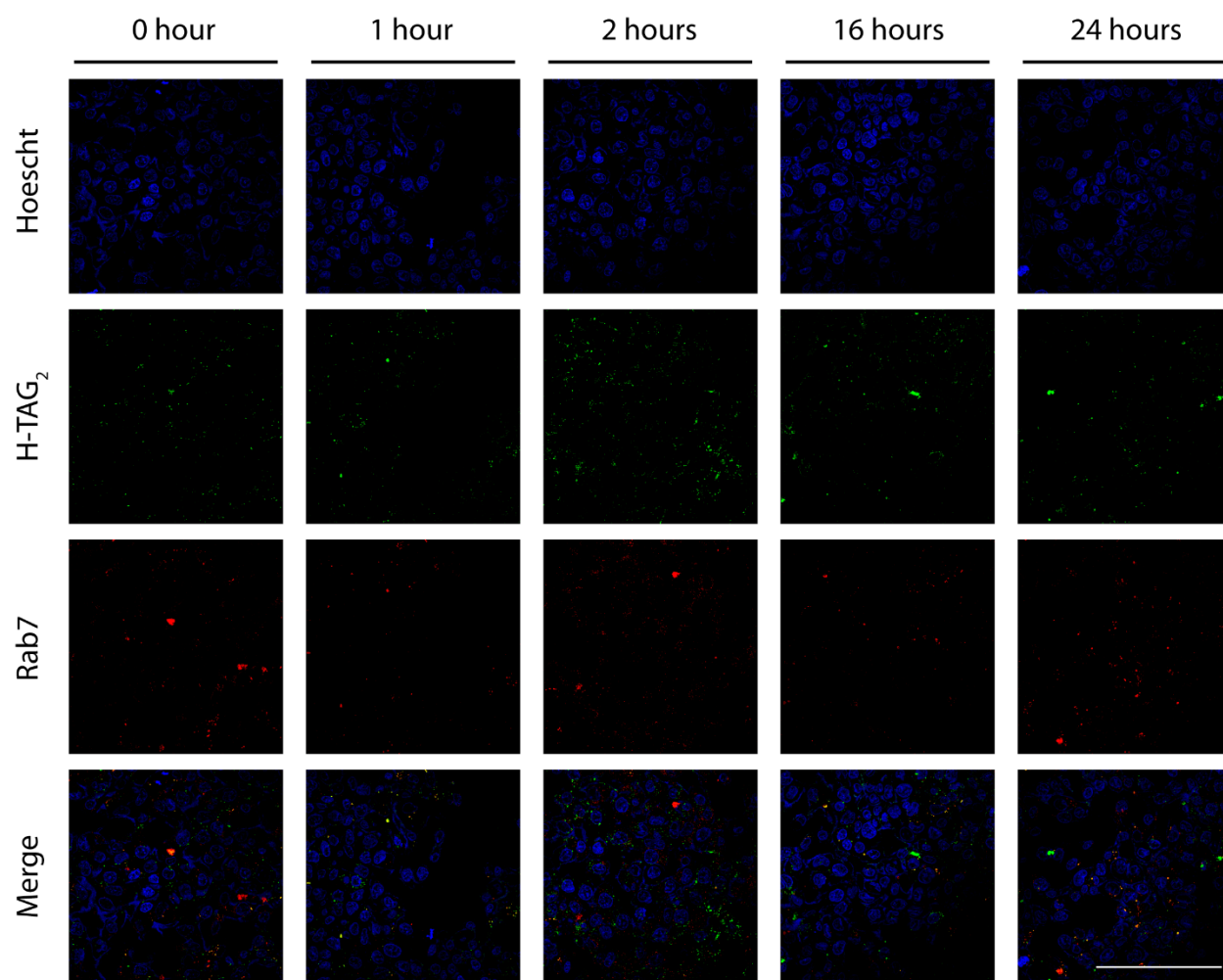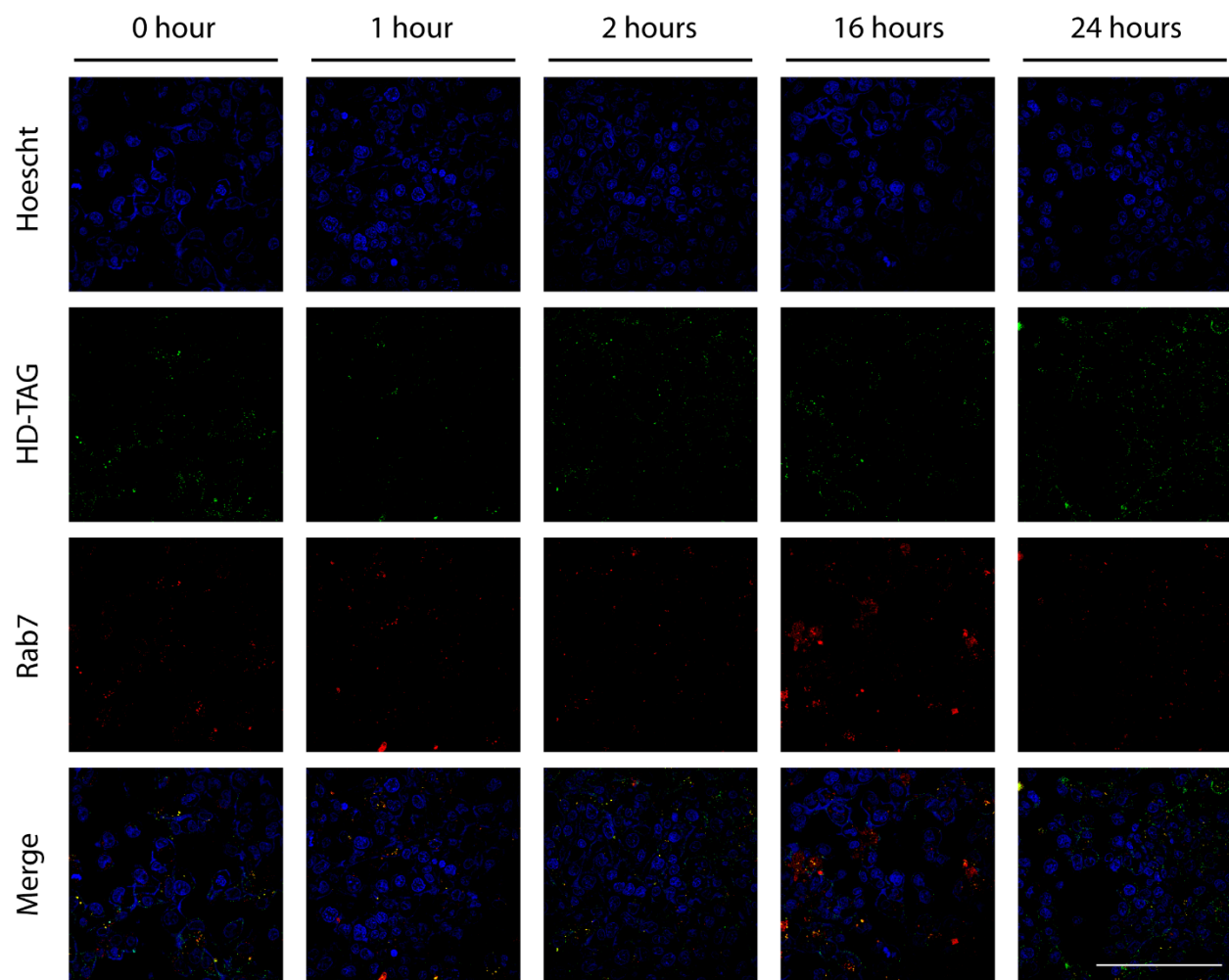**Appendix Figure 15. The intracellular distribution of H-GalNAc$_{50}$ and HD-GalNAc incubated for either 2 or 24 h with recycling endosomes (TfR1).** Images were acquired using Leica SP5 confocal scanning laser microscopy using a 63X objective with a 2X zoom. Recycling endosomes (TfR1) and the nuclei (Hoescht) were stained. Scale bar represents 1 μm. Representative images were shown.
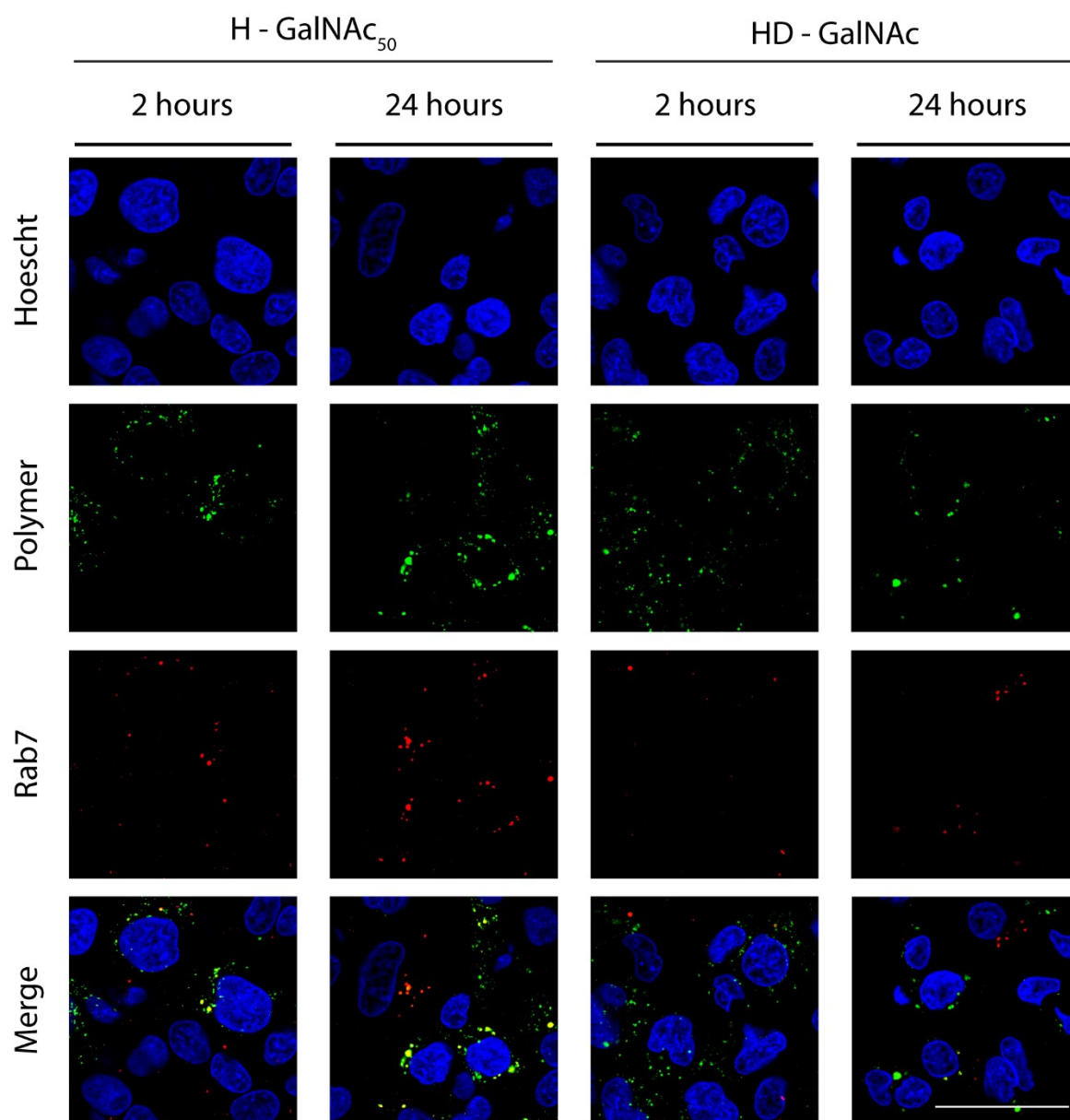
Appendix Figure 16. The intracellular distribution of H-GalNAc$_{50}$ and HD-GalNAc incubated for either 2 or 24 h with late endosomes (Rab7). Images were acquired using Leica SP5 confocal scanning laser microscopy using a 63X objective with a 2X zoom. Late endosomes (Rab7) and the nuclei (Hoescht) were stained. Scale bar represents 1 μm. Representative images were shown.
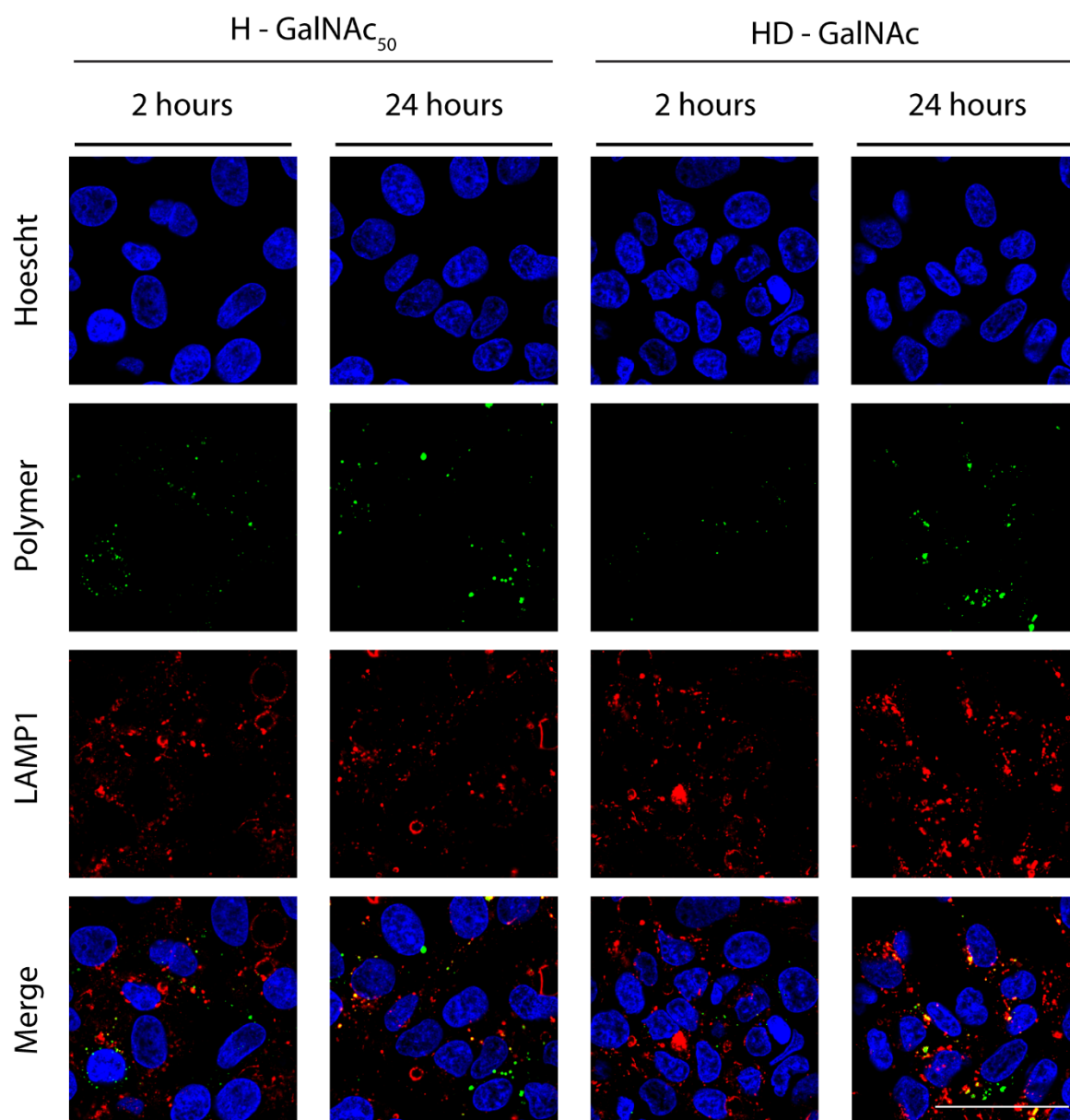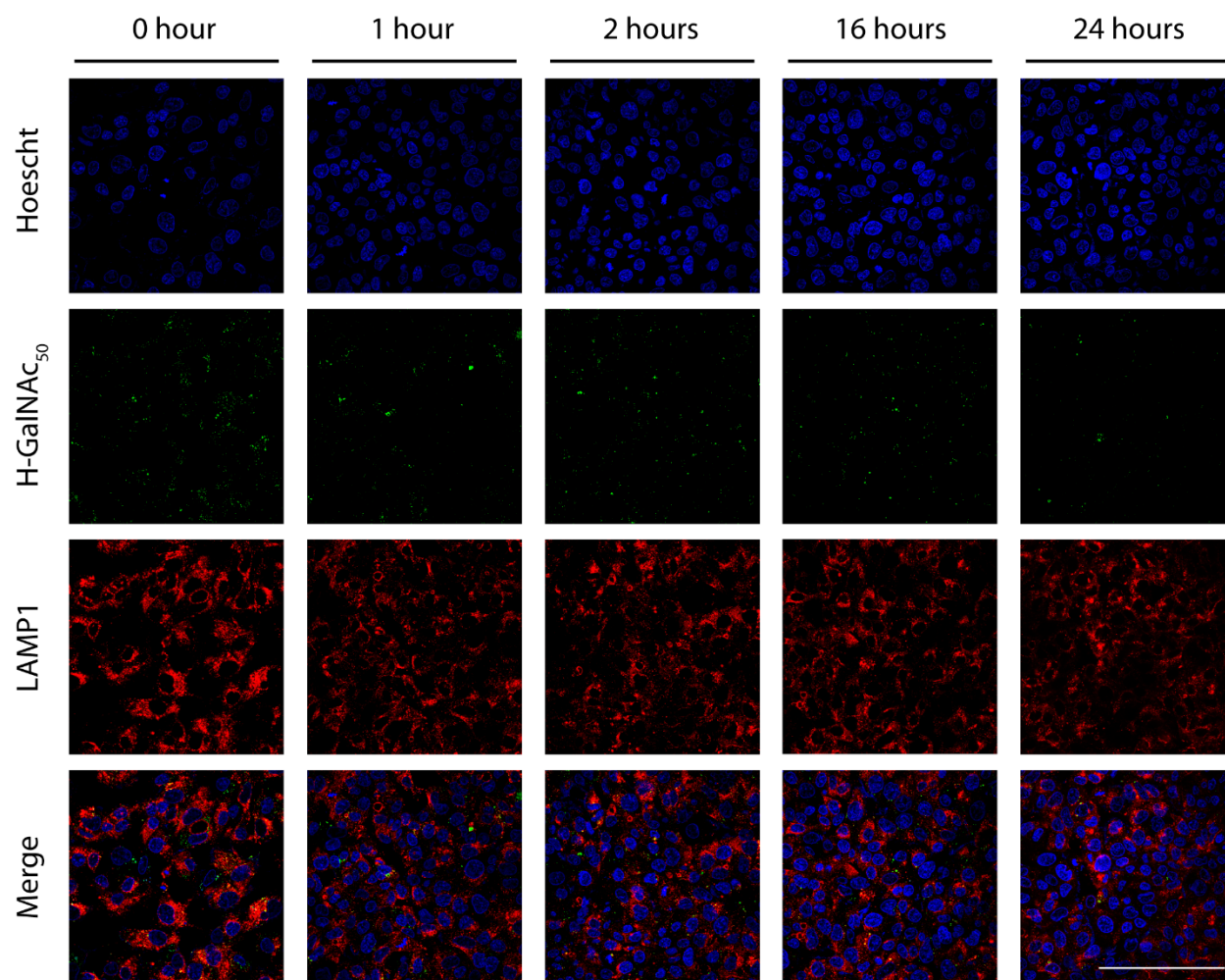
Appendix Figure 17. The intracellular distribution of H-GalNAc$_{50}$ and HD-GalNAc incubated for either 2 or 24 h with lysosomes (LAMP1). Images were acquired using Leica SP5 confocal scanning laser microscopy using a 63X objective with a 2X zoom. Lysosomes (LAMP) and the nuclei (Hoescht) were stained. Scale bar represents 1 μm. Representative images were shown.
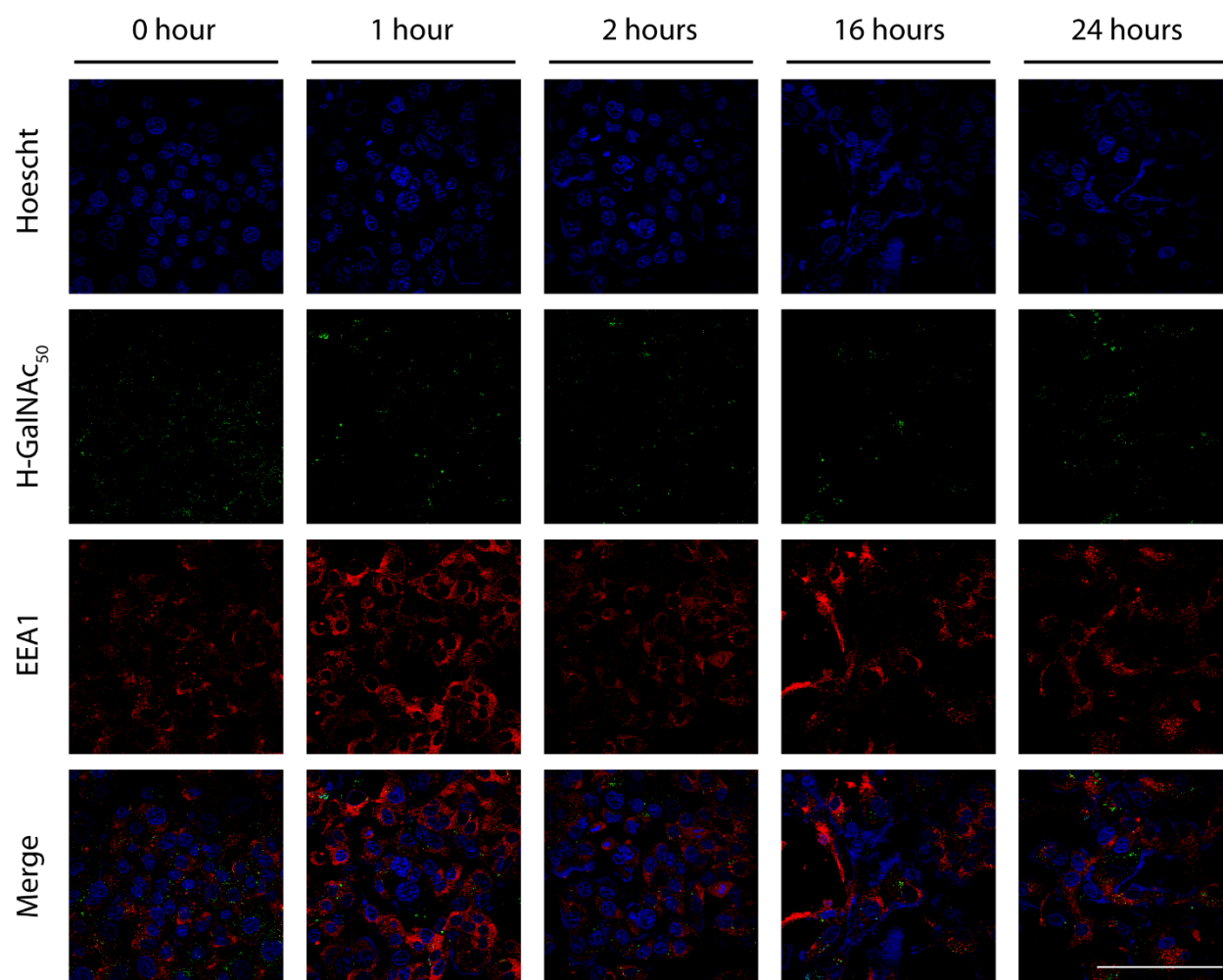
Appendix Figure 18. Kinetic analysis for the intracellular trafficking of H-GalNAc$_{50}$ with early endosomes. H-GalNAc$_{50}$ were pulsed for 30 mins and then chased for 0, 1, 2, 16 and 24 h with fresh media. Images were acquired using Leica SP5 confocal scanning laser microscopy using a 63X objective. Early endosomes (EEA1) and the nuclei (Hoescht) were stained. Scale bar represents 1 μm. Representative images were shown.
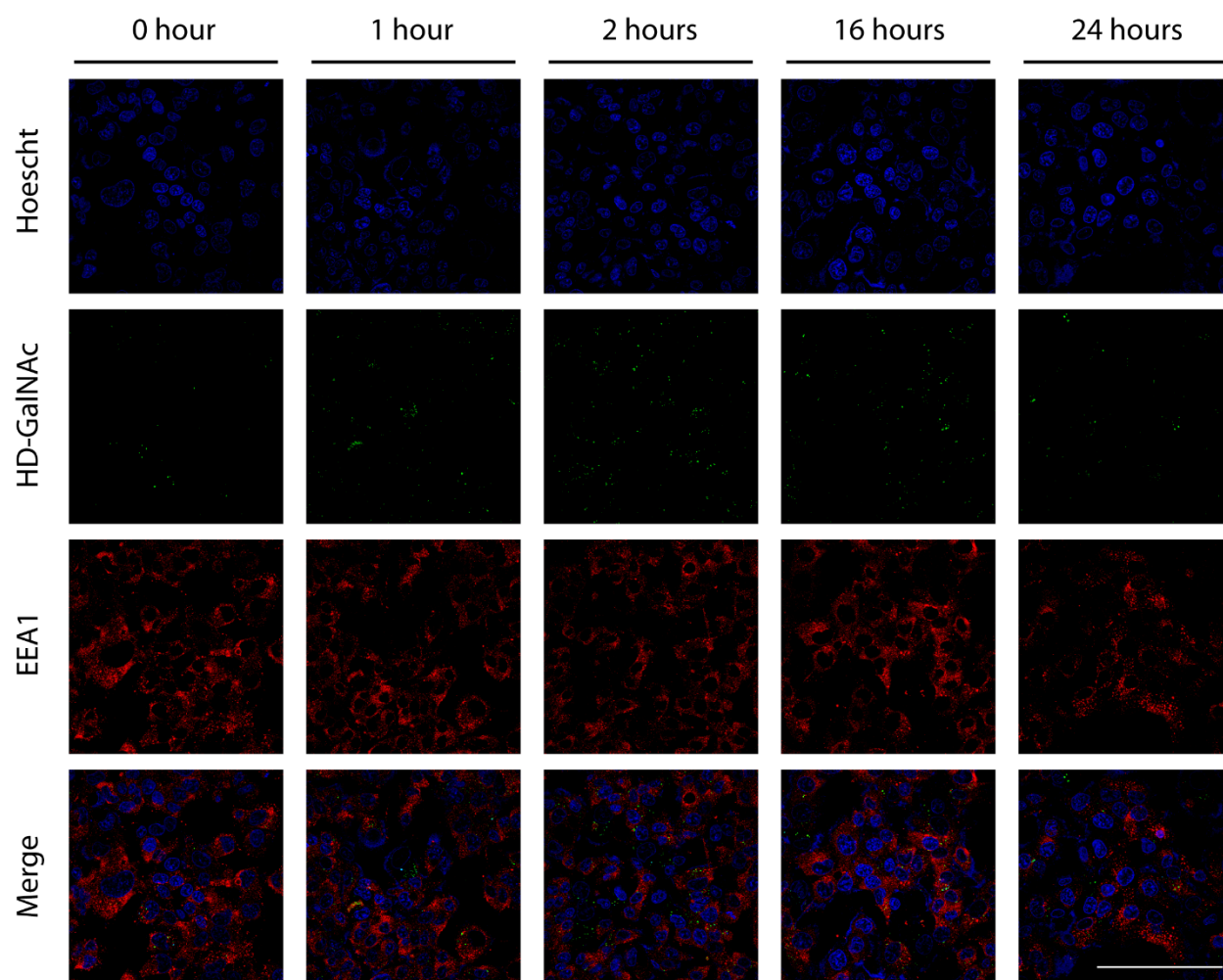
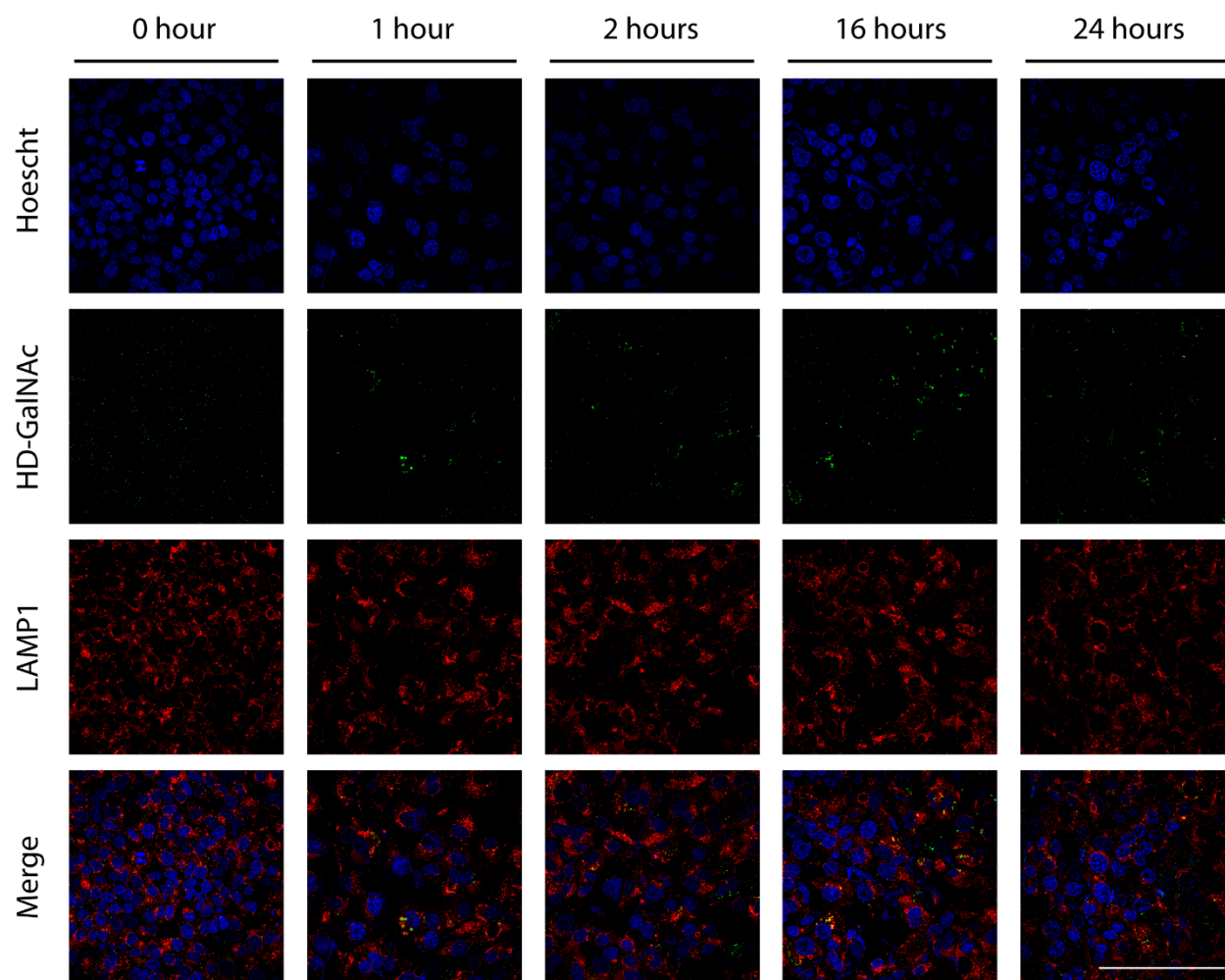**Appendix Figure 19. Kinetic analysis for the intracellular trafficking of HD-GalNAc with early endosomes.** HD-GalNAc were pulsed for 30 mins and then chased for 0, 1, 2, 16 and 24 h with fresh media. Images were acquired using Leica SP5 confocal scanning laser microscopy using a 63X objective. Early endosomes (EEA1) and the nuclei (Hoescht) were stained. Scale bar represents 1 μm. Representative images were shown.
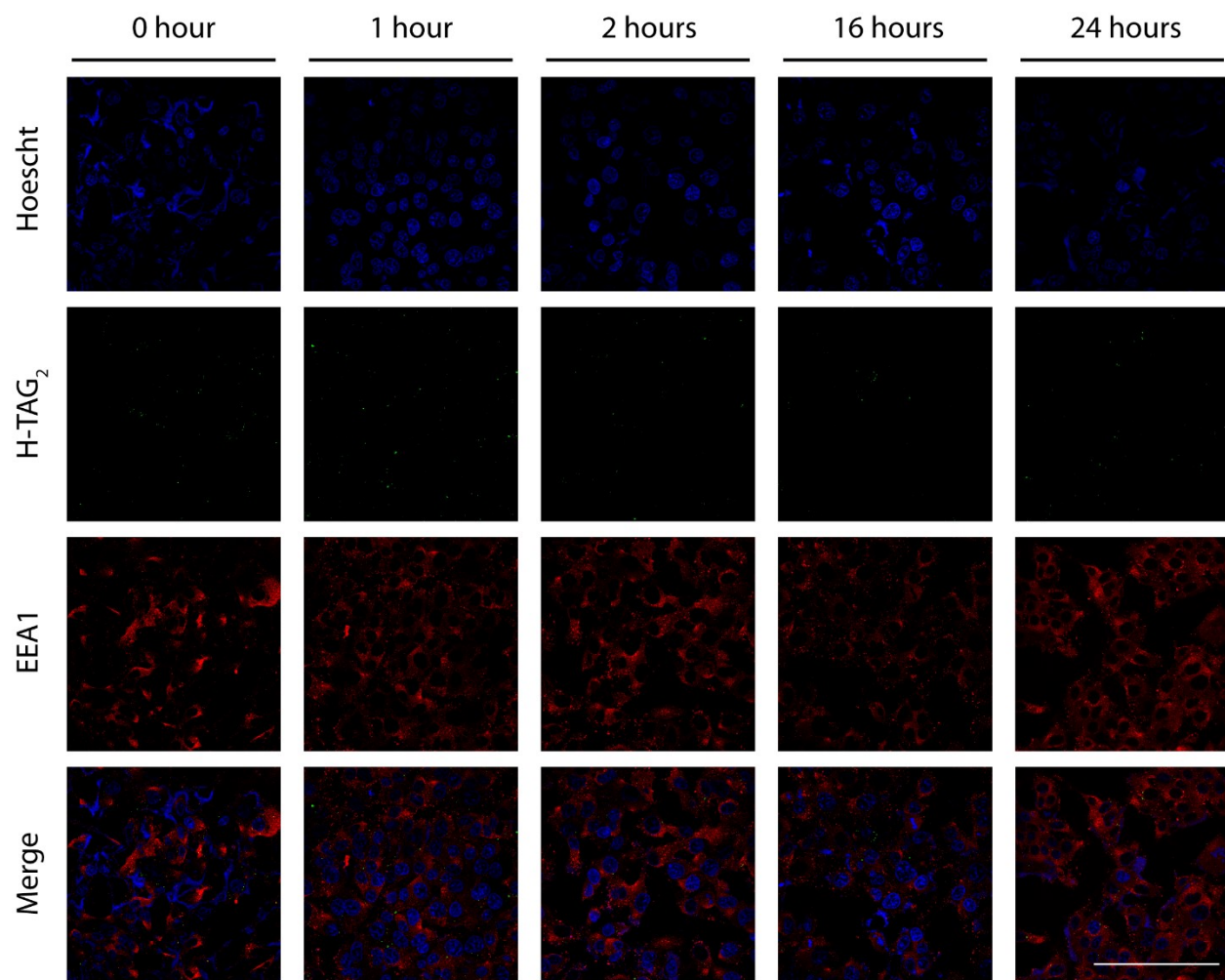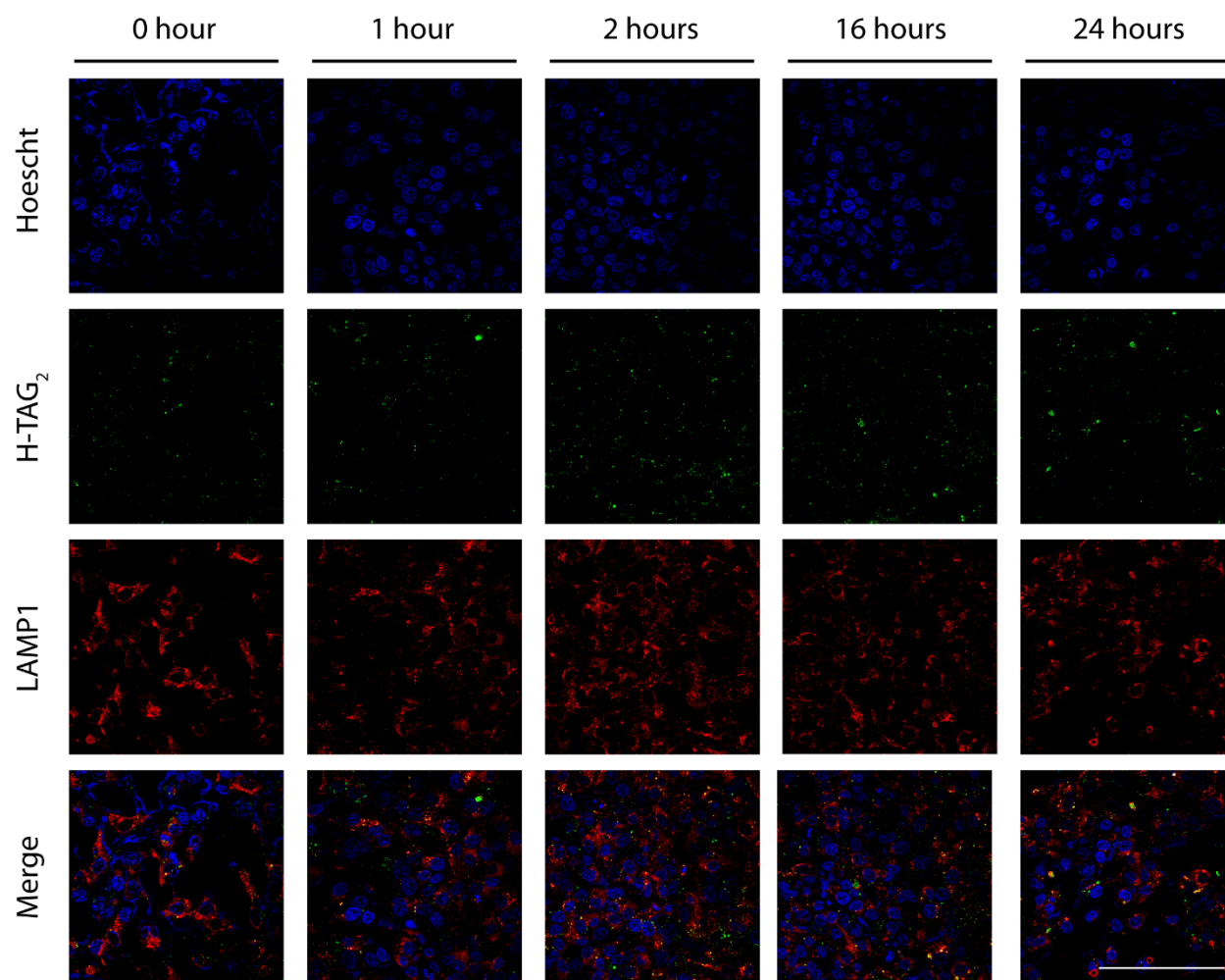
Appendix Figure 20. Kinetic analysis for the intracellular trafficking of H-TAG$_2$ with early endosomes. H-TAG$_2$ were pulsed for 30 mins and then chased for 0, 1, 2, 16 and 24 h with fresh media. Images were acquired using Leica SP5 confocal scanning laser microscopy using a 63X objective. Early endosomes (EEA1) and the nuclei (Hoescht) were stained. Scale bar represents 1 μm. Representative images were shown.
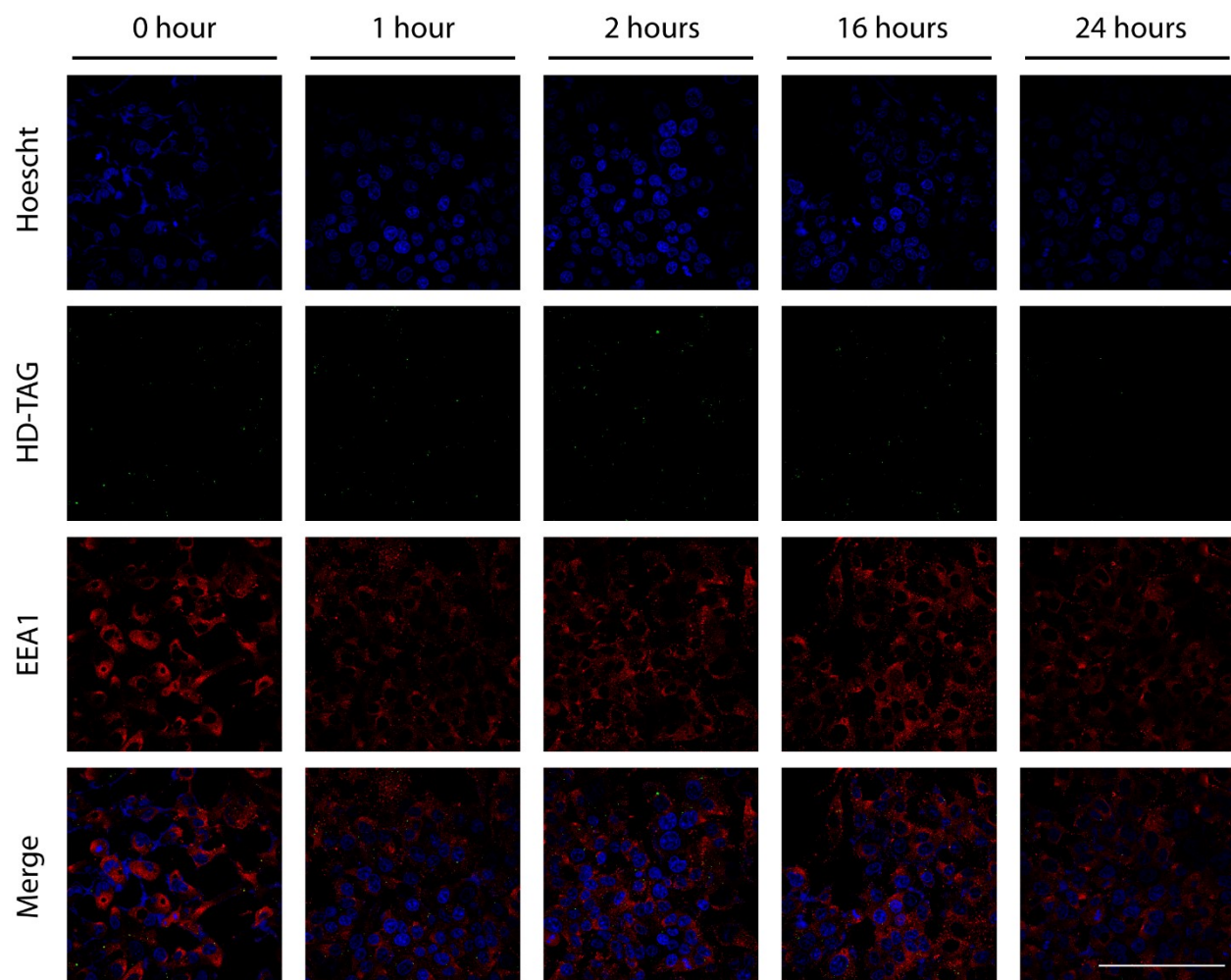
Appendix Figure 21. Kinetic analysis for the intracellular trafficking of HD-TAG with early endosomes. HD-TAG were pulsed for 30 mins and then chased for 0, 1, 2, 16 and 24 h with fresh media. Images were acquired using Leica SP5 confocal scanning laser microscopy using a 63X objective. Early endosomes (EEA1) and the nuclei (Hoescht) were stained. Scale bar represents 1 µm. Representative images were shown.
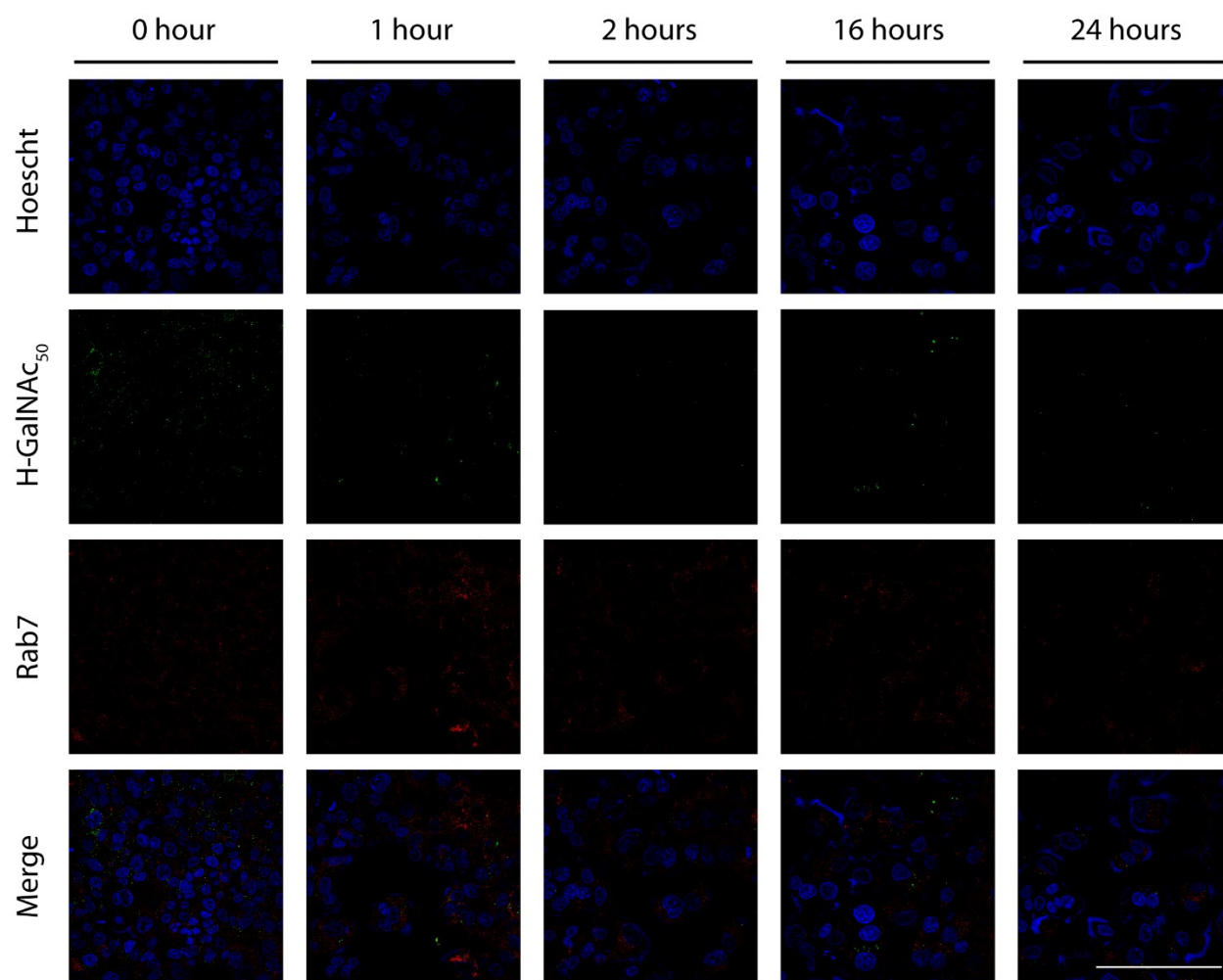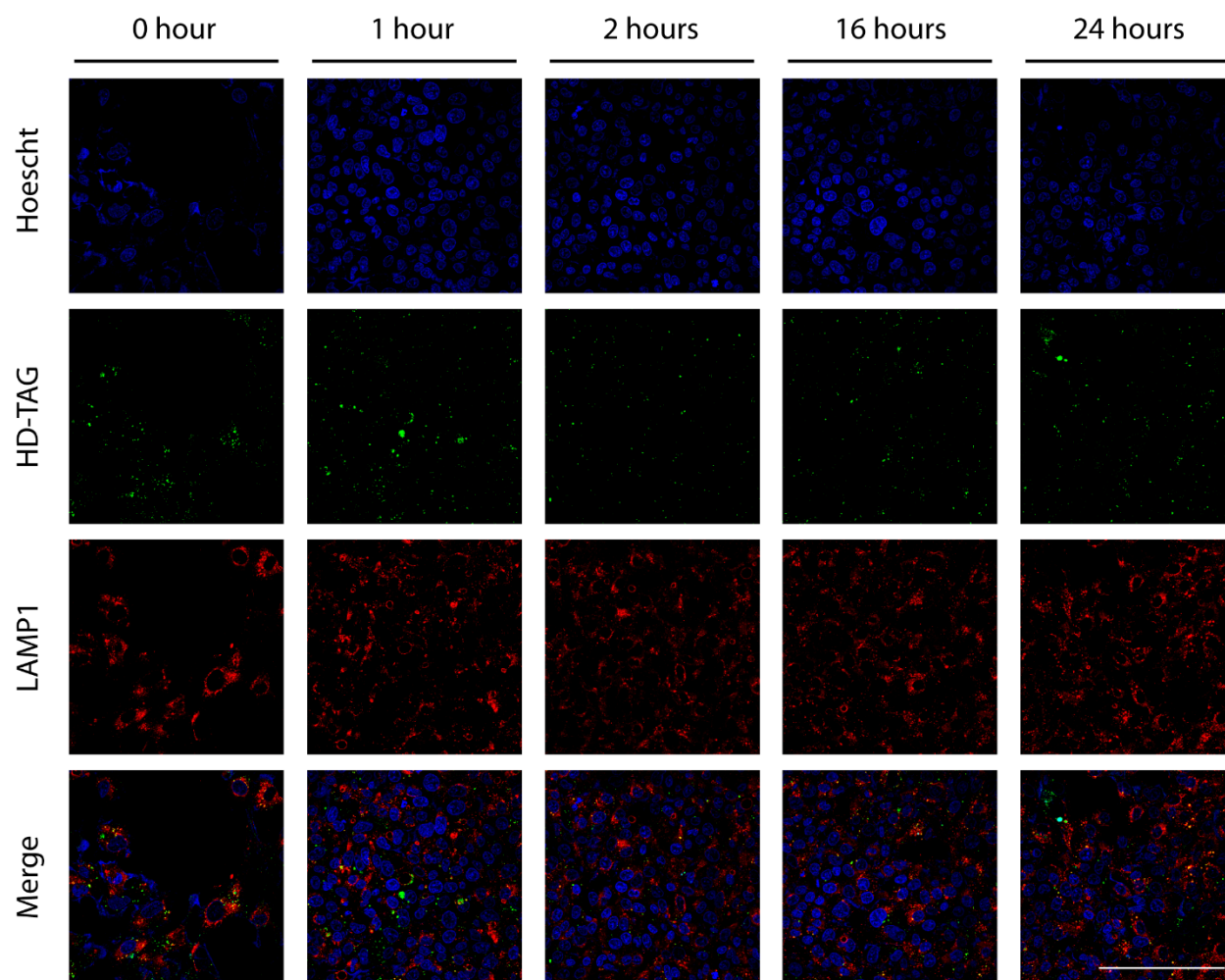
Appendix Figure 22. Kinetic analysis for the intracellular trafficking of H-GalNAc$_{50}$ with late endosomes. H-GalNAc$_{50}$ were pulsed for 30 mins and then chased for 0, 1, 2, 16 and 24 h with fresh media. Images were acquired using Leica SP5 confocal scanning laser microscopy using a 63X objective. Late endosomes (Rab7) and the nuclei (Hoescht) were stained. Scale bar represents 1 μm. Representative images were shown.
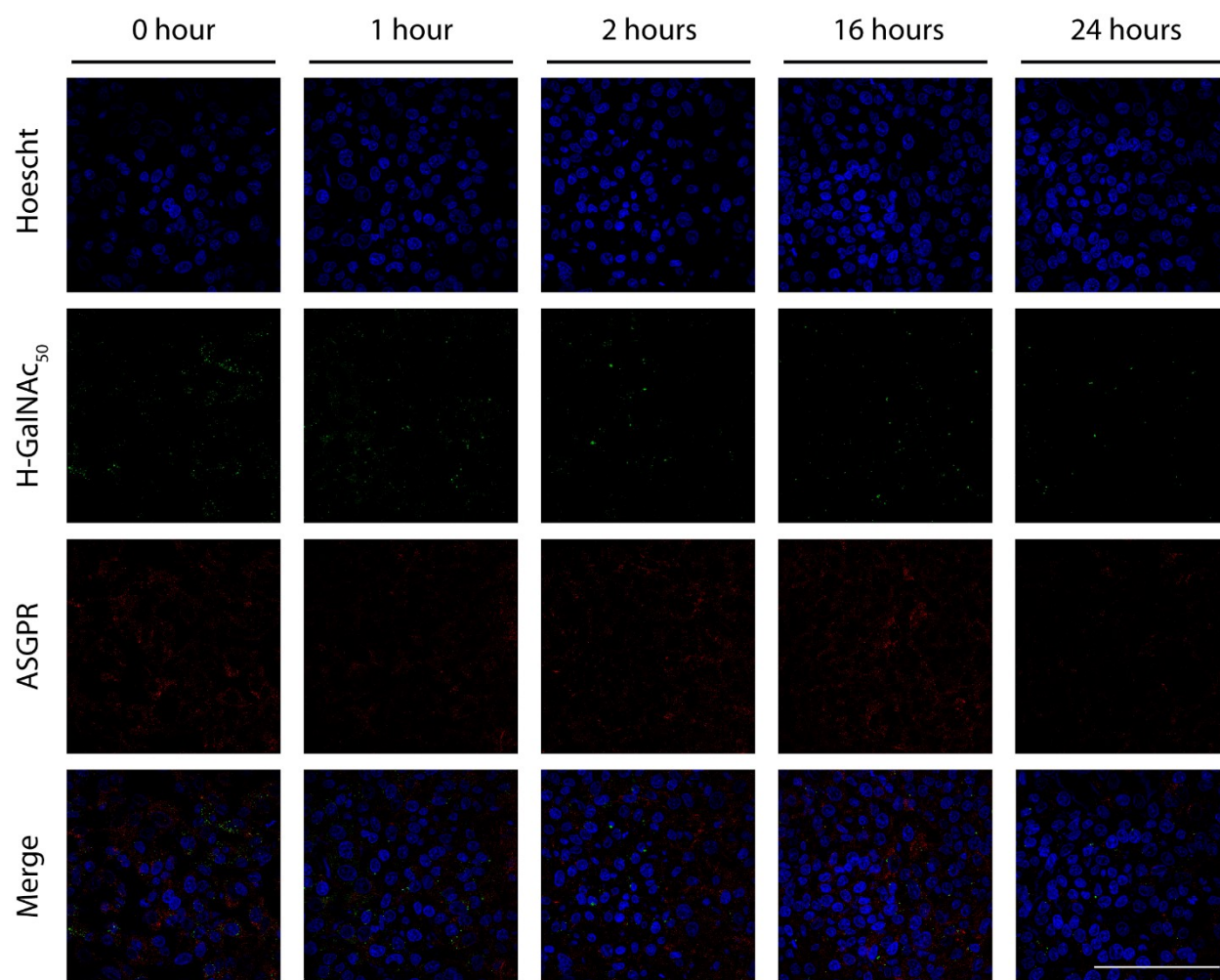
Appendix Figure 23. Kinetic analysis for the intracellular trafficking of HD-GalNAc with late endosomes. HD-GalNAc were pulsed for 30 mins and then chased for 0, 1, 2, 16 and 24 h with fresh media. Images were acquired using Leica SP5 confocal scanning laser microscopy using a 63X objective. Late endosomes (Rab7) and the nuclei (Hoescht) were stained. Scale bar represents 1 μm. Representative images were shown.
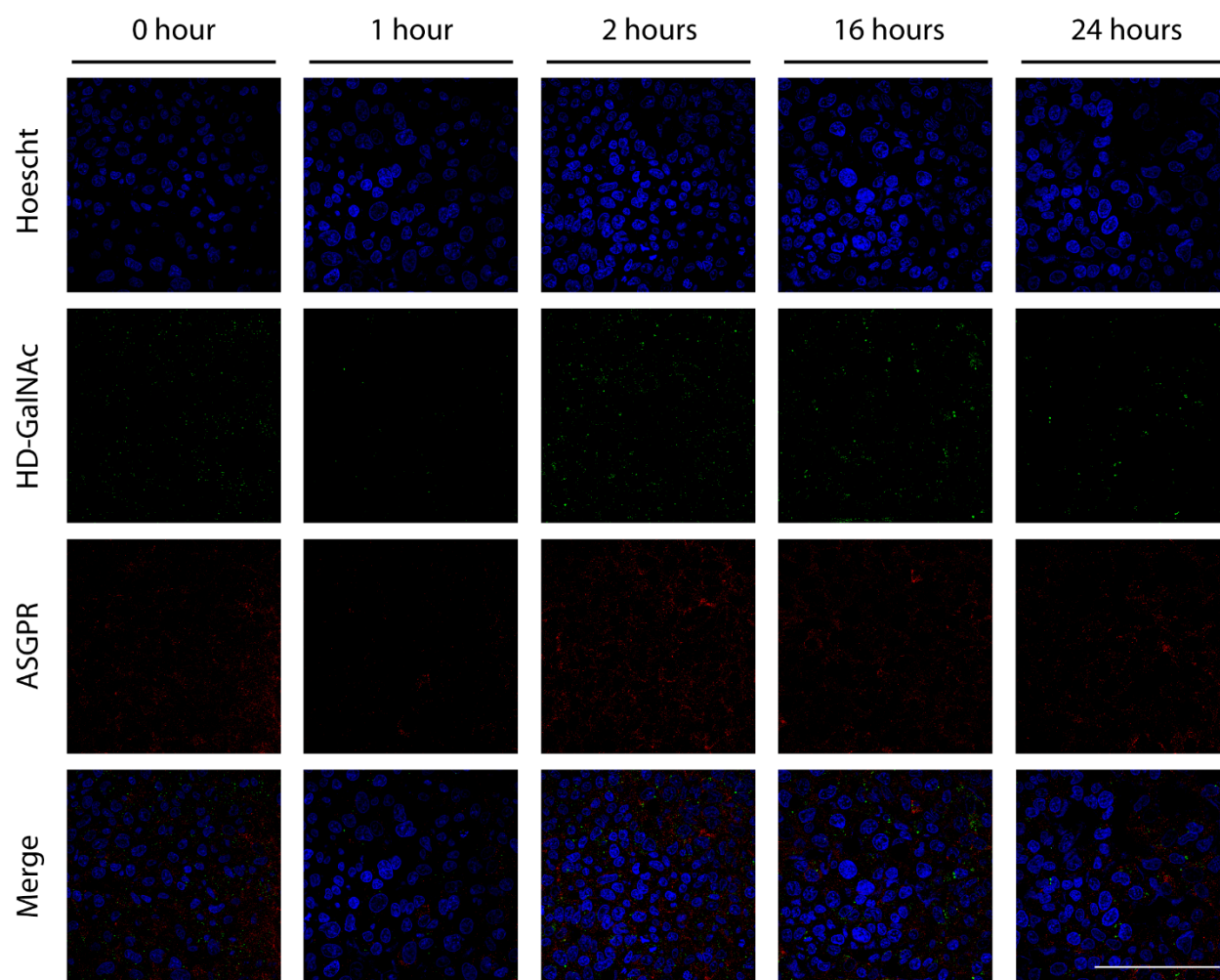
Appendix Figure 24. Kinetic analysis for the intracellular trafficking of H-TAG$_2$ with late endosomes. H-TAG$_2$ were pulsed for 30 mins and then chased for 0, 1, 2, 16 and 24 h with fresh media. Images were acquired using Leica SP5 confocal scanning laser microscopy using a 63X objective. Late endosomes (Rab7) and the nuclei (Hoescht) were stained. Scale bar represents 1 μm. Representative images were shown.
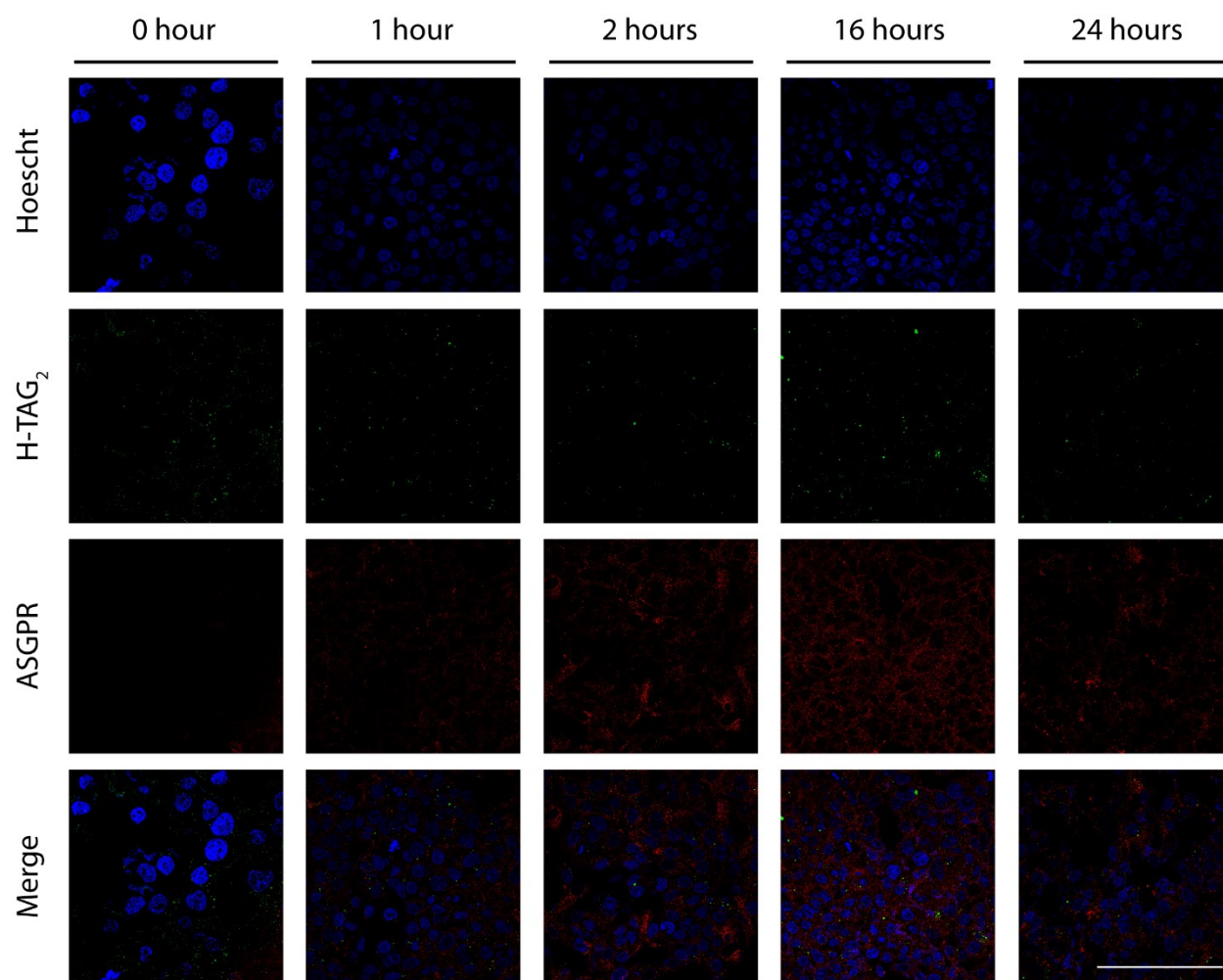
Appendix Figure 25. Kinetic analysis for the intracellular trafficking of HD-TAG with late endosomes. HD-TAG were pulsed for 30 mins and then chased for 0, 1, 2, 16 and 24 h with fresh media. Images were acquired using Leica SP5 confocal scanning laser microscopy using a 63X objective. Late endosomes (Rab7) and the nuclei (Hoescht) were stained. Scale bar represents 1 μm. Representative images were shown.
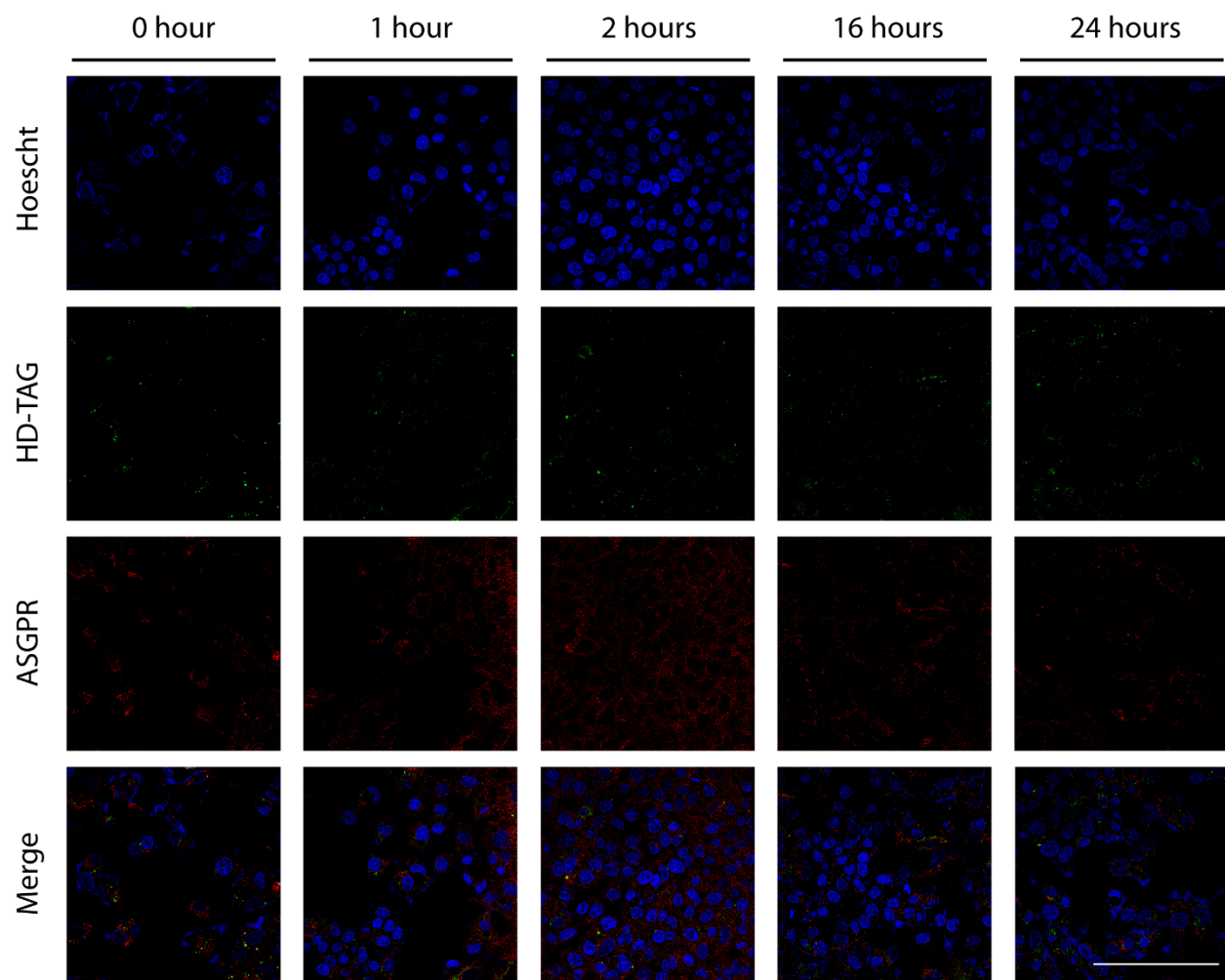
Appendix Figure 26. Kinetic analysis for the intracellular trafficking of H-GalNAc$_{50}$ with lysosomes. H-GalNAc$_{50}$ were pulsed for 30 mins and then chased for 0, 1, 2, 16 and 24 h with fresh media. Images were acquired using Leica SP5 confocal scanning laser microscopy using a 63X objective. Lysosomes (LAMP1) and the nuclei (Hoescht) were stained. Scale bar represents 1 μm. Representative images were shown.
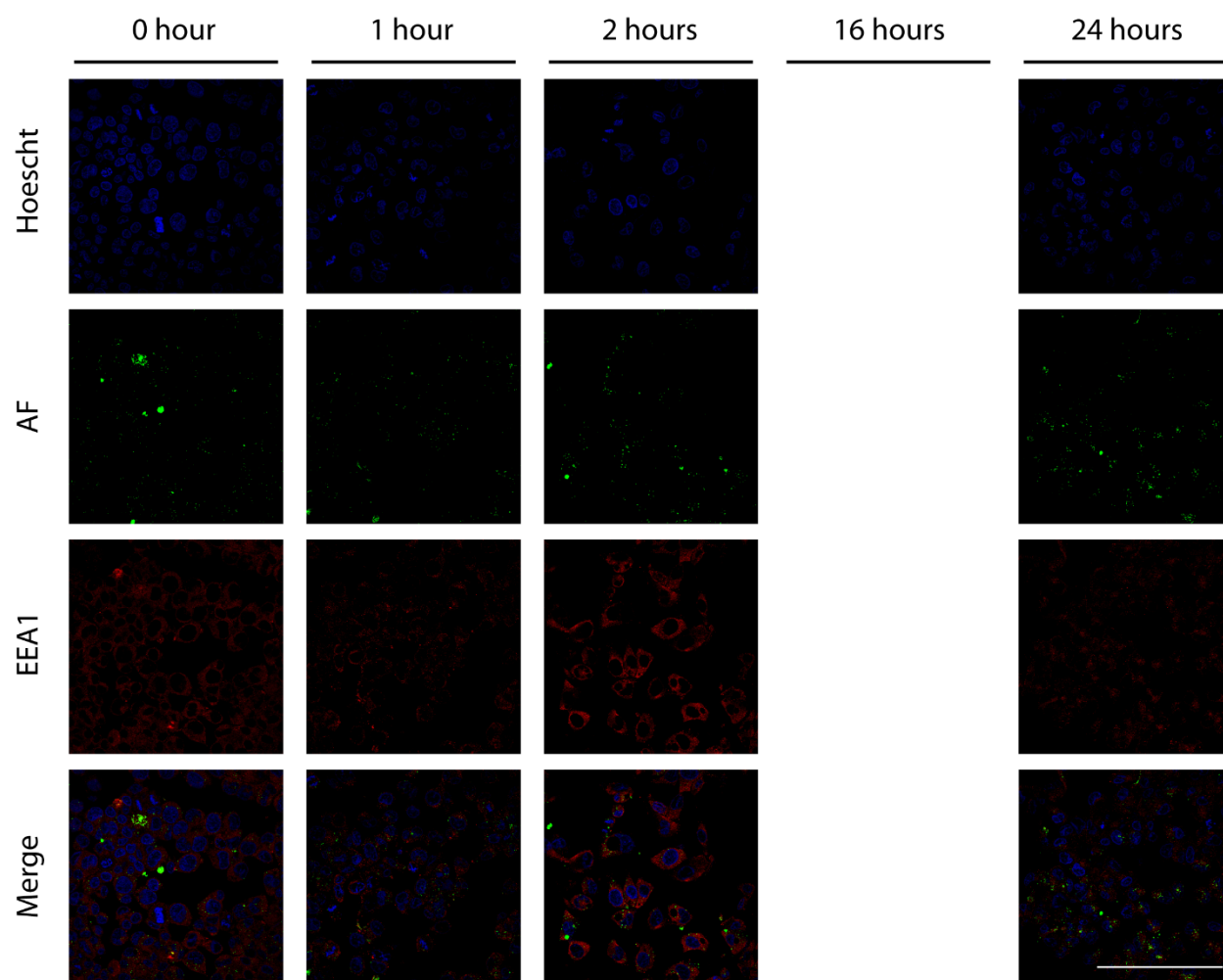
Appendix Figure 27. Kinetic analysis for the intracellular trafficking of HD-GalNAc with lysosomes. HD-GalNAc were pulsed for 30 mins and then chased for 0, 1, 2, 16 and 24 h with fresh media. Images were acquired using Leica SP5 confocal scanning laser microscopy using a 63X objective. Lysosomes (LAMP1) and the nuclei (Hoescht) were stained. Scale bar represents 1 μm. Representative images were shown.

Appendix Figure 28. Kinetic analysis for the intracellular trafficking of H-TAG$_2$ with lysosomes. H-TAG$_2$ were pulsed for 30 mins and then chased for 0, 1, 2, 16 and 24 h with fresh media. Images were acquired using Leica SP5 confocal scanning laser microscopy using a 63X objective. Lysosomes (LAMP1) and the nuclei (Hoescht) were stained. Scale bar represents 1 μm. Representative images were shown.
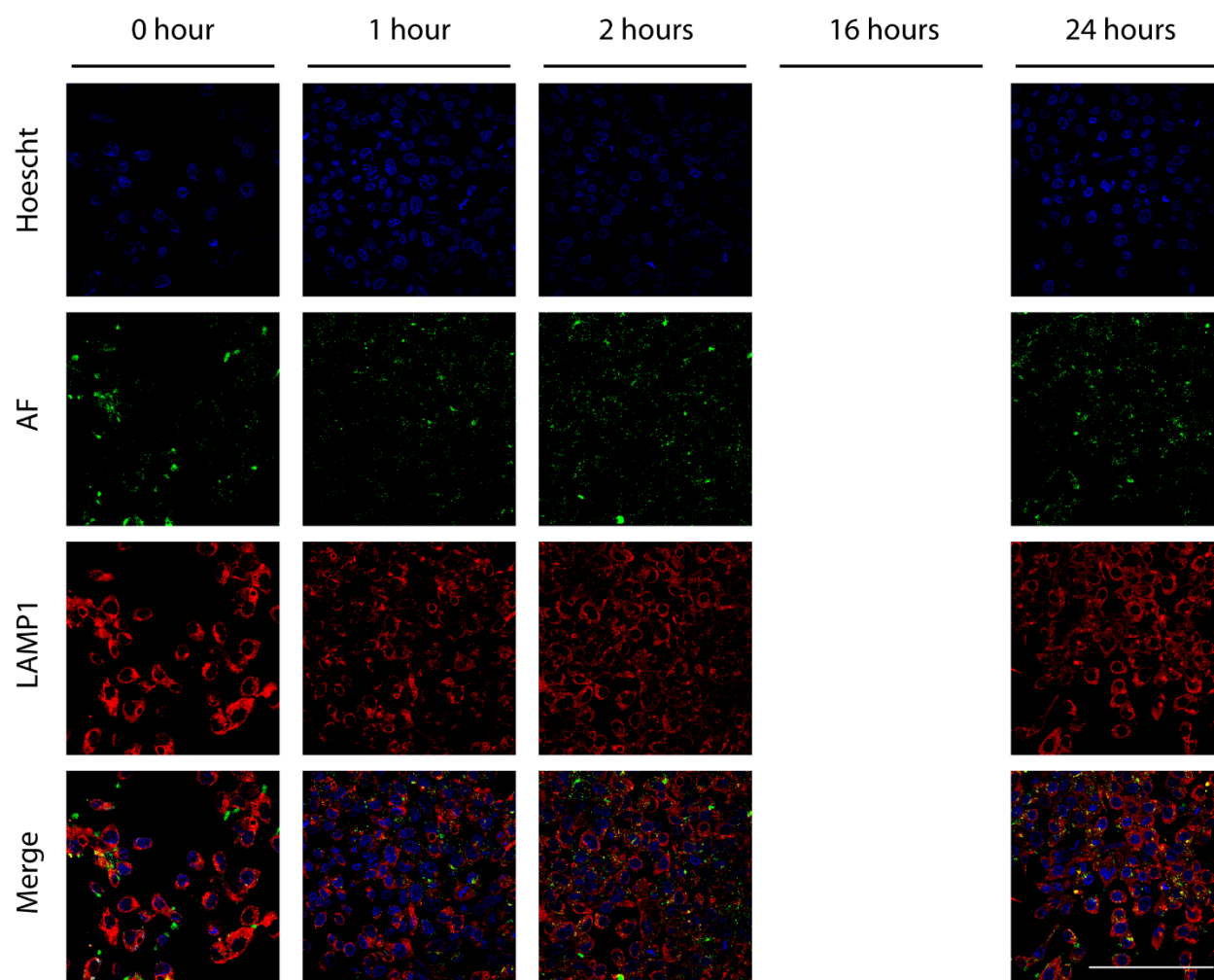
Appendix Figure 29. Kinetic analysis for the intracellular trafficking of HD-TAG with lysosomes. HDTAG were pulsed for 30 mins and then chased for 0, 1, 2, 16 and 24 h with fresh media. Images were acquired using Leica SP5 confocal scanning laser microscopy using a 63X objective. Lysosomes (LAMP1) and the nuclei (Hoescht) were stained. Scale bar represents 1 μm. Representative images were shown.

Appendix Figure 30. Kinetic analysis for the intracellular trafficking of H-GalNAc$_{50}$ with ASGPR. H-GalNAc$_{50}$ were pulsed for 30 mins and then chased for 0, 1, 2, 16 and 24 h with fresh media. Images were acquired using Leica SP5 confocal scanning laser microscopy using a 63X objective. AGPR (ASGPR) and the nuclei (Hoescht) were stained. Scale bar represents 1 μm. Representative images were shown.

Appendix Figure 31. Kinetic analysis for the intracellular trafficking of HD-GalNAc with ASGPR. HD-GalNAc were pulsed for 30 mins and then chased for 0, 1, 2, 16 and 24 h with fresh media. Images were acquired using Leica SP5 confocal scanning laser microscopy using a 63X objective. AGPR (ASGPR) and the nuclei (Hoescht) were stained. Scale bar represents 1 μm. Representative images were shown.

**Appendix Figure 32. Kinetic analysis for the intracellular trafficking of H-TAG$_2$ with ASGPR.** H-TAG$_2$ were pulsed for 30 mins and then chased for 0, 1, 2, 16 and 24 h with fresh media. Images were acquired using Leica SP5 confocal scanning laser microscopy using a 63X objective. AGPR (ASGPR) and the nuclei (Hoescht) were stained. Scale bar represents 1 μm. Representative images were shown.

**Appendix Figure 33. Kinetic analysis for the intracellular trafficking of HD-TAG with ASGPR.** HD-TAG were pulsed for 30 mins and then chased for 0, 1, 2, 16 and 24 h with fresh media. Images were acquired using Leica SP5 confocal scanning laser microscopy using a 63X objective. AGPR (ASGPR) and the nuclei (Hoescht) were stained. Scale bar represents 1 μm. Representative images were shown.

Appendix Figure 34. Kinetic analysis for the intracellular trafficking of AF with early endosomes. AF were pulsed for 30 mins and then chased for 0, 1, 2, 16 and 24 h with fresh media. Images were acquired using Leica SP5 confocal scanning laser microscopy using a 63X objective. Early endosomes (EEA1) and the nuclei (Hoescht) were stained. Scale bar represents 1 µm. Representative images were shown.

Appendix Figure 35. Kinetic analysis for the intracellular trafficking of AF with lysosomes. AF were pulsed for 30 mins and then chased for 0, 1, 2, 16 and 24 h with fresh media. Images were acquired using Leica SP5 confocal scanning laser microscopy using a 63X objective. Lysosomes (LAMP1) and the nuclei (Hoescht) were stained. Scale bar represents 1 μm. Representative images were shown.
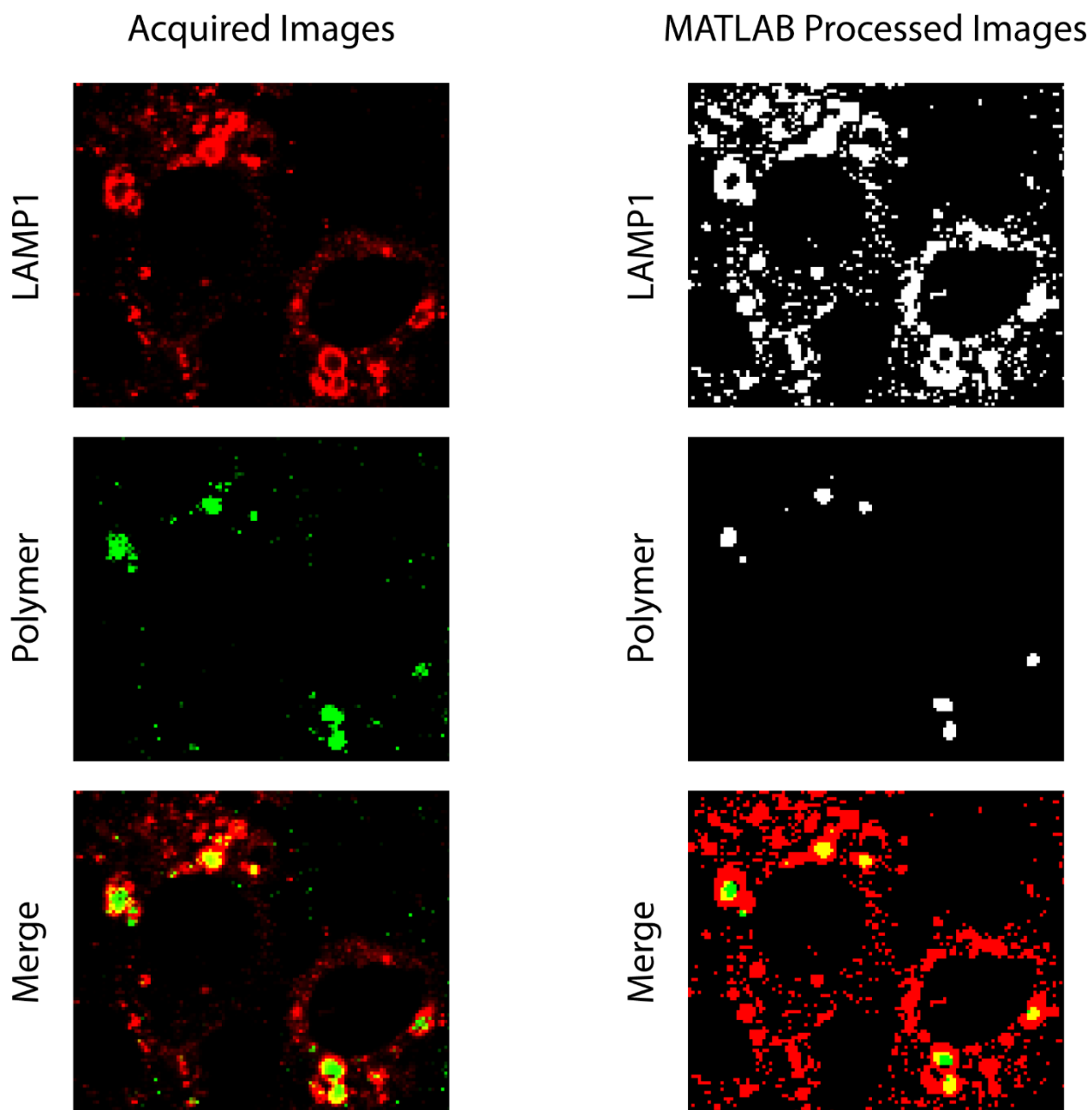
Appendix Figure 36. The encapsulation of polymers by LAMP1 antibody signal. "Acquired Images" refer to images acquired from the Leica SP5 inverted confocal microscope. "MATLAB Processed Images" refers to the processing of acquired images as described in section 3.3.5.6. It is important to note that while all polymer signals were encapsulated by the LAMP1 antibody signal, the Mander's Co-localization Coefficient overlap does not reach a 100%, as visually represented by the green and yellow pixels. This is an inherent limitation and justifies why a 100% overlap was not achieved.
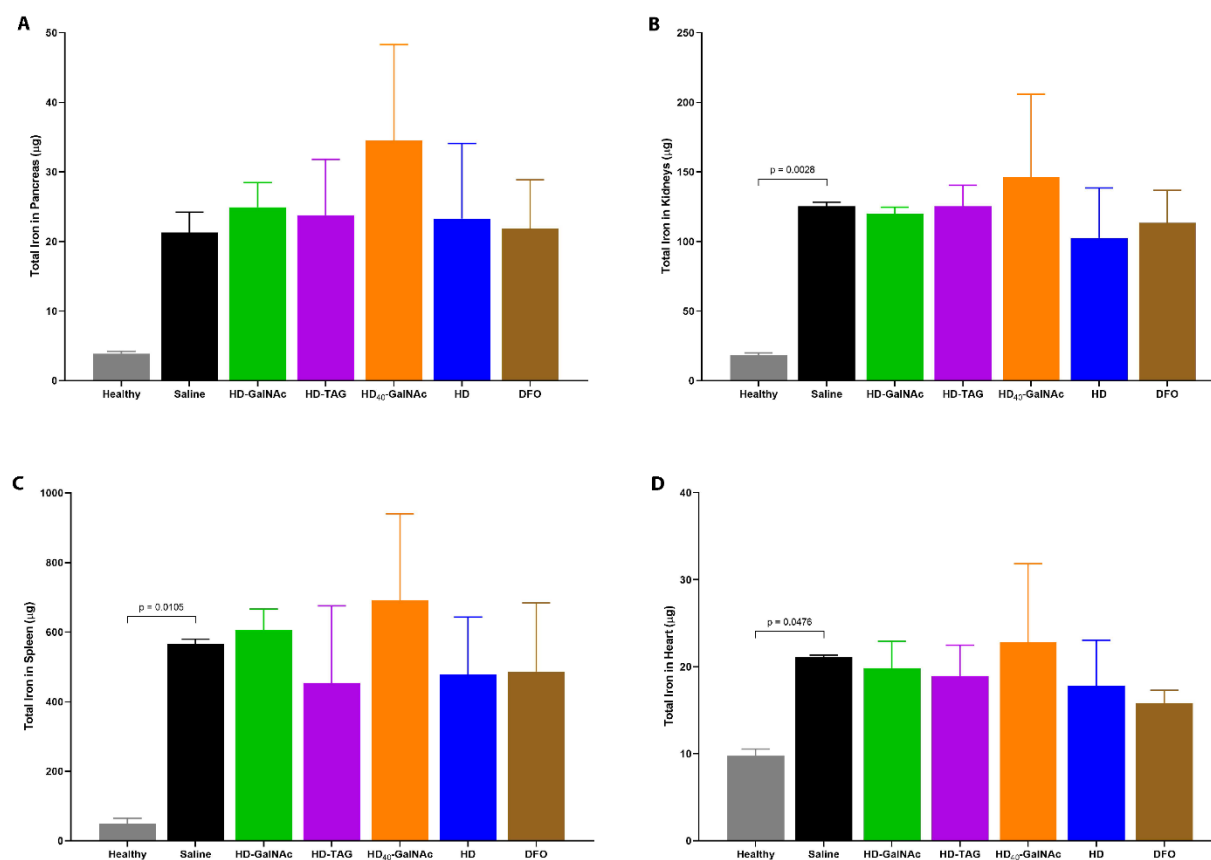
Appendix Figure 37. The iron burden in other organs after liver targeting chelation treatment. Iron overloaded C57Bl/6 mice were treated with liver targeting chelating systems and their controls. The iron content was measured using the u-ferene assay in (A) pancreas, (B) kidneys, (C) spleen and (D) heart. Error bars show standard deviations from 3 independent replicates, each with an intraassay replicate. A 1-way ANOVA with Sidak's multiple comparison tests were performed to compare the differences in treatment groups against iron overloaded saline control using GraphPad Prism.
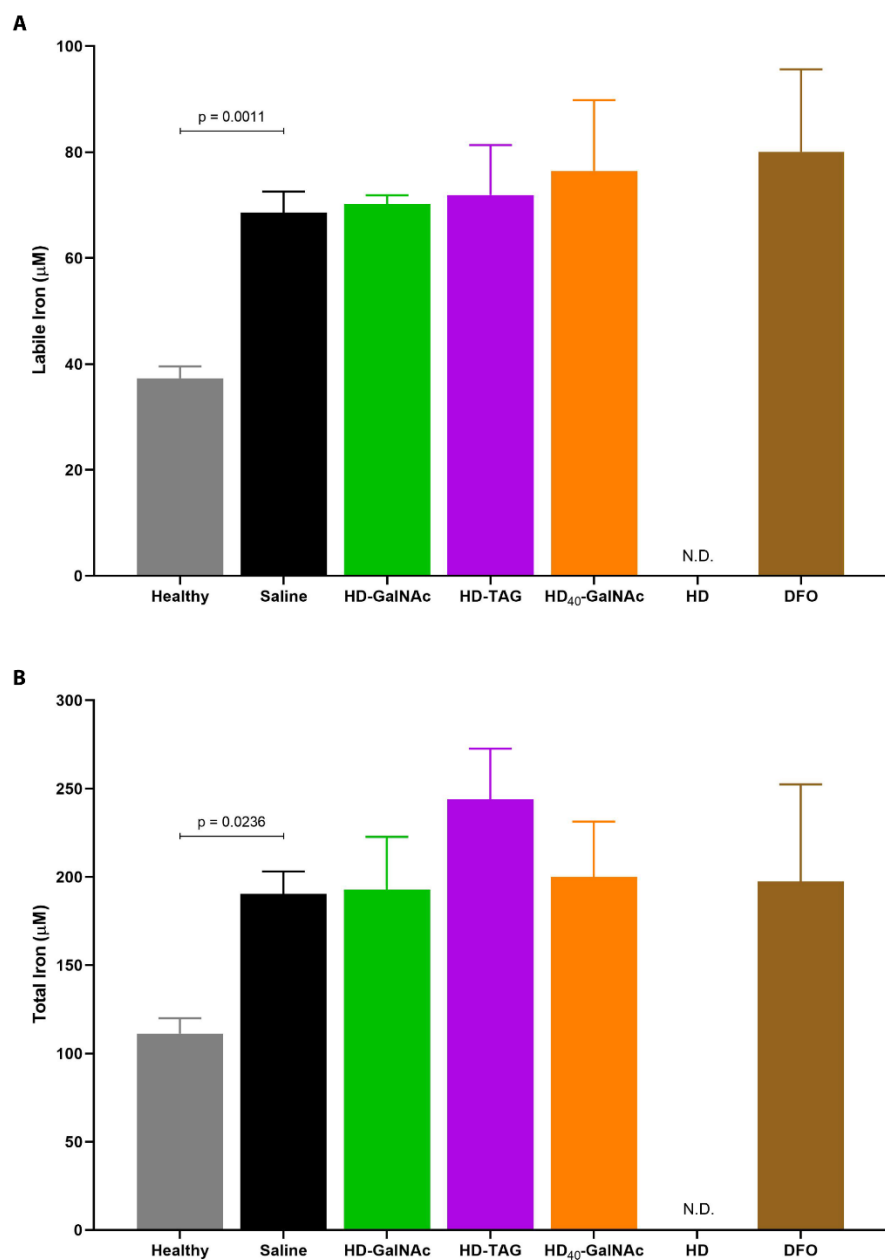
Appendix Figure 38. The plasma labile and total iron concentrations in iron overloaded mice treated with liver targeting chelating systems and their controls. The *u*-ferene assay was used to quantify both (A) labile and (B) total iron concentrations. Error bars show standard deviations from 3 independent replicates. A 1-way ANOVA with Sidak's multiple comparison tests were performed to compare the differences in treatment groups against iron overloaded saline control using GraphPad Prism. Concentrations for mice treated with HD were Not Determined (N.D.).
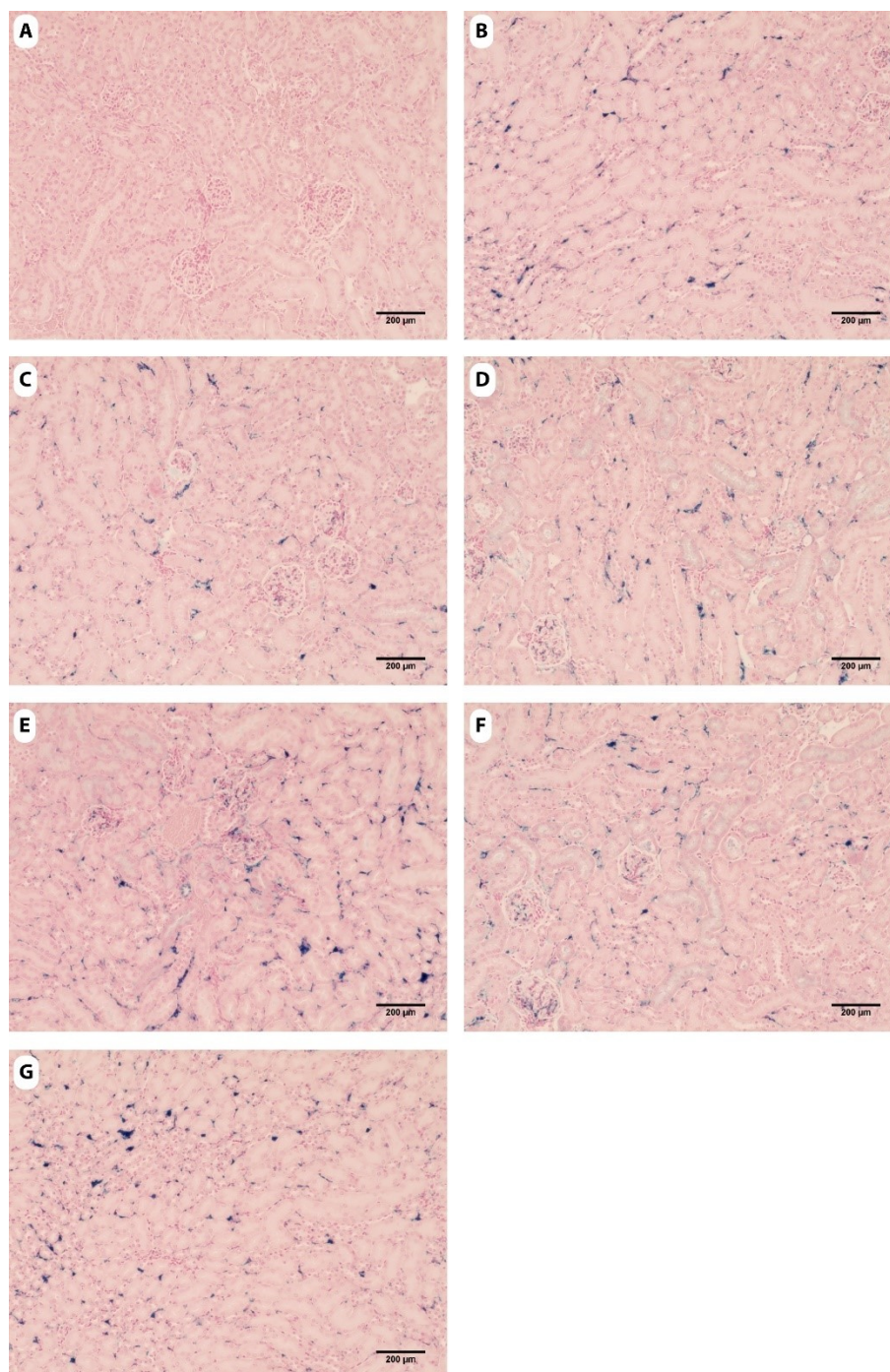
Appendix Figure 39. Histological examination of kidneys in iron overloaded C57Bl/6 mice. Kidneys sections were stained with Prussian blue to detect iron deposits, counter stained with nuclear fast red. Photomicrographs were acquired at 20X magnificent using EVOS XL Core imaging system. Representative micrographs were shown for (A) non-iron overload healthy control, (B) iron overload saline control, (C) HD-GalNAc, (D) HD-TAG, (E) HD$_{40}$-GalNAc, (F) HD, and (G) DFO treatment groups.
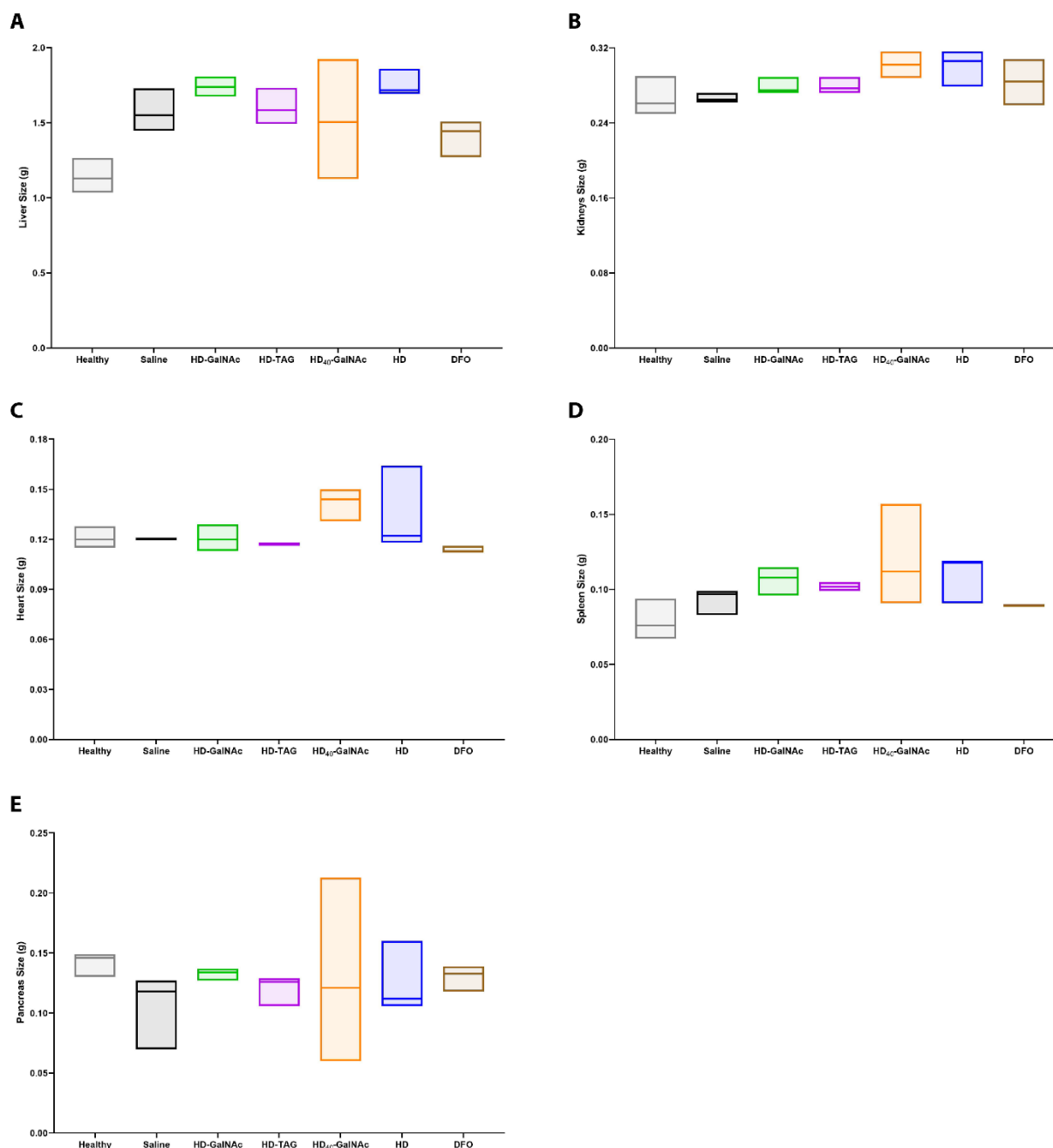
Appendix Figure 40. The changes in organ size after liver targeting chelating treatments. Iron overloaded C57Bl/6 mice were treated with liver targeting chelating systems and their controls. Organs were weighed; (A) liver, (B) kidneys, (C) heart, (D) spleen, and (E) pancreas. Error bars show standard deviations from 3 independent replicates. A 1-way ANOVA with Sidak's multiple comparison tests were performed to compare the differences in treatment groups against iron overloaded saline control using GraphPad Prism.
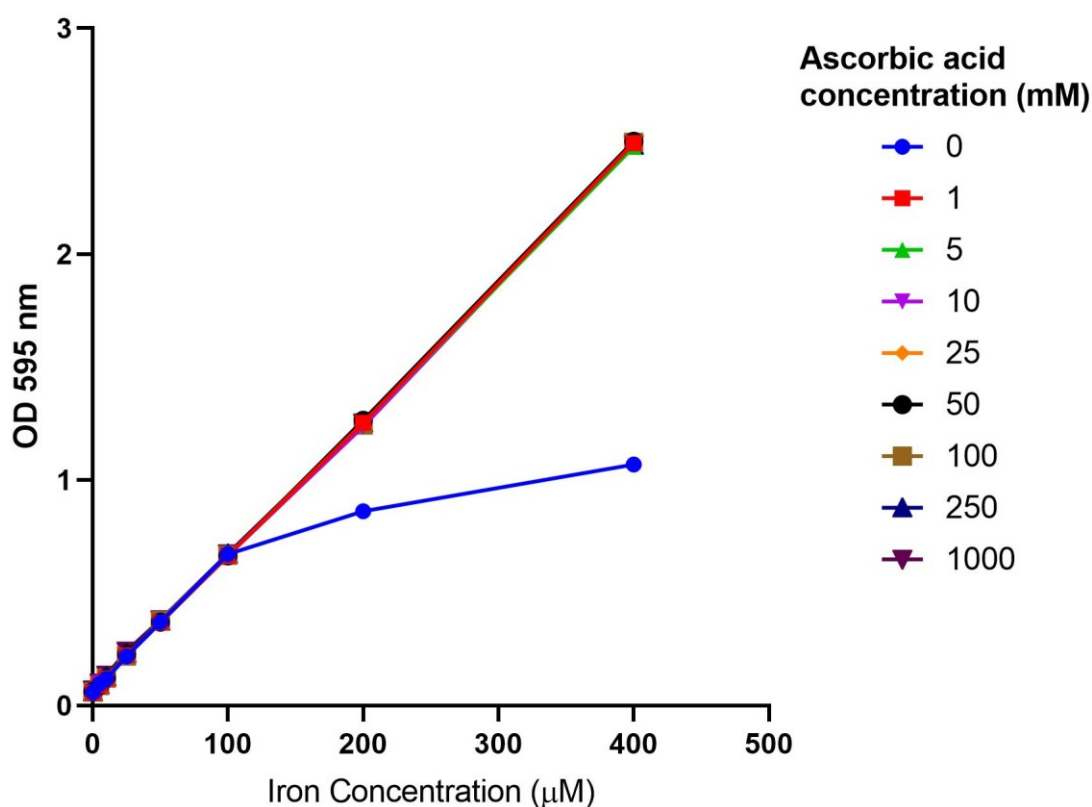
Appendix Figure 41. The standard curve for the ferene assay with different concentrations of ascorbic acid in the working solution. While ascorbic acid concentrations is critical for the differentiation of labile iron and total iron measurements, the standard curve was prepared under different ascorbic acid concentrations (mM). The linear regression for these three iron standard curves are not different. All experiments were done in at least triplicates. Error bars show standard deviations.
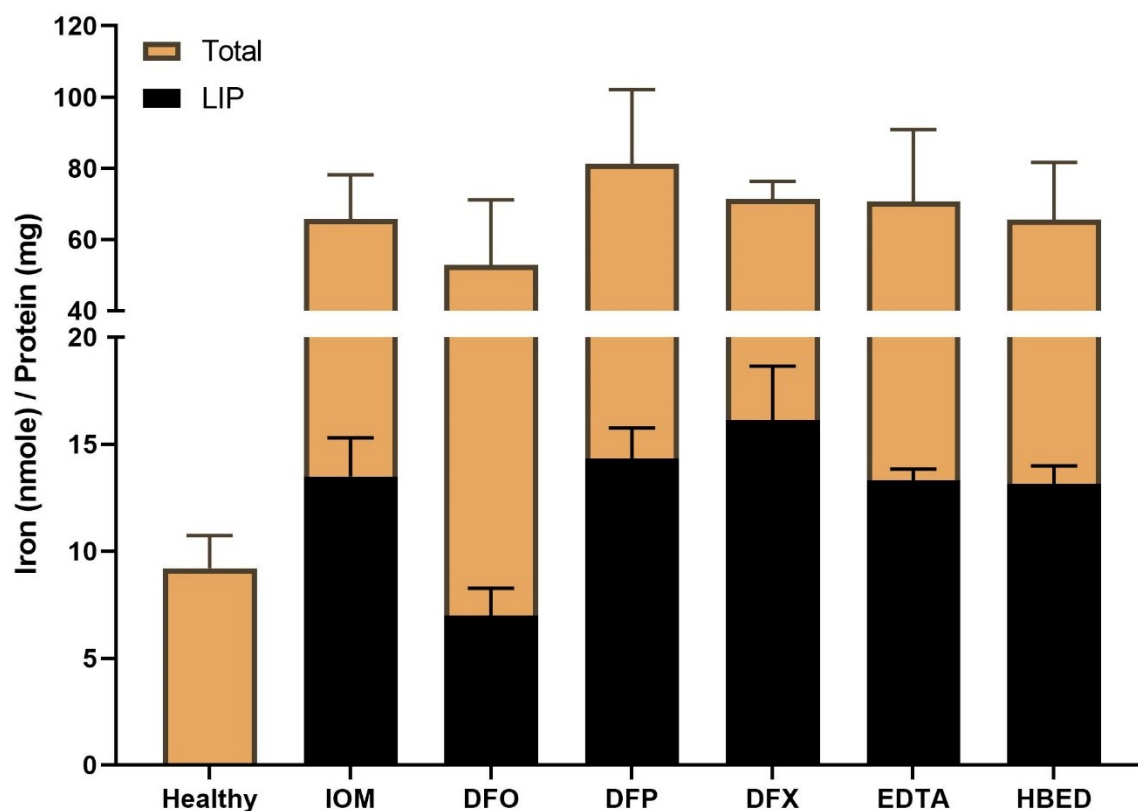
Appendix Figure 42. Changes in the labile iron pool in the presence of different chelators. Iron concentrations were determined using the u-ferene assay; the labile iron pool (LIP) was quantified using 10 mM ascorbic acid in the working solution, and the total iron was quantified using 1 M ascorbic acid in the working solution. Iron concentrations were measured from HepG2 cell lysates; IOM – iron overload model with no chelator, DFO – deferoxamine, DFP – Deferiprone, DFX – Deferasirox, EDTA - Ethylenediaminetetraacetic acid, and HBED - N, N-bis(2-hydroxybenzyl)ethylenediamine-N,N-diacetic acid. Healthy cell lysates were used a control for changes in LIP and total iron. At 10 mM ascorbic acid concentration in working solution, only DFO treated lysates had a significant reduction in the LIP (p<0.0001). All experiments were done in at least triplicates. Error bars show standard deviations. Statistical analysis were performed using GraphPad Prism.
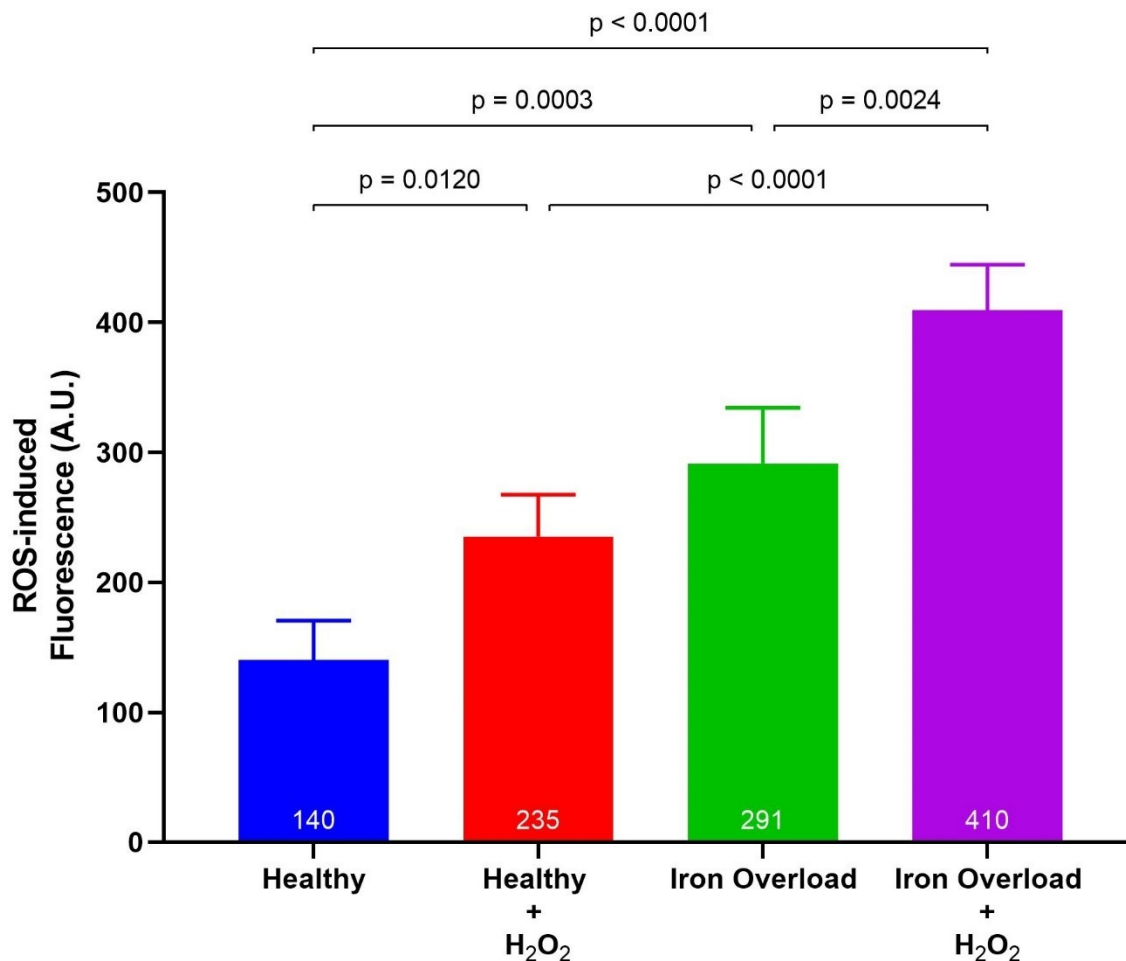
Appendix Figure 43. The ROS generation in HepG2 cells. The ROS generation were measured in both healthy cells and cells iron overloaded with 200 μM of iron from ferric ammonium citrate. The ROS generation were also measured in these cells treated with 50 μM of hydrogen peroxide (H_2O_2) for an additional 24 hours. The fluorescence induced by ROS generation were measured in using a kit. Error bars show standard deviations from 3 replicates. A 1-way ANOVA with Tukey's multiple comparisons test was performed to compare the changes in ROS induced fluorescence using GraphPad Prism.
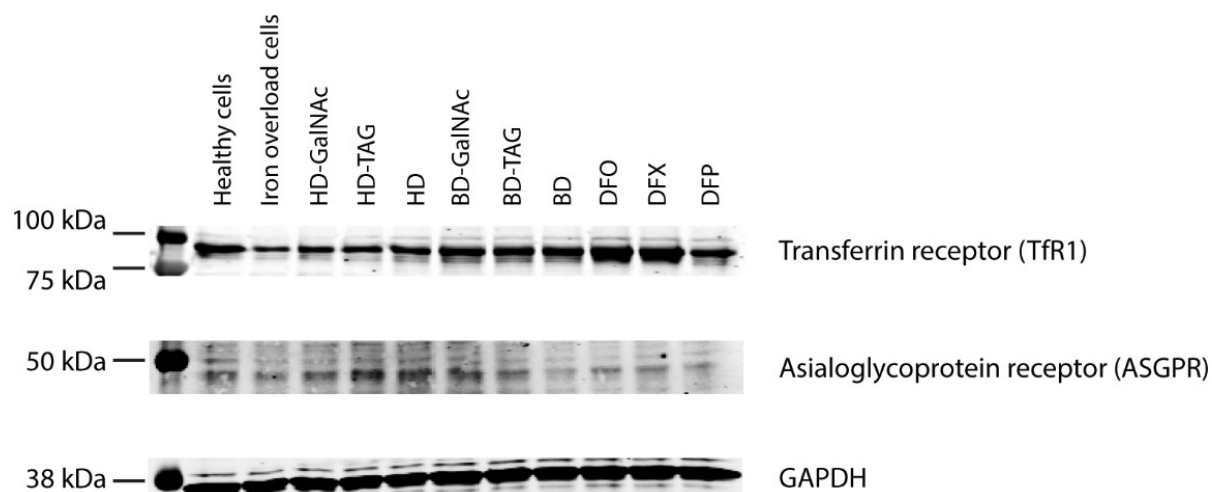
Appendix Figure 44. Western blots for HepG2 cells treated with liver targeting systems and their controls. HepG2 cells were iron overloaded with 50 μM of iron from ferric ammonium citrate and then treated with 15 μM of chelators for 24 hrs. Cell lysates were separated using 10% SDS-PAGE and transferred to a nitrocellulose membrane. The expressions of the transferrin receptor (TfR1) and asialoglycoprotein receptor (AGPR) were obtained. These were normalized against the house keeping protein Glyceraldehyde 3-phosphate dehydrogenase (GAPDH). Healthy cells were used as a negative control. For the purpose of the **Chapter 5**, HPG based polymers were of interest; HD-GalNAc, HD-TAG and HD. For the purpose of the **Chapter 6** and **Appendix: Additional Experimental Data**, biodegradable HPG polymers were of interest; BD-GalNAc, BD-TAG and BD. Small molecule chelators were used as controls for the current available chelation therapy; DFO (deferoxamine), DFX (deferasirox) and DFP (deferiprone).

A.3. Additional Experimental Data

A.3.1. The design, development and investigation of biodegradable polyglycerol based liver targeted chelating systems.

A.3.1.1. *In vitro* cellular responses towards biodegradable liver targeting chelating systems

The optimization of HPG systems were carried forward on to a biodegradable polyglycerol, BHPG, system with respect to the number and identity of ASGPR specific ligand and the density of DFO. These include the following polymers; BHPG with 50 GalNAc (B-GalNAc$_{50}$), BHPG with 15 DFO and 50 GalNAc (BD-GalNAc), BHPG with 5 TAG (B-TAG$_5$), BHPG with 15 DFO and 5 TAG (BD-TAG), BHPG with 15 DFO (BD) and BHPG with 15 DFO and 50 Glucose (BD-Gluc).

First, the binding and uptake of these systems were assessed (**Appendix Figure 45** and **Appendix Figure 46**). BHPG systems decorated with ASGPR specific ligands showed significantly differences when compared to their control (BD-Gluc) (**Appendix Figure 45A**); B-GalNAc$_{50}$, B-TAG$_5$ and BD-GalNAc had significantly higher cellular responses at 50 nM, 10 nM and 10 nM ($p < 0.0001$, $p = 0.0001$, and $^\#p = 0.0369$ respectively) whereas BD-TAG was similar to BD-Gluc at all concentrations. Additionally, the conjugation of DFO influenced the binding and uptake of these systems. Significantly higher binding and uptake was observed for B-GalNAc50 when compared to BD-GalNAc at 200 nM (****$p < 0.0001$). Similarly, significantly higher cellular responses was observed for B-TAG5 when compared to BD-TAG at 10 nM (***$p = 0.0002$).
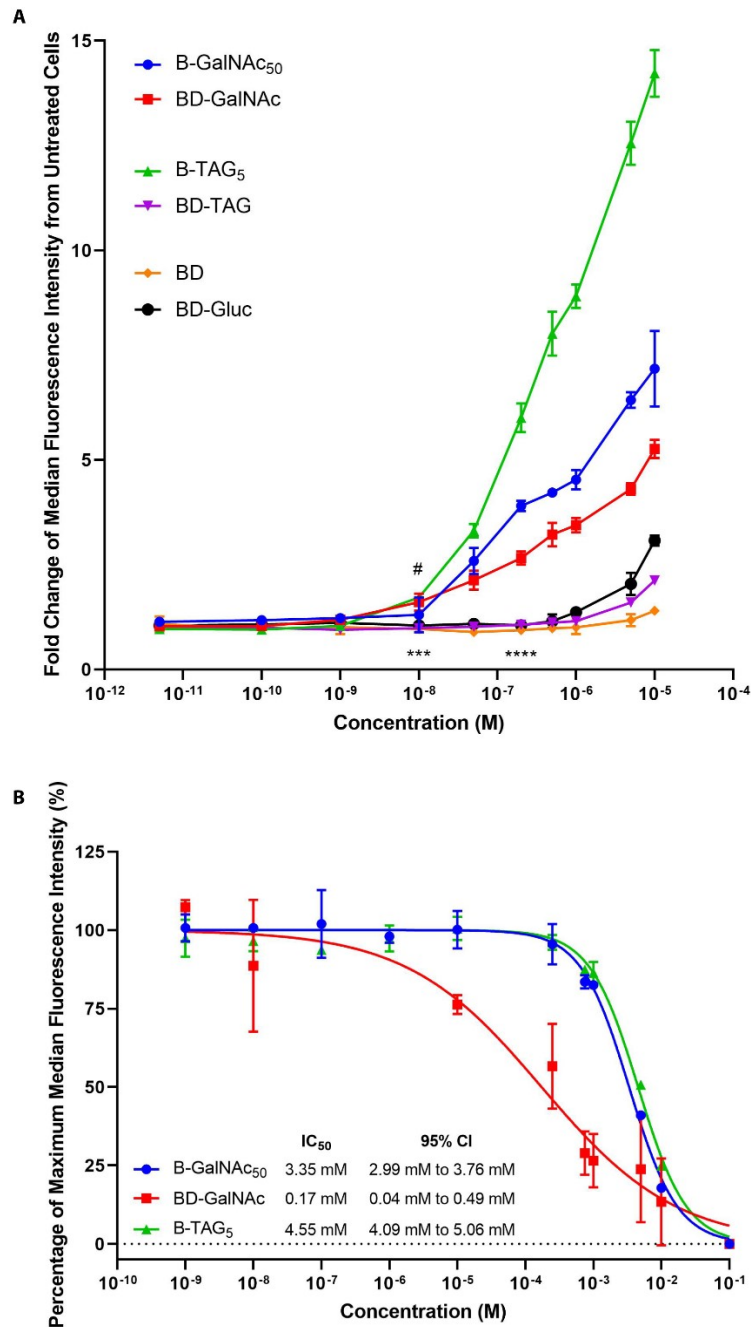
Then, the competitive inhibition of binding and uptake were investigated using unlabelled GalNAc as the antagonist (**Appendix Figure 45B**). The half-maximal inhibitory concentrations (IC$_{50}$) were determined for B-GalNAc$_{50}$, BD-GalNAc and B-TAG$_5$. Statistically, B-TAG$_5$ had the highest IC$_{50}$ concentration of 4.55 mM followed by B-GalNAc$_{50}$ with an IC$_{50}$ concentration of 3.35 mM and then BD-GalNAc with the lowest IC$_{50}$ of 0.17 mM. Remarkably, BHPG conjugated with DFO followed by the conjugation of GalNAc resulted in approximately 20 fold decrease in the IC$_{50}$ value compared to BHPG conjugated with GalNAc only. Moreover, no inhibition in cellular responses were observed for BD-TAG.

In order to assess the non-specific or ASGPR-independent binding and uptake responses, concentration profiles of BHPG systems were investigated in HepG2 cells maintained on ice to prevent receptor

mediated endocytosis (**Appendix Figure 46A**) and an ASGPR negative cell line - HeLa cells (**Appendix Figure 46B**). When compared to BD-Gluc, no significant differences were observed in HepG2 cells maintained on ice. Whereas at 5 μM, B-GalNAc$_{50}$, B-TAG$_5$ and BD-TAG showed significantly higher binding and uptake when compared to BD-Gluc in HeLa cells (**p = 0.0078, ****p < 0.0001 and ***p = 0.0007). BD-GalNAc exhibited similar cellular responses as BD-Gluc. The binding and uptake for BD-GalNAc and BD-TAG were also examined in a murine macrophage cell line, RAW cells (**Appendix Figure 46C**). Only at 10 μM, both BD-GalNAc and BD-TAG displayed almost a 3 fold increase relative to untreated cells with BD-TAG being significantly higher than BD-GalNAc (p = 0.0011).

Next, the cytocompatibility of BHPG based chelators were investigated in both healthy and iron overloaded HepG2 cells (**Appendix Figure 47**). In both healthy and iron overload cells, BD-TAG was better tolerated than BD-GalNAc and BD; at 10 μM of BD-TAG, a significant difference was observed from untreated cells (p < 0.0001 for healthy and iron overloaded cells) whereas at 1 μM of BD-GalNAc and BD exhibited significant differences when compared to untreated cells (p = 0.0019 for BD-GalNAc in healthy cells, p < 0.0001 for BD-GalNAc in iron overload cells, and p < 0.0001 for BD in both healthy and iron overload cells).

Appendix Figure 45. The binding and uptake of biodegradable liver targeting systems. The binding and uptake of BHPG systems were analyzed in at least 10,000 cells (A) over a range of concentrations incubated at 2 h and (B) competitive inhibition over a range of GalNAc concentrations with a fixed concentraiton of polymer (0.5 µM) at 2 h. Error bars show standard deviations for a sample size of 3 independent replicates. A 2-way ANOVA with Tukey's multiple comparisons test was performed using GraphPad Prism. **** represents $p < 0.0001$ and *** or ### $p < 0.0010$.
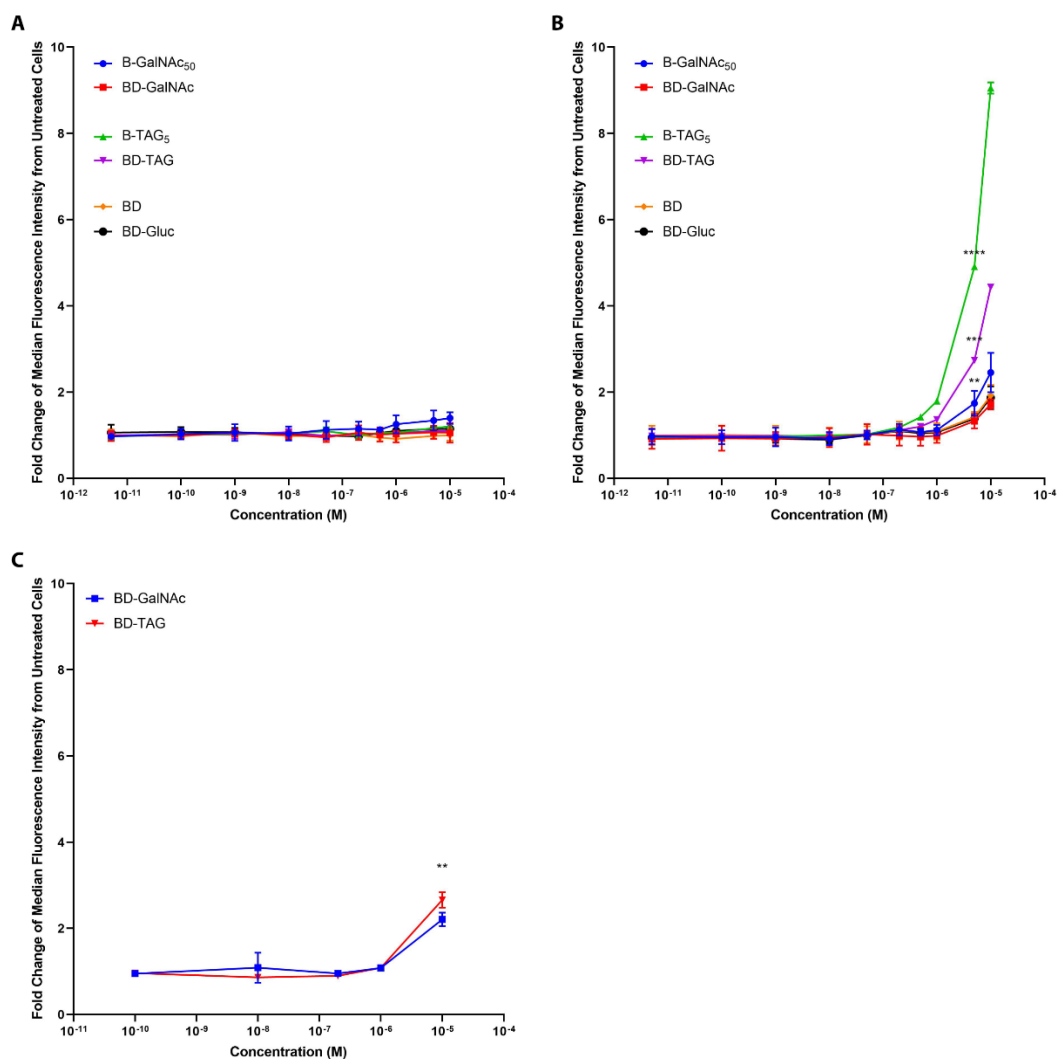
Appendix Figure 46. The non-specific or ASGPR-independent binding and uptake of all biodegradable liver targeting chelating systems and their controls. The response of all carboxyrhodamine-tagged polymers were measured over a range of concentrations. At least 10,000 cells were analyzed using the 488 nm laser and the FITC emission filter (530/20 nm). (A) HepG2 cells incubated with polymers at 4°C minimizes receptor mediated endocytosis. (B) HeLa cells have been used as an ASGPR negative cell line. (C) RAW cells were used to model the murine macrophages and their cellular responses. Error bars show standard deviations for a sample size of 3 independent replicates. A 2-way ANOVA with Dunnett's multiple comparison tests were performed to compare the cellular responses to BD-Gluc. A 2-way ANOVA with Sidak's multiple comparison test were performed for cellular responses in RAW cells. All statistical comparisons were performed using GraphPad Prism. ** represents $p < 0.0100$, *** represents $p < 0.0010$ and **** represents $p < 0.0001$.
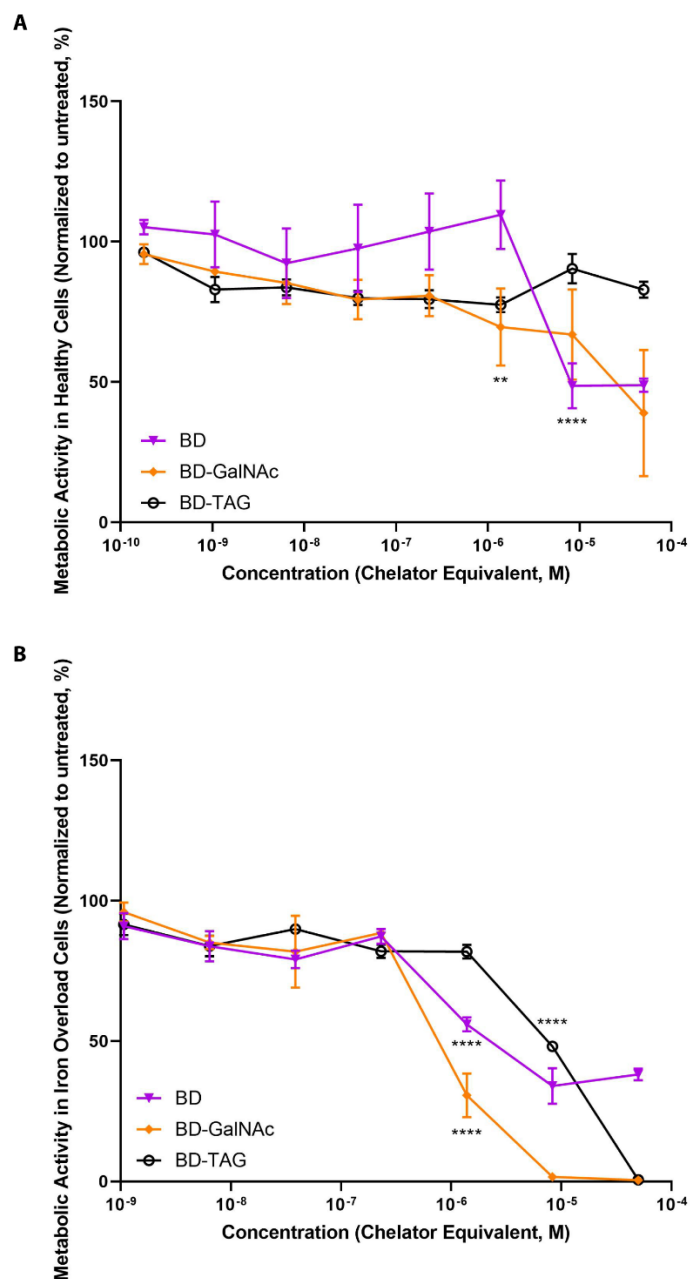
Appendix Figure 47. The cytotoxicity of biodegradable liver targeting chelating systems and its non-liver targeted control in HepG2 cells. The metabolic activity were measured by the MTT assay in response to chelator treatments in HepG2 cells that were (A) non-iron loaded and (B) iron overloaded cells. A wide range of chelator-equivalent concentrations (from 1 nM to 50 μM) were assessed. Error bars show standard deviations for a sample size of 3 independent replicates. A 2-way ANOVA with Dunnett's multiple comparison tests were performed using GraphPad Prism. **** represents $p < 0.0001$ and ** represents $p < 0.0100$.

A.3.1.2. Kinetic investigations into the intracellular trafficking of biodegradable liver targeting chelating systems

The kinetic differences in the endocytosis of biodegradable liver targeted polymers towards the lysosomes were investigated in detail using pulse-chase investigations. HepG2 cells were 'pulsed' with fluorescent polymers for 30 min and then 'chased' by replacing the media with fresh media (i.e. no fluorescent polymer) for an additional 0, 1, 2, 16 and 24 h (**Appendix Figure 48**). The endocytic pathway was traced using endocytic markers to identify early endosomes (EEA1), late endosomes (Rab7), and lysosomes (LAMP1). The ASGPR was also traced (ASGPR). Co-localization of polymers – B-GalNAc$_{50}$ (**Appendix Figure 48A**), BD-GalNAc (**Appendix Figure 48B**), B-TAG$_5$ (**Appendix Figure 48C**) and BD-TAG (**Appendix Figure 48D**) with different endocytic compartments were measured and quantitatively compared using MCCs.

Cells treated with all polymers exhibited rapid lysosomal co-localization. Immediately after pulsing the cells with polymers (0 h chase), the MCCs for LAMP1 were significantly higher when compared to the MCCs for the endocytic markers; B-GalNAc$_{50}$ showed 42% overlap with LAMP1 compared to the 32% overlap with EEA1, 1% overlap with Rab7, and 0% overlap with ASGPR (p < 0.0001 for all comparisons), BD-GalNAc showed 71% overlap with LAMP1 compared to the 30% overlap with EEA1, 1% overlap with Rab7, and 0% overlap with ASGPR (p < 0.0001 for all comparisons), B-TAG$_5$ showed 39% overlap with LAMP1 compared to the 27% overlap with EEA1, 1% overlap with Rab7, and 0% overlap with ASGPR (p < 0.0001 for all comparisons), and BD-TAG showed 74% overlap with LAMP1 compared to the 25% overlap with EEA1, 3% overlap with Rab7, and 0% overlap with ASGPR (p < 0.0001 for all comparisons). Further, the percentage of polymer signal overlapping with LAMP1 significantly increased when comparing the MCCs determined from a chase of 0 h to 1 h; B-GalNAc$_{50}$ increased from 42% to 60% (p < 0.0001), B-TAG$_5$ increased from 39% to 50% (p < 0.0001), and BD-TAG increased from 74% to 84% (p < 0.0001). Whereas, the percentage of polymer signal overlapping with LAMP1 significantly decreased when comparing the MCCs determined from a chase 0 h to 1 h for BD-GalNAc (71% to 60%; p < 0.0001) and from a chase of 1 h to 2 h for BD-TAG (84% to 71%; p < 0.0001). Notably, the MCCs for polymer signal overlapping with Rab7 and ASGPR were between 0% to 3% for all polymers at all chase times.

Next, distinct differences were observed between GalNAc decorated systems and TAG decorated systems for LAMP1 co-localization, especially when assessing the influence of DFO conjugation. GalNAc decorated systems showed a statistical difference when comparing the overlap of non-chelator B-GalNAc$_{50}$ and BD-GalNAc with LAMP1 at 0 h chase; the MCC was 42% for B-GalNAc50 with LAMP1 compared to the MCC of

71% for BD-GalNAc with LAMP1 (p < 0.0001). No statistical differences were observed in the MCCs of B-GalNAc$_{50}$ and BD-GalNAc with LAMP1 at all other chase hours. On the other hand, TAG decorated systems conjugated with DFO showed significant increases in the MCCs overlapping with LAMP1 when compared to TAG decorated systems without DFO (p < 0.0001 for all comparisons); the MCCs at 0 h for B-TAG$_5$ vs BD-TAG was 40% vs 74%, the MCCs at 1 h for B-TAG$_5$ vs BD-TAG was 50% vs 84%, the MCCs at 2 h for B-TAG$_5$ vs BD-TAG was 54% vs 71%, the MCCs at 16 h for B-TAG$_5$ vs BD-TAG was 57% vs 68%, and the MCCs at 24 h for B-TAG$_5$ vs BD-TAG was 58% vs 69%. When comparing the GalNAc and TAG decorated systems, the MCCs for B-GalNAc$_{50}$ with LAMP1 at 1 h was 60%, which was significantly higher compared to the MCCs of 50% for B-TAG$_5$ (p < 0.0001). However, the MCCs for BD-TAG were significantly higher when compared to the MCCs for BD-GalNAc at all chase times (p < 0.0001 for all comparisons).
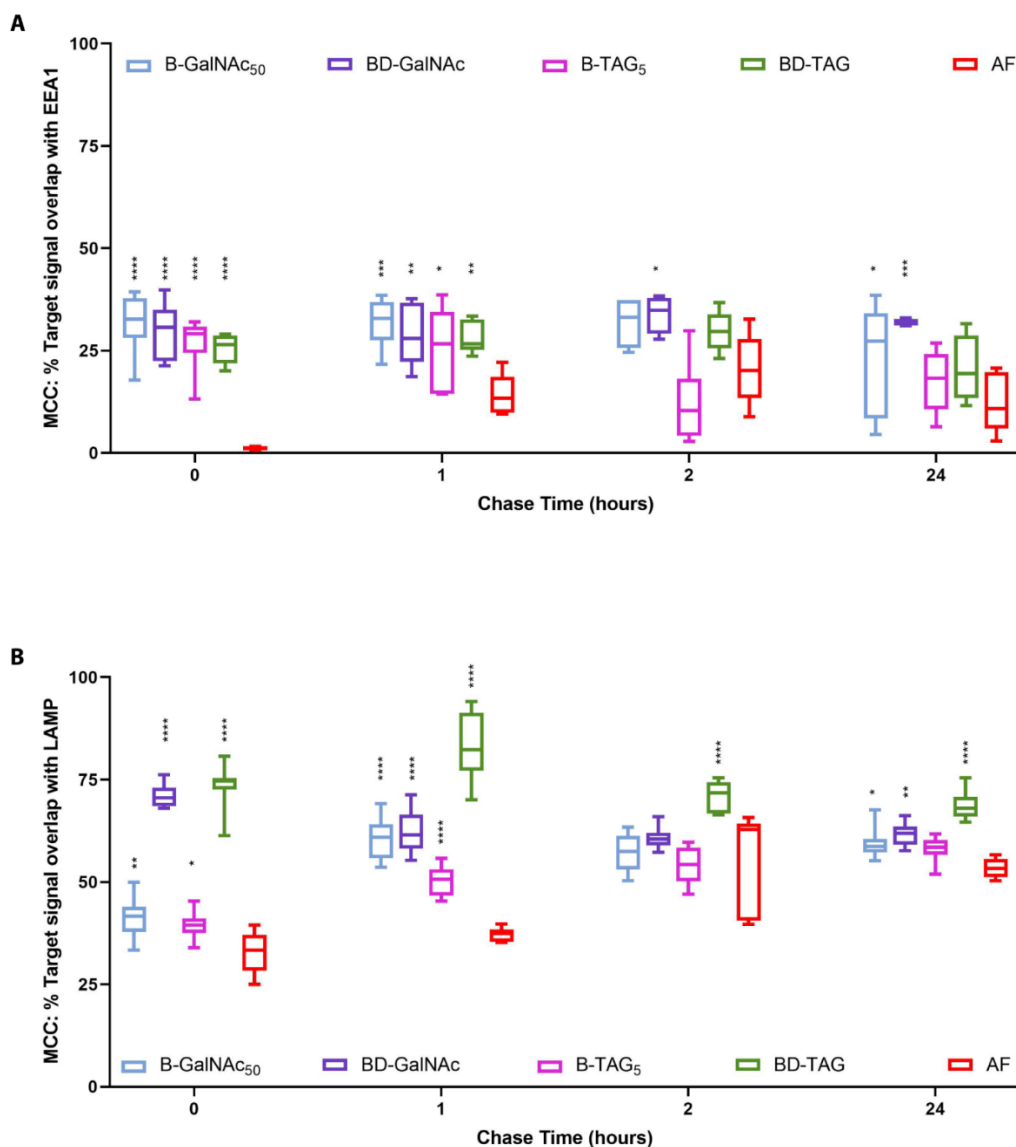
It is evident that both the ASGPR-specific ligand identity and DFO conjugation influenced the observed intracellular trafficking kinetics. To better contextualize these differences, similar pulse chase experiments were compared to asialofetuin (AF) which is a natural ligand that is targeted to the lysosome for degradation.

With respect to the early endosomes (EEA1) (**Appendix Figure 49A**), AF revealed an increasing trend was observed over the first 2 h followed by a slight decrease after 24 h. When compared to all liver targeting polymers, AF exhibited a slower increase in the MCCs for EEA1 overlap. Immediately after a 30 min pulse, all biodegradable liver targeting polymers showed significantly higher signal overlap when compared to AF (****p < 0.0001 for all comparisons). AF showed a 1% signal overlap whereas B-GalNAc$_{50}$, BD-GalNAc, B-TAG$_5$ and BD-TAG showed 32%, 30%, 27% and 25% signal overlap respectively. Similarly, at 1 h chase, all polymers significantly higher signal overlap with EEA1 when compared to AF; AF showed 14% whereas B-GalNAc$_{50}$ showed 32% (***p = 0.0003), BD-GalNAc 29% (**p = 0.0040), B-TAG$_5$ showed 26% (*p = 0.0300) and BD-TAG showed 28% (**p = 0.0061).

With respect to the lysosomes (LAMP1) (**Appendix Figure 49B**), AF revealed an increased trend in LAMP1 signal overlap which plateaued by 24 h. All polymers showed significantly higher overlap with LAMP1 at 0 h and 1 h chase when compared to AF. After 0 h chase, all liver targeting polymers had significantly higher signal overlap with LAMP regardless of DFO conjugation; 33% of AF signal vs 42% of B-GalNAc$_{50}$ (**p = 0.0012), 71% of BD-GalNAc (****p < 0.0001), 39% of B-TAG$_5$ (*p = 0.0276), and 74% of BD-TAG (****p < 0.0001). Additionally, after 1 h chase, all liver targeting polymers had significantly higher signal overlap with LAMP (p < 0.0001 for all comparisons).
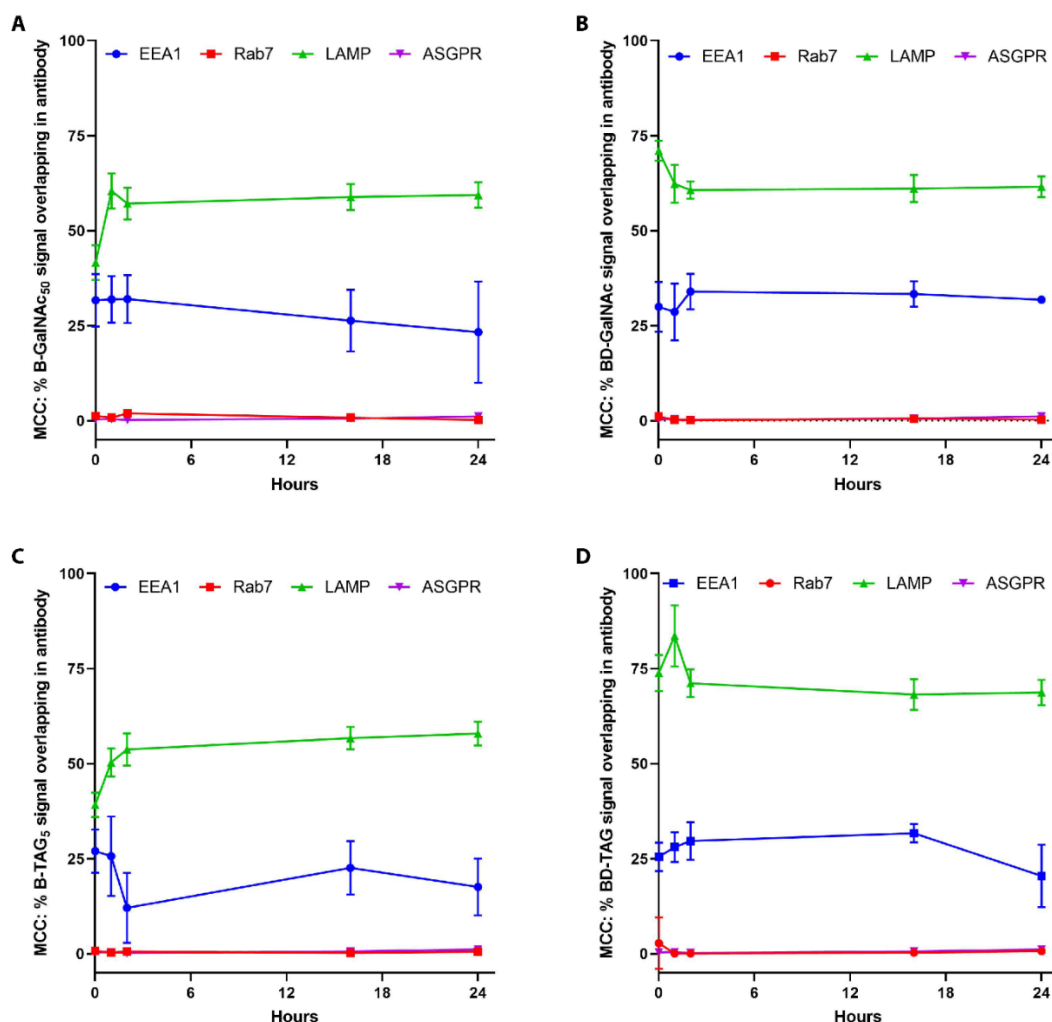
Appendix Figure 48. The kinetic investigation into the intracellular distribution of fluorescently labelled biodegradable liver targeting systems and their chelator counterparts. Mander's Co-localization Coefficients (MCCs) were reported as a percentage of (A) B-GalNAc$_{50}$, (B) BD-GalNAc, (C) B-TAG$_5$, and (D) BD-TAG overlapping with immunostaining signal for the different antibodies used to trace the endocytic pathway. The endocytic pathway was traced using fluorescent immunostaining to asialoglycoprotein-receptors (ASGPR), early endosomes (EEA1), late endosomes (Rab7) and lysosomes (LAMP1). At least 100 cells were acquired using Leica SP5 confocal scanning laser microscopy. MCCs was calculated from 5 to 18 independent regions of interest. The error bars show standard deviations. A 2-way ANOVA with Tukey's multiple comparisons test was performed to compare the differences in signal overlap with endocytic markers within the same polymer treatments. A 2-way ANOVA with Dunnett's multiple comparisons test was performed to compare differences in signal overlap with endocytic markers between polymer treatments. All statistical analysis were performed using GraphPad Prism.

Appendix Figure 49. A comparative kinetic investigation into the intracellular distribution of fluorescently labelled biodegradable liver targeting systems and their chelator counterparts against the endogenous ASGPR-specific protein, AF. Mander's Co-localization Coefficients (MCCs) were reported as a percentage of B-GalNAc$_{50}$, BD-GalNAc, B-TAG$_2$ and BD-TAG polymer signal overlapping with immunostaining signal for (A) early endosomes (EEA1) and (B) lysosomes (LAMP1). At least 100 cells were acquired using Leica SP5 confocal scanning laser microscopy. MCCs was calculated from 5 to 18 independent regions of interest. The error bars show standard deviations. A 2-way ANOVA with Dunnett's multiple comparisons test was performed to compare the MCCs for all liver targeting polymers to AF. All statistical analysis were performed using GraphPad Prism. **** represents p < 0.0001, *** represents p < 0.0010, ** represents p < 0.0100, and * represents p < 0.0500.

A.3.1.3. Evaluation of the *in vivo* pharmacokinetic profiles for biodegradable liver targeting chelating systems

Detailed pharmacokinetic investigations were performed to assess circulation half-life and the biodistribution for BD-GalNAc whereas the excretion profiles were observed for BD-GalNAc and BD-TAG over a 48 h after injection (**Appendix Figure 50**). The circulation half-life for BD-GalNAc was calculated using a two compartment model (**Appendix Figure 50A**), which revealed a distribution half-life of 0.39 h and a elimination half-life of 7.45 h. The biodistribution of BD-GalNAc also exhibited significant liver accumulation ($p < 0.0001$ at all time point when compared to all organs) with a 20% hepatic accumulation 30 mins after injection which was maintained for 8 h (**Appendix Figure 50B**). A significant decrease was observed from 18% at 8 h to 13% at 24 h ($p < 0.0001$). Minimal accumulation was observed in other organs, with less than 6% measured. The excretion profiles were compared for both BD-GalNAc and BD-TAG (**Appendix Figure 50C** and **D**). Both systems exhibited significantly more excretion via the hepatobiliary route when compared to the renal route ($p = 0.0007$ for BD-GalNAc and $p = 0.0050$ for BD-TAG). Additional work will be needed to compare the pharmacokinetic profiles of appropriate controls.

Given the rapid excretion observed for both BD-GalNAc and BD-TAG, these polymers were assessed for the in vivo chelation efficiency (**Appendix Figure 51**). No significant changes were observed for iron excretion via the feces, likely due to the DFO density on these systems. Whereas, BD-TAG exhibited a significant increase in urinary iron when compared to both BD and DFO (216 µg from BD-TAG vs 175 µg from BD, $p = 0.0015$; vs 180 µg from DFO, $p = 0.0037$). No significant changes were observed with respect to the liver burden and a decreasing trend was observed in serum ferritin. Although only 36 µg to 41 µg of additional iron was removed, this is encouraging as it suggests that this proof-of-concept has therapeutic potential and requires additional work on DFO density optimization.
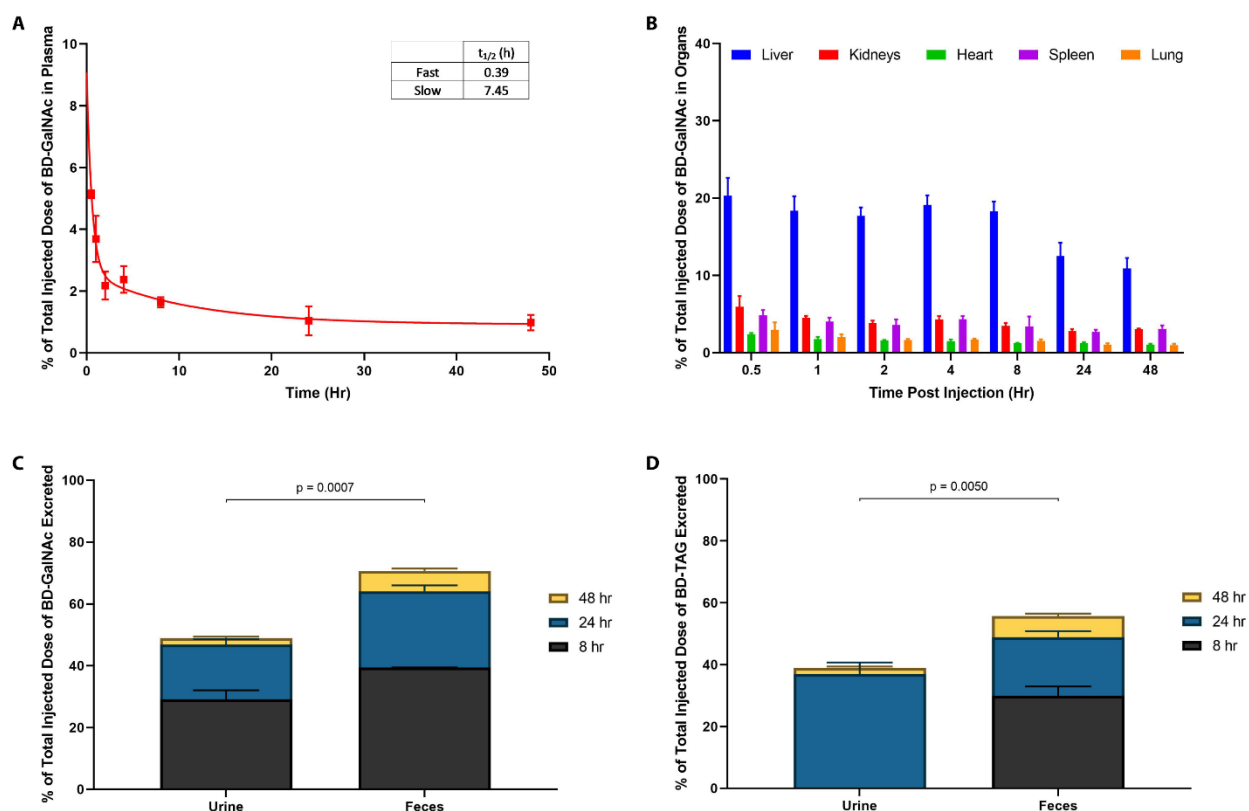
Appendix Figure 50. Pharmacokinetic properties of tritium labeled biodegradable liver targeting macromolecular chelating systems in C57BL/6 mice. Tritium labelled systems were injected at 10 mg/kg dose into mice. Radioactivity of BD-GalNAc was measured through scintillation counts in (A) plasma and (B) organs including the liver, kidneys, heart, spleen and lung. The excretion of biodegradable liver targeting chelating systems over the first 48 h for (C) BD-GalNAc and (D) BD-TAG. Error bars show standard deviations for a sample size of 3 mice. Circulation times were determined using a two-phase decay non-linear regression analysis in GraphPad Prism. A 2-way ANOVA with Dunnett's multiple comparisons test were performed to compare the accumulation of these biodegradable liver targeting systems in the liver against other organs. Unpaired t-tests were performed to compare the excretion between urine and feces after 48 h. All statistical analyses were performed using GraphPad Prism.
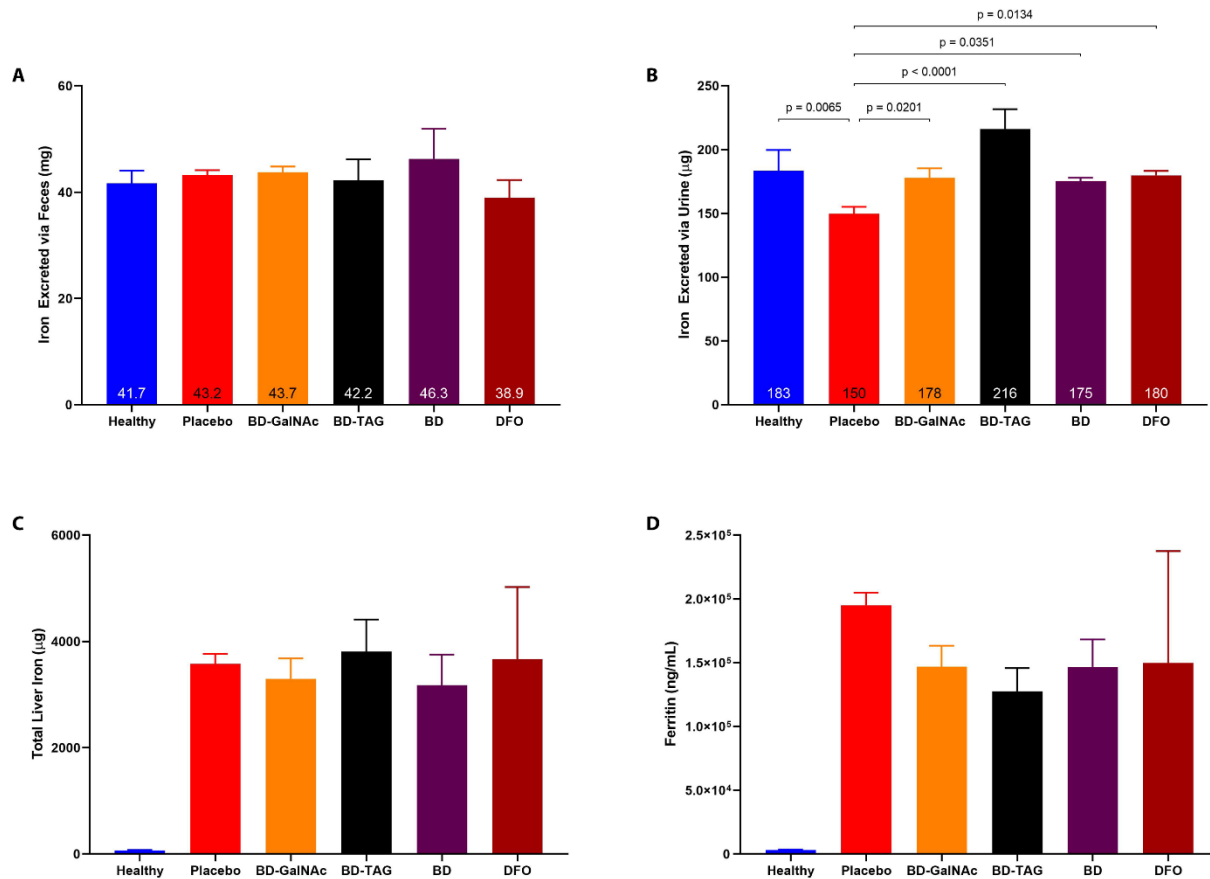
Appendix Figure 51. In vivo efficacy of biodegradable liver targeting chelating systems using iron overloaded C57Bl/6 mice. The excretion of iron in (A) feces and (B) urine, and (C) the liver iron burden were measured using the established *u*-ferene assay. (D) Serum ferritin was measured using an ELISA kit. Healthy mice represents non-iron overloaded C57Bl/6 mice treated with saline instead. Error bars show standard deviations from 3 independent replicates, each with an intraassay replicate. A 1-way ANOVA with Dunnett's multiple comparison tests were performed to compare the differences in treatment groups against iron overloaded saline control using GraphPad Prism.

A.3.1.4. Iron-dependent cellular responses to iron chelation in iron overload HepG2 model

Iron overloaded HepG2 cells were treated with 15 μM of small molecular weight chelators – DFO, DFX and DFP, or with 15 μM chelator equivalent of macromolecular systems - BD, BD-GalNAc, and BD-TAG (**Appendix Figure 52**). The reported clinically-relevant steady state concentration of DFO is between 10 to 28 μM and therefore, a concentration of 15 μM was used.

When comparing to untreated iron overload cells, all BHPG based polymers chelators showed a significant increase in iron concentrations (**Appendix Figure 52A** and **B**). BD and BD-GalNAc treated cells had a significant increase in both LIP and total iron concentrations ($p < 0.0001$ for all comparisons). BD-TAG treated cells only had a significant increase in LIP concentrations ($p = 0.0426$). DFO treated cells only had a significant reduction in total iron concentrations ($p = 0.0330$).

Further, BD, BD-GalNAc, BD-TAG, DFO and DFP showed a significant reduction in intracellular ROS generation (**Appendix Figure 52C**) when compared to untreated iron overload cells ($p < 0.0001$, $p < 0.0001$, $p < 0.0001$, $p < 0.0001$ and $p = 0.0119$, respectively). Remarkably, BD, BD-GalNAc, BD-TAG and DFO treated cells showed ROS levels comparable to the non-iron loaded control cells. DFX showed no significant changes in ROS.

In addition, transferrin receptor 1 (TfR1) expression was measured as cellular response to iron overload (**Appendix Figure 52D**). Under iron overload conditions, TfR1 expression decreased when compared to control and iron overloaded HepG2 cells ($p < 0.0001$). Upon treatment with iron chelators, TfR1 expression significant increased when compared untreated iron overload cells ($p < 0.0001$). While BD, BD-GalNAc, BD-TAG and DFP exhibited significant elevation in TfR1 expression, DFO and DFX increased expression beyond the non-iron overload control cells.
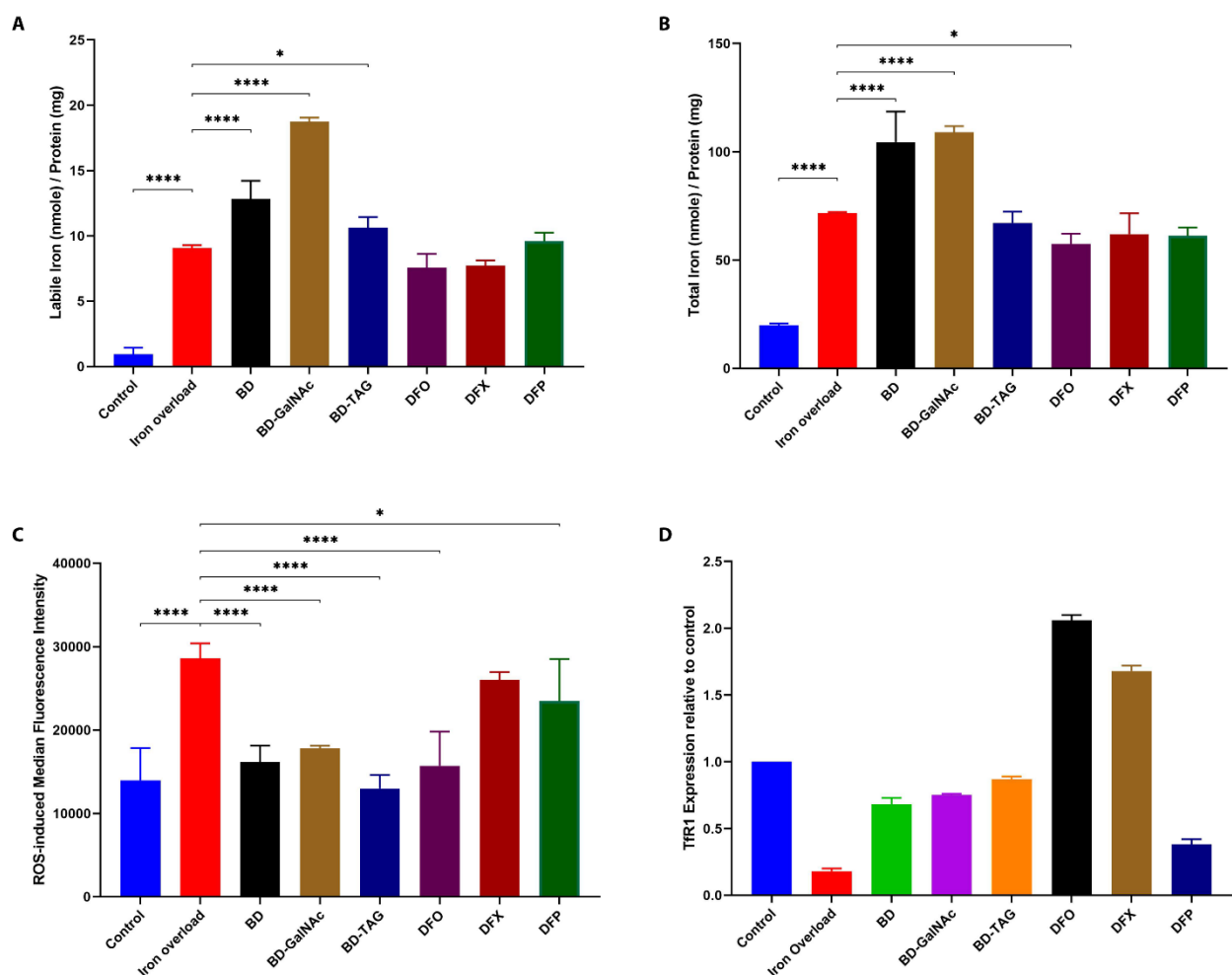
Appendix Figure 52. Effect of iron chelation in iron overload HepG2 cells. Labile iron (A) and total iron (B) were quantified using the u-ferene assay. (C) ROS generation was measured using a DCFDA/DCF ROS kit in at least 10,000 cells via flow cytometry. (D) Relative expression of TfR1, normalized to control cells, were measured using western blot and quantified using LI-COR's Odyssey Software Application. HepG2 cells were loaded with 50 μM following the established protocol. Error bars show standard deviations for N = 3 independent replicates. A 1-way ANOVA with Dunnett's multiple comparisons test were performed to compared iron overloaded cells with the either control or chelator treated cells. Statistical analysis were preformed using GraphPad Prism. **** represents $p < 0.0001$, *** represents $p < 0.0010$, ** represents $p < 0.0100$ and * represents $p < 0.0500$.

A.3.2. The design and development of small molecule liver targeted chelating systems.

A.3.2.1. *In vitro* cellular responses towards small molecular liver targeting chelating systems

Small molecular liver targeting chelating systems were developed by attaching TAG sugar groups directly to DFO, without a polymeric backbone. The rationale for this approach stems from the significant liver targeting and subsequent rapid excretion displayed by both non-biodegradable and biodegradable polyglycerol polymers, HPG and BHPG. Whilst DFO displays a very short half-life (approximately 5 minutes in mice), we hypothesized that conjugating TAG directly to the DFO will result in a liver specific accumulation of DFO which can then stably chelate and remove hepatic iron.

In order to do so, the number of TAGs on a linker – with either 1 TAG (1 TAG-NH$_2$) or 2 TAG (2 TAG-NH$_2$), were first optimized with respect to binding and uptake over a wide range of concentrations (**Appendix Figure 53**). 2 TAG-NH$_2$ displayed significantly higher binding and uptake response at concentrations of 5 μM and above (p < 0.0001 for all comparison at 5 μM and above) (**Appendix Figure 53A**). At 5 μM, 1 TAG-NH$_2$ showed a 11 fold increase whereas 2 TAG-NH$_2$ exhibited a 23 fold increase. To further characterize the interaction of both 1 TAG-NH$_2$ and 2 TAG-NH$_2$, the cellular responses were competitively inhibited using unlabelled GalNAc (**Appendix Figure 53B**). The half-maximal inhibitory concentrations (IC$_{50}$) for 1 TAG-NH$_2$ was 750 μM [650 μM, 870 μM] which was significantly higher than the IC50 value for 2 TAG-NH$_2$, 350 μM [320 μM, 490 μM]. 1 TAG-NH$_2$ exhibited IC$_{50}$ values almost twice as high as 2 TAG-NH$_2$, suggesting of a much tighter interaction with the ASGPR on HepG2 cells. Additionally, in order to assess the non-specific or ASGPR-independent binding and uptake responses, the binding and uptake were investigated in both HepG2 cells maintained on ice to prevent receptor mediated endocytosis (**Appendix Figure 53C**) and an ASGPR negative cell line - HeLa cells (**Appendix Figure 53D**). Both systems showed similar cellular responses with no significant differences between the two small molecule liver targeting systems.

Given this, 1 TAG-NH2 was conjugated with 1 DFO, TAG-DFO, and the intracellular distribution was compared with 1 TAG-NH$_2$ (**Appendix Figure 54** and **Appendix Figure 55**). HepG2 cells were incubated with 2 μM of either 1 TAG-NH$_2$ or TAG-DFO for either 2 h or 24 h. Lysosomes were identified using anti-LAMP1 antibodies. The MCCs of 1 TAG-NH$_2$ or TAG-DFO overlapping with LAMP1 were compared. The MCCs of 1 TAG-NH$_2$ significantly increased from 27% after 2 h incubation to 52% after 24 h incubation (p = 0.0340) whereas the MCCs of TAG-DFO significantly decreased from 42% after 2 h incubation to 18% after 24 h (p = 0.0383).
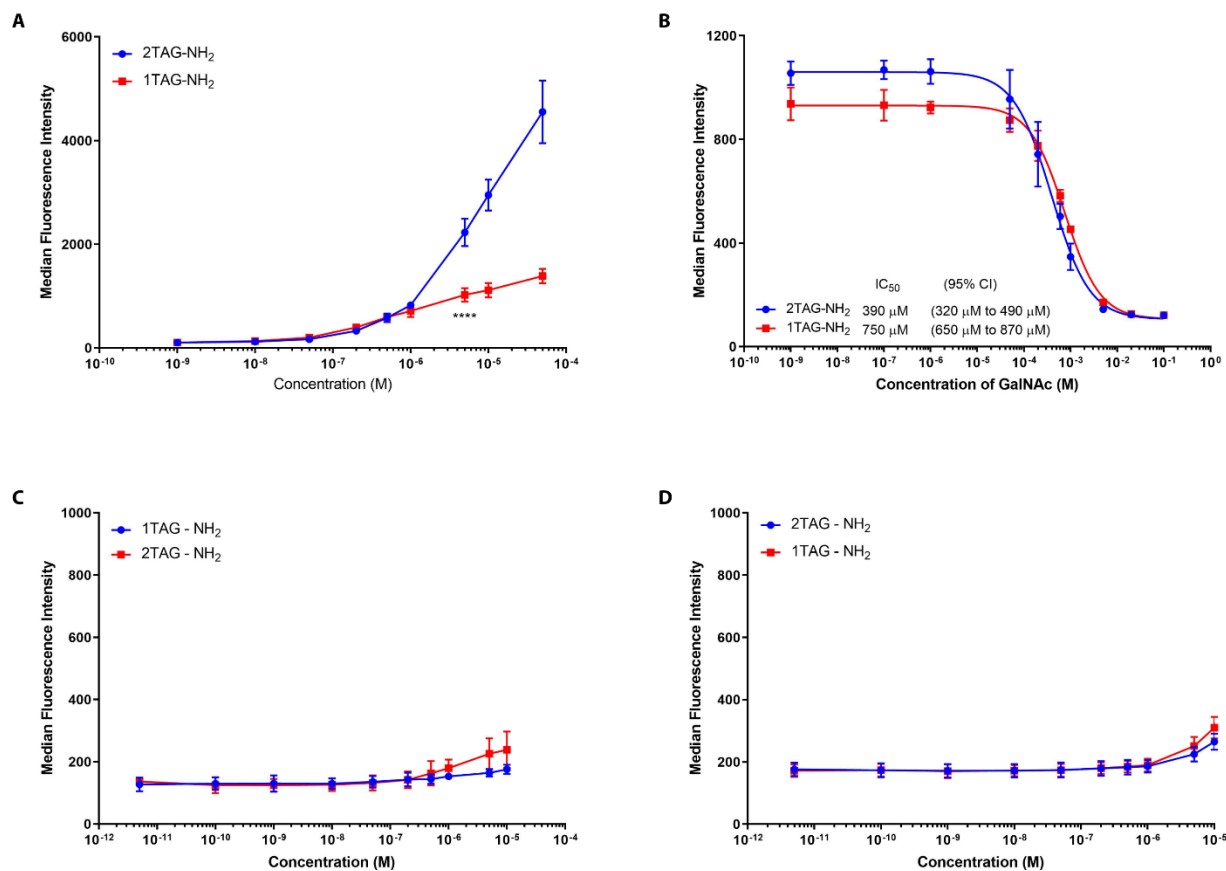
Appendix Figure 53. The binding and uptake of small molecular liver targeting systems. (A) The concentration profiles for small molecular liver targeting systems were measured in at least 10,000 cells. (B) The IC_{50} values were determined by increasing the concentration of unlabelled GalNAc as a competitive inhibitor for ASGP-R. The non-specific or ASGPR-independent binding and uptake of small molecular liver targeting systems were investigated in (C) HepG2 cells incubated with polymers at 4°C minimizes receptor mediated endocytosis and (D) HeLa cells have been used as an ASGPR negative cell line. Error bars show standard deviations for a sample size of 3 independent replicates.
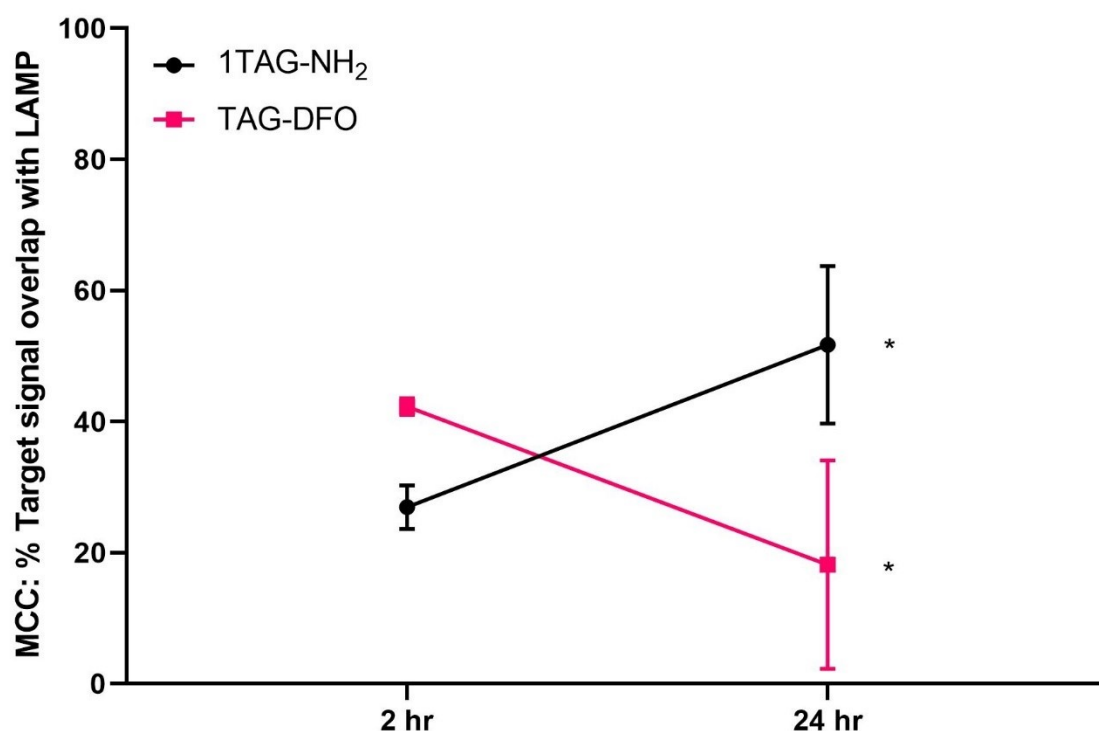
Appendix Figure 54. The intracellular distribution of 1 TAG-NH$_2$ and TAG-DFO at 2 μM incubated for either 2 or 24 hours in HepG2 cells. HepG2 cells were incubated with 2 μM of 1 TAG-NH$_2$ or TAG-DFO for the full duration of either 2 h or 24 h at 37°C. At least a 100 cells were acquired and analyzed. Lysosomes were immunostained using anti-LAMP1 antibodies (LAMP1). Mander's Co-localization Coefficients (MCCs) were reported as a percentage of small molecule liver targeting systems signal overlapping with LAMP1. MCCs were calculated from at least 5 different regions of interest and the error bars show standard deviations. A 2-way ANOVA with Sidak's multiple comparison test was performed to compare differences in MCCs for LAMP1 at 2 or 24 h. All statistical analysis were performed using GraphPad Prism. * represents $p < 0.0500$.
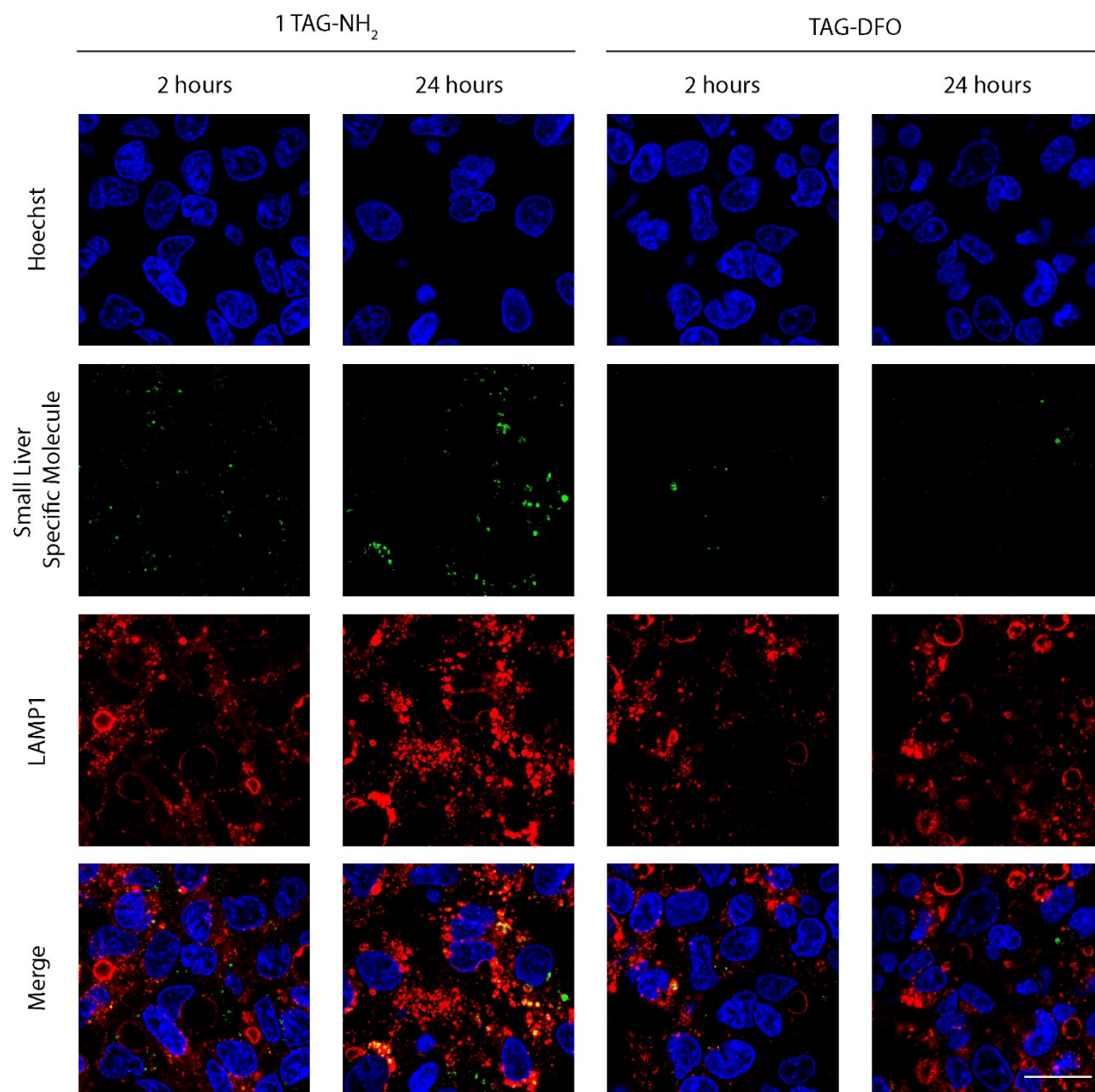
Appendix Figure 55. Intracellular distribution of fluorescently-labelled small molecular liver targeting linkers and their chelator in HepG2 cells. Cells were incubated with 2 μM of 1 TAG-NH$_2$ or TAG-DFO for either 2 h or 24 h. Images were acquired using confocal laser scanning microscopy with immunostaining to identify lysosomes (LAMP1). Nucleus was stained using Hoechst, represented as blue. Lysosomes were stained using mouse anti-human LAMP antibodies, represented as red. Polymers were fluorescently labelled with carboxyrhodamine, represented as green. At least 100 cells were imaged. Representative confocal micrographs are shown here. The scale bar represents 0.5 μm.